Integrated seismic and structural interpretation of reactivated fault systems in sedimentary basins

Abubakar Maunde

A project thesis submitted to the School of Earth and Environmental Sciences, Cardiff University in partial fulfilment of the requirements for the award of the degree of Doctor of Philosophy (Ph.D.) in Earth Sciences.

September, 2021

Integrated seismic and structural interpretation of reactivated fault systems in sedimentary basins

Abubakar Maunde

(B.sc: Unimaid; M.sc: Leeds)

Dedication

I dedicate this PhD research work to my late father (Alhaji Maunde)

Author's note and status of publications

- **Chapter 4** has been published as Maunde, A. and Alves, T.M. (2020). Impact of tectonic raft's gravitational instability on faut reactivation and geomerty. Journal of Structural Geology, 130, 103916. https://doi.org/10.1016/j.jsg.2019.103916.

- **Chapter 5** has been published as Maunde, A. and Alves, T.M. (2021). Effect of tectonic inversion on supra-salt faut geometry and reactivation histories in the Southern North Sea. Journal of Marine and Petroleum Geology, 135 (2022) 105401.

- **Chapter 6** has been published as Maunde, A., Alves, T.M. and Gregory F. M. (2021). Shallow fault systems of thrust anticlines responding to changes in accretionary prism lithology (Nankai, SE Japan). Tectonophysics, 812, 228888. https://doi.org/10.1016/j.tecto.2021.228888.

Although the articles are jointly co-authored with the project supervisory team, the work presented in the three articles is that of the lead author, Abubakar Maunde. Editorial work was provided by the supervisory team in accordance with a normal thesis chapter.

Acknowledgements

Abstract

This thesis investigates the impact of tectonic shortening on the reactivation and growth histories of normal fault systems from the Espírito Santo Basin (SE Brazil), Broad Fourteens Basin (Southern North Sea) and Nankai accretionary prism (SE Japan). In the Espírito Santo Basin, 3D seismic data were used to assess the impact of tectonic rafting, and associated gravitational instability of the continental slope, on the geometry and reactivation histories of faults formed above rollover anticlines. The data showed that the complex fault geometries observed above rollover anticlines are primarily due to three distinct stages of downslope gravitational instability of tectonic rafts. Stage 1 (post-Albian to Coniacian) caused the supra-salt strata to fragment into discrete blocks of strata (rafts) separated by large listric (roller) faults and associated wide rollover anticlines in their hanging-walls. In stage 2 (Early Santonian), the continued evacuation of salt from upper-slope regions to the base of the continental slope promoted the progressive downslope translation of rafted strata and triggered the reactivation of rollover faults in the form of crestal fault systems associated with local extensional collapse. Stage 3 (Middle/Late Eocene) caused tectonic rafts to be translated downslope until salt welds were formed and post-salt strata became grounded over pre-salt successions. The grounding (welding) of tectonic rafts over the pre-salt successions was progressive and accompanied by moderate translation of blocks during the Cenozoic. Differences in the degree of downslope translation of un-welded rafts further enhanced the reactivation of rollover faults, a phenomenon that promoted the migration of hydrocarbons from welded sub-salt source units into supra-salt reservoirs. As a corollary, this Chapter shows that tectonically generated pulses of compression and uplift, commonly related to the Andean Orogeny, are not the only mechanisms deforming post-salt overburden units in proximal extensional dominated regions of the southeast Brazilian margin. In fact, the close control of tectonic rafts gravitational instability induced a continuum of overburden deformation and contributed significantly to shaping the supra-salt overburden in the Espírito Santo Basin.

In the Broad Fourteens Basin, 3D seismic and borehole datasets were used to investigate the effect of lithological variations on fault-throw distribution and segmentation, as well as on the geometry and reactivation histories of faults developed due to tectonic inversion. It was shown that the Late Cretaceous to Paleogene tectonic inversion

affecting the Broad Fourteens Basin induced a continuum of deformation and contributed significantly to the formation and subsequent reactivation of Late Mesozoic faults. Late Cretaceous inversion (i.e., the Sub-Hercynian inversion episode) led to the formation of broad anticlines associated with normal faults in Upper Mesozoic strata. The progressive bending and stretching of outer-arc Mesozoic strata during the Early Paleocene inversion episode (i.e., Laramide episode) reactivated the older Sub-Hercynian faults. In a last stage, the Pyrenean (Oligocene) and Savian (Miocene) inversion episodes reactivated some of these faults upward into Tertiary strata.

Offshore Nankai (SE Japan), 3D pre-stack depth migrated seismic data were used to analyse the geometry and growth of shallow faults associated with tectonic shortening in prominent thrust anticlines. These thrust anticlines show a trenchward increase in horizontal shortening and deform the seafloor at present in response to plate subduction off Nankai. It was shown that the presence of closely spaced vertically segmented fault arrays at shallow stratigraphic levels - with relatively small local throw maxima - relate to the existence of more incompetent (soft) intervals blanketing the Nankai accretionary prism. These shallow fault geometries accommodate a significant part of the bending and stretching strain occurring during the development of thrust anticlines and subsequent local stress redistribution during seismic events.

The anomalous vertical fault throw distributions documented in the three study areas in this thesis are inconsistent with models of fault growth by uniform slip distribution and radial tip-line propagation. It is concluded that fault reactivation and growth by segment dip-linkages characterised the evolution and growth of all the faults interpreted in the three study areas. Where two separate faults with local throw maxima propagate towards each other and linked in throw-minimum in the throw-depth (T-Z) profiles. Fault segments with local throw maxima in the throw-depth (T-Z) profiles are early-stage fault segments and represent regions where faults localise first in competent intervals. Each segment of these early-stage faults propagates outwards until they encounter other fault strands and link together. Linkage points are located where local throw minima are recorded in less competent intervals. Consequently, the propagation of slip from fault segments (with local throw maxima) in the competent intervals into the incompetent intervals resulted into vertically segmented fault arrays. Vertical fault segmentation increases the chances of strata compartmentalisation and localised fluid

flow through fault linkages, at the same time presenting significant risks when injecting CO_2 in subsurface traps.

Table of Contents

CHAPTER 1: Introduction and Literature Review

2. Geological setting of the three study areas in the thesis

3. Data and Methods

4. Impact of tectonic raft's gravitational instability on fault geometry and growth histories

5. Effect of tectonic inversion on supra-salt fault geometry and reactivation histories

6. Shallow fault systems of thrust anticlines responding to changes in accretionary prism lithology (Nankai, SE Japan)

7. Summary and Discussion

List of Figures

Fig. 6.12. a) Uninterpreted and b) interpreted seismic sections highlighting the geometry of shallow fault populations around the hinge region of Thrust Anticline C. These faults are closely spaced and vertically segmented, with some propagating and linking with other faults, c) Representative vertical throw distribution of shallow faults. These faults are vertically segmented with relatively larger fault throw maxima. Fault segments with throw maxima nucleate first in more competent (stronger) intervals and

List of Tables

List of Equations

CHAPTER 1

Introduction and Literature Review

1.1. Background and hypotheses of research

1.1.1. Research background

Fault reactivation has been described as reflecting the further propagation of a pre-existing fault (Peacock and Sanderson, 1991; Cowie and Scholz, 1992; Cartwright et al., 1995; Holdsworth et al., 1997; Nicol et al., 2005; Walsh et al., 2002; Kim and Sanderson, 2005). Such reactivated fault zone represents an important control on fluid transport in the crust, affecting all kinds of fluids, including hydrocarbons, CO_2 and other volatiles, hydrothermal solutions, metamorphic fluids, magma, and ground water. The main reason for this is the increased structural complexity found at reactivated fault zones, with increased numbers of faults and fractures and a wider range of orientations (Peacock and Parfitt, 2002; Fossen et al., 2005).

Multiple researchers have used seismic data, outcrop data and numerical modelling to investigate the reactivation and growth history of tectonic faults, later proposing several fault-growth models (Walsh and Watterson, 1988; Peacock and Sanderson, 1991; Cowie and Scholz, 1992; Cartwright et al., 1995; Kim et al., 2000; Walsh et al., 2002; Kim and Sanderson, 2005). Largely, the published literature demonstrated, or suggested, that in the early stages of fault development each fault grows as an isolated fault, with subsequent growth continuing through soft linkages between different faults and, finally, through hard linkages. This process results in the formation of a large range

of fault scales and a saw-like plane on the surface (Fossen, 1997). It is now recognised that larger faults are a result of fault-segment linkage associated with propagation in both the vertical and horizontal directions (Cartwright et al., 1995; Mansfield and Cartwright, 2001; Dawers and Anders, 1995). However, Morley (1999) argued for an early linkage of multiple smaller faults, rather than growth following the isolated fault model. A supplementary model was presented by Lohr et al. (2008) who demonstrated that most faults grow by the linkage of multiple smaller fault segments, whereas tip propagation is of relatively minor importance.

Fault reactivation and growth histories are controlled by multiple variables such as the interplay between the local stress field and mechanical stratigraphy. Mechanical stratigraphy strongly influences fault reactivation and, especially, the ability of faults to reactivate across distinct mechanical intervals, their deformation mechanisms, and fault zone architecture (Wilkins and Gross, 2002; Ferrill and Morris, 2008; Welch et al., 2009; Childs et al. 2009; Libak et al., 2019). Reactivated faults are often seen to be vertically restricted and segmented by mechanically incompetent layers (Childs et al. 2009; Roche et al., 2013; Maunde et al., 2021). Incompetent layers can act as detachments that cause decoupling and prevent the propagation of faults across specific intervals. In addition, the locus of deformation can be shifted laterally across the incompetent layers (Withjack and Callaway 2000; Bahroudi et al. 2003; Gabrielsen et al. 2016). Such a shift in fault position across an incompetent layer can result in vertical fault segmentation whereby fault segments can be hard-linked or soft-linked.

As mechanical differences in distinct strata, or rock interval, control fault reactivation and geometries (Peacock and Sanderson, 1991; Gross et al. 1997; Soliva et al. 2005;

Ferrill et al. 2017), the relationship between faulting and mechanical stratigraphy can be used either to predict fault geometries or, conversely, interpret mechanical stratigraphy based on characterisation of the fault geometries (Ferrill and Morris, 2003, 2008; Ferrill et al., 2017). To better understand the effect of fault reactivation and growth histories on fault zone architectures is therefore crucial, as it can provide insights into the timing of fault activity, with direct application to hydrocarbon migration and sealing of faults in petroleum reservoirs, CO_2 reservoirs, and even geothermal prospects (McClay, 1990; Caine et al. 1996; Wiprut and Zoback, 2000, 2002; Cartwright et al., 2007; Ward et al., 2016).

1.1.2. Research hypotheses

Using high quality 3-D seismic reflection and borehole datasets, detailed mapping of stratigraphic horizons, fault geometries and vertical component of dip separation (throw) characterises the effect of distinct magnitudes of tectonic shortening on the reactivation and growth histories of normal faults in three study areas: i) a salt-withdrawal basin from the Espírito Santo Basin, SE Brazil, ii) a tectonically inverted basin in the Broad Fourteens Basin, offshore The Netherlands (Southern North Sea), and iii) a tectonically subducted basin in the SE Japan (i.e. the Nankai accretionary prism). Consequently, this thesis aims to test the following research hypotheses:

a. **Downslope gravitational instability of tectonic rafts induced crustal shortening of overburden rocks and enhanced the reactivation of pre-existing faults in crestal collapse systems of rollover anticlines, a process favouring the migration of hydrocarbons from welded sub-salt source units into supra-salt reservoirs**. If this hypothesis is true, the whole of the thick, outer-arc region of the rollover anticline undergoes extension and associated faults propagate almost to the

base of the anticline. If this hypothesis is false, some reverse faults will be identified associate with the crestal collapse of the interpreted rollover anticlines.

b. **Tectonic shortening affecting reservoir units promotes the reactivation of pre-existing faults and potentially allows the secondary migration of hydrocarbons into shallower reservoir units, consequently reducing the integrity of traps.** If true, reactivated segments of pre-existing faults will be identified as offsetting shallower reservoir units. If false, reactivated fault segments will be limited to the deepest reservoir units and will not reduce the integrity of traps.

c. **Mechanical stratigraphy strongly influences fault localisation and growth histories, especially the ability of faults to propagate across mechanical layers, their displacement distributions, and overall fault zone architecture.** If this hypothesis is true, systems of vertically segmented faults will be identified whereby fault segments with local throw minima in incompetent (ductile) intervals are linked to pre-existing fault segments with local throw maxima in competent (brittle) intervals. If false, no significant segmentation in fault throw will be observed as faults propagate through multilayer sequences.

The following section comprises a literature review of the relevant topics studied in this thesis, describing reactivation and growth of normal faults through mechanically layered sequence and salt tectonics.

1.2. Mechanical stratigraphy and faulting

The term 'mechanical stratigraphy' encompasses the rock mechanical properties, layer thickness, and frictional properties of mechanical boundaries (Groshong, 2006; Ferrill and Morris, 2008; Laubach et al., 2009; Ferrill et al., 2017). Together, these components

lead to variations in stiffness and strength in layered sedimentary rocks (Ferrill et al., 2017). Differences in the mechanical behaviour of rock layers have long been recognized as influencing structural style related to normal faulting (Forster, 1809, 1821; Wallace, 1861).

In mechanical stratigraphic studies, the terms strong vs. weak, stiff vs. compliant, hard vs soft, or competent vs. incompetent provide a conceptual framework for structural interpretations and descriptions, but they are inherently qualitative and interpretative (Ferrill and Groshong, 1993; Ferrill and Morris, 2008; Ferrill et al., 2017). In strong, stiff, or competent lithologies, rocks tend to resist deformation, maintain bed length and thickness during deformation, accommodate little deformation before brittle failure or have low ductility. In contrast, weak, soft, or incompetent lithologies tend to deform relatively easily, change bed length and thickness during deformation, accommodate significant deformation prior to brittle failure or have high ductility (Ferrill and Morris, 2008; Ferrill et al., 2017).

There is a number of variables capable of controlling the competence of sedimentary rocks; mineralogy, porosity, grain size and texture, confining pressure, temperature, and pore pressure. Mineralogically, the strongest constituents in sedimentary rocks generally include calcite, dolomite and quartz, whereas the weakest constituents are likely to be clay minerals, organic carbon and evaporite minerals such as salt, gypsum, or anhydrite (Donath, 1970). Strength can be highly sensitive to the proportion of clay minerals in rock (Laubach et al., 2009). Importantly, rock strength tends to increase with increasing cementation, compaction, welding, and with decreasing porosity (Dunn et al., 1973; Chang et al., 2006; Zoback, 2007).

Porosity plays a vital role in controlling the competence of sedimentary rocks (Davis et al., 2017). Porous rocks are usually less competent than non-porous rocks, even when dealing with similar lithologies (Chang et al., 2006). Porous rocks tend to deform via different deformation mechanisms to form non-porous rocks, since porous rock grains can reorganize themselves by translating and rotating without recording any cataclasis (Torabi and Zarifi, 2013). In the upper 2-3 km of the crust, the mechanical properties of clays are primarily controlled by mechanical compaction; hence, most claystones tend to be incompetent at these burial depths (Mondol et al., 2007). Below a depth of 2-3 km some clay types are chemically altered, which causes an increase in the competence of the rock depending on the type of the clay (Peltonen et al., 2009). Thus, porosity generally decreases at greater burial depths and, therefore, mineralogy and rock texture become the main variables controlling rock strength.

Sandstones are more prone to alteration by fluids than clays, due to higher permeability. The physical properties of shallow-buried sandstones are primarily controlled by mechanical compaction, although calcite cementation can occur even in shallow depths (Morad, 1998). At deeper burial depths (i.e., greater than 2 km) the porosity reduction is primarily caused by cementation, turning the incompetent sandstone into competent rocks (Stone and Siever, 1996). Carbonate rocks are normally considered as competent rocks. However, carbonates also behave as sandstones whereby porous rocks are relatively incompetent and low-porosity rocks are more competent (Ferrill et al., 2017). Carbonates are much more prone to alteration by diagenesis than siliciclastic rocks, and pore type strongly controls their elastic properties (Eberli et al., 2003).

Sedimentary sequences experience significant mechanical property changes related to their diagenetic histories (Laubach et al., 2009). Such changes can lead to strengthening the rock mass through mechanical compaction (porosity loss) and cementation and

increasing the frictional resistance to sliding of layer boundaries by pressure solution and the development of stylolitic contacts (Ferrill et al., 2017). However, unloading, weathering, thermal contraction, freezing, drying, and changes in the amount, phase, or composition of fluid in the rock can all influence rock strength characteristics (Ferrill et al., 2017).

In layered sedimentary rocks the interplay between the local stress field and mechanical stratigraphy of the host rock has been found to influence a rock's failure mode (Ferrill and Morris, 2003, 2008; Ferrill et al., 2012, 2014), fault nucleation and propagation (Eisenstadt and DePaor, 1987; Ferrill and Morris, 2008; Welch et al., 2009), fault dip geometry (Walsh and Watterson, 1988; Peacock and Sanderson, 1992; Childs et al., 1996; Ferrill and Morris, 2003; Ferrill et al., 2012, 2014), fault displacement gradient (Welch et al., 2009; Ferrill et al., 2011, 2012, 2016), displacement partitioning (Ferrill et al., 2011, 2016), and fault zone width (Childs et al., 1996; Ferrill et al., 2007, 2012).

1.2.1. Modes of rock failure

The failure, or yielding, of geologic materials is defined as the rapid increase in the accumulation of strain for a given increase in applied stress and is preceded by some amount of pre-failure strain (Ferrill et al., 2017). The failure mode is directly related to rock mechanical properties and the effective stress conditions affecting a volume of rock at the time of failure (Ferrill and Morris, 2003; Ferrill et al., 2017). Failure

envelopes are commonly used to summarise failure behaviour for a single rock type under a range of effective stress conditions (Hoek and Brown, 1988) (Fig. 1.1).

Studies have shown that brittle rocks can fail in opening, shearing or hybrid modes (Hancock, 1985; Ferrill and Morris, 2003) (Fig. 1.1). Tensile and shear failure modes are both common in the upper crust (Mandl et al., 1977; Price and Cosgrove, 1990; Mandl, 2005) and the transition from tensile to shear failure (for a similar material) occurs with an increase in effective mean stress. Kettermann and Urai (2015) defined two structural domains with a characteristic structural style: extensional failure with open fractures at low overburden pressures, and shear failure at higher overburden pressures. These represent end-members with robust structural styles that will not change by increasing or decreasing overburden pressure any further. There is no sharp boundary between these end-members. Instead a continuous transformation from tensile to shear failure occurs, which Kettermann and Urai (2015) referred to as hybrid failure (Fig. 1.1c).

1.2.1.1. Tensile failure

In tensile, opening-mode, or extension fractures (i.e., joints, veins), the displacement is perpendicular to the fracture surface (Figs. 1.1a). Such extensional fractures form perpendicularly to the minimum principal stress, σ_3, and have a sense of displacement that is characterised by fracture opening normal to its walls, with no appreciable movement parallel to these same walls (shear) (Fig. 1.1a).
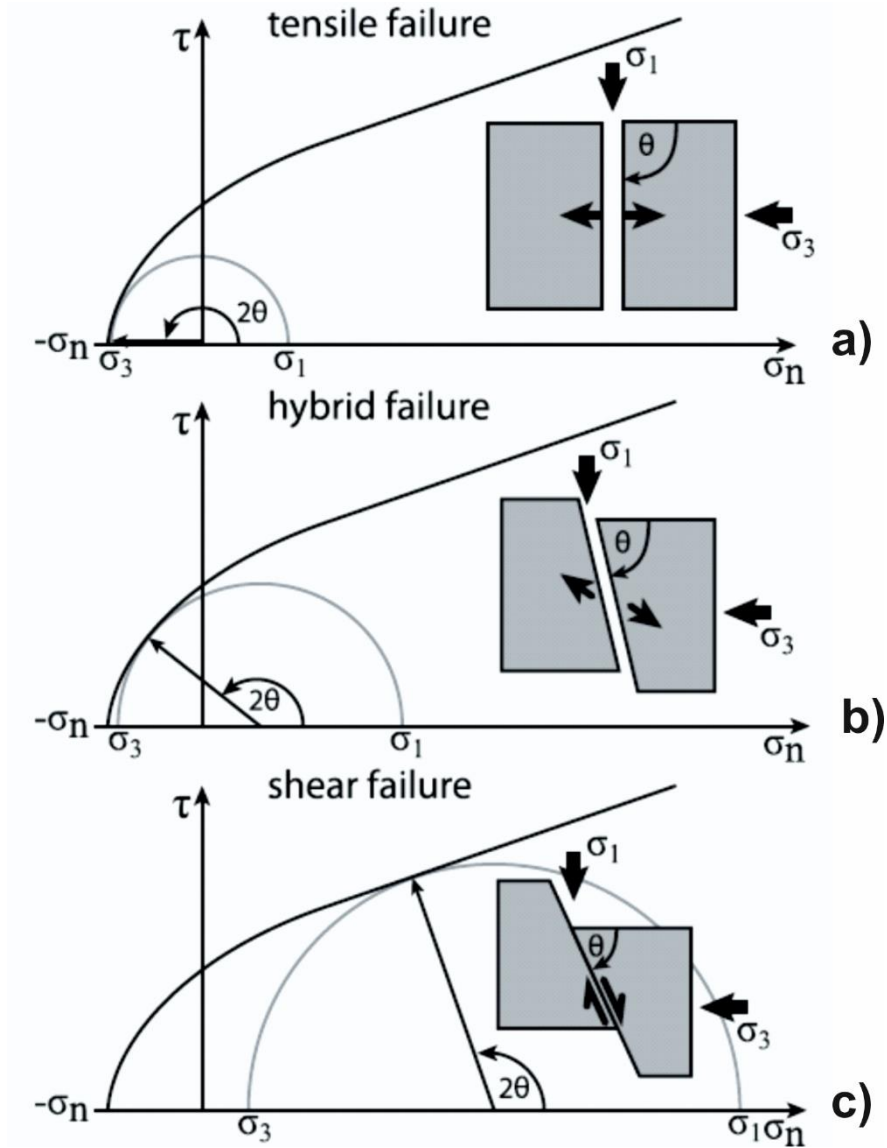
Fig. 1.1. Schematic illustration representing the Mohr-Coulomb failure criterion with respect to a normal faulting stress regime for a) tensile, b) hybrid and c) shear failure. In the figure, σ_1, σ_2 and σ_3 represent the maximum, intermediate and minimum principal effective stresses. Modified from Kettermann and Urai (2015).

1.2.1.2. Shear failure

The failure mechanism that is predominantly associated with fault formation is shear failure, which characterized by formation of a fracture surface with displacement parallel to the plane of the fracture (Hancock, 1985; Hoek and Brown, 1988; Mandl, 1988) (Figs. 1.1c and 1.2a). This shear failure surface commonly shows slip lineations or slickenlines that are parallel the direction of fault displacement.

Anderson (1951) described the relationships between distinct fault planes and the corresponding stresses acting perpendicular to each other, with one stress direction always near vertical (σ_v) while the other two directions are horizontal $(\sigma_H > \sigma_h)$. The orientation of each principal stress relates to the type of fault produced (Fig. 1.2). This leads to a prediction of the three most common fault types and their dips; normal, reverse and strike-slip faults (Fig. 1.2). A fault is termed normal or reverse based on the relative displacement of its hanging-wall with respect to the footwall. For a normal fault, the hanging-wall is displaced downwards with respect to the footwall (Fig. 1.2a), whereas in reverse faults the hanging-wall is displaced upwards with respect to the footwall (Fig. 1.2c). Normal faults typically dip ~60°, reverse faults average ~30°, and strike-slip faults are sub-vertical (Anderson, 1951).

Using the typical 'Andersonian model' in faults recording normal displacements (see Fig. 1.2a), the maximum principal stress (σ_1) is vertical, whereas the minimum principal stress (σ_3) is horizontal. Therefore, an intermediate principal stress (σ_2) can be inferred as being parallel to the fault plane (Figs. 1.1c and 1.2a). In reverse or thrust faults, the maximum principal stress (σ_1) is horizontal and the minimum principal stress (σ_3) is vertical. The intermediate stress (σ_2) is again horizontal, parallel to the strike of the fault plane (Fig. 1.2c). In strike-slip faults, both the maximum principal stress (σ_1) and

minimum principal stress (σ_3) are roughly horizontal, indicating that the intermediate stress (σ_2) is the vertical stress axis (Anderson, 1951) (Fig. 1.2b).

The transition between extension (tensile) failure and shear failure (i.e. Hybrid failure) has long been hypothesised, but its existence in naturally deformed rocks remained controversial (Hancock, 1985; Mandl, 1988). Recent work indicates that induced hydraulic fracturing can produce hybrid failure and associated shear and tensile fractures (Busetti et al., 2014; Smart et al., 2014) (Fig. 1.1b). Hancock (1985) described how failure mode is closely related to the differential stress, σ_d (i.e., difference between maximum principal stress (σ_1) and minimum principal stress (σ_3) at the time of failure, and the tensile strength **(T)** of the rock. Tensile fractures are expected to form where σ_d **< 4T,** whereas shear fractures are expected to form where σ_d **> 8T**. Finally, hybrid fractures are expected to form under conditions where **4T <** σ_d **< 8T** (Hancock, 1985).

1.2.2. Fault nucleation

The analysis of pre-failure strain for a variety of common sedimentary rock types demonstrates significant changes in ductility as a function of confining pressure and rock type (Handin and Hager, 1957; Donath, 1970). Incompetent lithologies (e.g., clay-rich strata, shales) can accommodate greater amounts of pre-failure strain when compared to competent lithologies (i.e., clay-poor strata, limestones or dolomites) under the same conditions of deformation (Ferrill and Morris, 2008; Donath, 1970) (Fig. 1.3a).

Experimental studies demonstrate that, as strain accumulates in a mechanically layered sedimentary section, brittle layers will fault first whereas ductile layers accommodate greater pre-failure strain prior to faulting (Donath, 1970; Ferrill and Morris, 2003, -
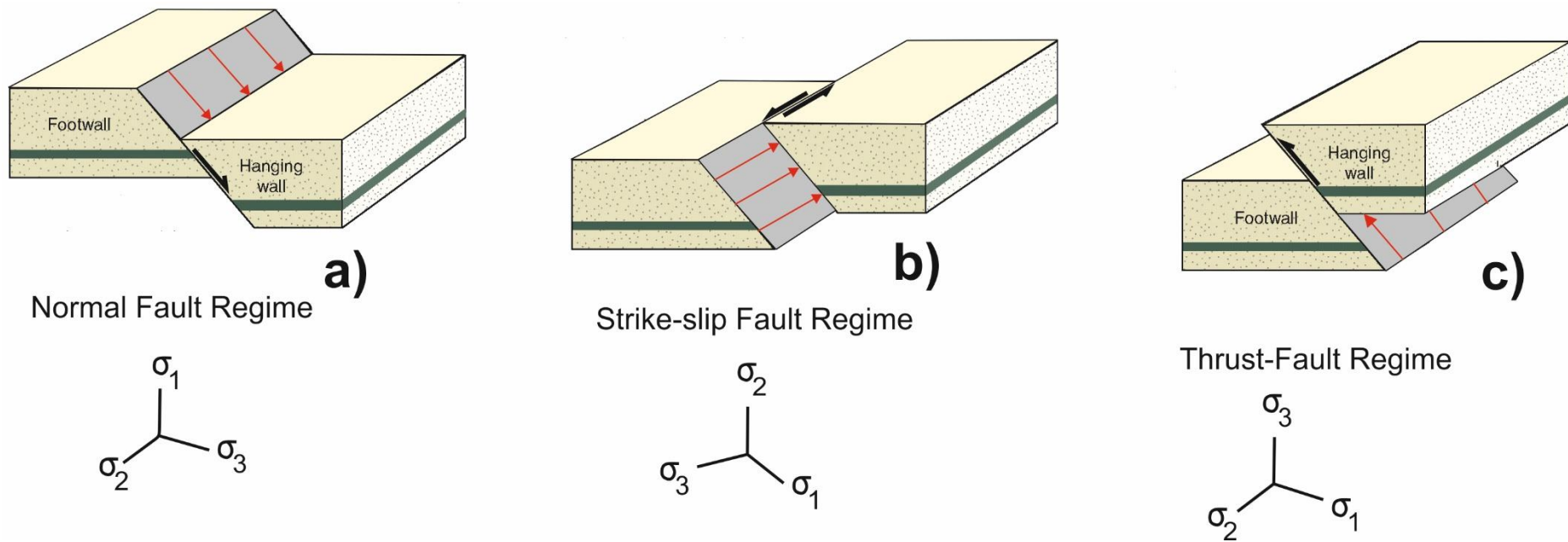
Fig. 1.2. Fault classification and orientations at the surface of the earth predicted from Andersonian stress theory, a) normal fault, b) strike-slip fault and c) thrust fault. Where σ_1, σ_2 and σ_3 represent the maximum, intermediate and minimum principal effective stresses.

2008; Welch et al., 2009; Ferrill et al., 2012) (Fig. 1.3b). Thus, faults are expected to nucleate first in more competent layers with throw maxima, and field investigations and this study show this to be the case (Eisenstadt and DePaor, 1987; Ferrill et al., 2012, 2016).

1.2.3. Fault reactivation

Fault reactivation has been described as reflecting the further propagation of pre-existing faults (Cartwright et al., 1995; Mansfield and Cartwright, 2001; Baudon and Cartwright, 2008). The ability for a fault to repeatedly reactivate is sensitive to its orientation with respect to the stress field, and to the mechanical properties of the fault surface or zone itself, including the cohesion and coefficient of friction that hinder slip on the fault (Ferrill et al., 2017). For a fault to reactivate, the applied shear stress ($\boldsymbol{\tau}$) must exceed the cohesive strength of the material ($\mathbf{S}$) plus the frictional resistance to sliding ($\boldsymbol{\mu}$) and resolved normal stress ($\boldsymbol{\sigma_n}$) on the fault surface (Price, 1966), as expressed by Equation 1.1:

$$\tau = S + \mu.\sigma_n \hspace{4cm} \text{Equation 1.1}$$

Therefore, reactivation tendency (Tr) is the ratio of resolved shear and normal stresses acting on a surface (Equation 1.2) (Morris et al., 1996):

$$Tr = \frac{\tau}{\sigma n} \hspace{4cm} \text{Equation 1.2}$$
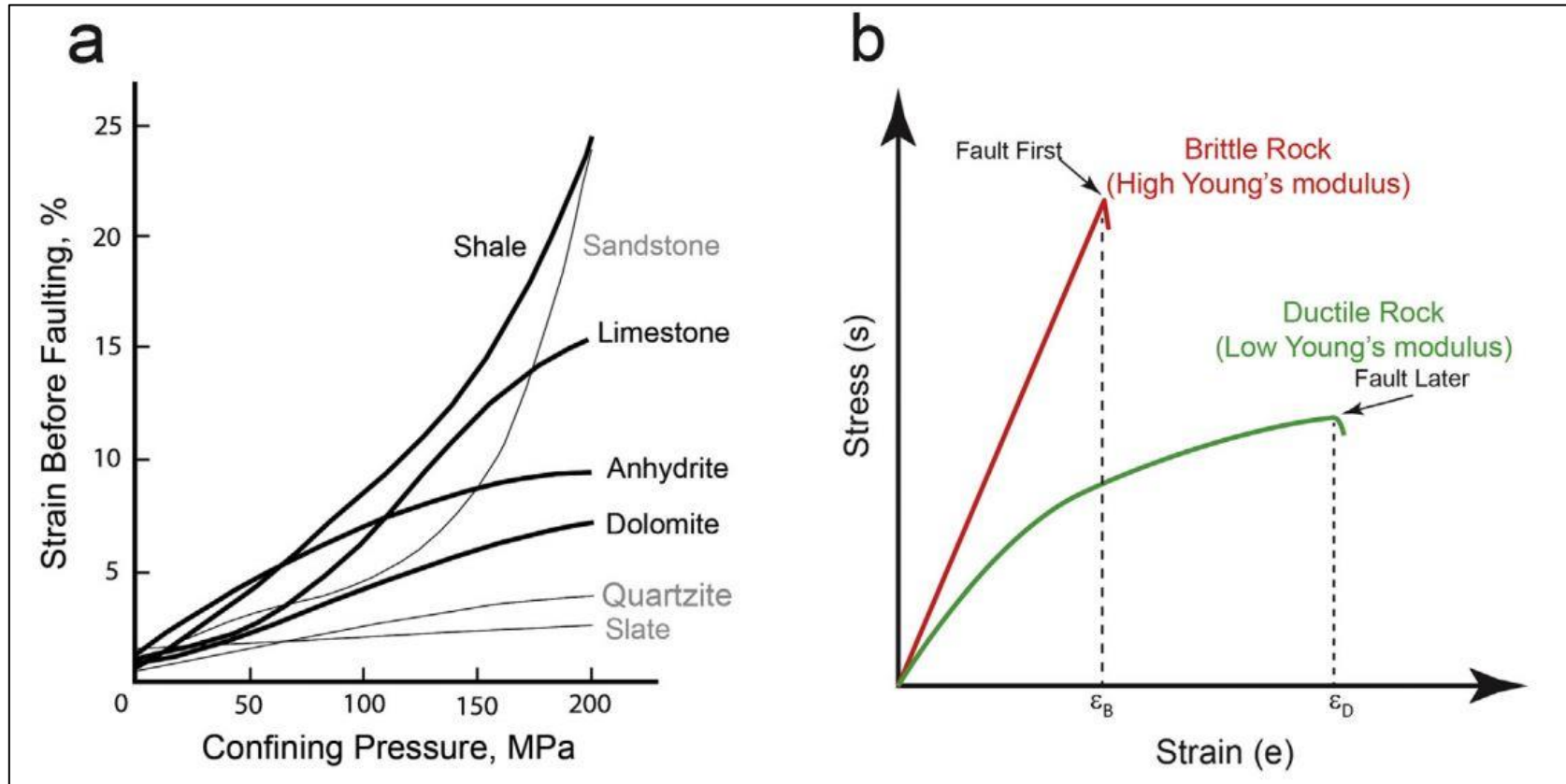
Fig. 1.3. (a) Graph of percent strain before faulting (ductility) versus confining pressure for a range of common rock types, including lithologies common in carbonate rock sequences (from Ferrill and Morris, 2008; Donath, 1970), b) Stress versus strain curves for brittle and ductile rocks illustrating the lower strain at faulting in brittle rocks versus that for faulting in more ductile rocks (from Ferrill et al., 2017).

For faults and fractures, reactivation is likely to occur on a surface when the resolved shear stress (τ) on that surface equals or exceeds the frictional resistance to sliding (Ferrill et al., 2017).

The coefficient of static friction (μ) is the value of reactivation tendency (T_r) at which slip occurs on a cohesionless surface and is often referred to as the fault "strength" in earthquake focal mechanism analysis (Harmsen,1994). According to Byerlee (1978) the coefficient of static friction for most crustal conditions is 0.6-0.85, so faults with T_r $\geq$0.6 record a reactivation tendency that equals or exceeds the commonly assumed coefficient of friction of 0.6 and, therefore, can be considered poised for reactivation or critically stressed (Zoback, 2007).

1.2.4. Fault propagation

Faults that first nucleated within a competent mechanical layer may propagate up- and down-dip until they encounter weaker mechanical layers, in which they may become arrested (Ferrill et al., 2017). In turn, incompetent layers may act as detachments causing decoupling of propagating faults from other layers and resulting in a preferable horizontal propagation for faults rather than favouring their vertical propagation (Pascoe et al., 1999; Withjack and Callaway, 2000; Richardson et al., 2005).

Experimental studies corroborate the concepts above, proving that incompetent layers can act as detachments that cause decoupling and prevent the propagation of faults across these layers, or intervals in which the locus of deformation can be shifted laterally across incompetent layers (Withjack and Callaway, 2000; Bahroudi et al., 2003; Gabrielsen et al., 2016). Such a shift in fault position across an incompetent layer can result in vertical fault segmentation where the fault segments can be hard- or soft-

linked (Mansfield and Cartwright, 1996; Tvedt et al., 2013; Libak et al., 2019) (Fig. 1.4).

1.2.5. Geometry of fault dip

In mechanically layered sedimentary rocks, normal faults commonly show changes in dip that are visible in cross-section (Peacock and Sanderson, 1991; Ferrill et al., 1998, 2000; Peacock and Zhang, 1993; Childs et al., 1996; Ferrill et al., 2017). These changes in dip can be caused by various mechanisms, including; a) differential compaction of sedimentary layers after fault formation (Xiao and Suppe, 1989), b) active fault deformation by slip or shear along layers or intersecting faults (Ferrill et al., 1998, 2000), c) linkage of an originally vertically segmented fault (Peacock and Zhang, 1993; Childs et al., 1996; Mansfield and Cartwright, 1996), and d) fault initiation with failure angles controlled by rock mechanical properties and effective stresses at the time of failure (Mandl, 1988; Peacock and Sanderson, 1992; Ferrill and Morris, 2003).

In relatively massive or homogeneous strata, faults are expected to develop following a consistent shear failure angle, a character resulting in consistent fault dips (Ferrill et al., 2017). However, faults that propagate through mechanically layered sections commonly have variable dips that can be related to the mechanical properties of the layers they propagated into (Peacock and Sanderson, 1991; Ferrill et al., 2017). These fault geometries, akin to refraction processes, are defined by steeper hybrid or shear failure segments in competent/strong layers and more gently dipping shear failure segments in less competent/weak layers (Peacock and Sanderson, 1991; Peacock, 2002; Ferrill and Morris, 2003; Ferrill et al., 2012, 2014; Kettermann and Urai, 2015) (Fig. 1.5a).
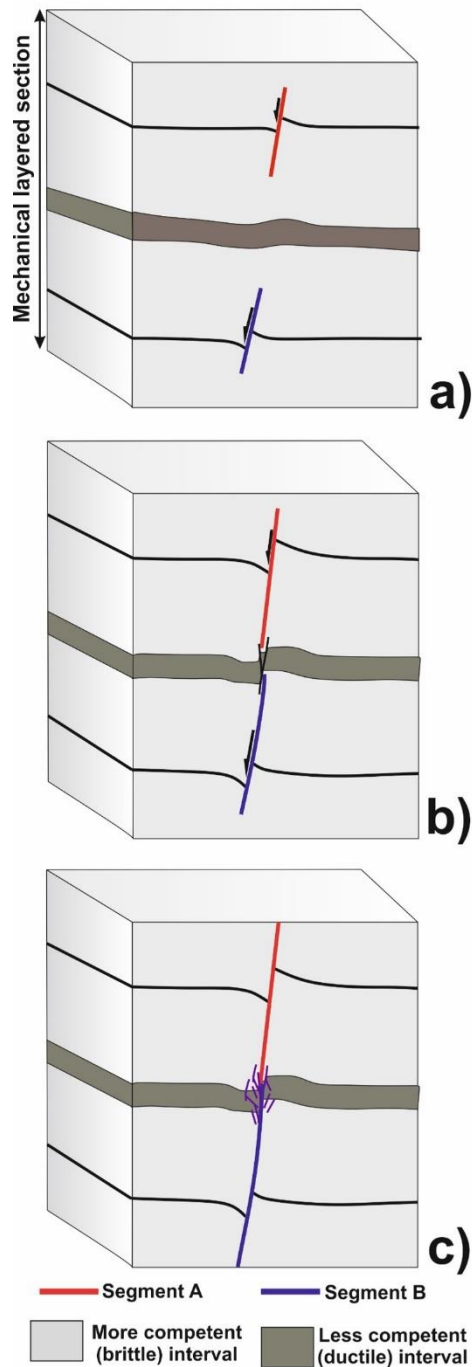
Fig. 1.4. a) Schematic model depicting the progressive evolution of a normal fault dominated by the dip linkage direction between two initially isolated fault segments. a) Faults nucleate first in more competent intervals, b) Each segment of these early-stage faults accumulates higher displacement and propagates outwards until they encounter other fault strands and soft link together in incompetent intervals, c) The soft linked segments rapidly accumulate displacement and hard-linked together.

Such differences in fault dip along a fault segment can locally lead to fault refraction that causes extensional (dilatational jogs) or contractional overlaps or relays (Peacock and Sanderson, 1991; Ferrill et al., 2017). Hence, slip along more gently dipping normal fault segments commonly results in the dilation of steep fault segments (Fig. 1.5b,c). Dilation of steep segments of refracted faults allows (and localises) fluid flow (Ferrill et al., 1999; Holland et al., 2006) and can also host economic mineral deposits (Dunham, 1988).

1.3. Fault propagation and growth modes

Research work has been carried out in the last few decades to investigate fault propagation and growth, revealing marked increases in the length, displacement and area of a fault, from the initial locus of fracture nucleation towards fully developed fault segments (Segall and Pollard, 1983; Walsh and Watterson, 1987). A number of fault growth models have been proposed by different authors, among which two end-members of fault growth models have predominantly been accepted by the scientific community: 'isolated' and 'coherent' (Cartwright et al., 1995; Cowie and Scholz, 1992; Cartwright et al., 2000; Jackson and Larsen, 2009; McLeod et al., 2000).

An early fault growth model was also proposed to explain the formation of 'ideal' blind faults that propagate in a radial direction, recording minimum migration of maximum displacement location(s) (Barnett et al., 1987) (Fig. 1.6). As argued by Lohr et al. (2008), faults grow most effectively by the coalescence of several smaller faults, whereas tip propagation is only of minor importance. Also, it is argued that the formation of a large fault is controlled by several small existing fault segments rather than a large fault created immediately (Sibson, 1985).
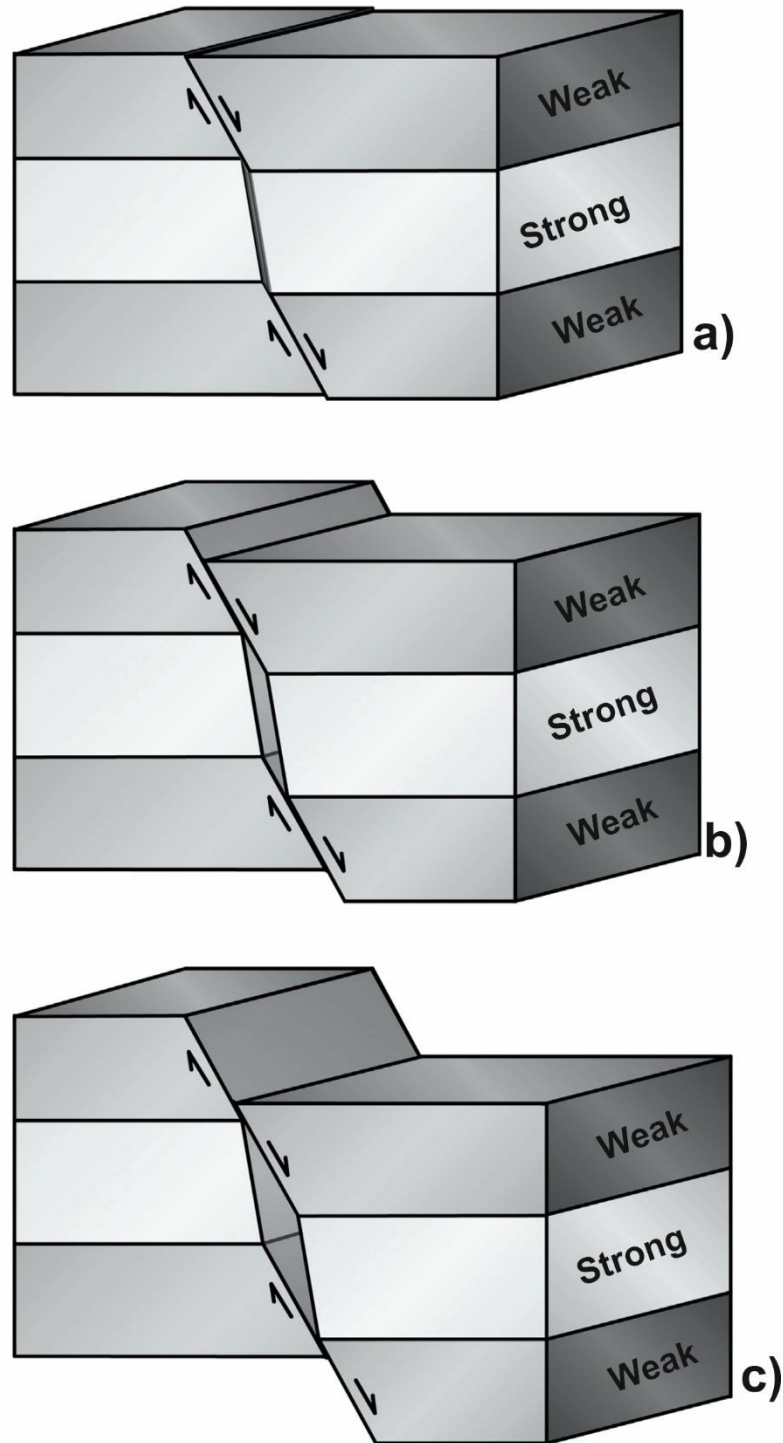
Fig. 1.5. Block diagrams illustrating fault refraction geometry formed by shear failure in weak layers and hybrid failure in strong layers. Slip parallel to moderate dip fault segments in weak layers causes dilation of steep segments through strong layers (from Ferrill et al., 2014; Ferrill et al., 2017)

Other researchers indicate that mature faults are often a result of fault-segment linkage (Lohr et al., 2008; Cowie et al., 2000; Cartwright et al., 1995; Stewart et al., 1997). Significantly, in all these models fault reactivation processes are thought to be an important parameter controlling fault growth (Walsh et al., 2002).

1.3.1. Relevant terminology

- *Fault length*: For structures resolved on seismic data, fault length refers to the longest horizontal or sub-horizontal dimension along a fault plane (Kim and Sanderson, 2005). For faults that are measured in the field, fault length refers to the longest trace of a fault that is exposed at the surface.

- *Fault throw:* The throw of faults, as observed on seismic or field data, is the vertical component of dip separation between correlative hanging-wall and footwall reflections. It is usually measured in seconds or metres. Fault throw decreases to zero towards the lateral-tip loops of an ellipse (fault surface) and increases to a maximum (D_{max}) close to the centre of a fault (Childs et al., 2003; Cowie and Scholz, 1992, Kim and Sanderson, 2005; Walsh and Watterson, 1988).

- *Sampling point:* Comprises the exact point, along the 'trace length' of faults, at which the throw values are measured; either at its maximum value, or its relative value across a fault surface, i.e. relative to depth along a fault surface.

- *Sampling interval:* Mathematically, the sampling interval in throw-distance (T-x) and throw-depth (T-z) plots is the distance, time, or depth, at which distinct throw measurements are acquired and recorded. These measurements are obtained along the 'trace length' of a fault and may record strong aliasing due to limited horizontal resolution in seismic data, data decimation (shot-point spacing), or poor-quality

imaging. The sampling interval can also be an important source of inaccuracy in field data if fault throws are sampled at too coarse an interval (Tao and Alves, 2019).

- *Throw-distance (T-x) plots:* T-x plots comprise systematic measurements of throw along the full length of resolved faults on structural maps, seismic data, or outcrops; the 'trace length in map view' as defined by Kim and Sanderson (2005). Maximum throw is measured along the strikes of normal faults or, preferably, interpreters should acquire throw-depth (T-z) data along the fully resolved length of faults in order to compile T-z plots (Baudon and Cartwright, 2008; Tao and Alves, 2019).

- *Throw-Depth (T-z) plots:* T-z plots comprise systematic measurements of throw along fault dips that are completed across the trace of faults by comparing the relative depth of correlative reflections across these same faults (Baudon and Cartwright, 2008). They provide a record, at depth, of throw variations across a fault surface, from its upper to lower tips.

1.3.2. Scaling laws

The apparent scaling of fault dimensions has principally been used to corroborate the fault growth model favouring radial propagation (Fig. 1.6). This model takes into acount an idealised blind fault with dimensions that increase proportionally to the elliptical slip events (Cartwright et al., 1995; Cowie and Scholz, 1992; Walsh and Watterson, 1988) (Fig. 1.6). The relationship between the maximum cumulative displacement on a fault (D_{max}) and the maximum linear trace length (L) is expressed by Equation 1.3.

$$D_{max} = c * L^n$$ Equation 1.3

Where c is an expression of fault displacement at unit length. For a linear scaling (i.e., n = 1), c is simple the ratio dmax/L ''Kim and Sanderson, 2005''. The exponent n varies from 0.5 to 2 (Walsh and Watterson, 1988; Cowie and Scholz, 1992, Scholz et al., 1993; Dawers et al., 1993; Fossen and Hesthammer, 1997). An exponent of 1 indicates a linear scaling law for fault dimensions, and n $\neq$ 1 reflects a scale-dependent fault geometry. This scale-dependent relationship often relates to distinct fault-slip events (Cowie and Scholz, 1992).

Significant data scattering is observed when discrete datasets are used and compared, often leading to misinterpretations of scale relationships between faults (Cowie and Scholz, 1992; Kim and Sanderson, 2005; Torabi and Berg, 2011) (Fig. 1.7). As noted by Kim and Sanderson (2005), data resolution, sampling effects, tectonic setting history and host lithology of interpreted faults can differ even for those faults formed under the same tectonic setting (Kim and Sanderson, 2005). Factors that can contribute to scattering in fault-scale relationships include:

a) Heterogeneous lithology in host rocks along the fault trace (Scholz et al., 1993; Cowie and Scholz, 1992);
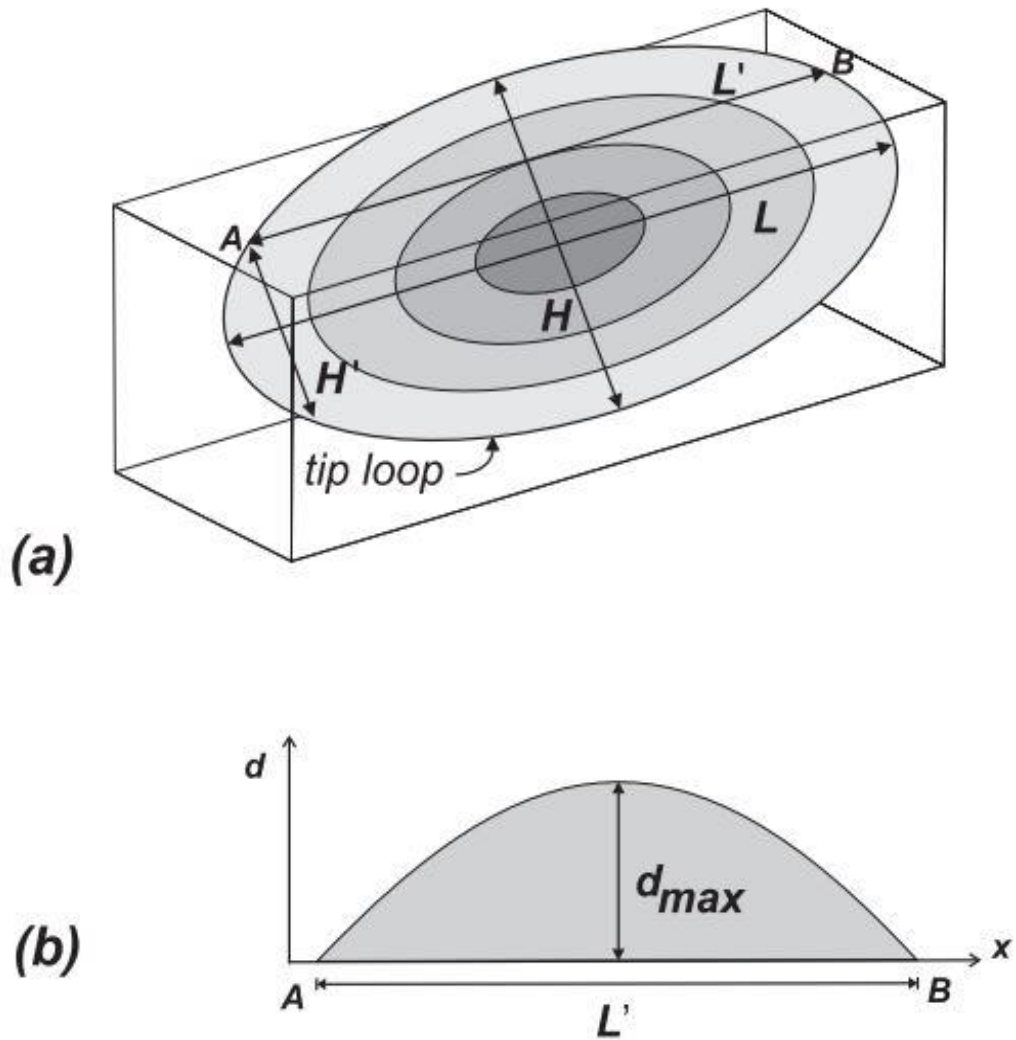
Fig. 1.6. (a) Diagram to illustrate displacement distribution on an elliptical fault surface of length (L) and height (H); the density of shading increases with increasing displacement towards centre of fault. The fault intersects the upper surface of the block along line A-B. (b) Displacement (d)-distance (x) plot of fault trace along line A-B (Barnett et al., 1987)
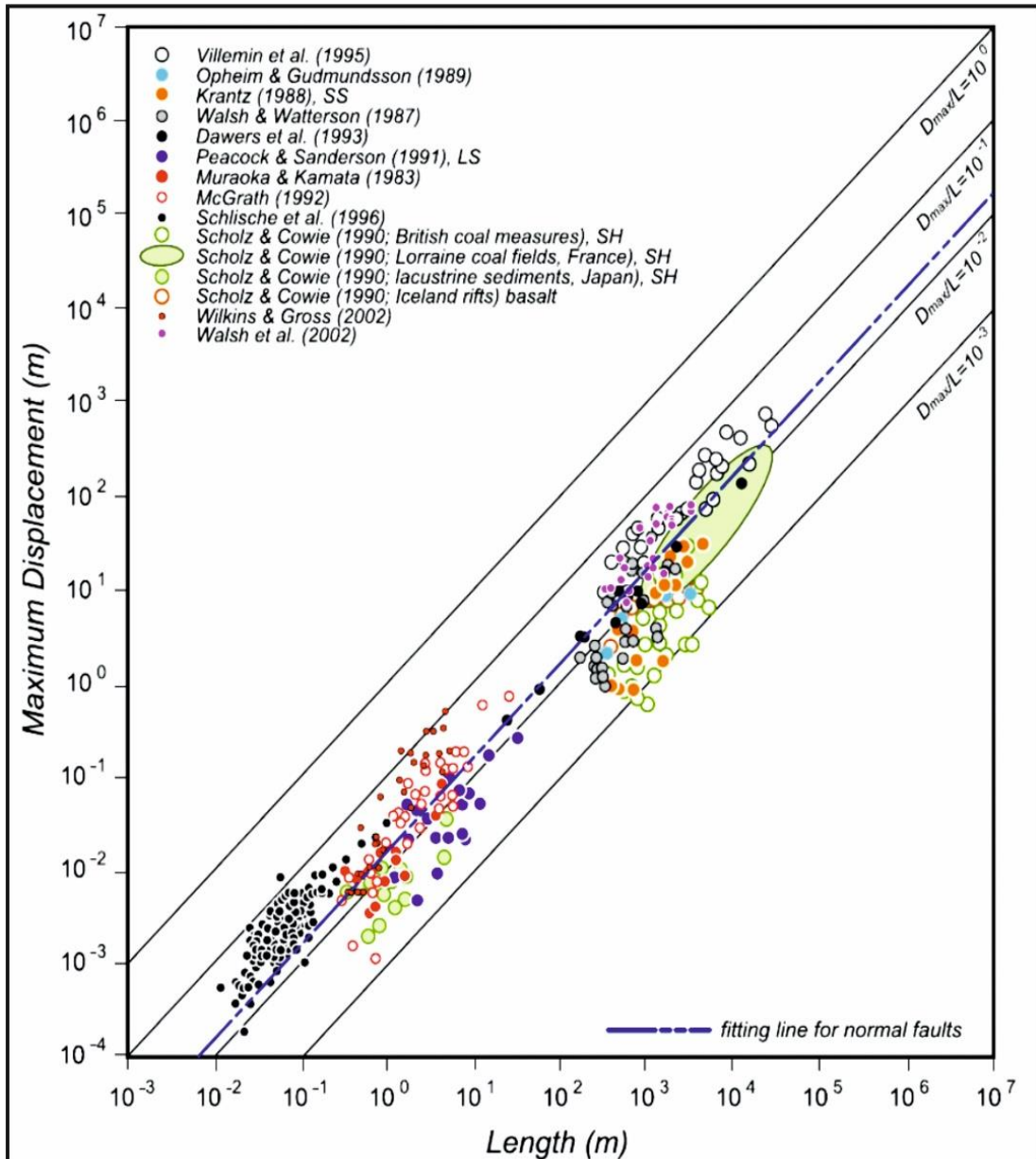
Fig. 1.7. (a) Compilation of previously published maximum displacement (d_{max}) vs. fault length (L) for normal fault. SS-sandstones; LS-limestones; and SH-shale. Figure from Kim and Sanderson (2005).

b) Incoherent sampling methods and measuring errors during fault growth analyses (e.g, Walsh and Watterson, 1988; Torabi et al., 2011; Tao and Alves, 2019);

c) Lithological and mechanical barriers hindering fault growth (Kim and Sanderson, 2005; Schultz and Fossen, 2002);

d) Fault segment-linkage and reactivation (Cartwright et al., 1995; Peacock and Sanderson, 1991; Dawers and Anders, 1995; Kim and Sanderson, 2005).

e) Complex and variable earthquake rupture and slip/propagation histories of faults (Kim and Sanderson, 2005).

1.3.2.1. Effects of sampling intervals on fault-growth analyses

This section summarises the effect of sampling intervals on throw-distance (T-x) plots (Fig. 1.8). For the discrete, isolated fault growth model, one fault segment can always be identified for all sampling intervals represented in Figure 1.8a. However, the geometry of the fault changes significantly when the sampling interval increases (e.g., Tao and Alves, 2019).

The maximum throw curve (T) shows an arching top with a sampling interval of 12.5m, 37.5m and 62.5m (e.g., Tao and Alves, 2019) (Fig. 1.8a1, a2 and a3). The details shown in Figures 1.8a4 and 1.8a5 are lost when sampling intervals are significantly larger. The apex of the fault (maximum throw point) also changes (Fig. 1.8a4). For the discrete, isolated fault growth, a maximum sampling interval of 62.5m is regarded as necessary to obtain accurate T-x plots (Fig. 1.8a3), i.e. reflecting accurate fault geometries without losing significant detail. For the coherent fault growth, the T-x plots at minimum sampling intervals identify five (5) distinct segments (Fig. 1.8b1). Important detail is lost in fault segment 1 when the sampling interval increases, in effect masking significant areas where fault overlap occurs (Tao and Alves, 2019) (Fig. 1.8b3). When

the sampling interval further increases, linkage zones between segments 1 and 2, and segments 2 and 3, are represented by only one minimum throw point. The width and geometry of the fault zone are significantly changed (Fig. 1.8b4). With these sampling intervals, maximum throw values are underestimated and fault segment 5 becomes unrecognisable (Tao and Alves, 2019) (Fig. 1.8b4). When the sampling interval further increases, only two fault segments can be identified in the T-x plot, while its maximum throw value is underestimated (Fig. 1.8b6). A minimum sampling interval is required to accurately resolve distinct segments (Fig. 1.8b2).

In summary, sampling interval has a significant effect on fault growth analysis in the regions where fault segments are linked (Fig. 1.8). When increasingly coarse sampling intervals are used to compile T-x plots, the following effects are recognised: a) fault geometry is significantly changed, b) maximum throws are underestimated, c) fault segmentation is lost on close analysis, d) the geometry of fault linkage points is changed, e) the width of fault linkage zones is underestimated, and f) fault interaction zones (relay ramps, fault stepovers, hard linkage points) are lost (Tao and Alves, 2019) (Fig. 1.8).

1.3.3. Isolated and coherent fault growth models

Overlapping, interacting, and linking fault segments have been observed in numbers of studies. Two end-members in the literature, differentiating fault growth histories according to whether fault segments are kinematic related or not, are the 'isolated' and 'coherent' fault models (Walsh et al., 2003).
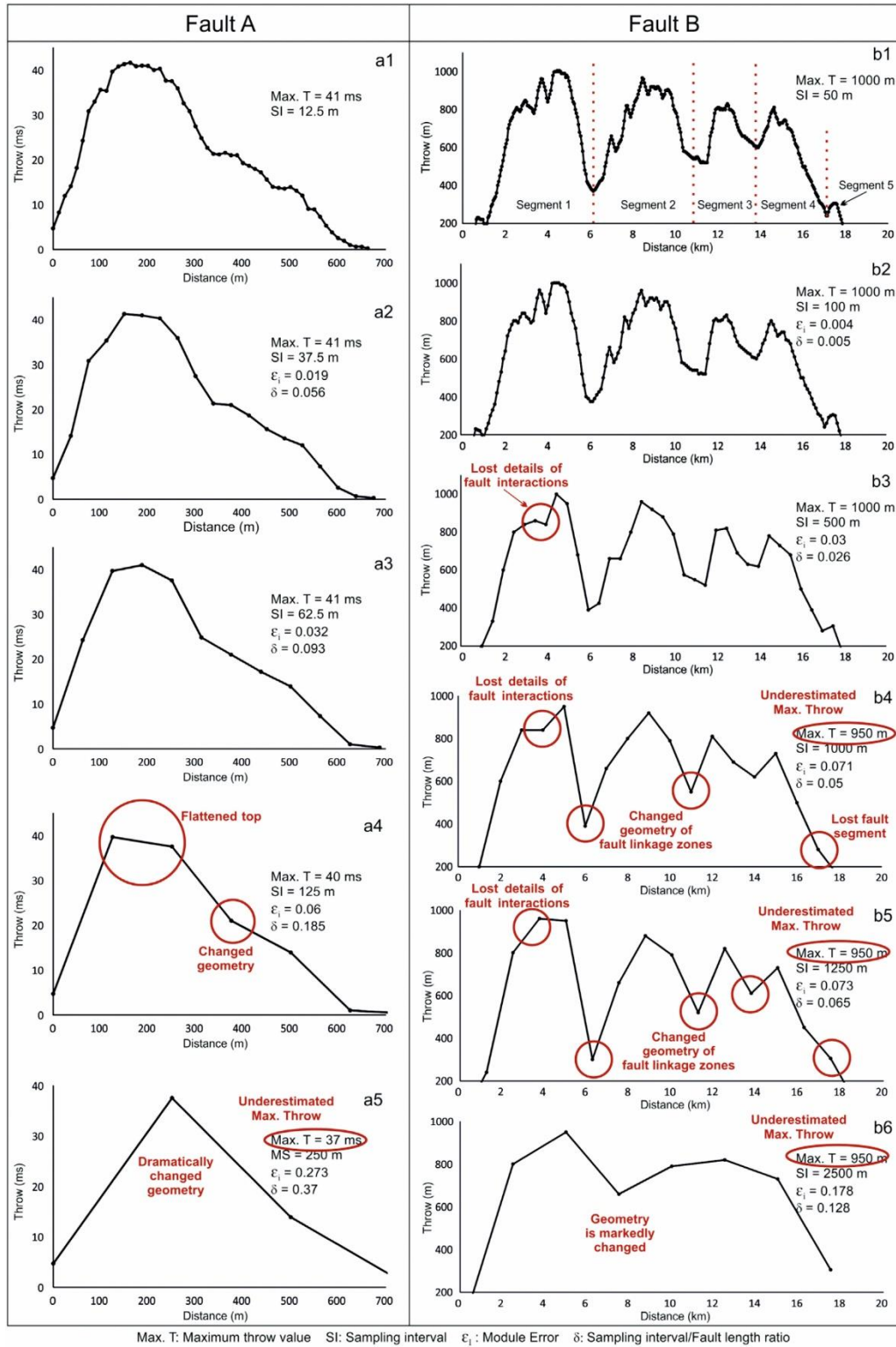
Fig. 1.8. Throw-distance plots highliting the effects of sampling intervals on fault growth analysis. a) For isolated fault growth, b) coherent fault growth (From Tao and Alves, 2019).

The isolated fault model is supported by multiple authors as explaining fault growth under the assumption that tip lines of fault propagate radially outwards with maximum displacement at the centre (Cartwright et al., 1995; Dawers and Anders, 1995; Mansfield and Cartwright, 1996; Peacock and Sanderson, 1991). However, as high-quality 3D seismic data becomes increasingly available, out-of-plane fault propagation models have been increasingly suggested as reflecting coherent fault models (Fig. 1.9). With the coherent fault model, fault segments initiate, propagate, and develop as part of a spatially, kinematically and mechanically organised fault array (Walsh et al., 2003).

Hard-linked or soft-linked faults can be formed during their propagation either by surface bifurcation or by the stepping of initial fault segments (Walsh et al., 2003) (Fig. 1.9). In the 'isolated fault' model, fault propagation is not hindered by other faults, in contrast with the coherent fault growth model in which fault propagation is closely associated with the growth of adjacent fault segments (Fig. 1.9). Throw-distance profiles for coherent fault growth will therefore show a coherent profile, which will be variable for 'isolated' faults (Tao and Alves, 2016; 2019).

1.3.3.1. Fault growth via radial propagation

Fault propagation refers to an increase in fault length and displacement from their initial nucleation point (Segall et al., 1983; Walsh and Watterson, 1987). An ideal blind fault, not reaching nor offsetting the surface, is often characterised by a maximum throw value at the centre of the fault plane, progressively diminishing towards its fault tips (Barnett et al., 1987) (Fig. 1.6). The propagation of an idealised blind fault, developed in a mechanical homogeneous medium, often follows a radial direction, and presents an elliptical fault plane geometry (Barnett et al., 1987) (Fig. 1.6). The depth in which

the maximum displacement values are recorded often indicates the initial point of fault nucleation.

1.3.3.2. Fault growth via segment linkage

Most of the Earth's upper crust comprises brittle rocks with multiple heterogeneities - complex faults resulting from the coalescence of distinct fault segments (Segall and Pollard, 1980; Walsh and Watterson, 1991; Mansfield and Cartwright, 1996; Kim and Sanderson, 2005). Faults developed in sedimentary basins often cover a wide range of scales, from centimetres to tens of kilometres, even when formed under the same tectonic setting (Granier, 1985; Pollard and Aydin, 1984; Tao and Alves, 2016).

Segmented faults can result in a general scattering of displacement-length data, making any single scaling law hard to be applied in a specific area, or when comparing distinct regions (Mansfield and Cartwright, 1996; Bürgmann et al., 1994; Cartwright et al., 1995; Childs et al., 1995; Peacock and Sanderson, 1991; Willemse et al., 1996).

Fault growth by segment linkage can be classified into two modes according to the observed linkage directions: a) lateral tip linkage, and b) dip linkage (Mansfield and Cartwright, 1996; Baudon and Cartwright, 2008). Faults linking at their lateral tips were initially observed in thrust faults, where the nucleation of fault segments can be recognised by displacement maxima and minima at the point of fault linkage (Ellis and Dunlap, 1988; Kim and Sanderson, 2005) (Fig. 1.10). Kinematic analyses for distinct normal fault zones revealing displacement variations due to segment linkage, suggest that faults show an approximately linear profile by initially developed isolated structures (Peacock and Sanderson, 1991). A three-stage model is often proposed to explain the growth of faults by lateral tip propagation and linkage (Ellis and Dunlap, 1988; Peacock and Sanderson, 1991; Kim and Sanderson, 2005) (Fig. 1.10). The first
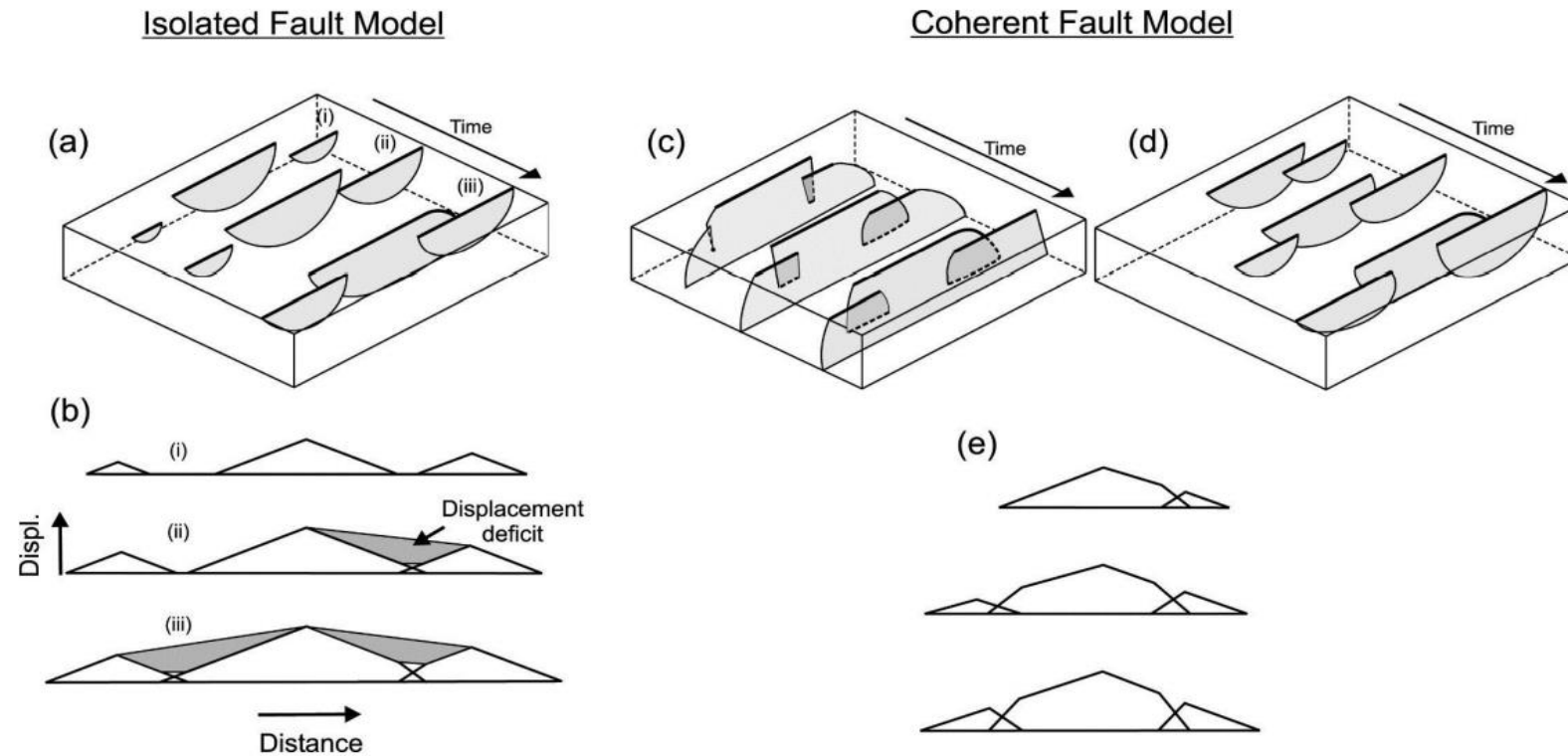
Fig. 1.9. Schematic comparison between the 'isolated fault' and the 'coherent fault' models. The block diagrams (a, c and d) show the growth stages of a segmented fault array (i–iii). The displacement-distance plots b and e are for fault traces on the upper surfaces of the block diagrams (bold lines). The coherent fault model is illustrated for hard-linked (c) and soft-linked (d) fault segments. Figure modified from Walsh et al. (2003).

stage 1 witnesses the formation of distinct isolated faults, with a blind propagation mode leading to their coalescence towards each other (soft linkage; stage 2). Eventually, lateral fault tips will interact with one another forming effective connections (hard links) in breached relay zones (stage 3) or showing no apparent connections between distinct fault segments (i.e., soft linkages) (Kim and Sanderson, 2005) (Fig. 1.10). In faults that are hard linked, the interaction zones (relay zones) will act as barriers for further fault propagation, a character often leading to the accumulation of displacement over a constant-length structure in the later stages of fault growth. This phenomenon usually results in high displacement/length ratios for hard-linked fault segments.

Fault-dip linkage refers to the linkage of the upper tip of faults growing in lower stratigraphic levels, with the lower tips of shallower faults. This linkage zone is often characterised by relay structures that are sub-parallel to the strike of faults (Mansfield and Cartwright, 1996) (Fig. 1.11). As the linked faults propagate further as one single structure, a progressive destruction of the linkage zone (relay zone) will occur. Yet again, this latter phenomenon often results in high displacement/length ratios (Childs et al., 1996). With enough data resolution, fault throw minima can be recognised to differentiate this mode of fault segment linkage.

1.3.3.3. Constant-length fault growth model

A constant fault model has also been proposed in the literature based on the postulate that fault length is established rapidly, resulting in essentially constant lengths for much of the duration of faults. With further fault propagation, faults can only accumulate-displacement in a vertical direction, returning high D_{max}/L ratios (Walsh et al., 2002) (Fig. 1.12).
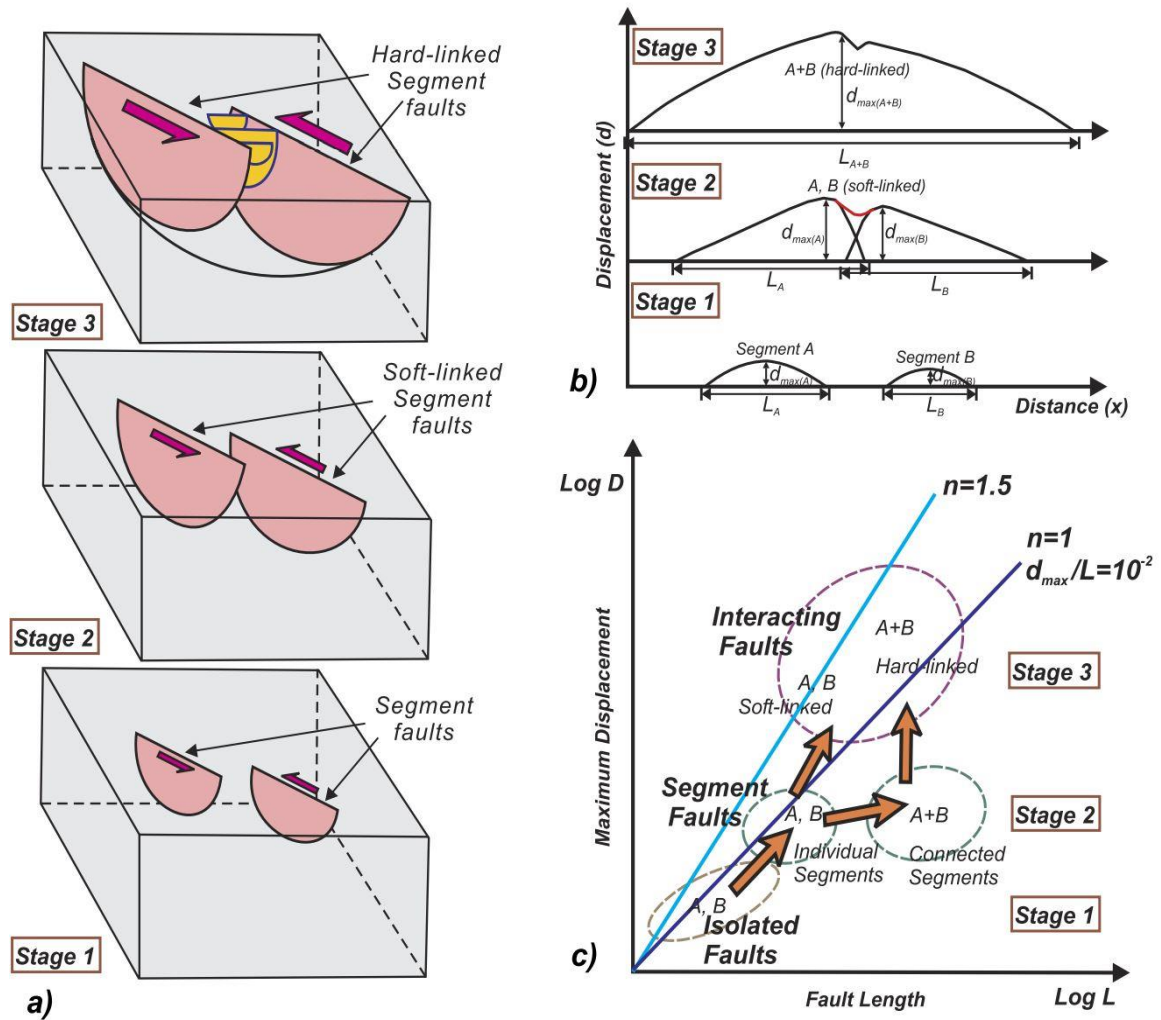
Fig. 1.10. Fault segmentation and linkage. Faults evolve from isolated faults to interacting faults through segment linkage. The ratio of d_{max}/L increases showing step-like evolution path. Fault lengths abruptly jump at the stage of segment linkage (Kim and Sanderson, 2005).
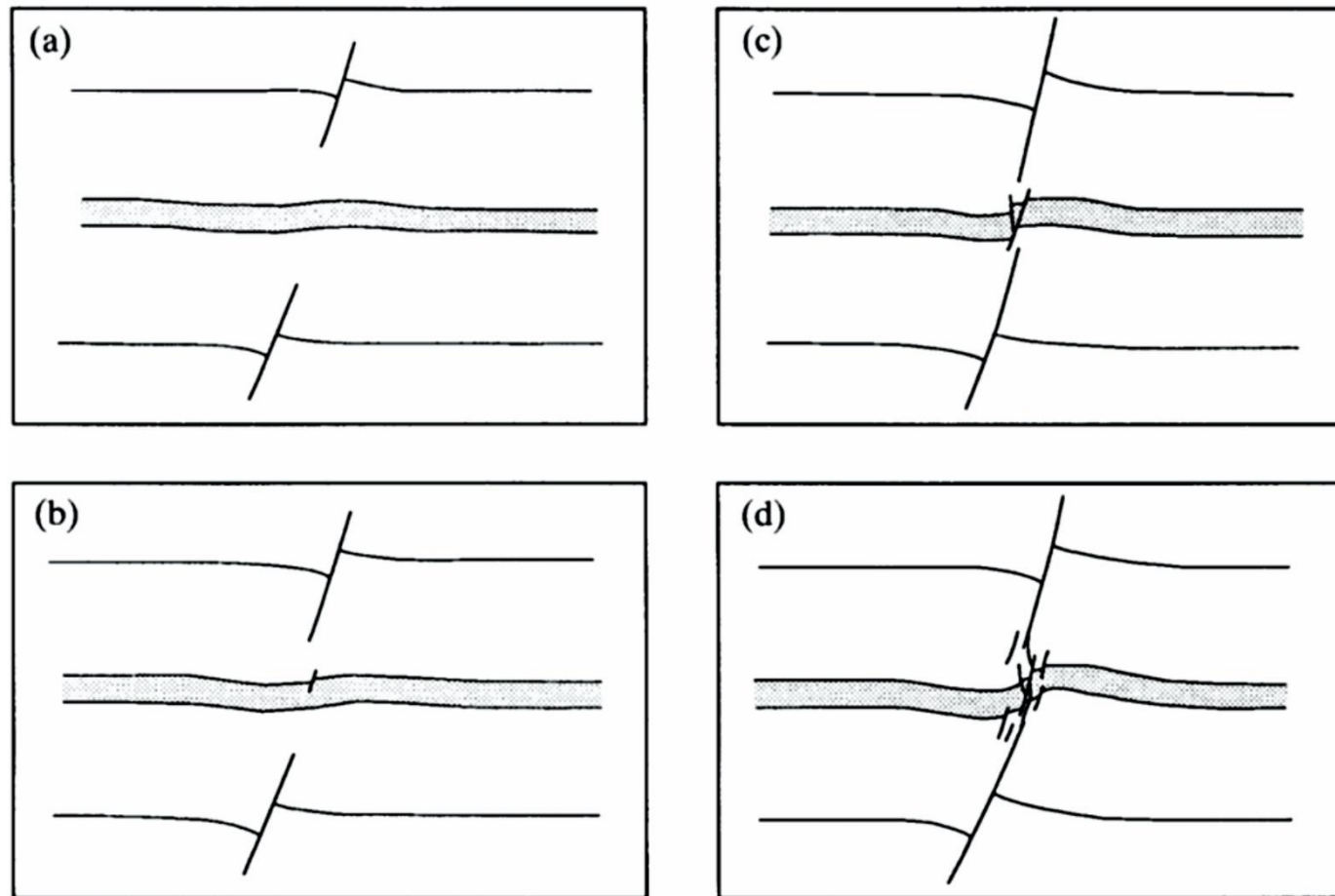
Fig. 1.11. Four-stage, schematic model depicting the progressive evolution of a normal fault dominated by the dip linkage direction between two initially isolated fault segments (Mansfield and Cartwright, 1996)

a. Pre-existing underlaying faults
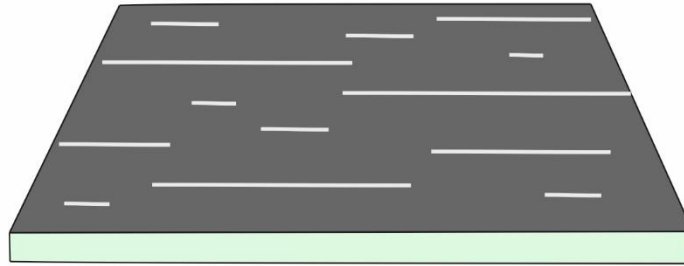
b. Fault initiation and rapid propagation

nucleation point

segment linkage
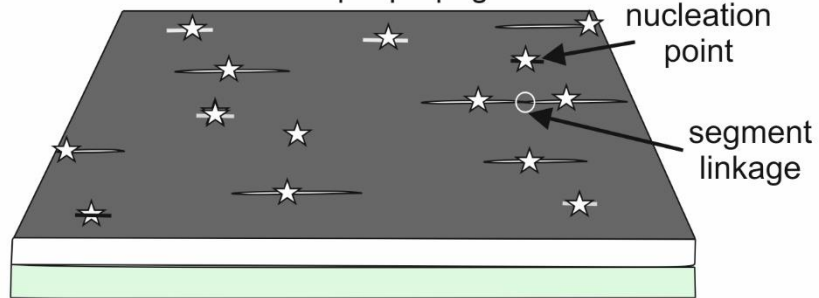
c. Fault length established

tip interaction
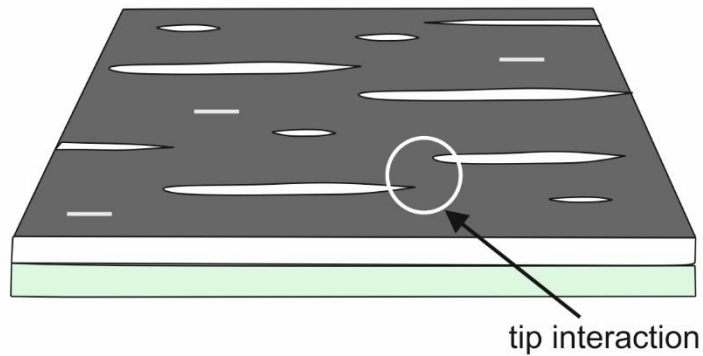
d. Displacement accumulation no propagation
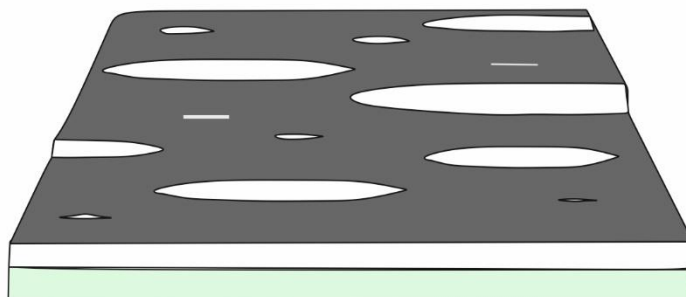
Fig. 1.2. Constant-length model, in which the fault length rapidly increases at an early stage of fault growth and then remains constant as displacement accumulates. Figure modified from Walsh et al. (2002)

1.4 Salt tectonics

Salt-rich continental margins such as the Gulf of Mexico, North Sea, and the conjugate continental margins of southeast Brazil and West Africa are characterised by large-scale withdrawal and forward movement of salt units under a sedimentary overburden (Demercian et al., 1993; Cramez and Jackson, 2000; Fort et al., 2004; Alves et al., 2009). Movement and withdrawal of salt units under prograding deltaic wedges triggered gravitational instability capable of deforming post-salt overburden strata to a great extent (Jackson et al., 1994). Salt systems often form genetically and kinematically linked groups of faulted intervals, diapirs, and welds connecting sub-salt and supra-salt strata (Rowan et al., 1999).

Salt-rich basins occurs under three main geological settings: a) Inter-cratonic basins as represented by the Zechstein Super Group of the North Sea (Cameron, 1992; Stewart and Coward, 1995), b) syn- and post-rift passive margins such as those developed along East Brazil and its conjugate West African margin (Mohriak et al., 2008; Mohriak et al., 2012; Chang et al., 1992, Petri, 1987), and c) continental collision zones and foreland basins such as the Tarim Basin in Northwest China (Yu et al., 2014).

Different classifications of salt basins have been proposed in the literature when considering the timings of salt deposition relative to rifting such as pre-rift, syn-rift, post-rift salt basins (Jackson and Vendeville, 1994), or pre-rift, syn-stretching, syn-thinning, and syn-exhumation salt basins (Rowan, 2014).

1.4.1 Mechanisms promoting salt flow

Pure salt comprises a crystalline aggregate of halite (NaCl) (Warren, 2006). However, salt units in sedimentary basins often include other (evaporite) minerals such as halite,

anhydrite and carnallite, and interbedded carbonate and siliciclastic sediments (Warren, 2006). The unique physical and chemical properties of salt contribute to its viscous-plastic behaviour when buried beneath non-evaporite deposits, resulting in its complex overburden deformation. The inherent viscosity of salt makes it sensitive to relative increases in temperature and pressure, and to stress variations imposed by an often-mobile and thickening overburden strata. Sedimentary rocks lose effective porosity within depth of several kilometres of burial, after which they will become less compressible. With salt, density will remain constant, for example 2160 kg/m^3 in pure halite (Talbot and Jackson, 1987). This property differs from that of siliciclastic sediments, which progressively lose their porosity and permeability because of compaction (Hudec and Jackson, 2007).

Different responses of salt and its overburden strata with increasing burial depths result in important density inversions. When overburden units exceed a certain thickness (500-2000 m according to 'ideal' compaction trends for different lithologies), salt layers start to concentrate important buoyancy forces (Hudec and Jackson, 2007). The viscosity of rock salt is usually inferred from laboratory experiments, field observations and numerical models, typically falling between 1010 to 1023 Pa (Mukherjee et al., 2010). If one disregards known impurities within rock salt, the viscosity of rock salt depends on factors, including i) water content, ii) temperature, iii) grain size and iv) differential stress (Talbot and Rogers, 1980; Van Keken et al., 1993). Impurities and spatial variations in viscosity are nevertheless important in evaporite sequences; though salt is viewed as an impermeable material that acts as a competent seal interval, saturated brine of different chemical compositions, and hydrocarbon residuals, are often observed in naturally deformed salt (Schoenherr et al., 2007).

Density inversion, which causes salt-rich basins to become gravitationally unstable, is postulated as the main mechanism for 'buoyant' salt rise to the surface. For salt to move due to density inversion, a minimum thickness of overburden strata between 1600 to 3000 m is necessary (Nelson and Fairchild, 1989) or 2000 to 4000 m (Jackson and Lewis, 2012). Apart from buoyancy, which can potentially contribute to important halokinesis, unloading of overburden strata by erosional and mass-wasting processes, together with regional extensional and compressional stresses, can also promote salt movement in a sedimentary basin (Stewart and Coward, 1995; Jackson and Vendeville, 1994; Evans et al., 2003). Conversely, important resisting forces retarding the flow of salt, such as the strength of overlying strata and mechanical friction between salt layers and surrounding sub- and supra-salt strata, have also been proposed in the literature (Hudec and Jackson, 2007; Alves et al., 2017) (Fig. 1.13).

Three driving forces are considered in the published literature as initiating and promoting salt flow on regional scales of analysis, 1) gravitational loading, 2) displacement loading and 3) thermal loading (Hudec and Jackson, 2007). Differential overburden loading is often regarded as the primary mechanism inducing salt movement from high- to low-pressure zones (Fig. 1.14). Gravitational loading results from the combined weight of the rocks overlying the salt and the gravitational body forced inside the salt (Fig. 1.14). Displacement loading refers to the movement of sediment towards or away from the salt, a phenomenon usually related to regional tectonics such as regional extension or shortening (Fig. 1.15). Thermal loading is postulated to have a significant influence on salt flow due to the high thermal conductivity of salt rock, with volume changes occurring whenever thermal conditions change.

The initial mechanism for salt flow varies in different salt basins (Rowan, 2014). Salt mobilisation and diapirism are suggested to be triggered by thick-skinned extension during the stretching stage in pre-rift salt basins. In syn-stretching salt basins, mobility begins as soon as the salt is deposited. In syn-exhumation salt basins, salt mobility is triggered by gravity gliding as the margin tilts oceanwards due to differential thermal subsidence (Rowan, 2014).

1.4.2. Structural styles in salt-rich passive continental margins

Salt tectonics within passive margins is mostly a gravity-driven process occurring over a décollement surface such as evaporites or shales (Fort et al., 2004), with evaporites/shales being considered a viscous material. The upper slope of salt-rich continental margins is generally dominated by an extensional domain, where salt pillow and rollers are associated with the formation of large faults (Rowan et al., 1999). In mid-continental, lower-slope domains salt structures grow into diapirs and salt walls, essentially making a transition between extensional upper-slope and lower-slope compressional domains. The latter compressional zones are dominated by salt ridges, thrust, allochthonous salt sheets and canopies (Fort et al., 2004, Omosanya, 2014).

Fiduk et al. (2004) studied the structural style of the salt-rich, passive continental slope margin of the SE Brazil and related the deformation structures on this margin to gravity gliding and spreading due to seaward progradation of sediment and resulting loading. Fiduk et al. (2004) identified three structural zones on the SE Brazilian continental slope, namely: 1) an upper extensional zone beneath the continental shelf, characterised by both basinward-dipping and counter-regional growth listric faults and associated rollovers depocenters, salt rollers, diapirs and rafts. This extensional zone is the main

interval of interest for part of this study (see Chapter 4), 2) Intermediate, translational, diapirism in the mid-slope region, characterised by passive, active, and reactive salt diapirs including salt overhangs, vertical salt diapirs and, 3) a compressional distal part of the continental slope, which is characterized by active and reactive salt diapirs including vertical salt diapirs, salt overhangs, allochthonous tongues and salt canopies (see Chapter 2; Fig. 2.2).

1.4.3. Modes of salt diapirism

The flow of salt can be diapiric or non-diapiric. In parallel, overburden sediment must be removed or replaced so that a diapir can be formed. Modes of diapirism include reactive, thrust, active, ductile, erosional, and passive piercement (Hudec and Jackson, 2007). The generation of salt structures, as observed on seismic data, involves complex processes, and diapiric salt structures often form due to regional extension in an initial stage, e.g. diapirs on the Brazilian continental margin and in the Gulf of Mexico (Vendeville and Jackson, 1992). After salt flow is initiated, mechanisms for salt growth and halokinesis vary due to regional and local controls on salt structures (Cartwright et al., 2001; Rouby et al., 2003; Yu et al., 2014). It is noted that a salt structure has a multi-stage nature, and that salt-diapir growth does not involve simple inward flow and thickening of salt (Jackson et al., 2014). In fact, known mechanisms forming salt diapirs include reactive, active, and passive diapirism (Fig. 1.16).
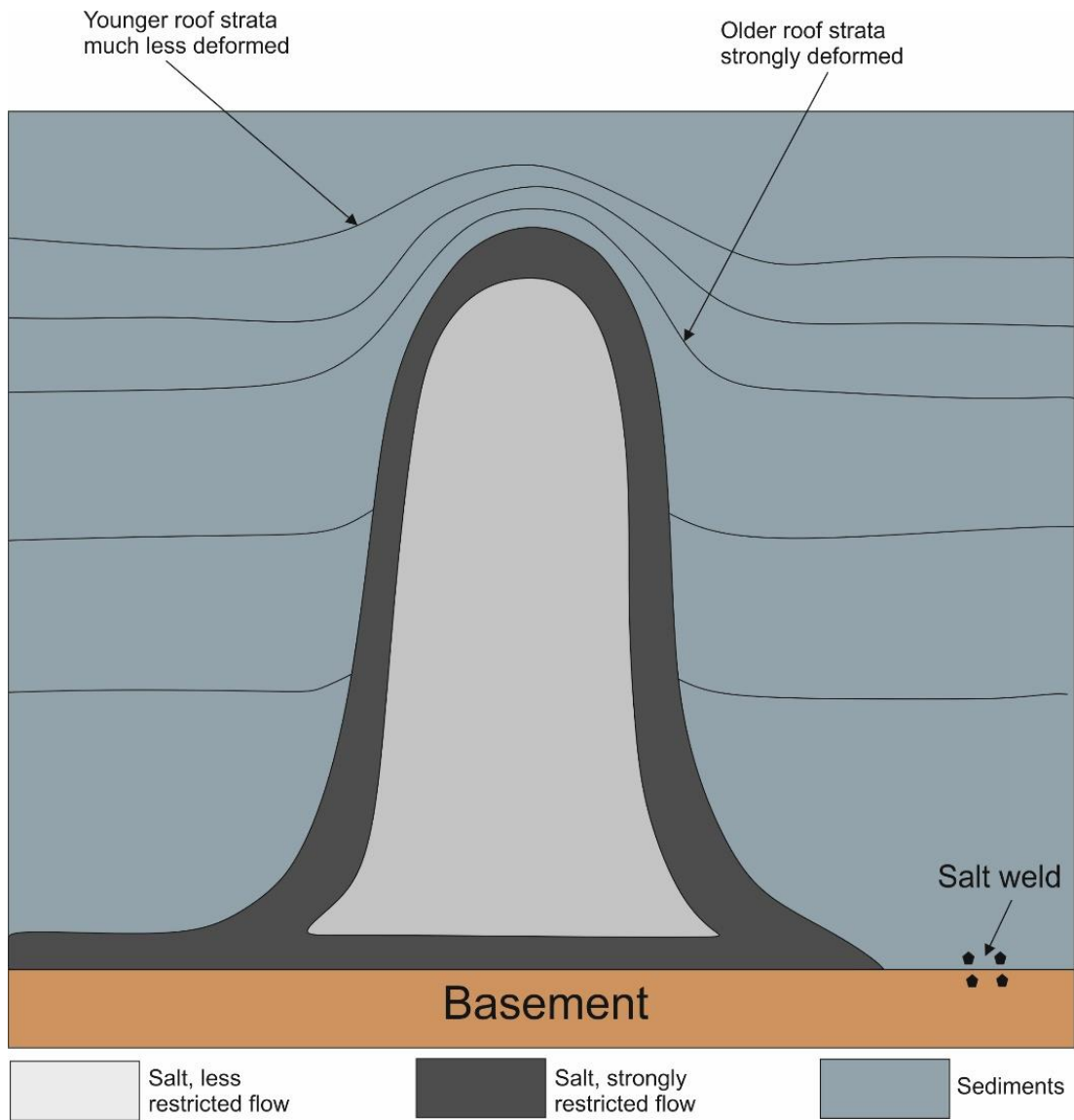
Fig. 1.13. Factors resisting salt flow. Salt deformation occurs if the roof is thin and weak but becomes progressively more difficult as the roof thickens. Salt is strongly sheared near the edges of salt bodies during flow, a phenomenon causing resistance to deformation. Salt flow is inhibited when the salt layer becomes too thin. Figure taken from Hudec and Jackson (2007).

Gravitational loading
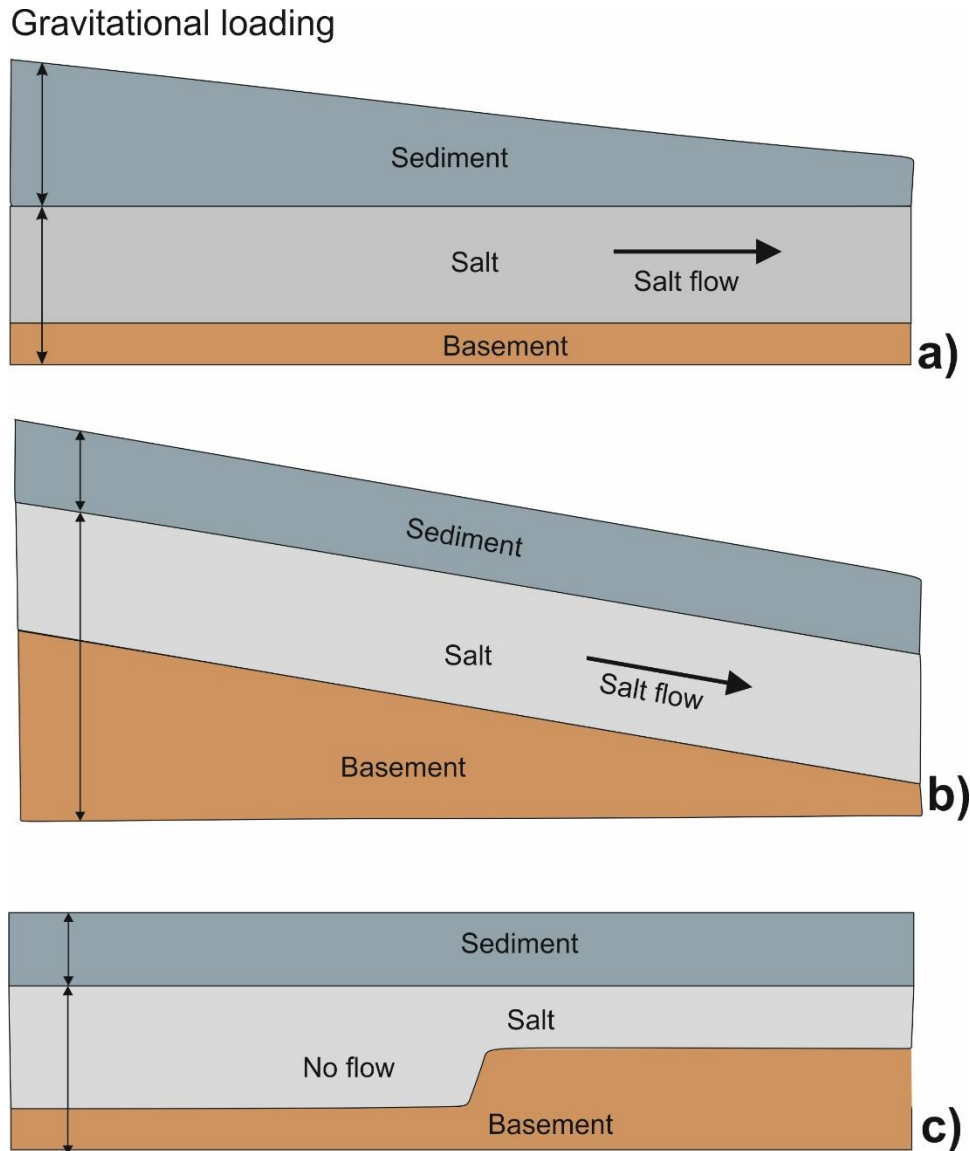
Fig. 1.14. Effects of gravitational loading on salt flow. a) A laterally varying overburden thickness above a horizontal head gradient. Salt will flow from left to right along the pressure head gradient. b) A uniform overburden thickness above an inclined, tabular salt layer produces an elevation head gradient. Salt will flow from left to right down the elevation head gradient. c) A uniform overburden thickness above a flat-lying salt layer produces neither elevation nor head gradients, even though the salt thickness varies. Figure modified from Hudec and Jackson (2007).
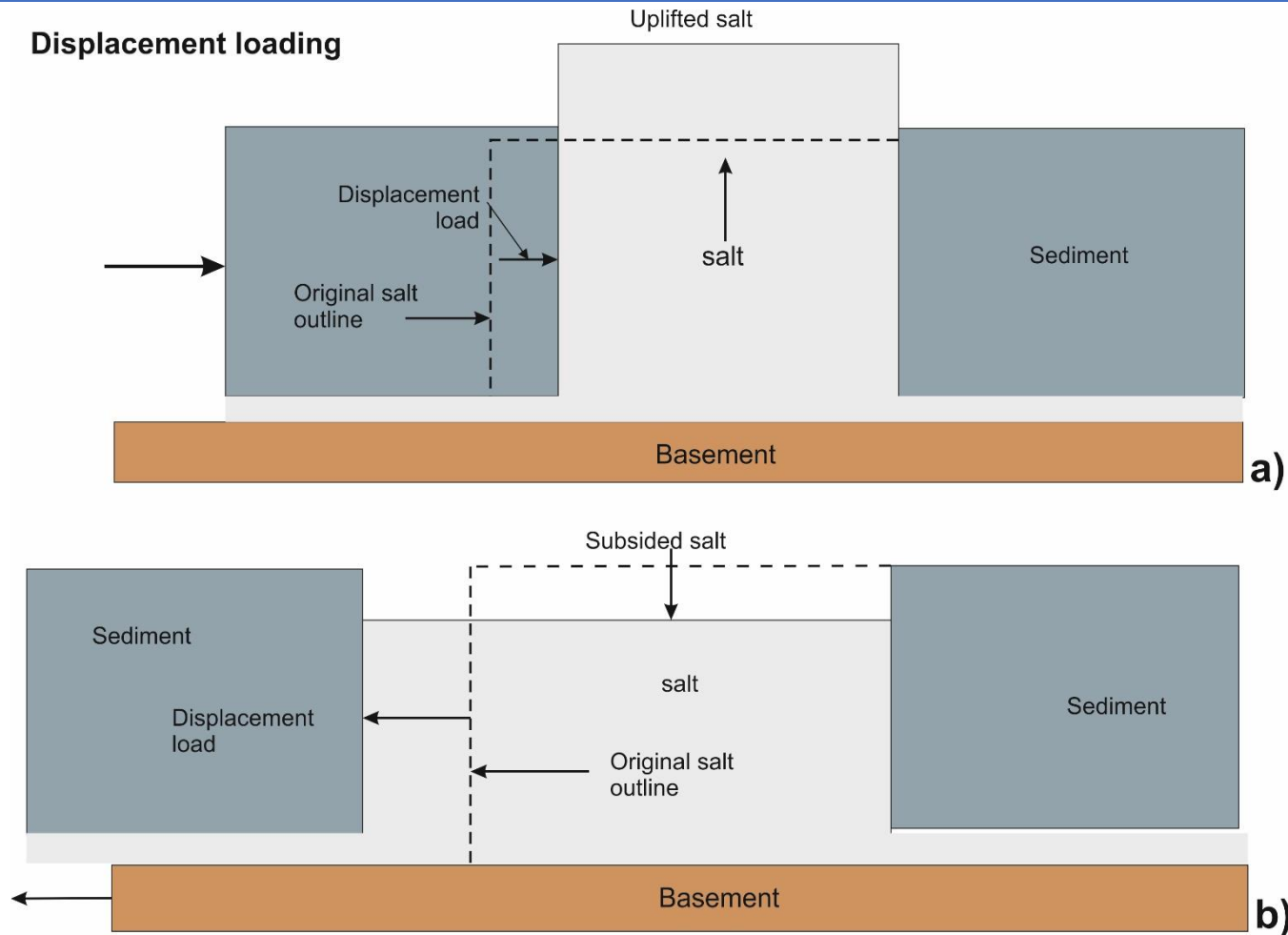
Fig. 1.15. The effects of displacement loading on salt structures. a) In shortening, salt is loaded horizontally by inward movement of one or both sidewalls where the horizontal displacement load exceeds the vertical gravitational load, forcing salt to rise. b) During extension, the salt is unloaded horizontally by movements of one or both sidewalls. The vertical gravitational load then exceeds the horizontal displacement load, so salt subsides. From Hudec and Jackson (2007).

1.4.3.1. Reactive diapirism

Regional extension, which thins the overburden above salt intervals, accounts for reactive diapirism (Jackson and Vendeville, 1994; Vendeville and Jackson, 1992). During this process, 'room' or accommodation space is created by the thinning overburden and, more frequently, by separating faulted blocks to create space for salt to intrude (Fig. 1.16a). During reactive diapirism, salt diapirs will stop rising on the condition that sufficient overburden remains above the salt structures when regional extension stops, as salt diapirism is controlled by regional extension (Jackson and Vendeville, 1994). As the breaching of the resisting forces that retard salt diapirism will result in weakened salt roofs, one possible phenomenon to consider is that of salt diapirs intruding the overburden strata up to the surface, a process involving both active and passive diapirism (Vendeville and Jackson, 1992; Jackson and Vendeville, 1994; Hudec and Jackson, 2007).

1.4.3.2. Active diapirism

An active salt diapir often presents an arching roof (Dooley et al., 2009) (Fig. 1.16b). The main driving forces for active diapirism are either regional compressional forces or buoyancy, especially when a previously formed salt structure is present in the area where the diapir is ultimately formed (Davison et al., 1996). As salt is weaker than other lithologies in sedimentary basins, the overburden strata above salt diapirs are often shortened during regional compression in greater degree than adjacent areas with relatively little salt. Shortening forces adding to previously deformed salt structures often amplify any pre-existing structures, such as crestal faults above salt diapirs (Hudec and Jackson, 2007). Buoyancy forces alone do not provide sufficient lift to form active diapirs in areas of thick overburden rocks (Dooley et al., 2009). A threshold of

260 m was suggested for buoyancy forces to raise the post-salt overburden (Davison et al., 1996). However, the validity of such a strict value can be argued since the strength of salt's roofs, and the retarding forces generated both within salt bodies and between salt structures and their flanking siliciclastic units are known to vary in many sedimentary basins. Jackson et al. (1994) suggested a 5:1 ratio between the thickness of strata flanking salt structures and the thickness of the overburden strata as a threshold for buoyancy to act as the main driver of diapirism. In fact, with an overburden thickness < 20% of the flanking strata thickness, active salt diapirism tends to occur without regional compressional forces.

1.4.3.3. Passive diapirism

Passive diapirism is often driven by differential loading between adjacent salt-withdrawal basins when diapirs are already exposed at the surface (Jackson et al., 1994), as in the case of the Persian Gulf. Here, large volumes of sediment deposited during the Late Cenozoic led to greater subsidence of salt-withdrawal basins and promoted passive diapirism of the (Lower Miocene) Fars's salt, as well as further inflation of Hormuz salt into neighbouring structures (Alsouki et al., 2011). Passive diapirism often places the salt's roof on the depositional surface (Fig. 1.16c). However, the contrast between salt supply and sedimentation rates often results in partially covered roofs in evolving salt structures. In any case, buoyancy is sufficient to drive further salt rise during passive diapirism (Rowan et al., 2003).

1.4.4 Salt-related structures

Once the driving forces of diapirism overwhelm the resisting forces, upwards movement of the salt through the overburden is set to begin. Salt piercement causes-
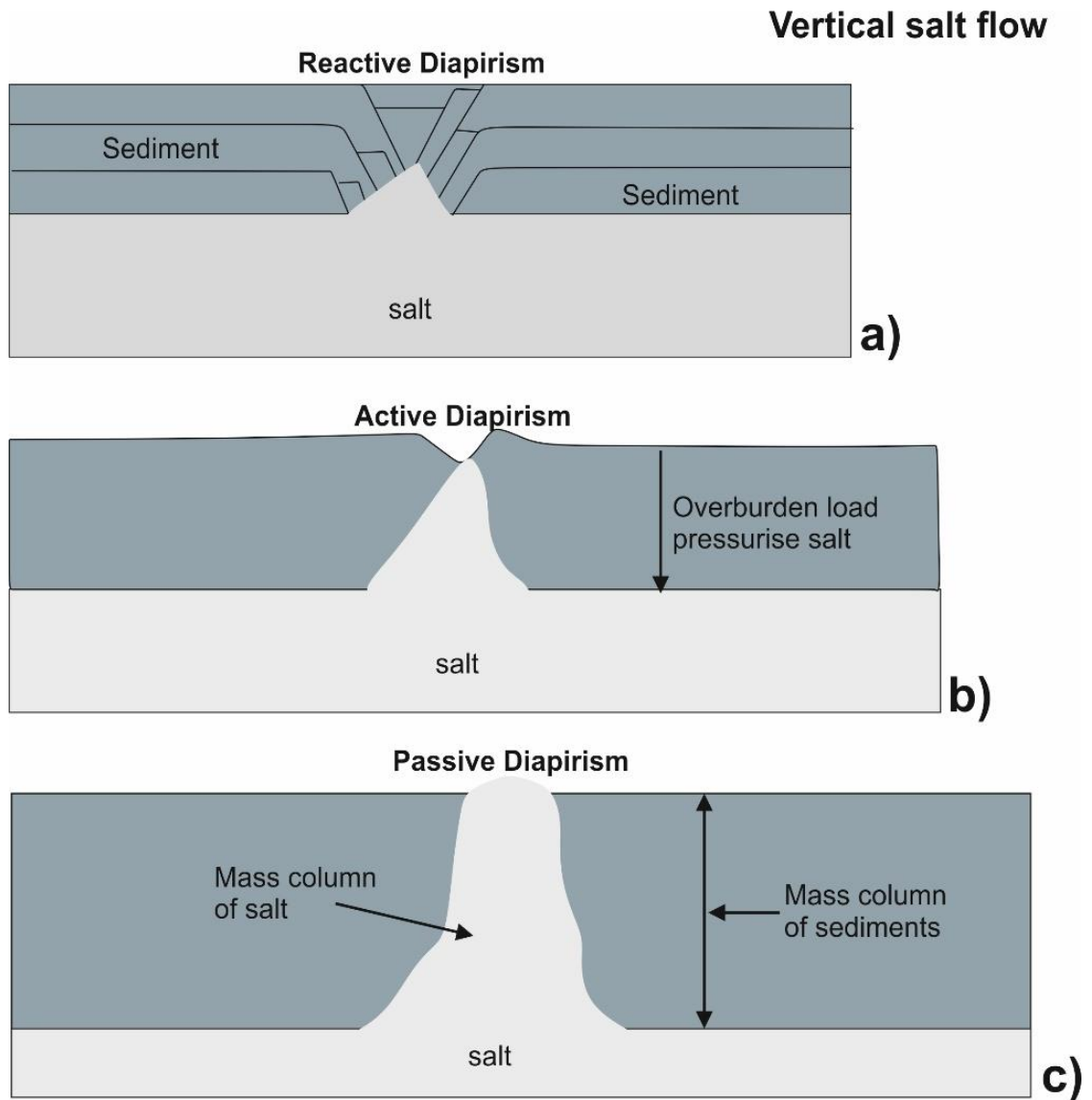
Fig. 1.16. Schematic modes of diapir piercement. a) Reactive diapir, b) Active diapir and c) Passive diapir. (Vendeville and Jackson, 1992; Hudec and Jackson (2007).

the roof rocks to be carried upwards by the salt, and a variety of structures related to halokinesis are formed consequently (Jackson et al., 1994; Rowan et al., 1999). The resulting salt structures can be categorised according to their forms, sizes, relationship to host and overburden rocks, and by considering any relationships between these structures and regional deformation styles. A full detailed account of how these structures is classified into distinct groups and sub-groups is given in Jackson and Talbot (1994) and Rowan et al. (1999). The term salt diapir is employed for all the salt-related structures in Jackson and Talbot (1994) regardless of the mechanism by which the salt pierced the overburden. However, different salt geometries may result from distinct modes of salt emplacement.

The largest and most mature groups of salt structures comprise salt-wall canopies and salt-stock canopies, whereas the least mature salt structures include salt rollers, salt anticlines and salt pillows (Fiduk et al., 2004). Salt-rich passive continental margins are dominated by extensional forces, which result in the formation of immature salt structures such as salt anticlines, salt pillows and rollers associated with large faults in upper slope regions (Alves, 2012; Rowan et al., 1999; Fiduk et al., 2004). At the transition zone separating the extensional upper-slope from the compressive lower-slope domains, dominant salt structures include salt walls, whereas in the compressive lower slope domain include mature salt structures such as thrust, allochthonous salt sheets and canopies (Fiduk et al., 2004). Faults that are salt-related (e.g. radial, concentric, crestal, keystone, roller, and rollover faults) have been documented in many areas such as southeast Brazil (Baudon and Cartwright, 2008; Alves et al., 2009, Alves, 2012) and the Gulf of Mexico (Rowan et al., 1999; Brun and Mauduit, 2009).

1.4.4.1. Roller faults

Roller faults are defined as dominantly basinward-dipping, listric growth faults that sole into a salt layer or its equivalent weld (Rowan et al., 1999). Where salt is present, the faults merge with the top salt at prominent cusps; where salt has been evacuated, the faults have triangular salt rollers (Bally, 1981; Jackson and Talbot, 1991) in their footwalls (Figs. 1.17 and 1.18). In both settings, the triangular salt roller has one flank (beneath the footwall) conformable to supra-salt bedding and the other flank (beneath the hanging wall) in fault contact with the overburden (Rowan et al., 1999) (Figs. 1.17 and 1.18).

The hanging walls of roller faults generally contain prominent landward-tilted rollover monoclines or anticlines with expanded growth sections, such that displacement increases downward, and strata thicken landward (Rowan et al., 1999) (Fig. 1.17). Roller faults accommodate gravity spreading or gliding of the overburden along the salt/weld detachment (Alves, 2012; Rowan et al., 1999; Fiduk et al., 2004).

1.4.4.2. Keystone faults

Keystone faults develop in the hinge zone of anticlines where strata are most strongly curved (Rowan et al., 1999) (Figs. 1.17 and 1.18). The faults are planar rather than listric, linear to curvilinear in map view, and form symmetric grabens (Rowan et al., 1999). They are like crestal faults, except that (1) they form over the crests of folds; (2) they do not root into salt, even though salt can core the fold; and (3) they are not growth faults generally, having displacements that decrease both upward and downward (Figs. 1.17 and 1.18).

The location of keystone faults in anticlinal hinges suggests that they are created by outer arc stretching during folding and thus do not normally accommodate any regional extension (Rowan et al., 1999) (Figs. 1.17 and 1.18). Folding is caused by either bending or buckling. Four settings for keystone fault families can be distinguished in the northern Gulf of Mexico (Rowan et al., 1999): (1) turtle anticlines, where bending of strata is caused by subsidence of both flanks into underlying salt; (2) rollover monoclines in the hanging walls of normal faults, where bending is related to extension; (3) contractional folds, where shortening is accommodated by buckling; and (4) domal structures above diapirs or salt pillows, where arching may be caused by active diapirism (bending) or by rejuvenation of diapirs during regional contraction (buckling) (Rowan et al., 1999).

1.4.4.3. Rollover faults

Rollover faults are associated with a monoclinal rollover in the hanging wall of a fault or weld (Rowan et al., 1999) (Fig. 1.18). A rollover fault family has a dominant dip direction antithetic to the bounding fault/weld; the faults dip in the same direction as the rollover strata (Rowan et al., 1999). The dominant fault dip can be basinward, as for a rollover above a counter-regional weld, or landward, as for a rollover above a roller fault (Rowan et al., 1999) (Figs. 1.17 and 1.18). The faults essentially are planar and dip uniformly. They cut the sub-horizontal limb just above the axial trace of the monocline and migrate up-section toward the master fault or weld (Rowan et al., 1999).

Growth-fault expansion is absent or negligible, and the faults do not extend downward into salt; they generally die out both above and below at their tip lines (Rowan et al., 1999). Rollover faults generally have linear map traces parallel to the trend of the monocline.
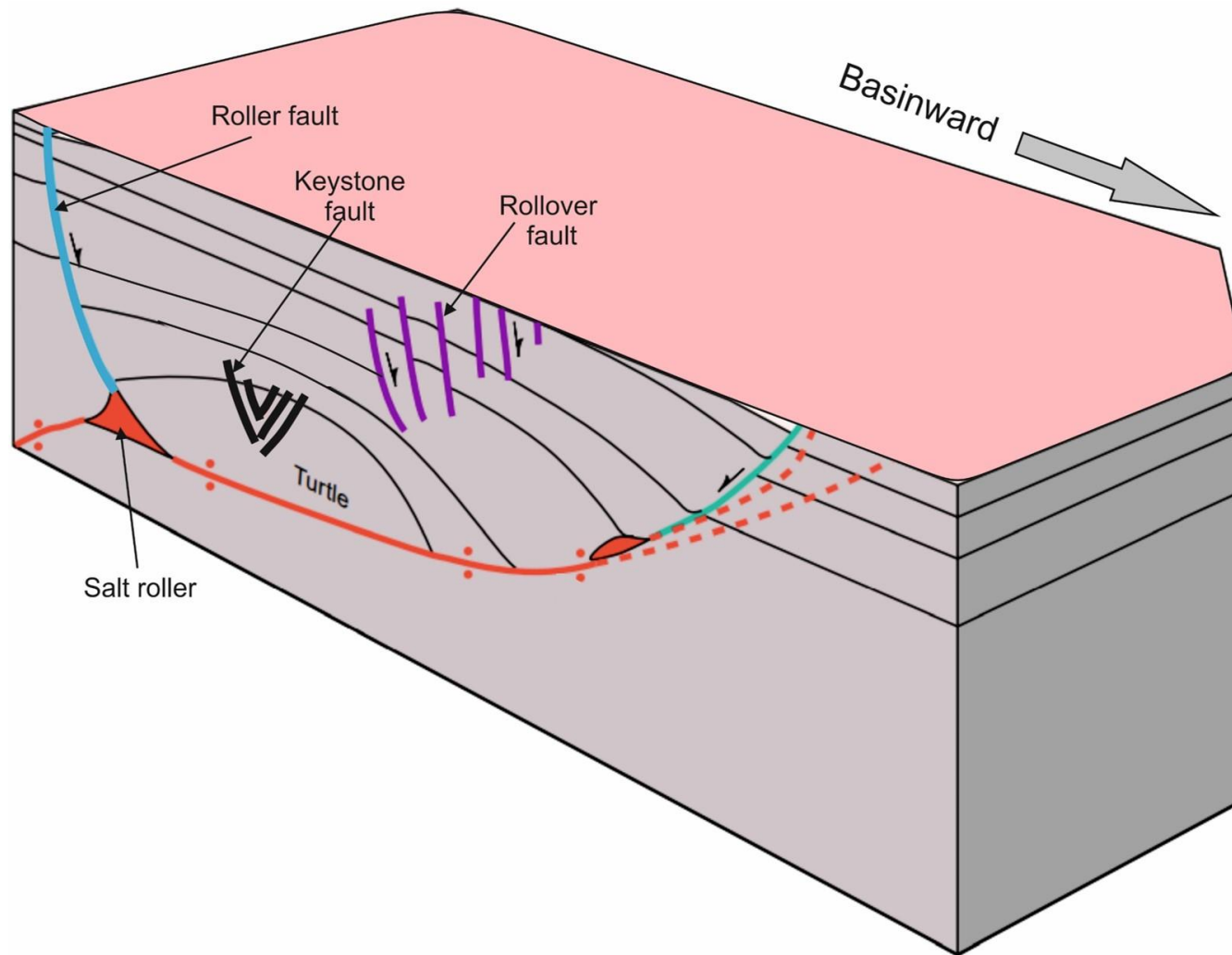
Fig. 1.17. Schematic diagram showing typical assemblages of salt-related structures including salt roller, roller fault, rollover faults and keystone faults. Figure modified from Rowan et al. (1999).

The association of these faults with monoclinal rollovers suggests they accommodate some of the bending strain in the hanging walls (Rowan et al., 1999). In this sense, they are like keystone faults; both form where strata are most sharply curved, and they can occupy similar settings in rollover folds (Rowan et al., 1999).

1.4.4.4. Crestal faults

Crestal faults are dominantly planar growth faults that root into the crests of triangular diapirs and form symmetric grabens (Rowan et al., 1999) (Fig. 1.18). The age of syn-kinematic strata, and thus of the faults, increases down the diapir flanks (Rowan et al., 1999). Offsets in the top salt where faults intersect the salt tend to be small. In map view, crestal faults form narrow, linear to curvilinear grabens that parallel ridges in the underlying salt (Rowan et al., 1999). Like the salt ridges, the grabens typically form complex polygonal patterns (Rowan et al., 1999).

The described fault geometries are characteristic of those overlying reactive diapirs, which form during extension above a salt layer (Vendeville and Jackson, 1992). Such grabens were termed "reactive grabens" by Schultz-Ela and Jackson (1996). Thus, Rowan et al. (1999) infer that crestal fault families form due to basin-ward translation of the overburden, where the faults strike roughly parallel to the coastline and shelf margin. Where they form true polygonal patterns, they probably record radial or multidirectional spreading of the salt and its overburden (Jackson and Vendeville, 1995).
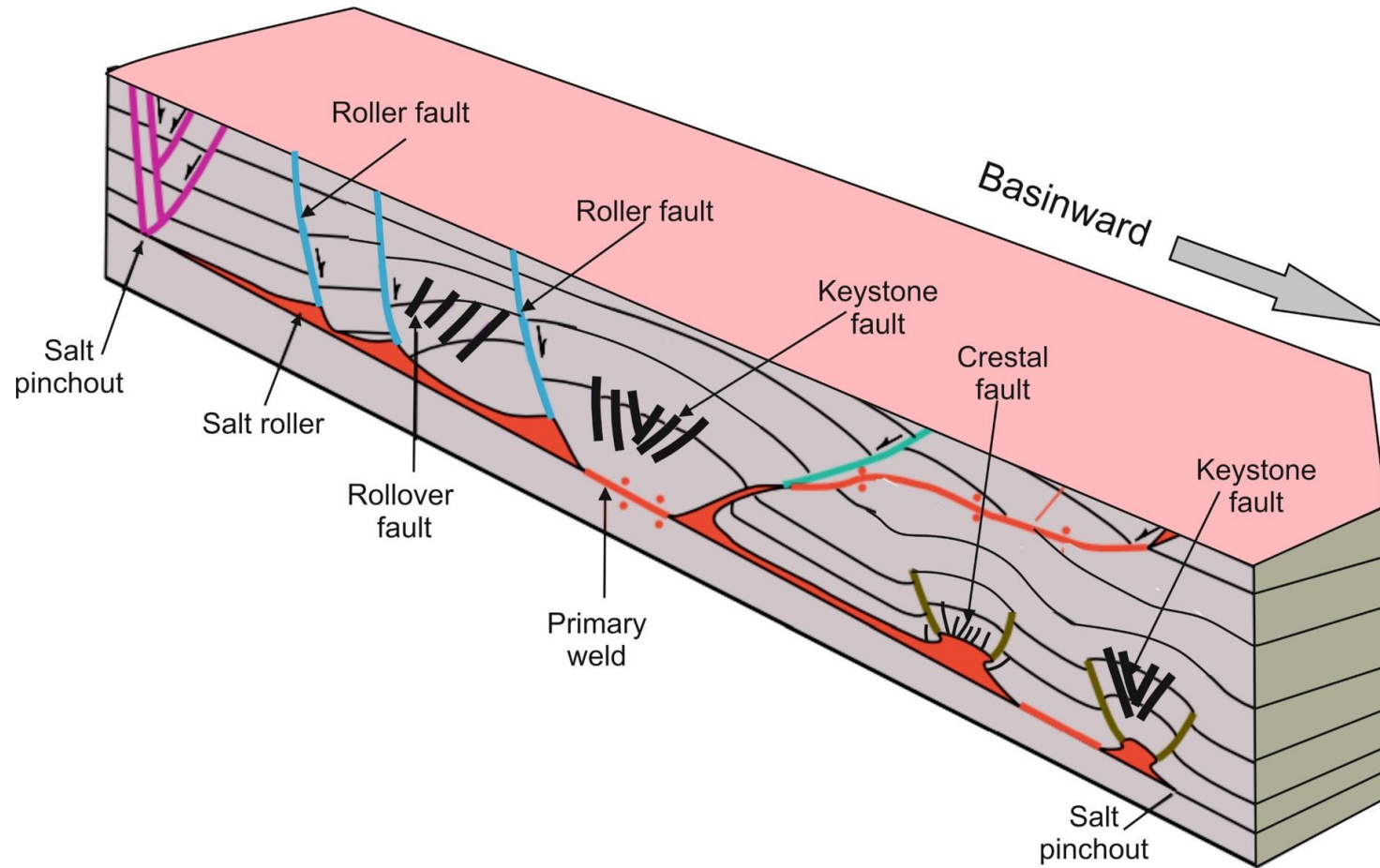
Fig. 1.18. Schematic diagram showing typical assemblages of salt-related structures including salt roller, roller fault, rollover faults and keystone faults. Figure modified from Rowan et al., 1999).

1.5. Thesis layout

This thesis is divided into eight (8) chapters. The current chapter (Chapter 1) comprises an introduction to the thesis, including its bacground and hypothesis. It also presents a literature review of the key concepts covered in this thesis. Specifically, mechanical stratigraphy and faulting, fault-growth models and salt-related structures. The literature review is followed by the Geological settings of the three study areas in Chapter 2. These areas include: the Espírito Santo Basin, (offshore SE Brazil); the Broad Fourteen Basin, offshore the Nertherands (Southern North Sea) and Offshore Nankai accretionary prism, (SE Japan).

Chapter 3 presents the methods used in the thesis, including a brief general description of seismic data acquisition, processing and interpretation methods. Also a brief description of seismic data used. Chapters 4, 5, and 6 are data-analysis chapters; some of these data are already published in international journals at the time of submission of this work. Chapter 4 investigates the impact of tectonic raft's gravitational instability on faut geomerty and reactivation in the Espírito Santo Basin, offshore SE Brazil. The chapter was published as Maunde, A., Alves, T.M., 2020. Impact of tectonic raft 'gravitational instability on faut reactivation and geometry. Journal of Structural Geology, 130, 103916. https://doi.org/10.1016/j.jsg.2019.103916.

Chapter 5 investigates the effect of tectonic inversion on supra-salt faut geometry and reactivation histories in the Southern North Sea. The chapter was peer-reviewed and re-submitted as Maunde, A., Alves, T.M., 2021. Effect of tectonic inversion on supra-salt faut geometry and reactivation histories in the Southern North Sea. Journal of Marine and Petroleum Geology, Ms. Ref. No.: JMPG-D-21-00702.

Chapter 6 explores a set of shallow fault systems from areas dominated by thrust anticlines in the outer wedge region of the Nankai accretionary prism (SE Japan). The chapter was published as Maunde, A., Alves, T.M. and Gregory F. M. 2021. Shallow fault systems of thrust anticlines responding to changes in accretionary prism lithology (Nankai, SE Japan). Tectonophysics 812 (2021) 228888. https://doi.org/10.1016/j.tecto.2021.228888. The results are compiled in Chapter 7 to discuss their wider importance. Final conclusions of the thesis are presented in Chapter 8.

CHAPTER 2

Geological setting of the three study areas in the thesis

2. Geological setting of the three study areas in the thesis

2.1. Introduction

This chapter aims to review the geological settings of the three study areas in the thesis. These three study areas include: 1) the Espírito Santo Basin (SE Brazil), 2) the Broad Fourteens Basin (Southern North Sea) and 3) the Nankai Accretionary Prism (SE Japan).

2.2. Espírito Santo Basin, Offshore SE Brazil

The study area of the Espírito Santo Basin is located on the continental margin of southeast Brazil (Fig. 2.1). The basin covers an area of about 125,000 km^2, of which 18,000 km^2 are onshore and 107, 000 km^2 are offshore (Fiduk et al., 2004). It is associated with the continental break-up of Gondwana, which lasted from the Late Jurassic to Early Cretaceous, and the subsequent opening of the South Atlantic Ocean (Chang et al., 1992; Davison, 1999; Meisling et al., 2001).

The Espírito Santo Basin shares a very similar geological history to other sedimentary basins in southeast Brazil (i.e., Campos and Santos Basins); all have accumulated a very thick stratigraphic succession that includes lithologies as variable as basalt flows in the pre-rift, continental sandstones and shales in the rift sequence, carbonate and evaporites in the transitional sequence, and deep-marine siliciclastic and carbonate sediments in the post-rift sequence (Bruhn and Walker, 1997; Mohriak et al., 1998). The basin is limited to the north by the Early to Middle Eocene volcanic Abrolhos Plateau and to the south by the Vitoria High, which separates it from the Campos Basin (Guardado et al., 1989; Bruhn and Walker, 1997; Fiduk et al., 2004; Alves et al., 2009; Alves, 2012) (Fig. 2.1).
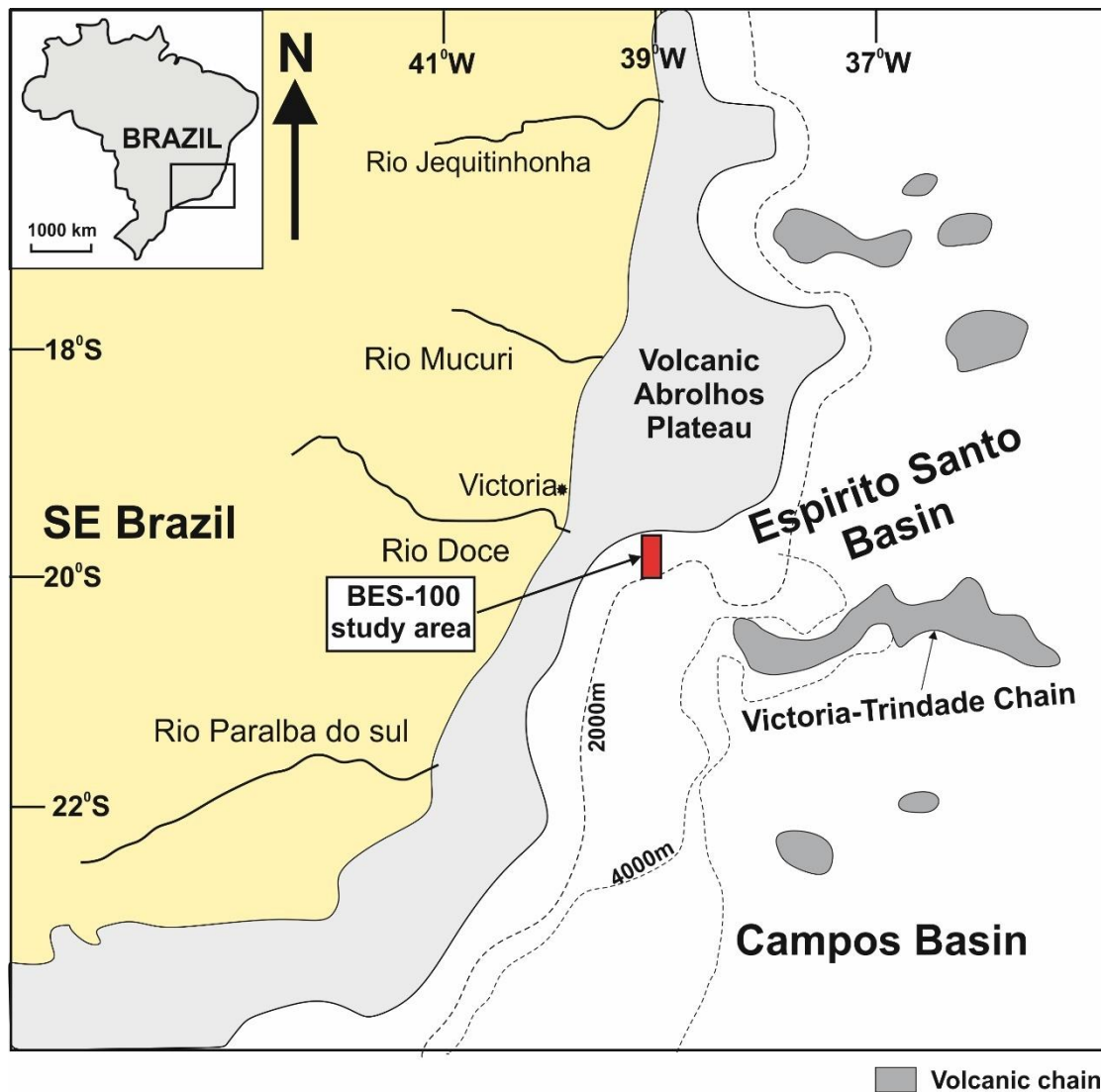
Fig. 2.1. Map of the southeast Brazilian margin showing the location of the study area (Espírito Santo Basin, seismic block BES-100).

2.2.1. Tectono-stratigraphic setting

The geodynamic evolution of the Espírito Santo Basin was primarily controlled by four tectonic stages common along most South Atlantic continental margins: the pre-rift, syn-rift, transitional and drift stages (Ojeda, 1982; Mohriak et al., 1998; Gibbs et al., 2003) (Figs. 2.2 and 2.3). The architecture of resulting tectonic megasequences was largely controlled by regional magmatism and thin-skinned gravitational gliding and spreading over Aptian evaporites (Fiduk et al., 2004; Gamboa et al., 2010).

Magmatic and volcanic events played significant roles in shaping the architecture of the basin. These events included flood basalts extruded prior to and/or during early rifting, lavas extruded just prior to continental separation during the transition stage, the emplacement of seaward dipping reflectors after continental separation during the early drift stage and, finally, early to middle Eocene volcanic activity, which was associated with emplacement of the Abrolhos volcanic complex to the north of the study area (Gibbs et al., 2003; Fiduk et al., 2004).

The deposition of Aptian evaporites and its subsequent deformation into rollers, diapirs, tongues, canopies, and imbricate thrusts during gravitational failure of the margin has strongly influenced the deposition of overlying and surrounding carbonate and turbidite bearing strata. This process occurred throughout the Cenozoic, peaking during the Eocene-early Oligocene (Fiduk et al., 2004; Alves et al., 2009; Alves, 2012). Fiduk et al. (2004) and Gamboa et al. (2010) related the deformations at the continental slope margin of the SE Brazil to gravity gliding and spreading as a result of seaward progradation and sediment loading. They then classified the SE Brazilian continental slope margin into three structural domains (Fig. 2.2).
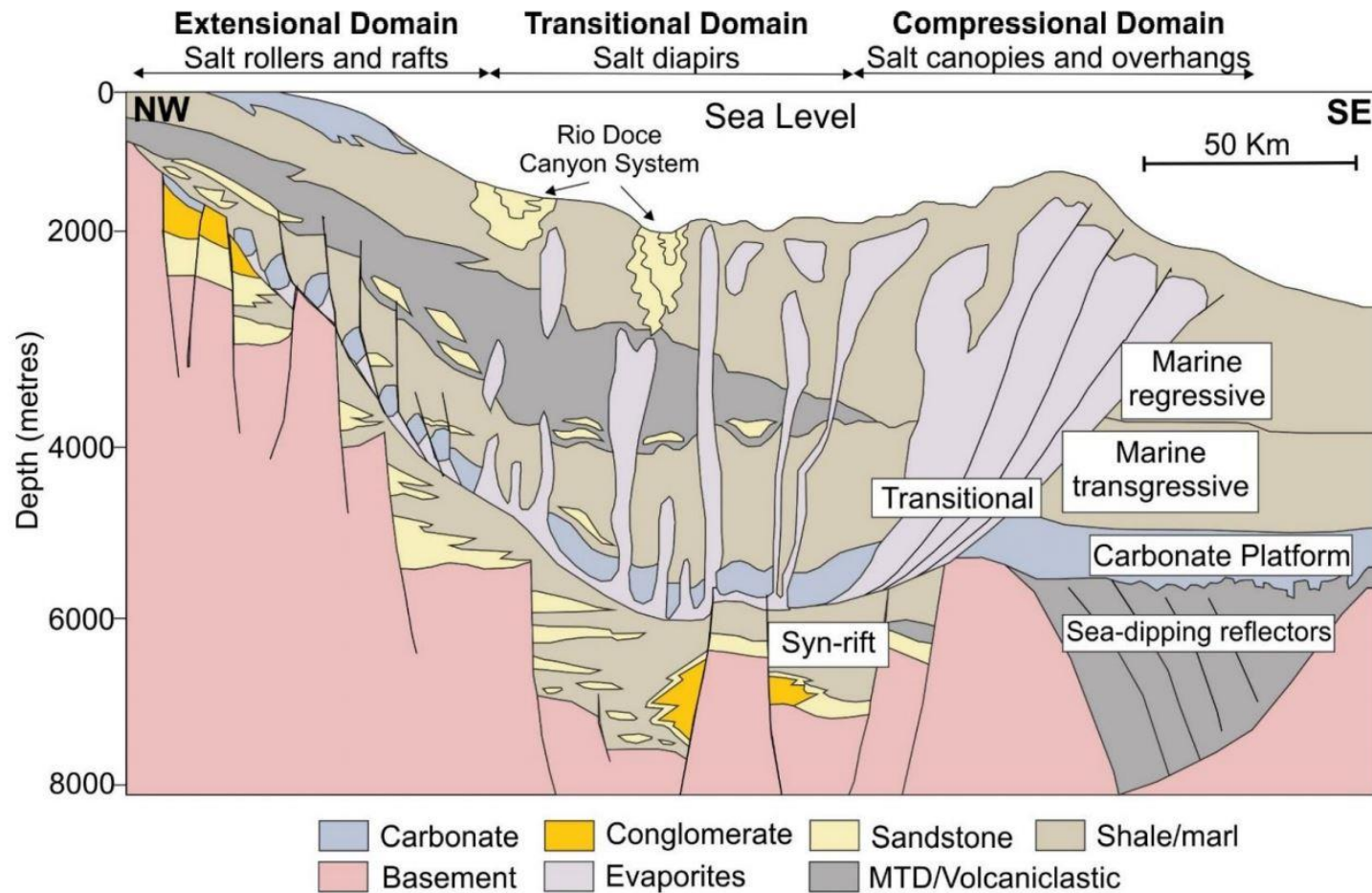
Fig. 2.2: Simplified regional section of the Espírito Santo Basin showing major depositional sequences and structures across three salt domains (extensional, transitional, and compressional). Modified from Fiduk et al. (2004) and Gamboa et al. (2010).

2.2.1.1. Tectonic phases and megasequences

Fiduk et al. (2004) and Gamboa et al. (2010) recognised four tectonic phases in the Espírito Santo Basin: 1) pre-rift/rift onset, 2) syn-rift phase, 3) post-rift (Transitional) phase, and (4) drift phase. Mohriak et al. (1998) correlated these tectonic stages with three main depositional megasequences: 1) a pre-rift megasequence (Late Jurassic to Earliest Cretaceous) dominated by extrusive magma, volcaniclastic material and tuffs deposited unconformably over a Pre-Cambrian basement (Asmus et al., 1971); 2) a syn-rift megasequence (Berriasian to Early Aptian), with continental sandstones, silts and shales, together with fault-related syn-tectonic conglomerates and basaltic volcaniclastic rocks (Ojeda, 1982; Mohriak et al., 1998; Gamboa et al., 2010; Chang et al., 1992); and 3) the post-rift megasequence (Aptian to Recent), the main interval of interest of this chapter dataset, which is subdivided into three sequences - transitional, early drift transgressive marine, and late drift regressive marine (Figs. 2.2 and 2.3).

The transitional sequence (Mid-Aptian to Early Albian) comprises thick layers of evaporitic sediments separated from the syn-rift sequence by an angular unconformity of regional expression (Ojeda, 1982; Chang et al., 1992; Demercian et al., 1993; Davison, 1999). The transitional stage in southeast Brazil records the deposition of >3000 m of evaporites, mainly halite and anhydride resulting from extreme marine evaporation in arid climatic conditions (França et al., 2007; Mohriak, 2003; Mohriak et al., 2008). The end of the transitional cycle is marked by the onset of extrusive igneous activity related to a newly-formed oceanic spreading ridge (Mohriak et al., 2008; Ojeda, 1982; Davison, 1999, 2007). Salt structures in the transitional sequence show a proximal to basinward shift from salt rollers to vertical diapirs (Fig. 2.2).

The early drift sequence (Albian to Early Eocene), which overlies the transitional sequence, comprises two marine-transgressive sub-sequences materialising the development of a shallow-water carbonate platform from the late Albian to Cenomanian (Chang et al., 1992). The onset of this carbonate platform is documented by the São Mateus and Regência Formations, which were deposited over the Itaúnas Member evaporites (Mohriak, 2003; França et al., 2007) (Fig. 2.3). The São Mateus Formation consists of sandstones deposited in a proximal marine setting over a succession of shales, siltstones, and carbonates. The Regência Formation (Asmus et al., 1971) comprises a relatively thick carbonate sequence of limestones, carbonate mudstones, and wackestones, with ostracods, gastropods and pelecypods fragments deposited in distal parts of the Espírito Santo Basin (Mohriak, 2003; França et al., 2007). The Albian carbonate platform is overlain by shales of Turonian to Palaeocene age, indicating a relative deepening of the basin (Gamboa et al., 2010, 2011; Ojeda, 1982; Demercian et al., 1993) (Fig. 2.3).

A mid-Eocene sequence boundary occurs across the entire southeast Brazilian margin and separates the early from the late drift stages (Gamboa et al., 2011) (Fig. 2.3). Above this boundary, Eocene to Holocene siliciclastic units were deposited during a regressive period recording sediment progradation on the continental slope (Demercian et al., 1993; Chang et al., 1992). At this time, clastic sediments filling the basin were derived from the erosion of coastal mountain ranges and from relatively local volcanic activity on the Abrolhos Plateau (Chang et al., 1992; Gamboa et al., 2010). Tuffs, volcanic breccias and hyaloclastites formed the bulk of the volcanoclastic input, whereas fine to coarse massive sandstones, conglomerates and siltstones were eroded from nearby mountains (Gamboa et al., 2010).
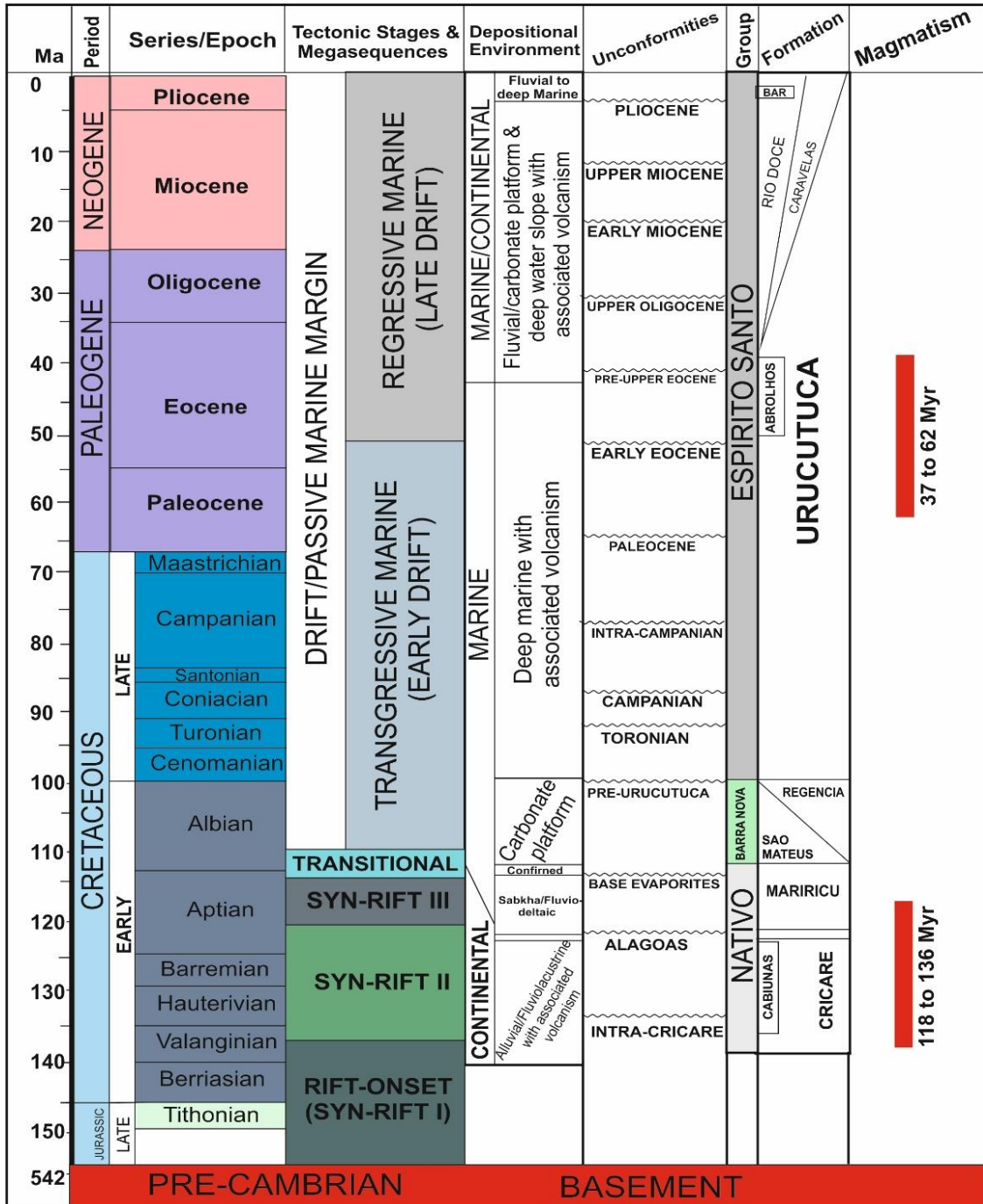
Fig. 2.3. Stratigraphic column of the Espírito Santo Basin highlighting the main tectono-sedimentary stages and magmatic events in the basin. Modified from França et al. (2007).

Sediment transport occurred on Brazil's eastern margin in both drift stages but was particularly important in the Late Oligocene to Holocene, as shown by the generation of vast channel systems (Viana et al., 2003; Fiduk et al., 2004; Alves, 2010). Between the Early/Mid Eocene and the Holocene, mass-transport deposits (MTDs) were also deposited in response to the uplift of coastal mountain ranges, subsequent tilting of the continental slope and halokinesis (Mohriak et al., 2008; Alves and Cartwright, 2010).

2.2.2. Hydrocarbon systems

The recent deep-water hydrocarbon discoveries made adjacent to the Espírito Santo Basin (e.g. Campos Basin) led to an intensive deep-water exploration of the basin. New discoveries have been made in deep-water settings above the Aptian evaporites (e.g. Golfinho Field) (Toniatti, 2003; Fiduk et al., 2004; Alves, 2012).

The hydrocarbon plays in the Espírito Santo Basin extend from the shallow to the deep-water slope region and involve a variety of reservoirs above and below the Aptian salt, including Neocomian-Barremian fractured basalts near the top of the continental basement, Barremian to Aptian carbonates and fluvial-deltaic successions, early Albian carbonates, and late Albian-Miocene turbidites. These intervals have been charged principally from late Barremian-early Aptian (syn-rift phase) source rocks deposited in graben sub-basins with restricted saline lacustrine environments (Mello and Maxwell, 1990).

2.2.2.1. Source rocks

The main source rocks in the Espírito Santo Basin comprise Cenomanian/Turonian deep-marine shales in the Urucutuca Formation, shallow to deep marine marls in the Albian Regência Formation, fluvio-marine shales in the Aptian Mariricu

Formation/Mucuri Member (Transitional), and lacustrine shales in the Barremian/Aptian Cricaré Formation/Sernambi member (Mello and Maxwell, 1990) (Fig. 2.3). Fine-grained lacustrine sediments consist of fine sand, silts and dark shales deposited in syn-rift depocentres (Ojeda 1982; Chang et al., 1992; Fiduk et al., 2004).

2.2.2.2. Reservoir rocks and traps

The Valanginian/Barremian (Cricaré Formation), Aptian (Maricuca Formation), Regência Albian) carbonates, transgressive sands (Campanian and Maastrichtian; Urucutuca Formation), and regressive sands (Cenozoic) represent the main reservoirs intervals in the Espírito Santo Basin (Fiduk et al., 2004; Franca et al., 2007) (Fig. 2.3).

The Middle to Late Aptian carbonate and fluvial-deltaic deposits and evaporites were distributed across the Espírito Santo Basin depocenters. The pre-salt hosts and grabens, and the thick cover of salt above these depocentres form trapping mechanisms and a regional seal for sub-salt hydrocarbon systems (Vieira et al., 2007). After continental break-up in the middle Aptian to Albian, the post-rift development of the basin was characterised by major carbonate progradation to aggradation (Regência carbonates) (Franca et al., 2007). The Regência carbonates have formed as shoals over salt induced highs and are reputed to be productive in the basin. The Regência Formation contains carbonates platform that form rafts and turtle-back structures, both common features in the basin (Fiduk et al., 2004).

Transgressive marine sands (Campanian and Maastrichtian; Urucutuca Formation) have been deposited in channels, canyons, and fan complexes throughout the Espírito Santo Basin. Identifying where these deposits are incorporated in turtle structures defines the deep-water prospects with greatest reserves potential (Fiduk et al., 2004). With the continental margin development, differential subsidence (basin tilting) and

increasing sediment load triggered intense salt remobilization. Salt-related structures (diapirs, rollover structures) form potential structural-stratigraphic hydrocarbon traps in the Late Cretaceous-Neogene succession. At the same time, salt welds and extensional faults formed migration pathways from the sub-salt source rocks (i.e. Late Barremian-Aptian lacustrine shales) to post-salt reservoirs, including Albian mixed carbonate-clastic successions and Late Cretaceous-Neogene turbidites (Davison, 1999).

2.3. Broad Fourteens Basin, offshore The Netherlands

The Broad Fourteens Basin is located in the Dutch sector of the Southern North Sea, encompassing blocks K, L, P, and Q offshore The Netherlands (Fig. 2.4). The basin trends northwest-southeast and is approximately 120 km long by 45 km wide (Verweij and Simmelink, 2002) (Fig. 2.4).

2.3.1. Tectonic setting

The Broad Fourteens Basin, part of the larger South Permian Basin, records a complex history of rifting, halokinesis and inversion (Verweij and Simmelink, 2002; Van Wijhe, 1987; Ziegler, 1990; Nalpas et al., 1995; Duin et al., 2006). It was formed during the Mesozoic in response to E-W extension associated with opening of the Atlantic Ocean (Verweij and Simmelink, 2002). The evolution of the basin can be divided into three intervals with distinct deformation styles and histories: 1) Pre-rift/rift onset phase (Carboniferous-Permian); 2) Syn-rift phase (Triassic-Jurassic); 3) Inversion phase (Late Cretaceous-Cenozoic) (Fig. 2.5).
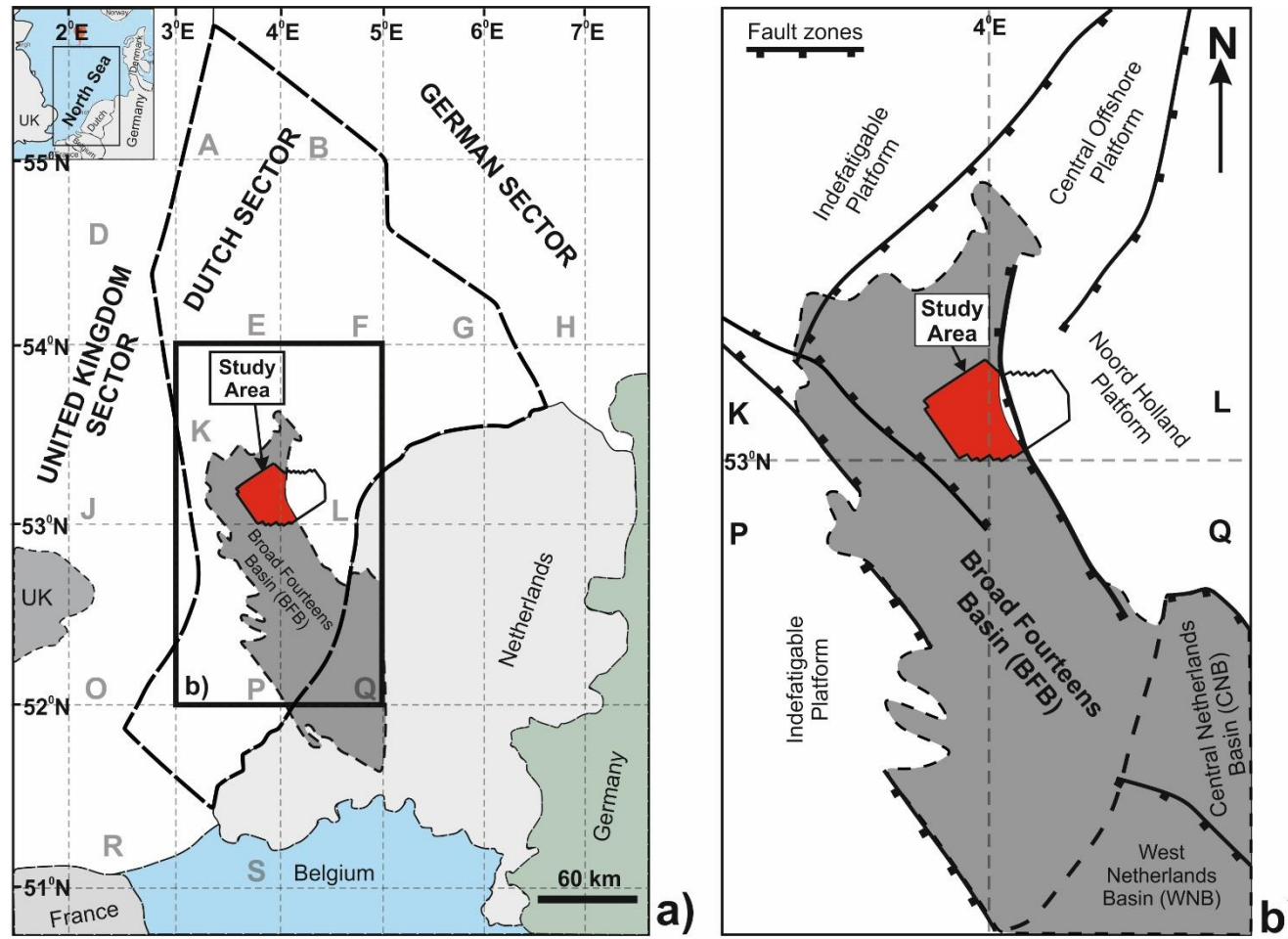
Fig. 2.4. a) Map of the Southern North Sea highlighting its Dutch sector and location of the study area in the northern end of Broad Fourteens Basin (BFB), offshore The Netherlands, b) Zoomed-in map of the NW-SE trending Broad Fourteens Basin and associated structural elements. Figures modified from van Verweij and Simmelink (2002). Letters A to S refer to hydrocarbon exploration blocks in the Southern North Sea.

2.3.1.1. Pre-rift/rift onset phase: Carboniferous-Permian

Towards the end of the Carboniferous, the Variscan Foreland basin developed in the Southern North Sea. Thick lacustrine and deltaic intervals with interbedded coal seams were deposited as part of the Limburg Group (Fig. 2.5). Included in this Group are the Westphalian Coal Measures, a major source of gas in the Southern North Sea (Gerling et al., 1999; Van Wijhe, 1987). Oblique-slip normal faulting predominated after the Variscan Orogeny, with the largest faults cutting through the Variscan fold belt to propagate along older NW-SE trending basement faults. The present-day structural grain of the Southern North Sea follows horst and graben structures formed by these faults (Ziegler, 1990; Duin et al., 2006; Van Wijhe, 1987; Oudmayer and De Jager, 1993).

Sedimentation in the Permian was interrupted by thermal upwelling from dolerite intrusions through oblique-slip dextral normal faults. This hiatus is expressed in the form of a Saalian unconformity separating Lower from Upper Rotliegend strata (Van Wees et al., 2000) (Fig. 2.5). Subsidence resumed in the Late Permian, and the South Permian Basin became separated from the North Permian Basin by the Mid North Sea High (Duin et al., 2006).

Upper Rotliegend terrestrial sandstones of the Slochteren Formation were deposited above the Saalian unconformity and became the major reservoir for the Permian gas plays offshore, the Netherlands (Verweij and Simmelink, 2002). The Zechstein Sea subsequently flooded the study area in the Latest Permian. Carbonate-evaporite cycles in Zechstein evaporites reflect fluctuations in sea level, but thick deposits of Zechstein evaporites in the North of the Broad Fourteens Basin became an effective seal rock for Permian gas plays (Coward, 1995) (Fig. 2.5).
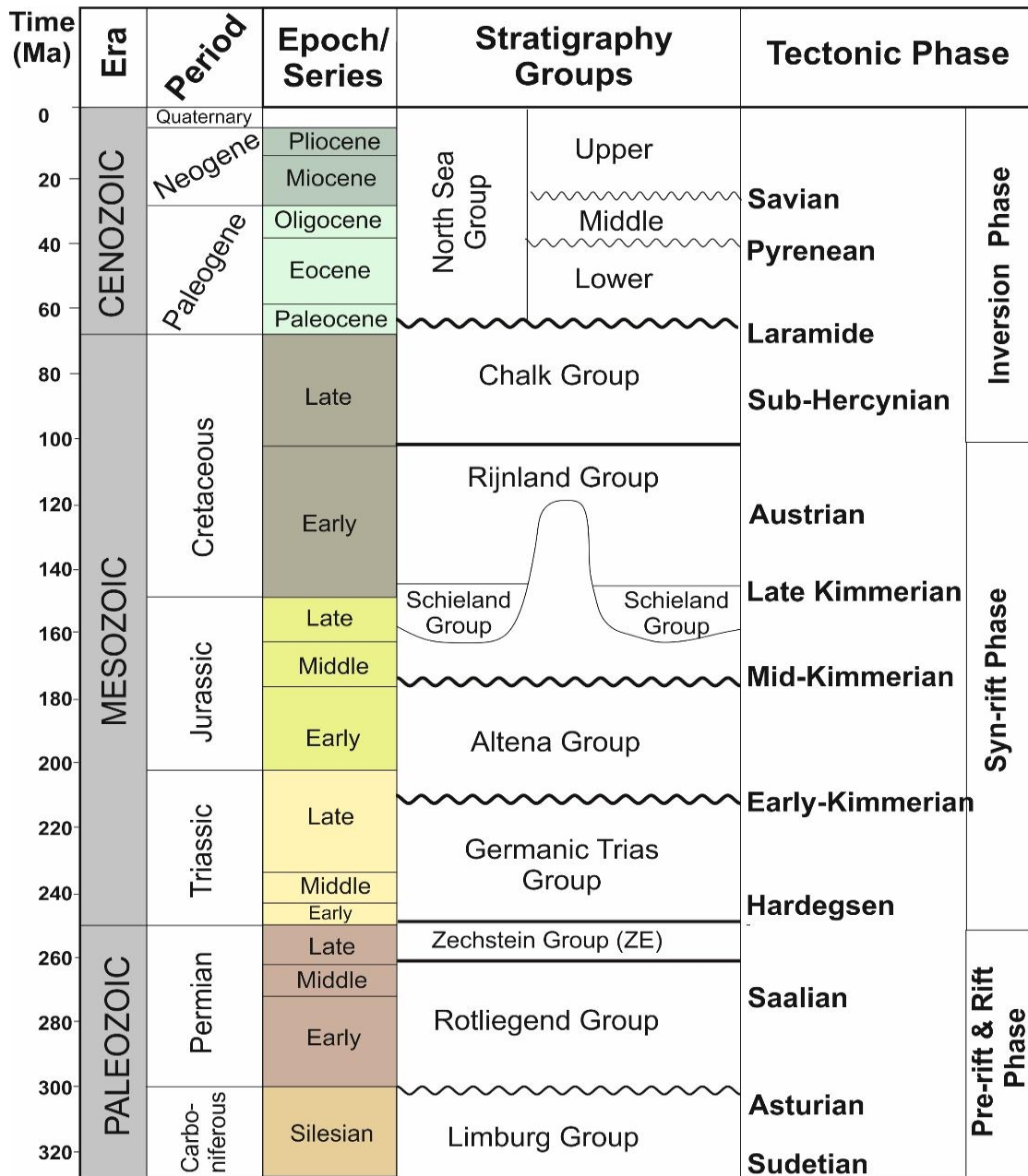
Fig. 2.5. Simplified stratigraphic column of the Dutch Sector of the Southern North Sea. Main stratigraphic groups, tectonic phases and unconformities related to regional tectonic events are based on Penge et al. (1999) and van Verweij and Simmelink (2002).

2.3.1.2. Syn-rift phase: Triassic-Jurassic

Rifting intensified during the Triassic, allowing for differential subsidence in the Southern North Sea (Alves and Elliott, 2014; Duin et al., 2006). In the rapidly subsiding Broad Fourteens Basin, aeolian sands and lacustrine claystones from the Lower and Upper Germanic Trias Group were deposited (Fig. 2.5). The Lower Buntsandstein is a prolific gas reservoir, particularly where Zechstein salt has been withdrawn and welds have formed between Triassic sequences and the Rotliegend Group (Van Hulten, 2010b).

Towards the end of the Triassic, salt tectonics and reactive diapirism became concentrated along extensional boundary faults (Stewart and Coward, 1995; Ziegler, 1992). Rift-raft tectonics led to the further deepening of the Broad Fourteens Basin and open marine conditions (Alves and Elliott, 2014; Penge et al., 1993). As a result, the deep-water Altena Shales were deposited in the Broad Fourteens Basin, with the more bituminous Posidonia Shale Formation comprising the source interval for Jurassic oil plays in the basin. The deposition of the Posidonia shales accompanied the significant isolation of the Southern North Sea in the form of confined sub-basins (Nalpas et al., 1995; Duin et al., 2006).

Deposition of the Altena Shales stopped during the Mid-Kimmerian upwarping event (Middle Jurassic). In areas of greatest uplift, up to 1500 m of Jurassic rocks are thought to have been eroded (Heim et al., 2013). Despite this localised uplift event, sharp pulses of NE-SW rifting continued to rotate the Broad Fourteens Basin to its present-day NW-SE orientation (Fig. 2.4b). Increased erosion of Triassic, Zechstein and Rotliegend rocks on active structural highs generated thick successions in the Delfland Subgroup

and Vlieland Sandstone - both comprising reservoirs for oil sourced from the Posidonia Shale (Van Wijhe, 1987; Verweij and Simmelink, 2002; Duin et al., 2006).

2.3.1.3. Inversion phase: Late Cretaceous-Cenozoic

A major episode of sea-level rise, accompanied by post-rift subsidence, led to the accumulation of thick layers of chalk both in individual basins and on adjacent marginal highs (Van Wijhe, 1987; Verweij and Simmelink, 2002). In the Turonian, N-S Alpine compression interrupted subsidence and Subhercynean inversion reactivated Variscan faults with a reverse-dextral motion (De Lugt et al., 2003; Nalpas et al., 1995). In such a setting, the localisation of a salt (Zechstein) décollement layer to the North of the Broad Fourteens Basin accounts for the lack of connectivity between sub-salt and supra-salt faults (Van Wijhe, 1987). Maximum erosion (~3000m) took place in the centre of the inverted basin, close to the axis of inversion (Nalpas et al., 1995; De Lugt et al., 2003).

Three additional inversion events took place in the Broad Fourteens Basin, separated by periods of subsidence. The Laramide inversion in the Cenozoic reactivated Subhercynean faults, creating a prominent Cretaceous-Tertiary unconformity (Oudmayer and De Jager, 1993; De Lugt et al., 2003). Major basin inversion events are recorded in the Cenozoic, the largest of which coincided with the Pyrenean Orogeny (Oligocene) and created an unconformity at the base of the Miocene (Oudmayer and De Jager, 1993; Verweij and Simmelink, 2002). It separated the Lower North Sea Group from the Middle North Sea Group (Wong et al., 2001).

The boundary between the Middle and Upper North Sea Groups is based on a break of sedimentation resulting from regional uplift and global low in sea level associated with the Alpine Orogeny (Savian unconformity; Middle Miocene) (Oudmayer and De Jager,

1993; Wong et al., 2001). Together with these tectonic phases occurs, at present, a general up-dip migration of hydrocarbons (Van Balen et al., 2000; Verweij and Simmelink, 2002; Isaksen, 2004). Broad folds formed in response to the inversion events, causing reservoirs to be tilted beyond spill-point, allowing secondary migration of fluids into shallower reservoirs (Van Balen et al., 2000). Since compression initiated in the Late Cretaceous, contemporaneous faulting and diapirism created fluid flow pathways (Isaksen, 2004).

2.3.2. Petroleum systems

Stratigraphic sequences including source, reservoir and seal rocks create economic and large hydrocarbon fields. Subsidence and uplift histories, along with fluctuations in eustatic sea-level have produced this stratigraphy and enabled the maturation and charging of the oil and gas (Verweij and Simmelink, 2002; Verweij et al., 2003; 1990; Van Hulten, 2010; Van Wijhe, 1987).

2.3.2.1. Permian gas plays

During the Westphalian stage, the Variscan Orogeny created a foreland basin in the southern North Sea. The equatorial terrestrial setting recorded at this time allowed the basin wide deposition of thick lacustrine sediments prograding into deltaic and fluvial fine-grained siliciclastics with intercalations of coal (Verweij and Simmelink, 2002; Van Wees et al., 2000; Quirk, 1993; Glennie and Provan, 1990). Most coal seams belong to either the Ruurlo or Maurits Formations of the Limburg Group (Fig. 2.5). It is a kerogen type III coal, with a total organic content (TOC) of at least 70% and comprising the main source rock in the Permian gas plays of the southern North Sea.

Coal content reaches 4% in the Ruurlo Formation, and 6% in the Maurits Formation (Verweij and Simmelink, 2002; Van Hulten, 2010).

The Limburg group has been measured to be >1000 m thick (Quirk, 1993), with individual coal seams having a cumulative thickness >10 m. Because the Limburg Group is so widely reaching and thick, the basin could have been charged with gas several times as different coal seams reached the gas window (Van Hulten, 2010). Verweij and Simmelink (2002) suggested that the central part of the Broad Fourteens Basin entered the gas window during the Jurassic (main syn-rift sequence), with peak gas expulsion in the Cretaceous (pre-inversion). The northern part of the basin likely remained out of the gas window.

The Upper Rotliegend Group lies unconformably over the Variscan basement; sandstones of this group are the main reservoir for Permian gas. The sandstones consist largely of the Slochteren and Silverpit Formations (Fig. 2.5). Thick aeolian and fluvial coarse-grained clastics of the Slochteren Formation were deposited in the late Permian throughout the southern North Sea. Finer-grained desert lake deposits of the Silverpit Formation increase in thickness towards the north of the basin (Verweij and Simmelink, 2002; Glennie and Provan, 1990). Thickness variation often depends on the palaeotopography of previous structures, with thinner deposits being recorded on structural highs and thicker strata occurring in late Permian basins.

Facies changes in the Upper Rotliegend Group occur at a large scale in the basin and are very gradual compared to the high concentration of faulting. Therefore, gas is often structurally trapped by dip closures rather than stratigraphically across the Broad Fourteens Basin (Van Hulten, 2010). Secondary permeability has been lowered due to diagenetic illite growth. Expulsion of K-rich brines from underlying Westphalian coal

and overlying Zechstein salts led to the illitization of kaolin group minerals during the Kimmerian, when the Rotliegends subsided to a depth of about 4000 m (Glennie, 1997; Glennie and Provan, 1990; Lanson et al., 1996; Purvis, 1992)

Deposition during the Late Permian (Zechstein Group) conformably overlies Upper Rotliegend rocks. The southern part of the Broad Fourteens Basin is rich in thick bordering facies of siliciclastics and carbonates, whereas the northern parts are characterised by diapiric salt (Nalpas et al., 1995; Verweij and Simmelink, 2002). Peri-marine carbonates make prospective reservoirs for Permian gas (Van Hulten, 2010; Glennie and Provan, 1990). However, the distinguishing feature of the Zechstein Group was the deposition of thick evaporite layers.

Five evaporite sequences are recognised in the Dutch offshore, each a contribution to the sealing capabilities of the Zechstein Group (Van Hulten, 2010). It was estimated by Quirk (1993) that halite in the Broad Fourteens Basin is between 100-1500 m thick. However, estimations of true and original thickness are hard because of the effects of halokinesis. Halite flowed diapirically during the Jurassic, allowing salt to be completely withdrawn around diapirs to create salt welds between Triassic and Rotliegend sandstones (Glennie and Provan, 1990; Davison et al., 2000).

Another important reservoir in The Netherlands belongs to the Lower Germanic Trias Group (Stewart and Coward, 1995) (Fig. 2.5). The Bunter Sandstone (referred to as Buntsandstein in Dutch and German literature) was deposited during the Triassic in a desert environment comparable to the Permian Rotliegend. Aeolian and fluvial sandstones are the dominant facies in the Buntsandstein and are constant over a large area (Van Hulten, 2010; Verweij and Simmelink, 2002). The Bacton Group (containing Bunter Sandstone) displays a coarsening upwards sequence, relating to a fall in eustatic

sea level (Coward, 1995). It has a varying thickness within the Broad Fourteens Basin but attains a maximum thickness between 1000-1500m (Van Wijhe, 1987).

Gas migrates upwards in areas where salt welds developed between Permian Rotliegend rocks and the Bunter Sandstone, and through basin-margin faults (Verweij and Simmelink, 2002). This gas can accumulate between units of the Lower Germanic Trias Group and diapirs which were activated during the Triassic (Van Hulten, 2010).

2.3.2.2. Jurassic oil plays

By the end of the Triassic, the Rhaetian transgression raised the eustatic sea level. Thick open marine Jurassic clays were restricted to basin centres and the Altena Group was subsequently deposited (Verweij and Simmelink, 2002; Van Wijhe, 1987) (Fig. 2.5). The original lateral extent of the Altena Group is uncertain due to Cretaceous tectonic inversion and its almost complete removal across structural highs (Duin et al., 2006; Van Hulten, 2010a).

The onset of the Toarcian oceanic anoxic event coincided with the deposition of a thin layer of bituminous clays in the Posidonia Shale Formation. This 15-30 m thick sequence is the main source rock of the Jurassic oil plays in the Broad Fourteens Basin and contains kerogen type II oil, with TOC values around 5 % (Van Hulten, 2010; Verweij and Simmelink, 2002; De Jager et al., 1996). Maturation was reached in the centre of the basin during the Lower Cretaceous (latter part of syn-rift sequence). The northern edge reached the oil window later in the Cretaceous (during post-rift sequence) (Verweij and Simmelink, 2002). Inversion in the latest Cretaceous and Palaeocene reduced the temperature of oil and allowed access of meteoric waters: aerobic bacteria consequently biodegraded the oil (De Jager et al., 1996).

Overlying the Posidonia Shales is the Delfland Subgroup, which acts as both reservoir and a secondary source rock. Fluctuations in sea level during the Jurassic generated fluctuations of lacustrine and fluvial deposits, resulting in the deposition of sandstone and interbedded bituminous shales and dispersed lignitic material (Verweij et al., 2003). The main reservoir unit in the Broad Fourteens Jurassic oil plays is the Vlieland Sandstone Formation. Transition from coastal to shallow marine deposits occurred during the Lower Cretaceous, characterised by slow sedimentation (Verweij and Simmelink, 2002; Verweij et al., 2003). This can be resolved seismically as a rapid change of facies, a character indicating a potential stratigraphic trap (Van Hulten, 2010).

The Vlieland Formation can only be found in depocentres, as it has been eroded from structural highs - similarly to the Altena Group of the Lower Jurassic (Duin et al., 2006). Charging of the Vlieland reservoir occurred by the Palaeocene. Migration of Posidonia oils linked to basin inversion filled the Vlieland Sandstones, with the Werkendam and Delfland sandstones act as secondary reservoirs, thus containing much lower volumes of hydrocarbons (Verweij et al., 2003).

The Vlieland Shale Formation is the top seal member for the Jurassic oil plays (Bruijn, 1996). However, shales, like the Cretaceous Vlieland Shale Formation, make an ineffective seal and most of the oil accumulations are structurally trapped by faulted anticlines formed in the Cretaceous-Palaeocene inversion (De Jager et al., 1996).

2.4. Nankai Trough accretionary prism, SE Japan

Accretionary prims such as the Nankai Trough in SE Japan are dominated by large-scale tectonic shortening and uplift driven by plate subduction (Miyazaki and Heki, 2001; Bird, 2003; DeMets et al., 2010; Tsuji et al., 2014). Offshore SE Japan, the

subduction of the Philippine Sea Plate beneath the southeast margin of Eurasia occurs at a variable convergence rate of 4.0 to 6.5 cm/year (Seno et al., 1993; Miyazaki and Heki, 2001; DeMets et al., 2010). This process has led, since the Pliocene-Pleistocene, to large-scale tectonic shortening and uplift of overburden strata above a subducted oceanic slab to form the Nankai accretionary prism, i.e. a mass of sediment that has been scrapped off from the subducting Philippine Sea Plate and accreted together with sediment derived from SE Japan (Taira, 2001; Miyazaki and Heki, 2001; Bird, 2003; Kimura et al., 2011, 2018).

The continuous movement of the subducted Philippine Sea Plate has induced a continuum of internal deformation that is expressed in the form of imbricate thrust faults, thrust anticlines, pop-up structures, megasplay faults, strike-slip faults, and normal to reverse faults (Kimura et al., 2011; Moore et al., 2013; Alves et al., 2013; Lin et al. 2015; Van Tuyl et al., 2015; Azevêdo et al., 2018).

2.4.1. Tectonic setting

The Nankai trough spans the boundary between the Eurasian and the Amurian Plates, being limited to the east by the Pacific Plate and to the south by the Philippine Sea Plate (Bird, 2003; Kimura et al., 2011, 2018) (Fig. 2.6a). The Philippines, Pacific, and Amurian Plates converge under the Tokyo metropolitan area, resulting in a uniquely complicated tectonic environment; the Amurian Plate overrides the Philippine Sea Plate at the same time the Pacific Plate dips beneath both the Philippine Sea and Amurian Plates (Bird, 2003; Kimura et al., 2011) (Fig. 2.6a). These convergent plate margins generate large earthquakes within and in between the latter tectonic plates, e.g. the 1944 Tonankai and 1946 Nankai earthquake events along the Nankai Trough, and the 1923

Great Kanto Earthquake along the Sagami Trough (Harris, 1998; Ide et al., 2011; Lee et al., 2011).

Three major subduction-related boundaries, marked by deep-ocean trenches or troughs, define the tectonic setting of Nankai: a) the Sagami Trough at the interface of the Philippine Sea and Amurian Plates, b) the Japan Trench between the Amurian and Pacific plates, and c) the Nankai Trough between the Philippine Sea and the Eurasian Plates (Bird, 2003; Kimura et al., 2011) (Fig. 2.6a). The Nankai Trough, which is the oceanward boundary of the study area, delineates an active (and seismogenic) convergent margin under which the Philippine Sea Plate is subducted at a variable convergence rate of approximately 4.0–6.5 cm/year, following an azimuth of 300^0 to 315^0 (Seno et al., 1993; Miyazaki and Heki, 2001; DeMets et al., 2010; Moore et al., 2013) (Fig. 2.6).

2.4.2. Stratigraphic setting

Integrated Ocean Drilling Programme (IODP) drilling sites provide valuable lithological and stratigraphic information on the shallow sedimentary cover, uppermost part of the accretionary prism, and underthrusted sediments from the Philippine Sea Plate (Figs. 2.6 and 2.7).

Multiple IODP campaigns reached strata within the outer wedge of the Nankai accretionary prism and collected stratigraphic evidence to show that the Nankai Trough is mainly composed of a relatively thin slope basin, overthrusted and underthrusted sediments (Expedition 315 Scientists, 2009; Expedition316 Scientists, 2009; Kimura et al., 2011; Strasser et al., 2014) (Fig. 2.7).
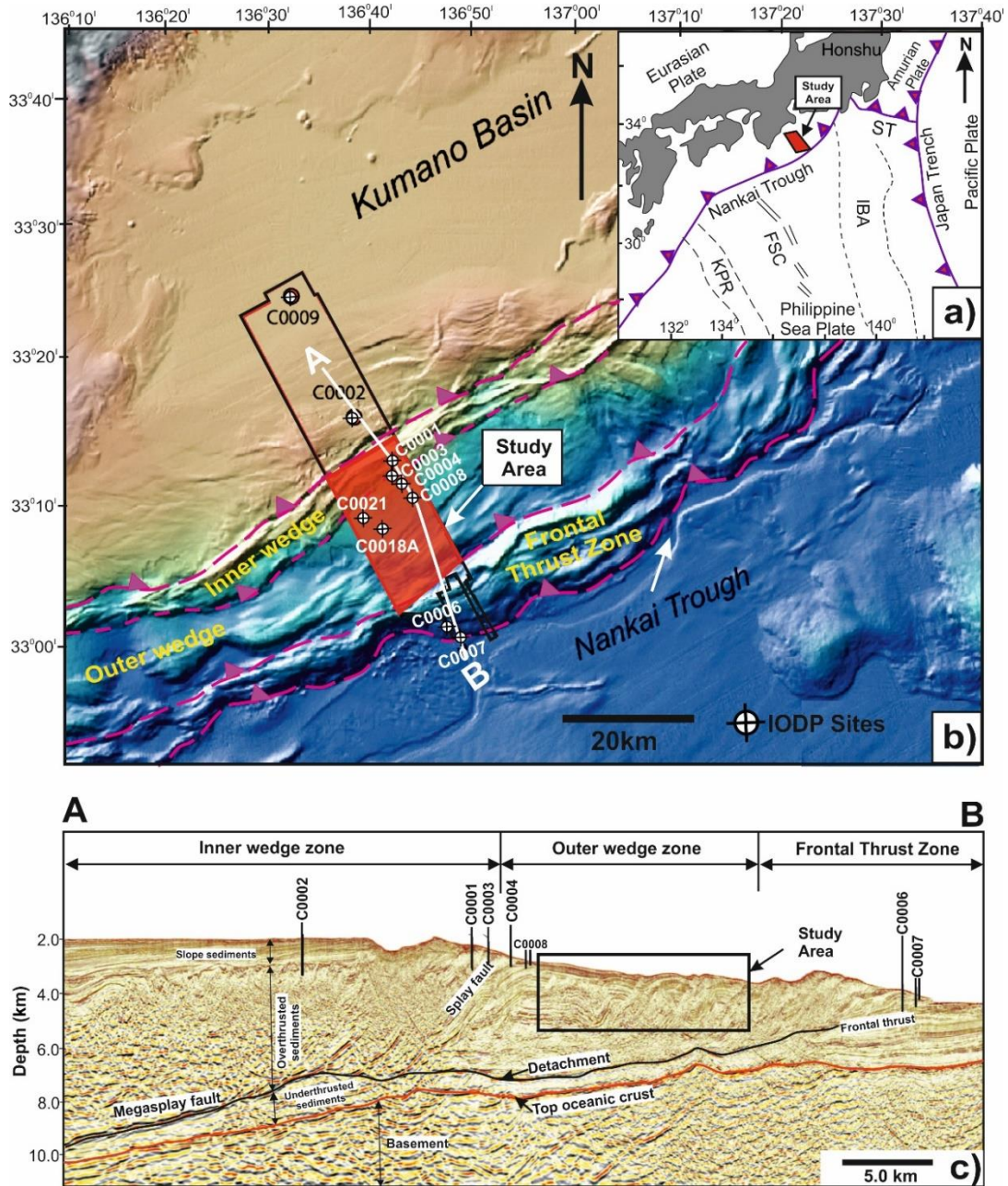
Fig. 2.6. a) Inset highlighting the three principal subduction trenches surrounding the Japanese Islands. i) the Nankai Trough, ii) the Sagami Trough (ST) and iii) the Japan Trench. The study area is shown by the red box. Figure modified from Bird (2003). b) Bathymetry map of the Kumano Basin and adjacent region to the Nankai accretionary prism highlighting structural zones, the location of IODP sites and the location of the study area (red box). Figure Modified from Moore et al. (2013). KPR-Kyushu-Palau Ridge; FSC –Fossil Spreading Centre; IBA-Izu-Bonin Arc; ST -Sagami Trough; OKP-Okhotsk Plate, MSFZ-Megasplay Fault Zone; IODP - Integrated Ocean Drilling Programme. c) Arbitrary line through the 3-D seismic volume along some of the sites drilled by IODP (Moore et al., 2009) highlighting structural zones and study area within the outer wedge zone.

Slope sediments were accumulated above an angular unconformity separating them from an underlying overthrusted/accreted sediment, this latter comprising strata belonging to the upper part of the accretionary prism (Kimura et al., 2011) (Fig. 2.7). In addition, cores collected at IODP Site C0006 drilled through a deep underthrusted sediments composed of deep-marine sediment from the subducting Shikoku Basin (Figs. 2.6c and 2.7).

Slope basin sediments can be up to ~2.4 Ma old and comprises slope-apron fine-grained turbidite facies spanning the latest Pliocene-Holocene. Data from IODP Sites C0008 and C0018A (Expedition 315 Scientists, 2009; Expedition 316 Scientists, 2009; Expedition 333 Scientists, 2012) divided slope basin sediments into three, which mark a gradual transition from upper-slope apron facies to base of slope apron facies: a) hemipelagic mud and silty-clayey sequences intercalated with multiple ash layers, b) hemipelagic mud, silty clay and silty turbidites with ash layers, and c) turbiditic sand and sandy silt intercalated with mud and ash layers (Expedition 315 Scientists, 2009; Kimura et al., 2011; Alves et al., 2013; Strasser et al., 2014).

IODP Sites C0006, C0008 and C0018 (Expedition 315 Scientists, 2009; Expedition 316 Scientists, 2009) define overthrusted/accreted sediments as reflecting the uppermost part of the accretionary prism (Figs. 2.6c and 2.7). This package is Pliocene in age or older. It comprises accreted sediments with mudstone- to sand-dominated lithologies (Expedition 315 Scientists, 2009; Kimura et al., 2011; Alves et al., 2013; Strasser et al., 2014).

Underthrusted sediments were identified below overthrusted sediments in the Frontal Thrust Zone, at IODP Sites C0006 and C0007 (Expedition 316 Scientists, 2009), and comprises hemipelagic mud interbedded with volcanic ash and tuffs. Overthrusted

sediments are deformed by thrust faults and transitions at depth into underthrusted Shikoku Basin sediment (Expedition 316 Scientists, 2009) (Fig. 2.7). In the inner wedge of the Nankai accretionary prism, the presence of an overlying forearc basin (Kumano Basin), and underlying thrust-and-fold accretionary prism, agrees with the stratigraphic units defined by IODP.

2.4.3. Main structural styles offshore Nankai

The mechanics behind the deformation of accretionary prisms have been explained by the Coulomb and dynamic coulomb-wedge theories (Davis et al., 1983; Dahlen, 1984; Wang and Hu, 2006). These two theories propose a transition between a highly compressional outer wedge and a less compressional (and moderately seismogenic) inner wedge. As a result, Wang and Hu (2006) described the outer wedge region of the Nankai accretionary prism as comprising a series of imbricate thrust faults that accommodate a zone of low shear strength, while the inner wedge region forms a zone of accreted sediment characterised by the absence of active compressional structures, thus normally acting as a backstop.

More recently, Wu et al. (2013) and Lin et al. (2015) used a compilation of borehole and core data to determine stress states and deformational styles across the Nankai accretionary prism. The authors showed that, in its inner wedge, horizontal maximum stresses relate to strike-slip faulting. However, the sediment overlying the inner wedge (Kumano Basin) records a vertical maximum stress, a configuration that reflects a normal faulting regime, leading to the conclusion that the Nankai accretionary prism is currently experiencing a predominantly (inter-seismic) extensional regime.
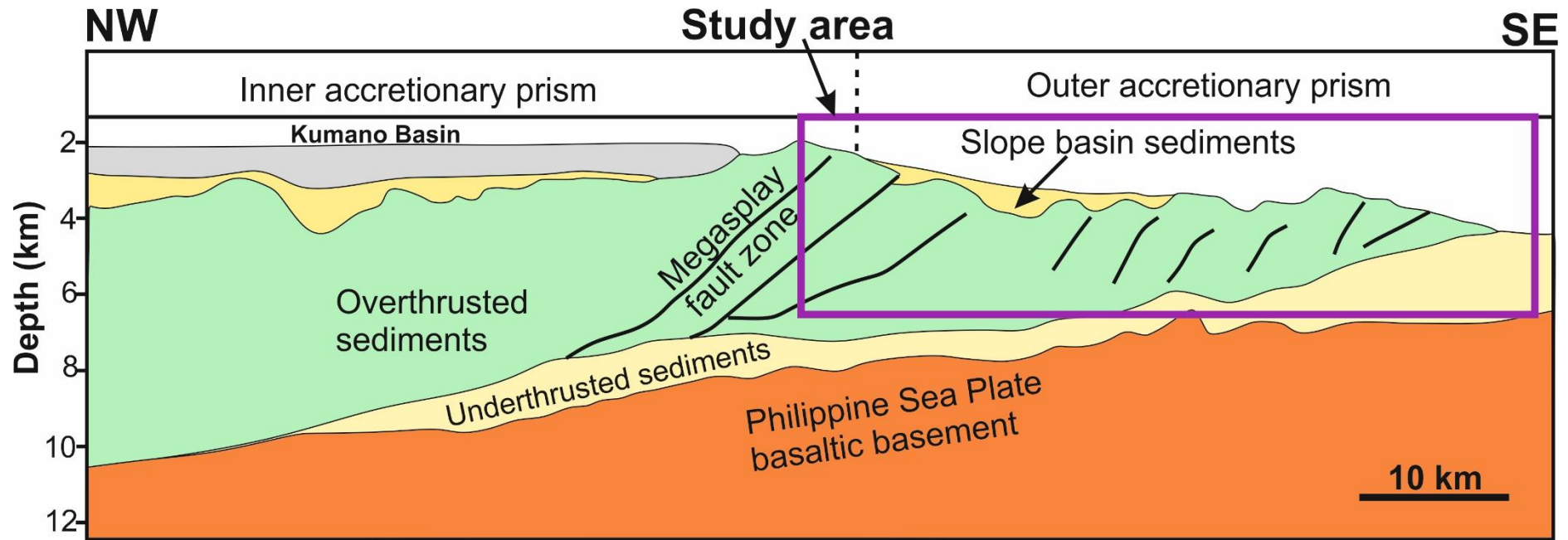
Fig. 2.7. Stratigraphic interpretation across the outer and inner wedge of the Nankai accretionary prism (Boston et al., 2016). The prism consists of slope basin, overthrusted and underthrusted sediments.

Lin et al. (2015) and Lackey et al. (2020) also showed evidence for compression seawards from a Megasplay Fault Zone, with a maximum principal stress parallel to the convergence vector. They stated that, at present, the Nankai accretionary prism is dominated by a shallow extensional regime and a relatively deep strike-slip to reverse faulting regime, mainly due to stress field reorganisation in the areas where maximum principal stress becomes horizontal. This transition between different tectonic regimes at depth is often referred to as Extension-Compression Depth (Lewis et al., 2013; Van Tuyl et al., 2015; Lin et al., 2015).

Azevêdo et al. (2018) recently interpreted seismic data in the outer wedge region of the Nankai accretionary prism to reveal a complex set of thrusts, pop-up structures, thrust anticlines and strike-slip faults hinting at a complex strain distribution across SE Japan. The authors suggest that lateral slip, together with thrusting and folding, are the major styles of deformation operating in the outer wedge region of the Nankai accretionary prism. Both styles of deformation reflect a transpressional tectonic regime in which the maximum horizontal stress is geometrically close to the convergence vector.

CHAPTER 3

Data and Methods

3. Data and Methods

3.1. Introduction

This research study uses high-quality three-dimensional (3D) seismic reflection datasets and well logs to understand the nucleation, reactivation and growth histories of normal faults, and their implications in sedimentary basins. The datasets were made available by Dr. Tiago M. Alves, the Research Leader of 3D Seismic Lab, School of Earth and Environmental Sciences, Cardiff University. This chapter aims to give a brief overview on how marine seismic data are acquired and processed. It also gives an overview and descriptions of seismic data and interpretation used in the study. However, specific details of seismic dataset and methods related to each result chapter are also provided in the corresponding Chapters 4, 5 and 6.

3.2. Seismic Exploration

Seismic exploration can provide the most complete subsurface picture of any surface-based geophysical technique. The essence of the technique is a real deployment of sources and receivers on a two-dimensional (2-D) grid, followed by processing and interpretation of the resulting densely sampled volumetric data (Gubins, 1990). A typical marine 3-D survey is carried out by shooting closely spaced parallel lines (line shooting) - the shooting direction is called the inline direction. A typical land or shallow water 3-D survey is done by laying out several receiver lines parallel to each other and placing the shot points in the perpendicular direction (swath shooting). For land 3-D survey, the receiver cable is along the inline direction (Bull et al., 2009). The direction that is perpendicular to the inline direction in a 3-D survey is called the crossline direction. The line spacing in 3-D surveys can be 50 m or less. Traces are collected as common cell gathers/bins (Posamentier and Kolla, 2003).

Three-dimensional (3-D) seismic surveys are distinguished from 2-D seismic data by the acquisition of multiple closely spaced lines that provides regular data point spacing that feeds 3-D data migration during processing (Vermeer, 2012). This leads to a true data volume from which lines, planes, slices, or 'probes' can be extracted in any orientation, with nominally consistent data processing characteristics (Vermeer, 2012). The close line spacing of 3-D seismic data means that they do not have the problems of spatial aliasing inherent to 2-D seismic data and, therefore, have the potential to yield better stratigraphic resolution, better migration, and imaging of structural and depositional dips (Biondi, 2006).

The density of subsurface reflection point coverage allows strata reflections to be mapped using automated or semi-automated trackers to provide continuous mapped surfaces that may in turn be used to derive a range of seismic and structural attributes (Biondi, 2006). These attributes feature increasingly in exploration and development workflows. Fundamentally, however, the greatest benefit of 3-D resides in its spatial resolving power both in terms of absolute spatial resolution and relative accuracy in image positioning (Yilmaz, 2001). Features such as fault systems can now be mapped in much more detail than with 2-D seismic data, with its inherent limitations of spatial aliasing (Freeman et al., 1990).

3.2.1. Marine streamer acquisition

The first marine 3-D surveys were carried out with the conventional 2-D geometry of a single boat towing one source (array) and one streamer (Watson, 2009) (Fig. 3.1). To increase efficiency in recording 3-D surveys, the industry has seen a gradual increase in the number of midpoint lines (also called bin lines) recorded in one boat pass.
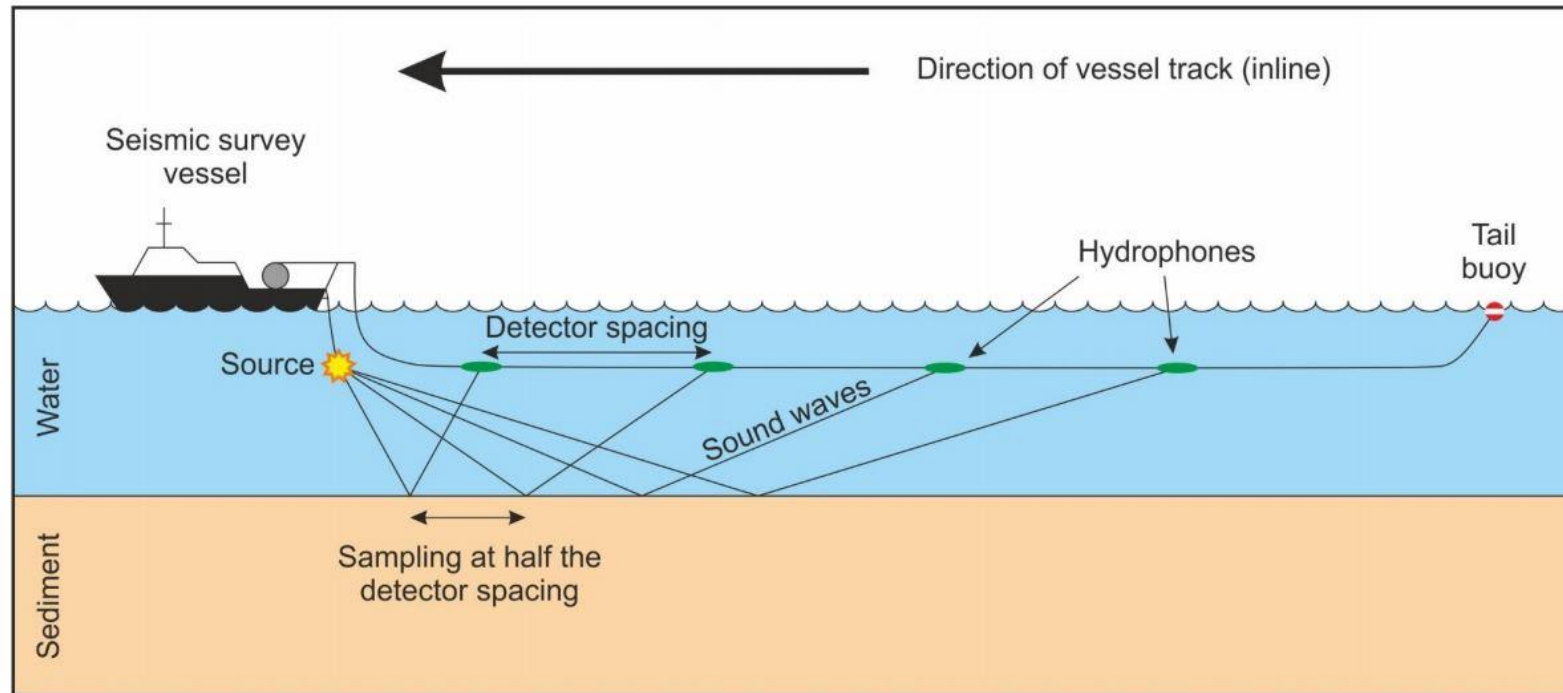
Fig. 3.1. Schematic section illustrating the method behind the marine streamer acquisition. The seismic survey vessel tows an acoustic source near the surface, which emits a loud sound wave. These waves travel through the water and into the sediment layer, reflecting to the receiver (hydrophones). Modified from Bacon et al. (2007).

The strongest vessels can tow 16 or more streamers, depending on the length of the streamers, allowing efficient single-boat operations (Vermeer, 2012).

Figure 3.2 illustrates the evolution from three or four streamers to 14 streamers with a schematic display of some multisource multi-streamer configurations. The sources represented by red stars, are always kept as close as possible to the boat to minimize the length of the umbilicals (pressure hoses from the vessel to the air-gun arrays). The sources take turn firing. The number of midpoint lines recorded by these geometries equals the product of the number of sources and the number of streamers (Brown, 2004; Vermeer, 2012). The configurations in Fig. 3.2 may still be adapted, or changed, depending on size of survey, operator, and concerns about illumination problems associated with wide-tow configurations. The length of the streamers may vary from 2 to 9 km, depending on depth to target. The width of the swath of streamers may be on the order of 1.0 km (Vermeer, 2012).

The survey areas are normally traversed by a seismic vessel along the longest dimension of the area to minimize the number of line turns, the areas are usually covered in a racetrack mode (Fig. 3.3); this means the area is split into pairs of elongated regions in which the shooting direction alternates between the members of each pair. This method accommodates the large radius of the line turns that are necessary to prevent tangling neighbouring streamers during the line turn (Vermeer, 2012). It also reduces the length of the turn to a semicircle rather than a nearly full circle, which would be needed if adjacent seismic boat passes were acquired sequentially (Vermeer, 2012).

The layout in Fig. 3.2 is such that each combination of a source and a streamer provides data for a unique midpoint line.
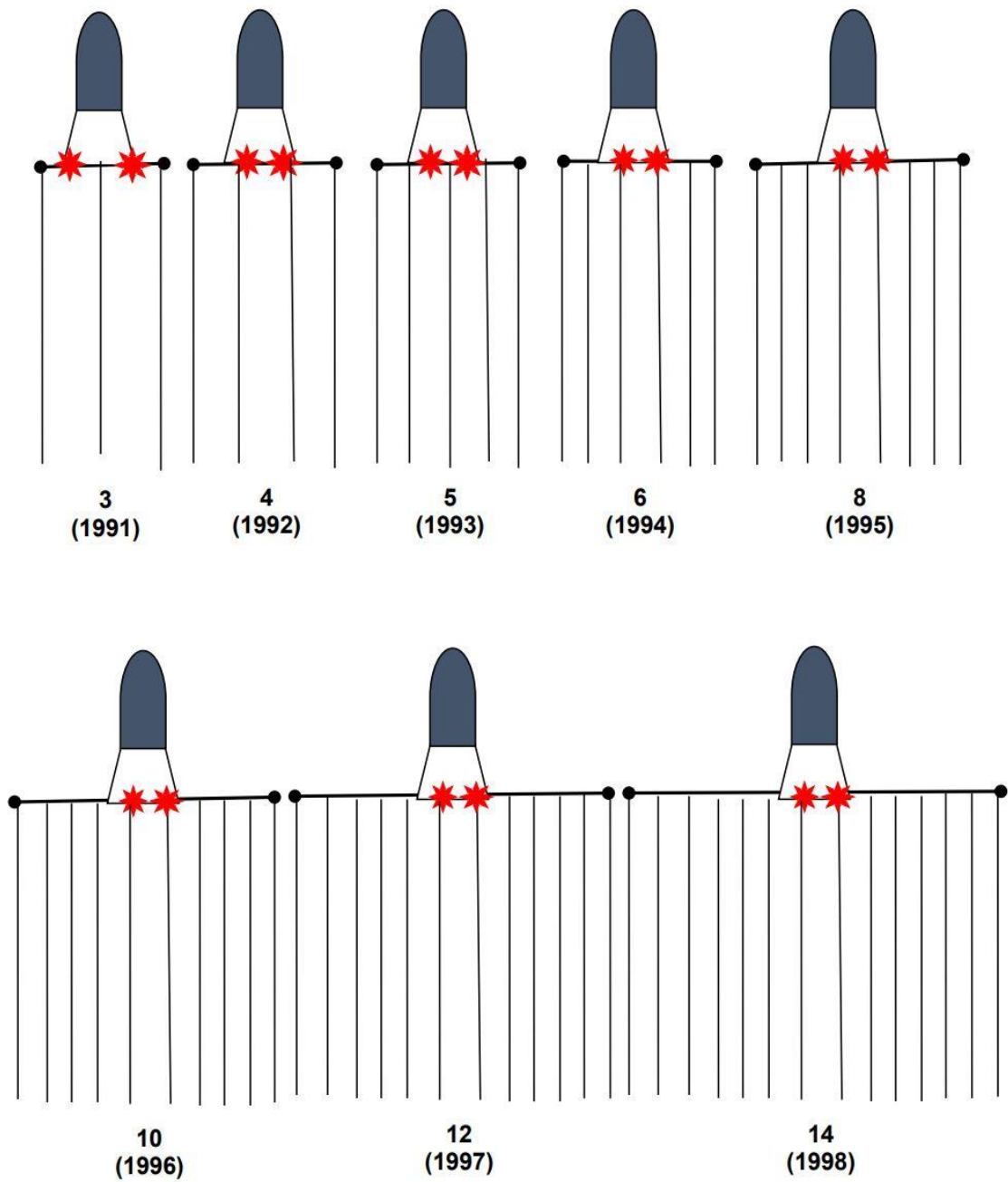
Fig. 3.2. Schematic description of various multisource multistreamer configurations. Red stars represent sources; vertical lines represent streamers. The values under the streamers represent number of streamers and time of introduction. Figure modified from Vermeer (2012).
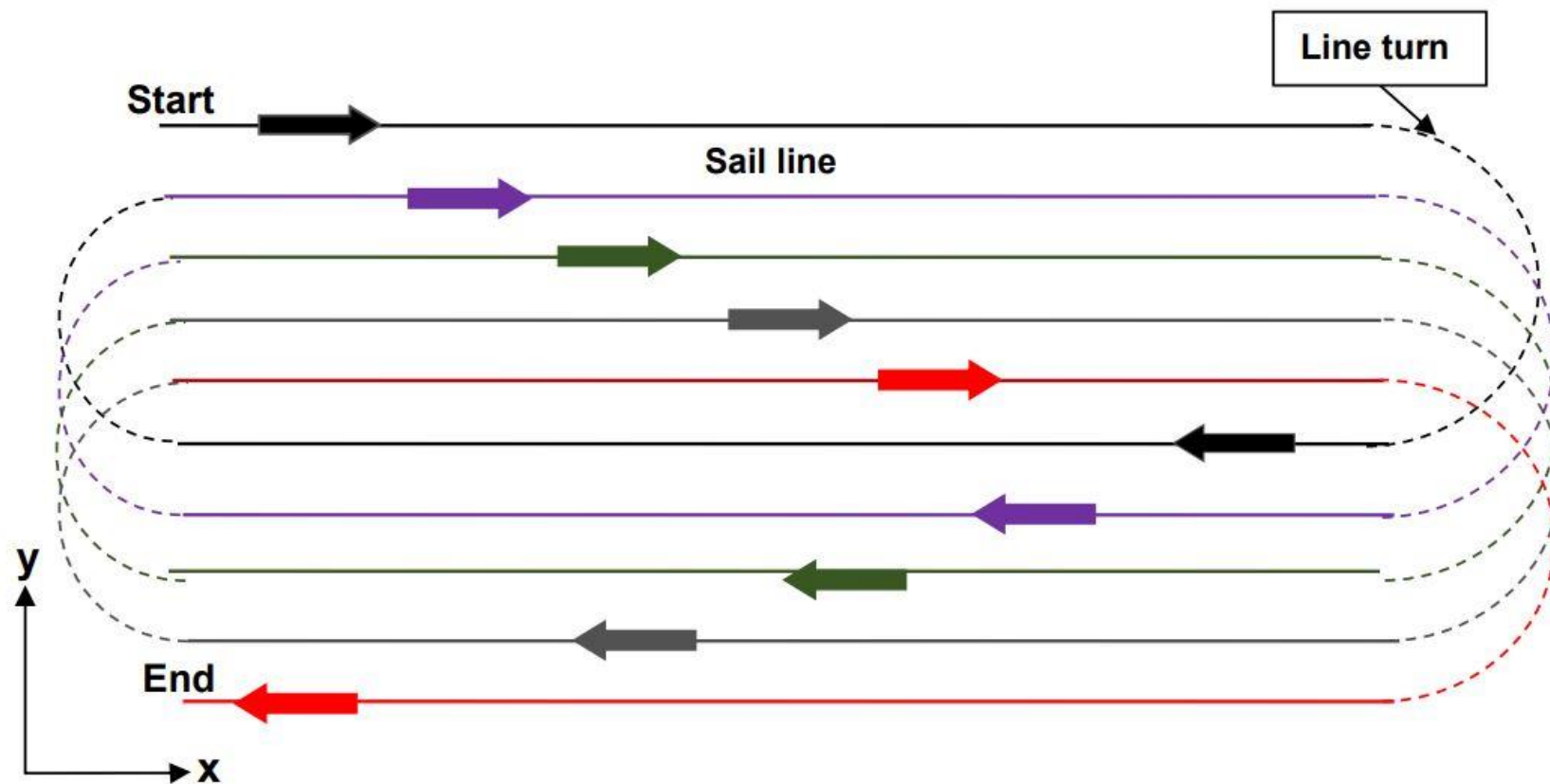
Fig. 3.3. Schematic description of racetrack method for covering survey area. In the figure, there are five sail lines (boat passes) on each side of the track. The width of the track is selected such that line turns take minimal time, given the acquisition configuration (number and length of streamers and distance between streamers). Usually, the survey area is split into several racetracks. Figure modified from Vermeer (2012).

The distance between the two sources equals one-half streamer interval (all streamer intervals are the same, nominally), and their distance from the nearest streamer equals one quarter streamer interval. This is also the interval between the midpoint lines (Yilmaz, 2001). It is important to note that this interval between midpoint lines constitutes, at the same time, the crossline bin size (Vermeer, 2012) (Equation 3.1).

$$\textbf{Crossline bin size} = \frac{\text{Streamer interval}}{2 \times \text{Number of sources}} \qquad \text{Equation 3.1}$$

In standard marine acquisition, the depth controllers in a streamer must ensure a constant depth along the length of the streamer. These controllers function properly only if the speed of the streamer is at least 4 knots, which corresponds to about 2 m/s (Vermeer, 2012). The time between shots depend on required record length and time required to dissipate the energy of the previous shot. This time is often on the order of 10 s, so the streamer vessel moves over at least 20 m between shots. A frequently chosen distance between consecutive shots is 18.75 m. In deep marine areas with deep targets, the distance between the shots is larger; in the Gulf of Mexico, 37.5 m is quite common (Vermeer, 2012).

$$\textbf{Inline Fold} = \frac{\text{Streamer length}}{2 \times \text{sources interval}} \qquad \text{Equation 3.2}$$

The advantage of using two sources is that it reduces the crossline bin size for the same streamer intervals (Equation 3.1). Clearly, crossline bin size tends to be one of the limiting factors in the resolution of marine streamer data (Yilmaz, 2001; Vermeer, 2012). Alternatively, using dual sources also allows for towing streamers with twice the streamer interval for the same crossline bin size. Often, the quality of data acquired by marine streamers is excellent, allowing for a lower fold resulting from the use of two sources (Vermeer, 2012). However, Hegna et al. (2001) show an example from offshore Norway where higher fold leads to substantially better data quality. For more details on seismic data acquisition, the reader to consult Vermeer, (2012).

3.2.2. Seismic Data Processing

Seismic signals are generated by seismic energy sources (air-gun, dynamite and vibroseis). These signals go into the earth and are reflected to the surface of the earth where geophones or hydrophones are used to detect them. The detected signals are amplified, recorded, and subjected to different types of seismic data processing. The processed data in the form of seismic sections are then subsequently handed over to interpreters who design geological models consistent with the seismic section. This section briefly highlights some of the seismic data processing stages that constitute the heart of most data processing. For more detailed on seismic data processing, the reader should consult (Yilmaz, 2001; Sheriff and Geldart, 1995).

3.2.2.1. Demultiplexing

In the early days of digital recording, field data were recorded in multiplex form (i.e. order in sample time). To be able to process these data they had to be in trace or channel

order. This sorting process is known as demultiplexing. Today, however, this should be necessary when reprocessing very old data, since modern seismic recording systems supply field data in demultiplexed form. Demultiplexing is usually carried out by computer program which sorts out given values into sequence for separate channels (Yilmaz, 2001). The United States' Society of Exploration Geophysicists (SEG) provide specified standard data file formats (SEG-Y), which is the most common standard data-file format; data are ordered into time-then offset-sequential traces, including header lines to each trace with all position coordinates, and acquisition details (Barry, 1975).

3.2.2.2. Amplitude recovery

The measured amplitudes are in digital counts, but for any given reflection event will decrease with increasing recorded time (TWT or two-way-time) and offset for three main reasons: intrinsic attenuation, energy partitioning at interfaces, or reflectivity and geometric spreading or spherical divergence (Yilmaz, 2001). The decreased amplitudes during data acquisition must be restored so that reflections can be seen and analysed. Amplitude recovery tools include Automatic Gain Control (AGC) and Velocity-Based Scaling (Ursin 1990).

3.2.2.3. Pre-Stack Deconvolution

Deconvolution is a process that improves the vertical resolution of seismic data by compressing the basic wavelet, which also increases bandwidth of the wavelet. In addition to compressing or shortening reflection wavelets, deconvolution can also be

used to attenuate ghosts, instrument effects, reverberations, and multiple reflections (Gadallah and Fisher, 1999).

A seismic trace can be modelled as the convolution of the input signature with the reflectivity function of the earth impulse response, including source signature, recording filter, surface reflections, and geophone response. This also includes primary reflections (reflectivity series), multiples, and all types of noise. If deconvolution was completely successful in compressing the wavelet components and attenuating multiples, it would leave only the reflectivity of the earth on the seismic trace. In so doing, vertical resolution is increased, and earth impulse response or reflectivity is approximately recovered (Sheriff and Geldard, 1995).

3.2.2.4. Frequency Filtering

The process of eliminating frequencies that do not carry seismic information is called filtering. Frequency filtering can be in the form of band-pass, band-reject, and high-pass (low-cut), or low-pass (high-cut) filters. All these filters are based on the same principle. Band-pass filtering is used because a seismic trace typically contains some low frequency noise, such as ground roll, and some high-frequency ambient noise (Yilmaz, 2001). The usable seismic reflection energy usually is confined to a bandwidth of approximately 10 to 70 Hz, with a dominant frequency around 30 Hz (Yilmaz, 2001).

Band-pass filtering is performed at various stages in data processing. If necessary, it can be performed before deconvolution to suppress remaining ground roll energy and high-frequency ambient noise that otherwise would contaminate signal autocorrelation (Yilmaz, 2001). It is a standard practice to apply a time-variant band-pass filter to stacked data to pass higher frequencies shallow in the section and lower frequencies at greater depths (Yilmaz, 2001).

3.2.2.5. Velocity Analysis

Velocity analysis is very important in reflection processing because once optimum primary velocity is computed, Normal Moveout (NMO) corrections can be applied to Common Mid-Point (CMP) gathers, which is concurrently stacked making signal stack in phase and noise out of phase thus increasing the signal-to-noise ratio (Yilmaz, 2001). Normal moveout is the basis for determining velocities from seismic data, computed velocities can be used to correct for normal moveout so that reflections are aligned on CMP traces (Sheriff and Geldart, 1995).

3.2.2.6. Multiple Suppression

Multiples are events which are reflected more than once between layers. They are a major problem in many areas and can seriously degrade the usefulness of the data. The three most used methods to eliminate multiples are: a) move-out differences against the primaries, b) periodicity of the multiples, and c) image-processing techniques (Sheriff and Geldart, 1995).

3.2.2.7. Seismic data migration

Migration is a "repositioning process'', which moves every reflection to their proper places with their correct amount of dips. This results in a section that more accurately represents a cross-section of the earth, delineating subsurface details such as fault planes (Yilmaz 2001). A vertical seismic section represents a cross section of the earth. It appears more like the real earth when layers are flat and much like it when they have gentle dip. With greater dip, the reflections are not where they are supposed to be in the Earth and, hence, have different dip values. In addition, irregularities on a reflection

produce diffracted wavelets, which interferes with the reflection on a seismogram (Sheriff and Geldart, 1995). On seismic sections, these diffractions produce arc like patterns (diffracted wavelet) creating an image that could be mistaken for an accurate reflector. Hence, seismic data migration involves repositioning data elements to make their locations appropriate to the location of the associated reflectors and to remove diffracting images from the section (Sheriff and Geldart, 1995; Yilmaz 2001).

The need to migrate seismic data to obtain structural picture was recognised at the beginning of seismic exploration. Generally, migration is based on the premise that data elements represent primary reflections or diffraction. The need for migration is usually judged by examining a seismic section. Where dipping images and diffraction images are found, migration is recommended. The quality of such a seismic section is considerably improved by modern migration processing (Yilmaz, 2001; Levin, 1971).

3.3. Seismic resolution

Seismic resolution is one of the key parameters used to assess the quality of seismic data and is related to the ability to recognise two points that are close to each other, and can still be detected (Yilmaz, 2001). In other words, seismic resolution is the measurement of how small a geologic feature, such as the thickness of a sedimentary bed, or a fault, can be distinguished in a seismic dataset (Zhou, 2014). Vertical resolution, also called temporal or depth resolution, quantifies the closeness of two reflections and constrain fault analyses through detailed mapping of fault throws alone fault planes (See section 7.5) (Yilmaz, 2001). The vertical resolution is determined along the direction of wave propagation by a reflected pulse-length on the seismic profile, and it is measured in terms of wavelength (Kearey et al., 2013).

Seismic wavelength varies from around 40 m in the shallower parts of seismic volumes and 250 m at depth (Brown, 2011). These values show an increasing tendency with depth since the velocity becomes higher at depth due to the effects of sediment compaction, and frequency decreases progressively due to wave (signal) attenuation (Kearey et al., 2013). As the resolution decreases with increasing wavelength, it is noted that the resolution deteriorates with depth. Sheriff and Geldart (1995) stated that the maximum possible resolution for a reflected pulse, represented as a wavelet, varies between one-quarter ($\lambda/4$) and one-eighth ($\lambda/8$) of the dominant wavelet wavelength. Typically, one-quarter of the wavelength is assumed by many authors as the preferred maximum resolution (Brown, 2011; Hart, 1999; Kearey et al., 2013; Liner, 2004; Yilmaz, 2001; Zhou, 2014).

The threshold for vertical resolution may depend on the noise level of the data allowing, for example, rock layers with a thickness of up to $\lambda/30$ may be detected (Yilmaz, 2001). However, the seismic amplitude and frequency may vary below the conventional limits of the seismic resolution, indicating the possibility of recovering the frequency beyond the seismic data bandwidth and inferring layer thicknesses below the seismic sample rate (Yilmaz, 2001). The detection of smaller features on seismic data can be achieved by increasing the dominant frequency of the stacked seismic data, either by recording or by processing the raw seismic data (Yilmaz, 2001). During the recording of seismic data, it is necessary to use adequate receiver arrays and antialiasing filters in order to prevent and reduce the loss of high-frequency signal due to the statics. During the processing of the obtained data, the primary concern is the removing of any statics that can reduce the high-frequency signal before stacking the data and with the preservation and display of the high-frequency signal. Deconvolution is the tool used to ensure that the high-frequency signal is displayed on the stacked data.

The horizontal or lateral resolution defines how close two points can be and still be recognised as two individual features, rather than one (Yilmaz, 2001). Compared to the vertical resolution, the quantification of horizontal resolution in more complex, as it is necessary to consider the detector (hydrophone) spacing and the properties of seismic waves (Kearey et al., 2013). The detector spacing is related to the position of the hydrophones as previously discussed in the section "Seismic Acquisition". Receivers must be kept closely from each other to make sure the reflection will be reliably correlated, as horizontal resolution decreases with reflection depth.

From Figure 3.4 it is noted that reflections must be spaced at a distance that is equal to half the detector spacing. Seismic-wave properties, such as the dominant frequency, the depth of the reflecting interface, and the velocity above a seismic reflector, must be considered when quantifying horizontal resolution (Kearey et al., 2013; Yilmaz, 2001). The seismic reflection method is better described when considering an infinite number of rays travelling down onto a horizontal reflector through a circular area called the Fresnel Zone (Fig. 3.5). The Fresnel Zone is also the horizontal resolution limit of the seismic data, defined by the energy that returns to the seismic detector within one-half of the wavelength of the primary wave front. This is the half-wavelength constructive condition necessary to reflect a coherent seismic signal (Kearey et al., 2013; Liner, 2004; Zhou, 2014).

The size of the Fresnel Zone is related to the reflector depth. The dominant frequency tends to be lower with depth after considering the effects of attenuation. This leads to an increase in wavelength and in velocity of seismic waves with depth, which consequently results in a lower seismic resolution (Brown, 2011; Kearey et al., 2013; Liner, 2004). The width of the Fresnel Zone is related to the dominant wavelength λ of the source, and to the reflector depth (z) as expressed in Equation 3.3.

$$w = \sqrt{2z\lambda}$$
<div align="right">Equation 3.3</div>

The limit of the receiver's horizontal resolution is also represented by the width of the Fresnel Zone, as closely spaced features separated at depth by a distance smaller than the Fresnel Zone cannot be distinguished (Liner, 2004). The lateral resolution limits of the Fresnel Zone apply to seismic data that are not migrated. Seismic data must be processed and migrated to produce a 3D volume or cube, which will be further interpreted. Data processing consists in the collection of seismic reflection events falling into the same area, the common midpoint (CMP) gather, to create a CMP stack that will improve the signal-to-noise ratio (Yilmaz, 2001; Zhou, 2014).

Migration of the stacked seismic data is another essential step in the processing sequence and involves the movement of dipping events to their correct position, rather than their recorded location. In addition, data migration focuses seismic energy that is spread over the Fresnel zone and collapses diffraction patterns from points and edges (Bacon et al., 2007). The Fresnel Zone is, thus, ideally reduced to a circle with a radius of a quarter the wavelength, as showed in Fig. 3.5. In practice, however, it is more likely for the Fresnel Zone to be reduced to approximately half of the radius (Brown, 2011). Data improvements resulting from the migration of seismic data include a reduction in noise and a relative increase in horizontal resolution.

3.4. Overview of seismic dataset used

This section gives an overview and description of the high-resolution 3-D seismic datasets used in this study. The datasets include: Espírito Santo Basin (SE Brazil),
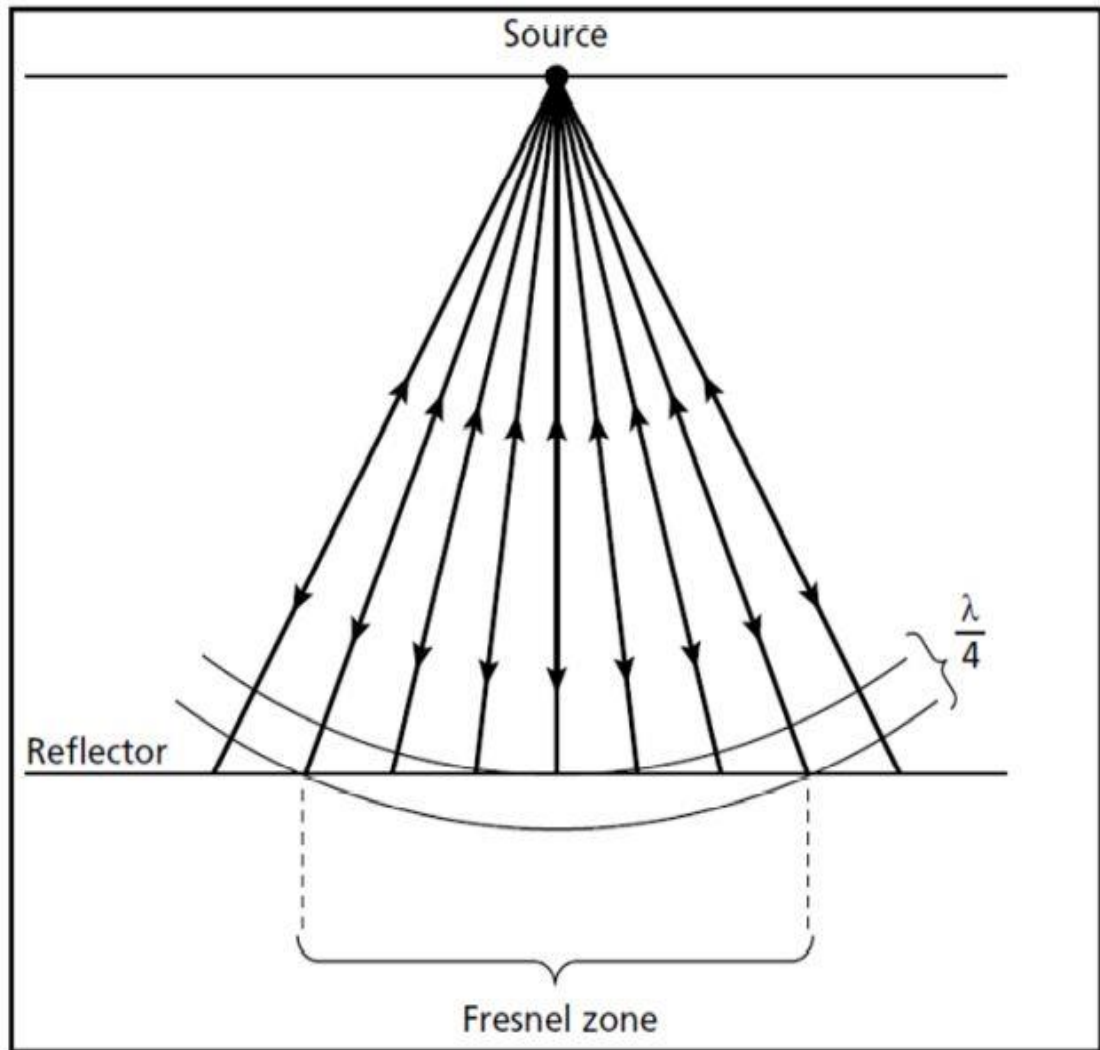
Fig. 3.4. The Fresnel Zone, or the horizontal resolution of the seismic data. The energy that returns to the seismic detector is half the wavelength of the detector spacing (Kearey et al., 2013).
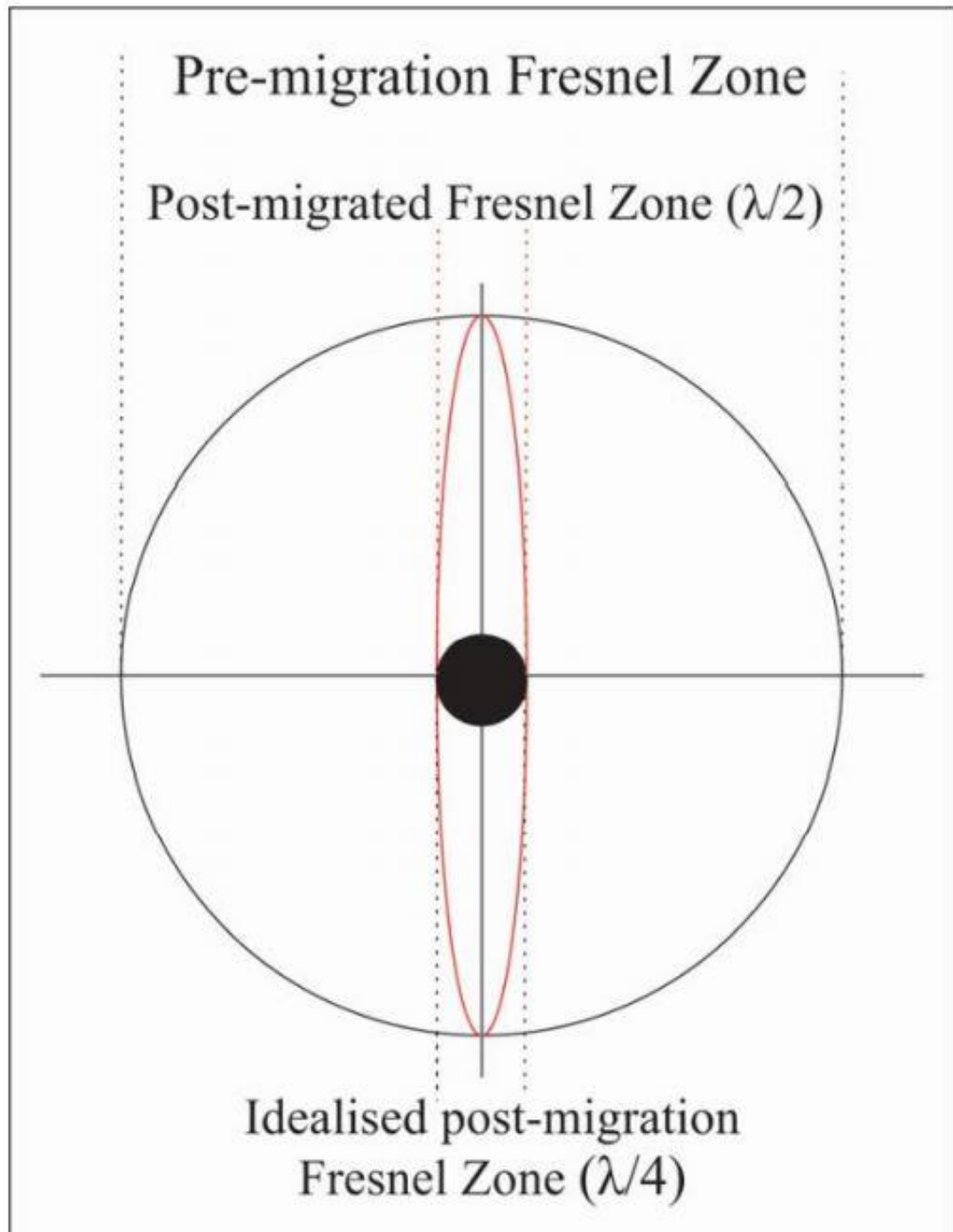
Fig. 3.5. The large circle represents the Fresnel Zone prior to data migration. The oval red form is the Fresnel Zone after migration, which shows the wavelength reduced by half. The black dot located in the centre of the circle represents the idealised post-migration of the Fresnel Zone, with the wavelength reduced by a quarter (Brown, 2011).

Broad Fourteens Basin (Southern North Sea) and Nankai accretionary prism (SE Japan) seismic surveys. The datasets include: Espírito Santo Basin (SE Brazil), Broad Fourteens Basin (Southern North Sea) and Nankai accretionary prism (SE Japan) seismic surveys. Specific details of seismic dataset related to each result chapter are also provided in the corresponding Chapters 4, 5 and 6.

3.4.1. Espírito Santo Basin (BES-100)

The seismic block **(BES-100)** used in result chapter 4 was acquired 60 km from the coastline of the Espírito Santo Basin (offshore Southeast Brazil), approximately between 19.4^0–20.5^0N and 38.3^0–39.5^0E, covering an area of about 2,450 km^2 within a range of water depths between 700 m and 1970 m (Fig. 2.1).

The seismic dataset was acquired by CGG-Veritas using CGG's Harmattan seismic vessel. The vessel towed two sources and six streamer cables (2/6). Each cable is 5700 m long separated by 50 m interval from one another. This survey layout has a 57-fold of coverage (Eqn. 3.2). The inlines and crosslines of the seismic base map ranges from 2000 to 6600 (i.e. 4601 inlines) and 840 to 4250 (i.e. 3411 crosslines) respectively, with equal spacing of 12.5 m between the lines. The inlines trends in the W-E direction perpendicular to the crosslines' direction.

The seismic dataset was originally acquired using 2 milliseconds sample interval, and later resampled to 4 milliseconds sample intervals. The seismic dataset was zero-phase processed and migrated using Stolt, 3D pre-stack time migration algorithm. It displays a normal positive polarity (European convention) so that an increase in acoustic impedance is represented by a peak on the seismic sections. The seismic dataset has a total available record length of about 5.0 seconds deep.

3.4.2. Broad Fourteens Basin

Three-dimensional (3-D) seismic and borehole data from the Broad Fourteens Basin, Southern North Sea, were used in Chapter 5 to investigate the geometry and reactivation history of faults that resulted from tectonic inversion. The data were acquired in the northern end of the Broad Fourteens Basin, offshore The Netherlands, between 53.1^0-53.3^0N and 3.8^0-4.2^0E (Fig. 2.4). The survey covers an approximated area of about 845 km^2 in a shallow water depth of 37.7 m.

The seismic data were recorded with a 2 ms vertical sampling interval, and a 12.5 x 12.5 m bin size, providing a maximum lateral resolution of 12.5 m. It was zero-phase time migrated and displayed with a normal positive polarity, so that an increase in acoustic impedance is represented by a peak (red seismic reflection). A decrease in acoustic impedance is represented by a trough (black seismic reflection) (SEG European Convention; Brown, 2003). The vertical scale of the seismic data is in two-way travel time (TWTT), up to a recording length of about 3.5 seconds. The vertical seismic resolution for the target intervals in Late Mesozoic to Paleogene strata is 17.8 m, based on a dominant frequency of 40 Hz and an average velocity of 2850 m/s.

3.4.3. Nankai Trough accretionary prism

Three-dimensional (3-D) pre-stack depth migrated seismic data were used in result chapter 6. The data were acquired in the outer wedge region of the Nankai accretionary prism, SE Japan, between 33.0^0-33.2^0N and 136.5^0-136.8^0E (Fig. 2.6). The survey area is oriented at 330^0 and covers an area of approximately 12 km by 23 km in water depths ranging between 2500 m and 5000 m (Fig. 3). The seismic data was acquired using dual

airguns and an array of 4 x 4500 long streamers spaced at intervals of 150 m. This configuration provided a 30-fold coverage, and a maximum lateral resolution of 12.5 m. Data were recorded with a 2 ms vertical sampling interval, and a 12.5 x 18.75 m bin size. The seismic data was zero-phase pre-stack depth migrated (Moore et al., 2009), and displayed with a normal positive polarity (European convention), so that an increase in acoustic impedance is represented by a red seismic reflection. Vertical seismic resolution approaches 6 m in shallow slope basin sediments based on the dominant wavelength of approximately 24 m (Alves et al., 2014), whereas vertical resolution in the overthrusted sediments approaches 14 m based on the dominant frequency of 40 Hz and velocity of 2200 m/s.

3.5. Seismic data interpretation

Seismic data interpretation is a fundamental constituent of this thesis, which was undertaken in the 3D Seismic Lab, Cardiff University, on Schlumberger's Petrel software. Seismic data interpretation session usually begins with viewing selected inline and crossline sections to acquire a regional understanding of the subsurface structural features. Data visualization techniques hold vast potential for improving both the quality and efficiency of seismic interpretation. The interpreter can develop a quick understanding of the structural setting, i.e. relationships between horizons and faults prior to any detail interpretation.

Visualisation of the seismic data is a valuable tool for data preview and interpretations. Colour, shaded, 3-D perspective displays allow the integration of information from horizon attributes and structure and interpretation of detailed faulting patterns. These displays are also used to explore the relationship between reservoir horizons and fault

surface structure and to integrate reservoir property estimations with structure (Geoffery et al., 1995).

3.5.1. Horizon and fault mapping

Several seismic reflections were mapped as horizons representing stratigraphic features in the study areas. These horizons were manually interpreted. The line spacing chosen to interpret each seismic horizon varied according to the structural complexity of specific areas. Laterally continuous reflections were mapped using a coarse grid line spacing or automatic picking tool's that Petrel software provided. Structurally complex areas were mapped using a finer grid spacing, i.e. from 5- to 10-line spacing.

Manually picked seismic reflections were used as seed points for the automatic horizon tracking. The autotracking (or autokicking) option on Petrel software consists of distinct algorithm operations that seek to identify similar features in terms of phase and amplitude in surrounding seismic traces (Dorn, 1998; Hart, 1999). If the autotracker finds similarities among neighbouring seismic traces, it will pick the trace and move on to the next trace. If the search criteria are not met, the autotracker stops at that trace (Dorn, 1998). In areas with relatively low signal-to-noise ratios, or with geological complexity, the autotracking option may face difficulties. Manual checking and constant edits of the autotracked horizons are thus necessary to establish a locally continuous, reliable stratigraphic framework (Hart, 1999).

Fault interpretation follows a similar approach to horizon mapping. Rather than mapping seismic reflections, this method revolves around mapping breaks or displacements in seismic reflections that are linear, crosscut, and offset packages of seismic reflections. Faults are mapped from the point where there offset starts to where

it ceases, and no offset is visible on the fault tips. Faults are picked manually, both vertically and laterally by moving between inlines and crosslines at intervals ranging from 10 lines to 1 line to capture structural complexity and generate an accurate 3D representation of the fault plane.

3.5.2. Seismic attributes

Seismic attributes are a valuable tool in the interpretation of seismic data as they can be used to derive further information on the stratigraphic and structural nature of the seismic dataset. In Petrel®, numerous seismic attributes are at the interpreter's disposal. The volume attributes used in this thesis include coherence (variance) and two-way-time structural maps.

Variance (or coherence) maps are created from a seismic volume, meaning the model produced has not yet been interpreted, and is therefore presented without any interpretation bias. This method uses algorithms to compare the similarity of adjacent waveforms, converting the seismic-amplitude volume of continuity into a volume of discontinuity (Brown, 2004). Therefore, it captures geological discontinuities along a horizon, such as a faults and channels. Two-way-time structural map provide the interpreter with a view of the topographic relief across the study area.

3.6. Faults throw analyses

Faults throw measurements along fault strike and fault throw measurements with depth are key techniques in fault analyses throughout this thesis. Throw-depth (T-z) and throw-distance (T-x) plots are interpretation techniques that document the growth

histories (both vertical and lateral) of a fault. Both techniques involve the analysis of fault throw along a specific horizon.

Throw is measured by the distance between the top of a horizon on the hanging-wall, and the respective horizon on the footwall i.e., vertical component of dip separation (Fig. 3.6). The depth is then taken at the top of the horizon on the hanging-wall. Throw-depth (T-z) plots are a collection of throw measurements taken at every resolvable horizon intersecting the fault on a single seismic line. Throw-distance (T-x) plots are fault-throw measurements on a single horizon taken at regular intervals along the fault strike. Therefore, they document the throw gradients from both tips (where throw is 0 m) and the throw maximum (Fig. 3.6).

Throw-depth (T-z) plots were analysed to determine whether a fault is blind or comprises a growth fault, and if it had been reactivated (Walsh and Watterson, 1989; Mansfield and Cartwright, 1996; Cartwright and Mansfield, 1998; Baudon and Cartwright, 2008). A reactivated fault is considered to have a stepped vertical throw profile. If there is a throw minimum and a negative gradient across a stratigraphic unconformity that has been offset by a fault, fault propagation is a result of "dip linkage" (Mansfield and Cartwright, 1996). If the throw has a stepped profile, but maintains a positive gradient, the fault is believed to have developed predominantly by "upward propagation" (Baudon and Cartwright, 2008).

Throw-depth (T-z) plots also offer information on the rock competence, nucleation, growth, segmentation, and linkage of individual faults (Baudon and Cartwright, 2008; Maunde and Alves, 2020). Discrepancies in throw gradients commonly result from mechanical heterogeneities, fault reactivation and fault segmentation (Childs et al., 1996; Baudon and Cartwright, 2008; Laubach et al., 2009).

106

Fig. 3.6. Schematic cross-section through a simple normal fault showing points of fault throw-depth (T-Z) measurements and their corresponding throw-depth (T-Z) plot. a) C-shape throw profile. Fault segment with local throw maximum in the throw-depth plot represents the interval where fault nucleate first. This segment propagates outwards until it encountered other pre-existing fault segments to link together. b) Throw-depth plot exhibits a regular upward decrease in throw values and maintain vertical, positively stepped gradients, revealing the classical model for fault growth by upward propagation.

Throw-distance plots are used to develop models for lateral fault growth. They show the geometric evolution of faults and the mechanical interaction between undeformed rock and the fault at its lateral tips (Jackson and Rotevatn, 2013, Cartwright et al., 1995). Idealistic faults have a central throw maximum, but this is often not the case. When there are multiple peaks of throw maximum, the fault can be interpreted as having grown by segment linkage (Cartwright et al., 1995).

CHAPTER 4

Impact of tectonic rafts' gravitational instability on fault reactivation and geometry

Co-author contributions to the paper:

Tiago Alves (Supervisor): checked for grammatical errors, ensured the scientific content was accurate and appropriately presented.

4. Impact of tectonic raft's gravitational instability on fault geometry and growth histories

4.1. Abstract

The downslope gravitational instability of tectonic rafts can deform large volumes of supra-salt strata on continental margins. Detailed mapping of fault throw and geometry using three-dimensional (3D) seismic reflection data from the salt-rich Espírito Santo Basin (SE Brazil) shows that the complex fault geometries observed are primarily due to downslope gravitational instability of tectonic rafts. Three main tiers of faults were identified and their geometry analysed in detail. Tier 1 faults are associated with the initial stage of fragmentation of supra-salt strata into individual blocks, or rafts, which are separated by listric (roller) faults and associated minibasins. These faults comprise closely spaced normal faults that resulted from outer-arc stretching of strata overlaying discrete tectonic rafts. The faults accommodate a significant part of the bending strain occurring in the hanging-wall blocks of roller faults, thus forming a curved-polygonal planform geometry adjacently to large roller faults. Tier 2 faults are associated with a renewed stage of downslope gravitational gliding of tectonic rafts. The progressive bending of overburden strata during this stage led to the progressive faulting of overburden strata by these faults. The faults comprise closely spaced normal faults with a restricted range in fault strikes, forming a rectangular-polygonal planform geometry over rollover anticlines. Tier 3 faults are associated with a later stage of diachronous grounding of tectonic rafts. Differences in the degree of diachronous grounding of tectonic rafts are responsible for the development of these faults and subsequent shortening of the overburden strata. These faults comprise densely spaced set of normal faults with diverse range of fault strikes, forming an irregular polygonal planform

geometry over rollover anticlines. The interpreted fault tiers show fault throw maxima ranging from 50 m to 60 m, spacings of 180–420 m and trace lengths of 120–650 m. The interpreted fault tiers were reactivated, and their growth is characterized by fault segment linkage. The diachronous downslope translation and grounding (welding) of tectonic rafts on sub-salt strata was an important process controlling the degree of deformation off Espírito Santo. Successive episodes of fault reactivation, and the subsequent generation of salt welds below tectonic rafts, potentially formed large conduits favouring fluid migration and the generation of hydrocarbon traps in supra-salt strata.

4.2. Introduction

The proximal continental slopes of salt-rich continental margins, such as offshore Angola–Congo and southeast Brazil, are characterised by large-scale withdrawal and downslope movement of salt under deltaic wedges (Demercian et al., 1993; Cramez and Jackson, 2000; Fort et al., 2004; Alves et al., 2009). This process triggers gravitational instability and has led, in the past, to the fragmentation of supra-salt strata into individual blocks, or rafts, separated by listric (roller) faults and associated minibasins. In places, these fragmented blocks of strata (rafts) are overlain by wide rollover anticlines (Duval et al., 1992; Cramez and Jackson, 2000; Alves, 2012). Importantly, the continuous downslope translation and grounding of rafts above sub-salt units have induced a continuum of overburden deformational styles not only in southeast Brazil, but through vast areas of West Africa (Duval et al., 1992; Gaullier et al., 1993; Mauduit et al., 1997; Penge et al., 1999; Alves, 2012; Pilcher et al., 2014). It also led to: a) significant subsidence in extensional basins located updip from moving rafts, b) the development of large listric (roller) faults controlling seafloor topography during supra-

salt extension, c) the development of growth strata infilling the accommodation space created by raft movement, and d) the development of reactivated structures, which at places developed into pop-up structures and wide rollover anticlines sub-parallel to the strike of individual rafts (Alves, 2012).

On the continental margin of southeast Brazil, deformation driven by the gravitational gliding of rafts has been a relatively continuous process. Local tectonic shortening began early after the deposition of supra-salt strata and continued unabated up to the present day. However, individual rafts ceased movement at different times depending on their geometry, salt supply and overburden thickness (Fiduk et al., 2004; Alves, 2012; Piedade and Alves, 2017). Earlier studies on tectonic rafts considered that differences in supra-salt overburden thickness can maintain the downslope gravitational gliding of rafts even if slope gradient is close to zero, if an efficient basal decollement is present at depth (Duval et al., 1992; Gaullier et al., 1993; Mauduit et al., 1997; Vendeville, 2005; Brun and Mauduit, 2009). Such a story of gravitational gliding will be potentially recorded by rollover faults, wide rollover anticlines, stratal shortening, and associated salt structures. For instance, Alves (2012) reported that distinct tectonic episodes of gravitational gliding in tectonic rafts controlled the Late Cretaceous-Paleogene evolution of the basin, inducing local shortening, wide rollover anticlines and fault reactivation.

Fault reactivation has been described as reflecting the further propagation of pre-existing faults after a significant period of quiescence (Cartwright et al., 1995; Mansfield and Cartwright, 2001; Peacock and Sanderson, 1991; Baudon and Cartwright, 2008). The classical model for fault reactivation assumes upward propagation from pre-existing structures as faults are generated at depth (Richard and

Krantz, 1991). The early fault growth model of Barnett et al. (1987) initially favoured the development of isolated normal faults propagating in a radial direction and records no migration of maximum displacement points. Recent work has focused on documenting changes in the dimensions and absolute fault displacements to build more reliable fault-propagation models (Cartwright et al., 1995; Mansfield and Cartwright, 2001, 1996; Cartwright and Mansfield, 1998). It is now recognised that larger faults are a result of fault-segment linkage associated with propagation in both the vertical and horizontal directions (Cartwright et al., 1995; Mansfield and Cartwright, 2001; Peacock and Sanderson, 1991; Dawers and Anders, 1995). Morley (1999) argued for an early linkage of multiple smaller faults, rather than growth following the isolated fault model. A supplementary model was presented by Lohr et al. (2008), who demonstrated that most faults grow by the coalescence of multiple smaller fault segments, whereas tip propagation is of relatively minor importance. Acknowledging this latter process of fault growth, Cartwright et al. (2000) and McLeod et al. (2000) defended that the geometry of large faults is essentially controlled by existing small fault segments.

This chapter aims at understanding the effect of gravitational gliding of rafts on fault reactivation and the subsequent geometry of rollover anticlines developed above tectonic rafts. Using a high-quality 3D seismic dataset from the Espírito Santo Basin, offshore southeast Brazil, results were extrapolate to other salt-rich continental margins where similar phenomena have occurred (e.g., offshore Angola-Congo, North Sea; Duval et al., 1992; Mauduit et al., 1997; Cramez and Jackson, 2000). Thus, this chapter aims to address the following questions:

a. How are faults over rollover anticlines reactivated in areas dominated by raft tectonics?

b. Does the geometry of faults over rollover anticlines document discrete episodes of gravitational gliding?

c. What are the modes of fault propagation developing during the gravitational gliding of tectonic rafts?

To simplify the analysis in this chapter, eight age constrained stratigraphic unconformities in Cretaceous and Cenozoic strata were mapped. These unconformities truncate the interpreted fault families, thus allowing for the relatively dating of fault movement below and above them (Fig. 4.2). Fault growth histories were further assessed through the collection of fault displacement data (Peacock and Sanderson, 1991; Cartwright and Mansfield, 1998; Mansfield and Cartwright, 2001; Stewart, 2001; Morley, 2002; Peacock, 2002; Baudon and Cartwright, 2008; Zhang et al., 2011; Anette et al., 2013). Throw-depth (T-Z) plots offer information on the nucleation, propagation, segmentation, and linkage of individual faults, providing at the same time important data for fault seal prediction (Stewart, 2001; Koledoye et al., 2003; Faulkner et al., 2010). In parallel, throw gradients have been used to assess the role of lithology and tectonic reactivation on the growth of faults (Cartwright and Mansfield, 1998; Baudon and Cartwright, 2008), as discrepancies in throw gradients commonly result from mechanical heterogeneities, fault linkage and fault segmentation (Baudon and Cartwright, 2008).

4.3. Chapter-specific dataset and methods

4.3.1. Dataset

The seismic block (BES-100) investigated in this chapter covers an area of 2,450 km^2 of the Espírito Santo Basin, in water depths ranging between 700 m and 1970 m (Fig.

2.1). It was acquired using dual airguns and an array of 6 x 5700 m long streamers. Data were recorded with a 2 ms vertical sampling interval, and a 12.5 x 12.5 m bin spacing. This configuration provides a 57-fold coverage and a maximum lateral resolution of 12.5 m.

The seismic dataset was zero-phase migrated using a 3D Stolt prestack time migration algorithm. It displays a normal positive polarity so that an increase in acoustic impedance is represented by a peak and is red on the seismic sections. The vertical scale of the seismic dataset is two-way travel time (TWTT) and, for this chapter, was limited to a recording length of about 5.0 s (Fig. 4.1). Velocity information obtained from Alves (2012) was used in the depth conversions in this chapter (Fig. 4.1). Based on a velocity range of 1900 - 2700 m/s, and the dominant frequency content of the seismic dataset (40 Hz), vertical seismic resolution ranges between 12 m in shallow Cenozoic strata and 17 m at Cretaceous level. Stratigraphic information from França et al. (2007) and Alves (2012) was used to identify, date, and correlate the interpreted seismic horizons across the study area (Fig. 4.1).

4.3.2. Methods

Horizons and faults were mapped using Schlumberger's Petrel®. Prior to its mapping, the entire seismic volume was visually scanned and inspected to assess data quality and develop a quick understanding of main structural features in the study area, e.g. main relationships between sedimentary units and structures. The overall quality of the seismic dataset is good. However, some of the reflections are weak and chaotic within Cretaceous strata (Unit S4) (Figs. 4.2 and 4.3). As a result, eight age-constrained seismic units were mapped and correlated them with stratigraphic data in França et al. (2007) (Fig. 4.1). For the purposes of this chapter, the interpreted seismic units were

grouped into two main seismic-stratigraphic packages: Cretaceous and Cenozoic (Fig. 4.1). The Cretaceous strata is crossed by seismic horizons H1 to H5, which span from the Aptian (118.5 Ma) to the Maastrichtian (67.2 Ma). Cenozoic strata is sub-divided by seismic horizons H6, H7 and the seafloor, spanning the Paleocene (67.5 Ma) to the Holocene (Fig. 4.1).

Distinct normal faults, including roller (listric), rollover, reactivated, radial and concentric faults, were imaged on TWTT structural maps (Figs. 4.4 and 4.7). A major advantage of the study area is that well-dated Late Cretaceous to Miocene unconformities truncate the interpreted fault families, thus allowing to relatively date the periods of fault movement below and above these unconformities. The growth histories of these fault families were investigated by measuring their throws at regular intervals of 25 m along the strike of faults, except for large listric faults, which were measured at 125 m intervals. This complied with the minimum sampling interval of Tao and Alves (2019). The length of the interpreted faults ranges from 120 - 12,522 m, with maximum fault throws of 58–530 m (Table 1). The measured throw values were plotted against depth to assess the vertical and lateral growth histories of faults in the study area (Figs. 4.8–4.11).

Throw-depth (T-Z) plots were analysed to determine whether a fault is blind or comprises a growth fault, and if it had been reactivated (Walsh and Watterson, 1989; Mansfield and Cartwright, 1996; Cartwright and Mansfield, 1998; Baudon and Cartwright, 2008). A reactivated fault is considered to have a stepped vertical throw profile. If there is a throw minimum and a negative gradient across a stratigraphic unconformity that has been offset by a fault, fault propagation is a result of "dip linkage" (Mansfield and Cartwright, 1996). If the throw has a stepped profile, but

maintains a positive gradient, the fault is believed to have developed predominantly by "upward propagation" (Baudon and Cartwright, 2008).

Uncertainties associated with the measurement of fault-throw values may arise from the vertical sampling rate. The sampling interval, rather than the vertical stratigraphic resolution, determines accuracy when matching two correlative seismic reflection peaks or troughs (Baudon and Cartwright, 2008). An uncertainty in the positions of stratal terminations does introduce a minimal error associated with the position in depth of the recorded displacements. This is a function of the frequency content of the seismic dataset (Mansfield and Cartwright, 1996). Errors associated with spurious velocity estimates may also affect the throw values when converted to meters. Vertical sampling for the interpreted seismic volume is 2 ms.

4.4. Interpreted seismic units

Eight seismic units bounded by Late Cretaceous to Pliocene unconformities were mapped and correlated with stratigraphic data from França et al. (2007) and Alves (2012) (Fig. 4.1). The interpreted seismic units are grouped into two main stratigraphic seismic units, Cretaceous and Cenozoic (Fig. 4.1).

4.4.1. Cretaceous seismic units

The Cretaceous seismic units were named Units S1 to S5, and range from Aptian to Maastrichtian in age (Fig. 4.1).

4.4.1.1. Unit S1 (Early Aptian to middle/late Aptian)

Unit S1 comprises the syn-rift III sequence and the early post-rift sequence (Fig. 4.1). The unit is bounded by the Alagoas unconformity at its base and by evaporites (Unit S2) at its top (Fig. 4.1).
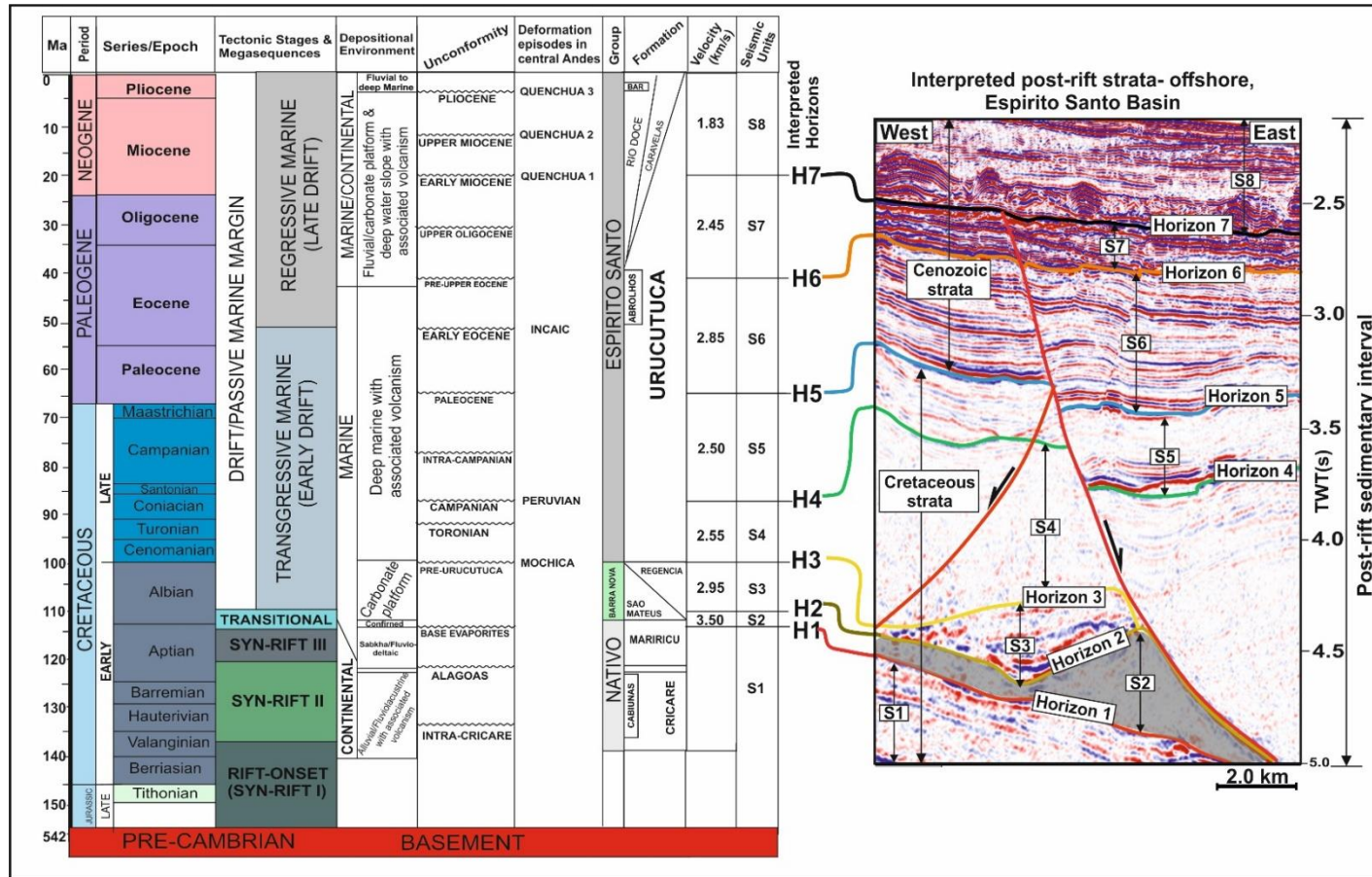
Fig. 4.1. Seismic-stratigraphic correlation between the interpreted post-rift seismic units and stratigraphic ages, tectonic phases/megasequences and unconformities related to regional tectonic events in the upper slope (extensional) region of the Espírito Santo Basin (modified from França et al., 2007). Velocity information taken from Alves (2012). Deformation episodes in the Central Andes are based on Megard (1984) and Gregory-Wodzicki (2010).

Unit S1 belongs to the upper Nativo Group (Mariricu Formation) and comprises conglomerates, sandstones and shales deposited in lacustrine and sabkha environments (França et al., 2007). The unit comprises moderate to high amplitude, low frequency reflections (Fig. 4.1).

4.4.1.2. Unit S2 (middle/late Aptian to Early Albian)

Unit S2 comprises main salt structures (e.g., salt rollers, pillows and diapirs) in the study area (Figs. 4.2 and 4.3). The lower boundary of the unit (top of early post-rift sequence; Unit S1) consists of an irregular reflection of moderate to high amplitude. Its upper boundary coincides with the first continuous high-amplitude strata (carbonate platform; Unit S3) covering Unit S2 (Figs. 4.2 and 4.3). In the study area, Unit S2 forms triangular salt rollers and vertical diapirs (Figs. 4.2 and 4.3).

4.4.1.3. Unit S3 (Early Albian to Cenomanian)

Unit S3 comprises high-amplitude, low-frequency seismic reflections and was deposited above the evaporites in Unit S2 (Figs. 4.2 and 4.3). The top of the unit is an angular unconformity in the proximal regions of the Espírito Santo Basin, changing laterally into a paraconformity in deeper waters (França et al., 2007). In the study area, Unit S3 is fragmented into discrete tectonic rafts (Figs. 4.2 and 4.3).

Unit S3 is part of the Barra Nova Group, which includes the São Mateus and Regência Formations, with siliciclastic and carbonate rocks deposited from the Albian to the Cenomanian on a shallow shelf (França et al., 2007). The São Mateus Formation consists of sandstones deposited in a proximal marine setting over a succession of shales, siltstones and carbonates (França et al., 2007).

The Regência Formation includes a relatively thick carbonate sequence comprising limestones, carbonate mudstones, and wackestones with ostracods, gastropods and pelecypods fragments deposited in distal parts of the Espírito Santo Basin (Asmus et al., 1971). The Barra Nova Group is bounded at its top by the Pre-Urucutuca unconformity (França et al., 2007) (Fig. 4.1).

4.4.1.4. Unit S4 (Cenomanian to Santonian)

Unit S4 comprises continuous, low-amplitude reflections (Figs. 4.2 and 4.3). The unit is locally deformed by closely spaced normal faults. The lower boundary of the unit is sharp, and marked by growth onto major regional and counter-regional roller faults above Horizons 2 and 3 (Fig. 4.3). The upper boundary of the unit (H4) is an irregular high-amplitude reflection representing an unconformity of Santonian age (França et al., 2007).

Unit S4 is part of the lower Espírito Santo Group and Urucutuca Formation, comprising shales interbedded with conglomerates, limestones, and sandstones deformed from the Cenomanian to the Coniacian due to halokinesis (França et al., 2007). On the distal margin, dark shales and sands have been described by Cainelli and Mohriak (1999) and França et al. (2007).

4.4.1.5. Unit S5 (Late Santonian to Maastrichtian)

Unit S5 comprises low-moderate amplitude strata above Unit S4. The lower boundary of the unit is marked by an unconformity related to the incision of a Late Cretaceous channel system (horizon H4 - Golfinho Field; Vieira et al., 2007; Alves, 2012) (Fig. 4.4). This same boundary (H4) is marked by the appearance of high-amplitude reflections above a faulted succession that shows growth of strata onto roller faults (Fig.

4.3). A regional unconformity of Late Maastrichtian age marks the upper boundary of the unit (Vieira et al., 2007).

Unit S5 comprises the middle portion of the Urucutuca Formation (Fiduk et al., 2004; França et al., 2007) (Fig. 4.1). During the Coniacian-Maastrichtian, the Urucutuca Formation recorded the deposition of sandy turbidites sourced by the Fazenda Cedro and Regência palaeocanyons (França et al., 2007), leading to the accumulation of turbidites at its base and predominantly shales and sandstones in proximal parts of the basin (França et al., 2007). Unit S5 correlates with the topmost Cretaceous strata mapped in the study area (Fig. 4.1).

4.4.2. Cenozoic seismic units

The Cenozoic seismic units comprise the S6 to S8 units, which span the Paleocene to Holocene (Fig. 4.1).

4.4.2.1. Unit S6 (Paleocene to Early Eocene)

Unit S6 is shown as a unit with high-amplitude reflections that are locally deformed by closely spaced normal faults (Figs. 4.2 and 4.3). Its lower boundary coincides with an unconformity of Maastrichtian age (H5; Fig. 4.1). The upper surface of the unit is marked by another regional unconformity above which moderately faulted high-amplitude strata were deposited (H6). In Unit S6, the volcaniclastic Abrolhos Formation is interbedded with thick turbidites forming channelised bodies whose distribution was controlled by halokinesis (Cainelli and Mohriak, 1999; França et al., 2007; Mohriak, 2003).

4.4.2.2. Unit S7 (Eocene to Early Miocene)

Unit S7 is composed of prograding high-amplitude reflections (Figs. 4.1 and 4.3). Moreira and Carminatti (2004) relate this unit to successive regressive and transgressive events affecting the Brazilian margin. Unit S7 comprises turbidite sands intercalated with volcaniclastic deposits (França et al., 2007).

4.4.2.3. Unit S8 (Early Miocene to Holocene)

Unit S8 overlies Unit S7 in a concordant manner and is bounded at its top by the seafloor (Fig. 4.2). It consists of a package of high frequency, continuous and moderate to high-amplitude reflections (Fig. 4.1). The overall thickness of Unit S8 changes significantly where erosion occurred due to the development of channel complex systems.

Unit 8 correlates with the Rio Doce, Caravelas and the upper Urucutuca Formations (França et al., 2007). Strata in this unit comprise sandstones (Rio Doce Formation), calcarenites (Caravelas member) and turbidite sands and marls (Urucutuca Formation) (França et al., 2007). Thus, where Unit S8 is eroded by submarine channels, mass-transport complexes and channel-fill deposits predominate in Mid-Miocene and younger strata (França et al., 2007).

4.5. Rollover anticlines and associated structures

Seismic imaging shows that the study area is characterised by wide rollover anticlines developed above tectonic rafts, tectonic rafts separated by large listric (roller) faults and associated minibasins, rollover faults over wide rollover anticlines, salt rollers in the footwall of listric (roller) faults, reactivated pop-up structures and drag folds (Fig. 4.3).
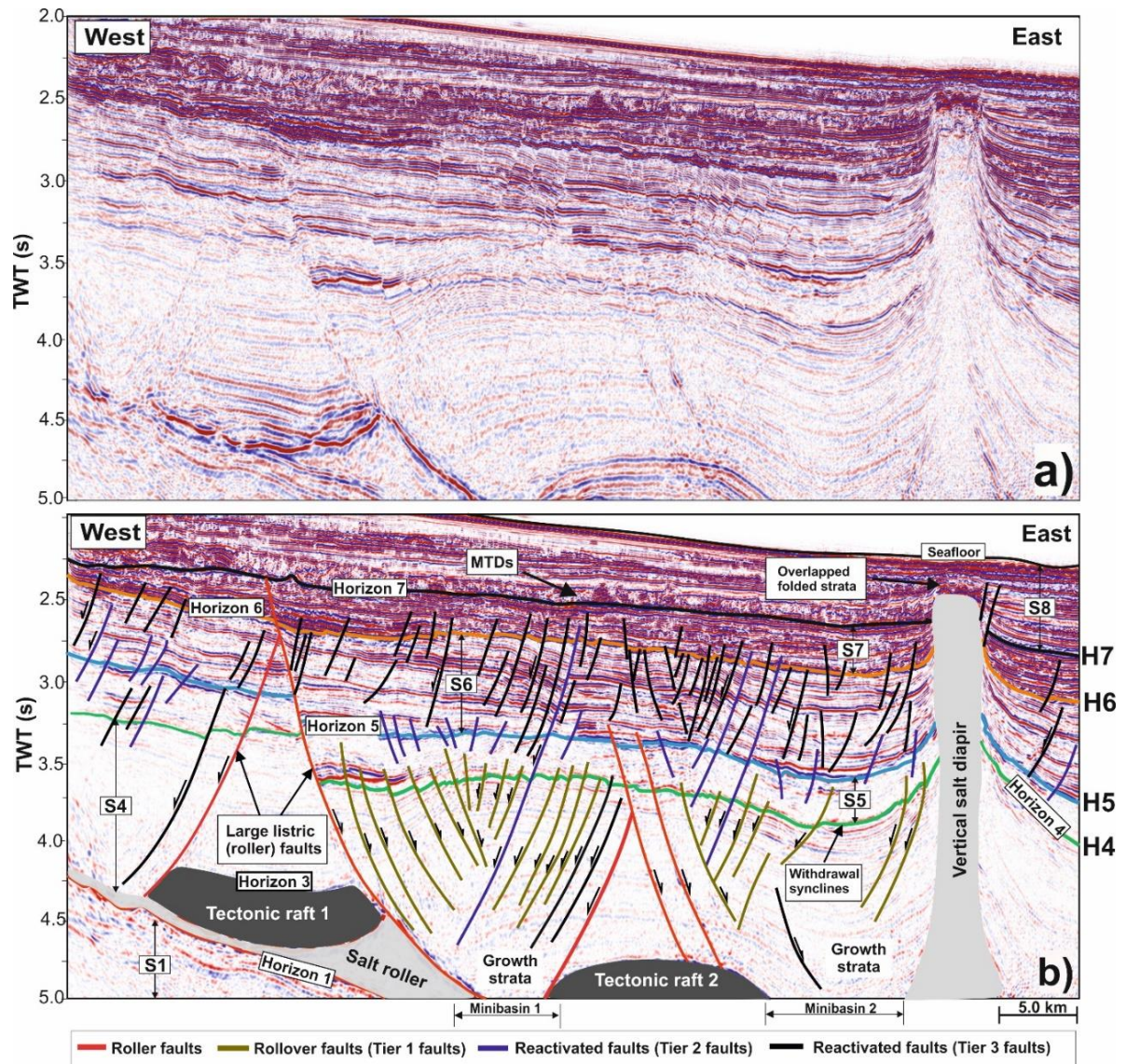
Fig. 4.2. a) Uninterpreted, and b) Interpreted seismic section across the study area. The section highlights the large roller faults bounding Cretaceous minibasins, normal faults over rollover anticlines, withdrawal synclines adjacent to roller fault and diapir, tectonic rafts between and above salt structures. Tectonic raft 2 forms the core of wide rollover anticlines. Tier 1, 2 and 3 faults dominantly cross-cut horizons H4, H5 and H6, respectively. Salt rollers, diapirs and tectonic rafts occur in Units S2 and S3. MTDs - Mass Transport Deposits.
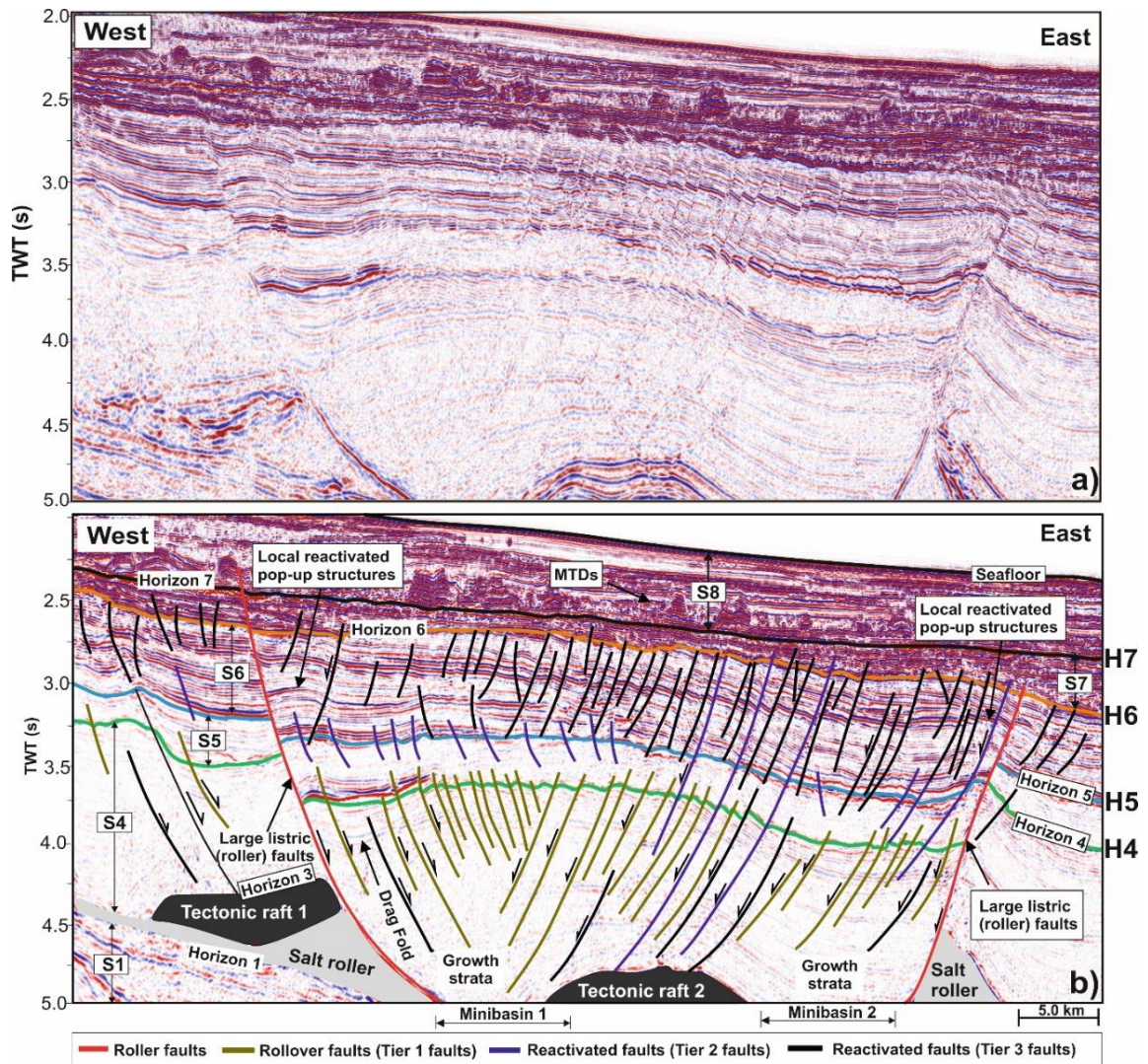
Fig. 4.3. a) Uninterpreted, and b) Interpreted seismic section across the study area. The section highlights large roller faults bounding Cretaceous minibasins, normal faults over rollover anticlines, drag folds adjacent to roller faults, tectonic rafts between and above salt rollers and local reactivated pop-up structures. Tectonic raft 2 forms the core of rollover anticlines. Tier 1, 2 and 3 faults dominantly cross-cut horizons H4, H5 and H6, respectively. The presence of reactivated pop-up structures in Paleogene strata (Unit S6), and the drag folds adjacent to the roller fault, materialise the diachronous grounding of tectonic rafts. MTDs - Mass Transport Deposits.

Tectonic rafts (Unit S3) form the core of broad rollover anticlines and commonly lie between or above salt rollers (Figs. 4.2 and 4.3).

Where extension has been greatest and salt (Unit 2) completely evacuated, tectonic rafts lie directly on pre-salt units (Unit S1) (Fiduk et al., 2004; Alves, 2012) (Fig. 4.3). It is clear in the seismic sections (Figs. 4.2 and 4.3) that the downthrown blocks associated with listric (roller) faults exhibit a larger component of vertical slip adjacent to the fault plane than it does at some distance from the fault plane, so that a rollover anticline develops.

These rollover structures are of interest to the hydrocarbon industry as they may provide potential structural traps for hydrocarbons. The rollover geometry is the inevitable result of movement on a listric (roller) fault (Hamblin, 1965). Movement on such a curved fault plane will tend to generate a 'gap' between the hanging-wall and footwall blocks (Fig. 4.13a, b), which will be accommodated by the extensional collapse of the hanging-wall in either a ductile or brittle manner (Fig. 4.13c, d). More frequently, deformation occurs because of a combination of both modes of deformation (brittle and ductile) to form a rollover anticline and associated fault structures (Fig. 4.13). In the study area, rollover anticlines trend in the N–S direction, sub-parallel to the strike of tectonic rafts (Figs. 4.4 and 4.5).

Moving into the basin (eastwards), salt rollers developed into a vertical salt diapir province (Fig. 4.2). Diapirs commonly form in relative deep water, where the rift basin had subsided more and correspondingly thicker autochthonous salt was deposited (Fiduk et al., 2004). Depending on their salt budget, some diapirs have ceased movement in the Cretaceous (Fiduk et al., 2004), while others are still growing near the modern seafloor (Fig. 4.2). The presence of withdrawal synclines adjacent to the salt

diapir, and folded strata overlapping this diapir near the seafloor, suggest that the salt diapir is actively growing at present (Fig. 4.2). Radial faults are localised and distributed around the salt diapir and intersect both roller and rollover faults (Fig. 4.4). The TWTT structural maps in Fig. 4.7 highlight the geometry of rollover anticlines and their associated faults.

4.5.1. Roller (listric) faults

Roller (listric) faults comprise large regional (basinward-dipping) and counter-regional (landward-dipping) growth faults bounding tectonic rafts and minibasins (Fig. 4.3). These faults sole out at salt level (Unit S2) and the syn-rift III (Unit S1), in the places where the salt unit was almost completely removed (Fig. 4.3). Triangular salt rollers are observed towards the footwalls of these faults (Fig. 4.3). Some of the roller faults propagated vertically into Mid-Paleogene strata (Unit S7) and terminate at the base of mass-transport deposits (H7), with no faults extending near the seafloor (Figs. 4.2 and 4.3). These faults accommodated gravity gliding of the overburden units along the basal salt (Unit S2) generating, at the same time, significant subsidence in adjacent salt minibasins (Fig. 4.3). In their immediate hanging-wall, salt minibasins show significant subsidence and denote the formation of drag folds, reactivated local pop-up structures and wider rollover anticlines (Fig. 4.3). The roller faults are less than 13 km long (average 8.56 km), with a maximum throw of 530 m (average throw 470 m) (Table 4.1).

4.5.2. Rollover faults

Rollover faults comprise closely spaced sets of normal faults that are localised on top of the Cretaceous rollover anticlines (Figs. 4.2 and 4.3). These faults resulted from outer-arc stretching of strata overlying anticlinal structures. The faults dip in both basinward and landward directions, offsetting the Cretaceous Unit S4 (Figs. 4.2 and

4.3). In the study area, a significant part of rollover faults overlie tectonic rafts at depth (Alves, 2012). The progressive bending of rollover anticlines developed above rafts led to the progressive faulting of the Cretaceous Unit S4 by rollover faults (Figs. 4.2 and 4.3). These rollover faults accommodate a significant part of the bending strain affecting the hanging-wall blocks of large roller faults, and areas recording supra-salt extension of the supra-salt overburden.

4.5.3. Reactivated faults

Reactivated faults comprise densely spaced normal faults that are dominantly localised in the Paleogene strata (Unit S6) (Figs. 4.2 and 4.3), with some faults propagating into Late Cretaceous strata. Reactivated faults were initially formed by arching of the Late Cretaceous overburden above tectonic rafts but were later deformed into local pop-up structures (Fig. 4.3). These faults were essentially rollover faults that suffered significant compression during the Late Cretaceous and Earliest Paleogene (Alves, 2012).

4.5.4. Concentric faults

Concentric faults are localised above extensional minibasins, i.e. in the space created by tectonic rafts. These faults occur within extensional minibasins bounded by roller faults and are concentrically arranged, dipping towards the centre of such minibasins (Figs. 4.4 and 4.7). Concentric faults accommodate local strain on the tips of the oval-shaped salt minibasins formed on the hanging-wall blocks of roller faults during the main periods of raft-related extension. These faults are less than 5 km long (average 2.650 km), with a maximum throw of 55 m (average throw 50 m) (Table 4.1).

4.6. Fault geometries over rollover anticlines

The seismic sections in Figs. 4.2 and 4.3 highlight some of the features in the faults formed above rollover anticlines. Above horizon H7, seismic reflections are chaotic and not affected by faults. Between H6 and H5 (Unit S6), the seismic expression of strata is markedly different in that seismic reflections are affected by closely spaced normal faults. Seismic reflections between H5 and H4 (Unit S5) are sparsely affected by faulting. Between H4 and H3 (Unit S4), the seismic expression of strata is again distinct from the units immediately above in that seismic reflections are highly disrupted and affected by closely spaced normal faults. Thus, three distinct tiers of faults can be recognised above rollover anticlines (Figs. 4.2 and 4.3).

4.6.1. Tier 1 faults

Tier 1 faults comprise closely spaced normal faults that offset horizon H4 (Figs. 4.2 and 4.3). Throws die out downward towards the top of tectonic rafts, which are apparently unfaulted and flat-topped due to Santonian erosion (Vieira et al., 2007). These faults have a maximum throw of 58 m, an average spacing of 250 m and trace lengths of 220–620 m (Table 4.1). Tier 1 faults are located on top of the Late Cretaceous rollover anticlines (Unit S4) and are thus interpreted as rollover faults (Figs. 4.2 and 4.3). These faults are aligned concentrically in front of listric (roller) faults, generating large half-moon structures and a curved-polygonal fault pattern over rollover anticlines (Figs. 4.6a and 4.7a). Tier 1 faults are dated as Cenomanian to Campanian (Figs. 4.1 and 4.12).

4.6.2. Tier 2 faults

Tier 2 faults comprise sparsely spaced normal faults that offset horizon H5 (Figs. 4.2 and 4.3). Throws die out downwards towards horizon H4, which is highly faulted, and upward into Unit S6.

TWTT structural map of horizon H4

Interpreted TWTT structural map of horizon H4
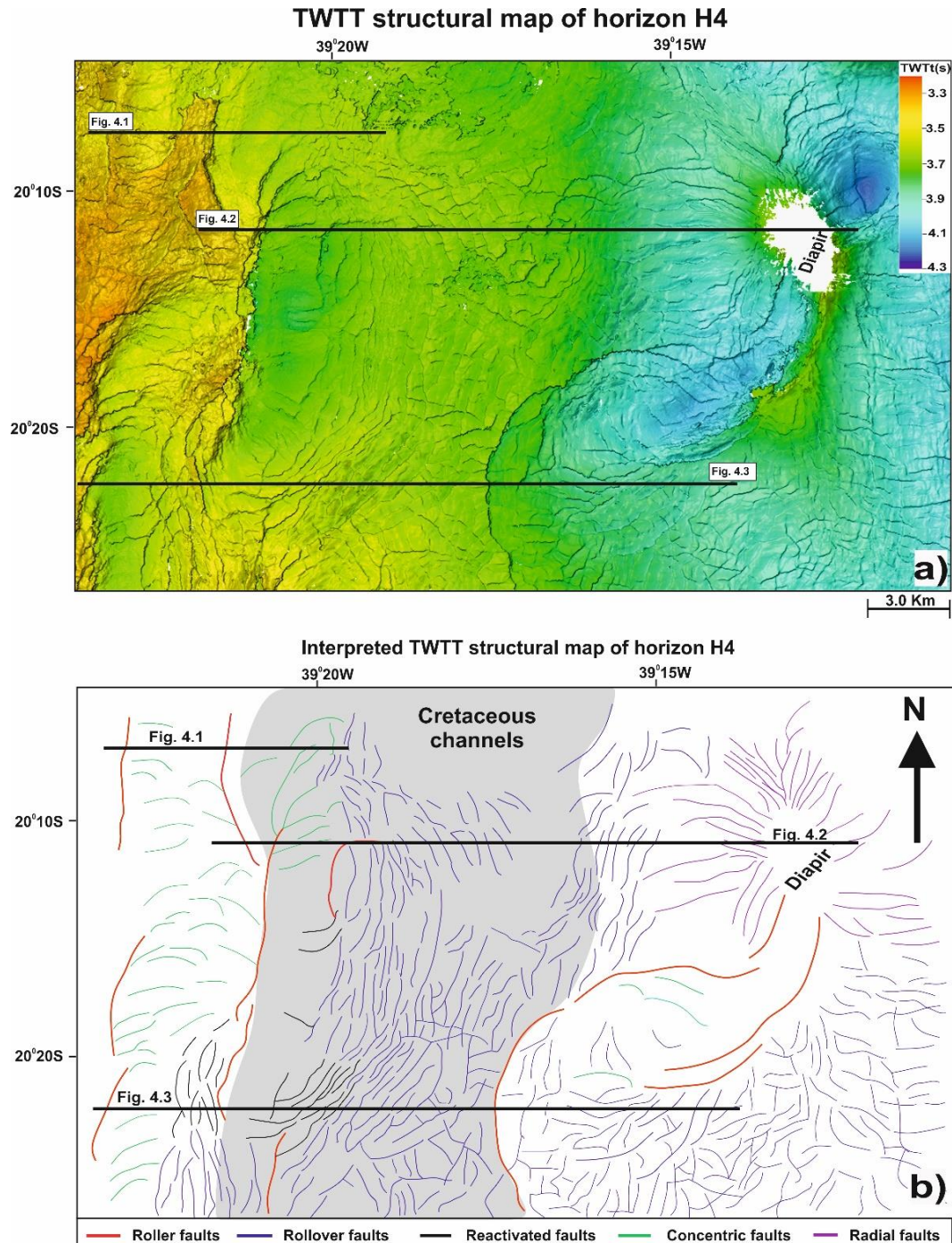
Fig. 4.4. a) TWTT structural map of Horizon H4 showing the distribution of fault families in the study area; b) Interpreted sketch highlighting the geometry of fault families and the N–S strike of wide rollover anticlinal zones (grey panel) sub-parallel to the strike of tectonic raft 2.
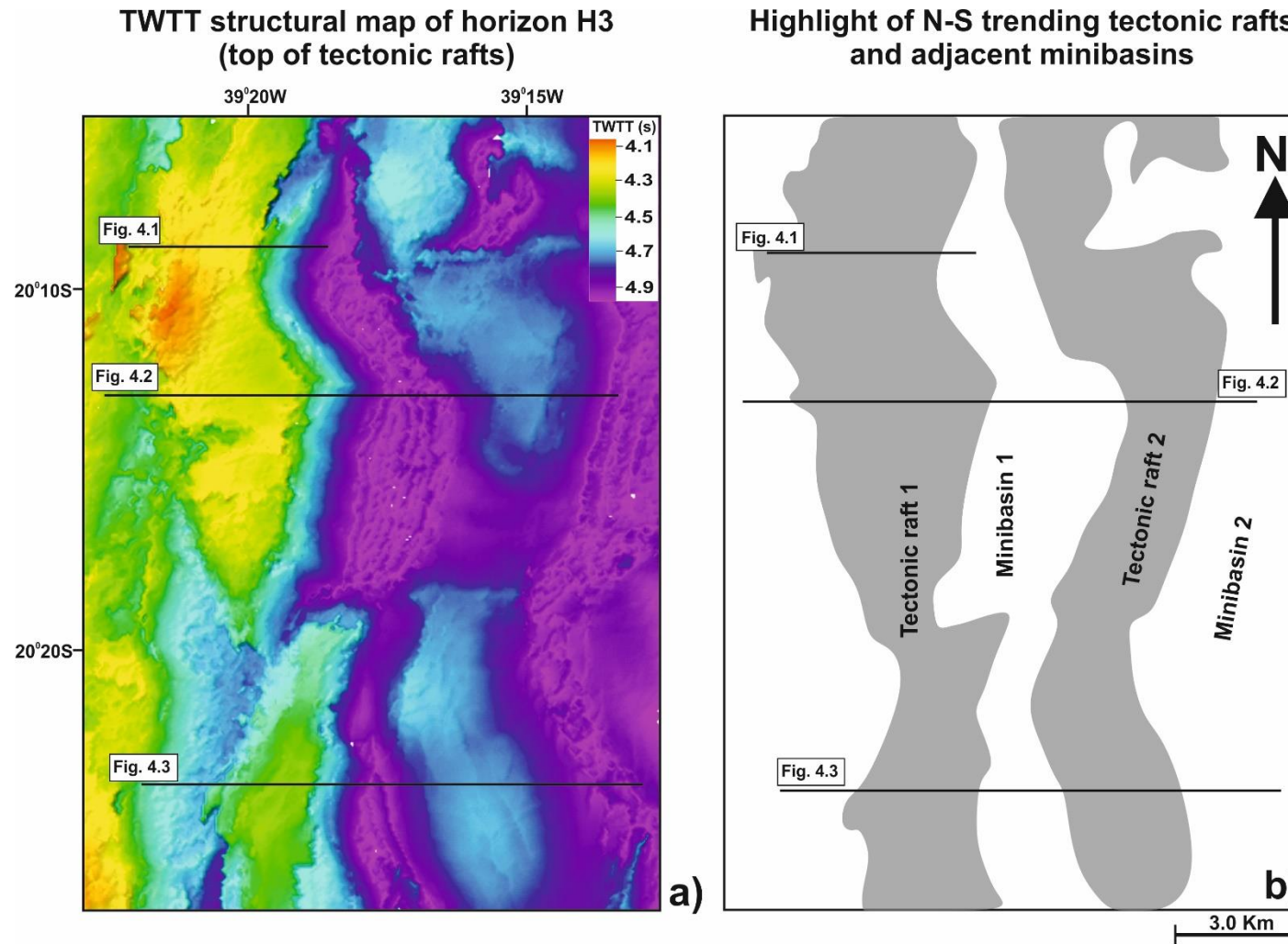
Fig. 4.5. a) TWTT structural map of horizon H3; b) Interpreted diagrams highlighting the geometry of N–S trending tectonic rafts separated by salt minibasins. Tectonic raft 2 forms the core of rollover anticlines in the study area.

These faults appear to overlap and link with other faults offsetting horizons H4 and H6 (Fig. 4.3). Tier 2 faults have a maximum throw of 55 m, an average spacing of 310 m and trace lengths of 280–650 m (Table 4.1). These faults are localised on top of the Late Cretaceous rollover anticlines (Unit S5) and are characterised by a large range of strikes, rarely showing an equal distribution of fault strikes.

As a result, they form a rectangular polygonal pattern over rollover anticlines (Figs. 4.6b and 4.7b). Tier 2 faults accommodate some part of the bending strain occurring in the hanging wall block of large roller faults. These faults were essentially rollover faults that suffered significant compression in the Late Cretaceous. Tier 2 faults are dated as Late Santonian to Maastrichtian (Figs. 4.1 and 4.12).

4.6.3. Tier 3 faults

It is clear in the seismic sections (Figs. 4.2 and 4.3) that several densely spaced normal faults offset Unit S6. Throws die out downwards in Unit S6 and below horizon H5. Their upper tips terminate in Unit S6 and above horizon H6 (Figs. 4.2 and 4.3). Thus, these faults were classified as Tier 3 faults. Tier 3 faults dominantly offset the Paleogene strata (Unit S6), with some faults propagating and linking with Tiers 1 and 2 faults (Fig. 4.3). These faults have a maximum throw of 50 m, an average spacing of 210 m and trace lengths of 120–550 m (Table 4.1). Tier 3 faults are characterised by a diverse range of strikes, and rarely show equal distribution of fault strike orientations - thus forming an irregular polygonal pattern over rollover anticlines (Figs. 4.6c and 4.7c). Tier 3 faults are dated as Paleocene to Eocene (Figs. 4.1 and 4.12).
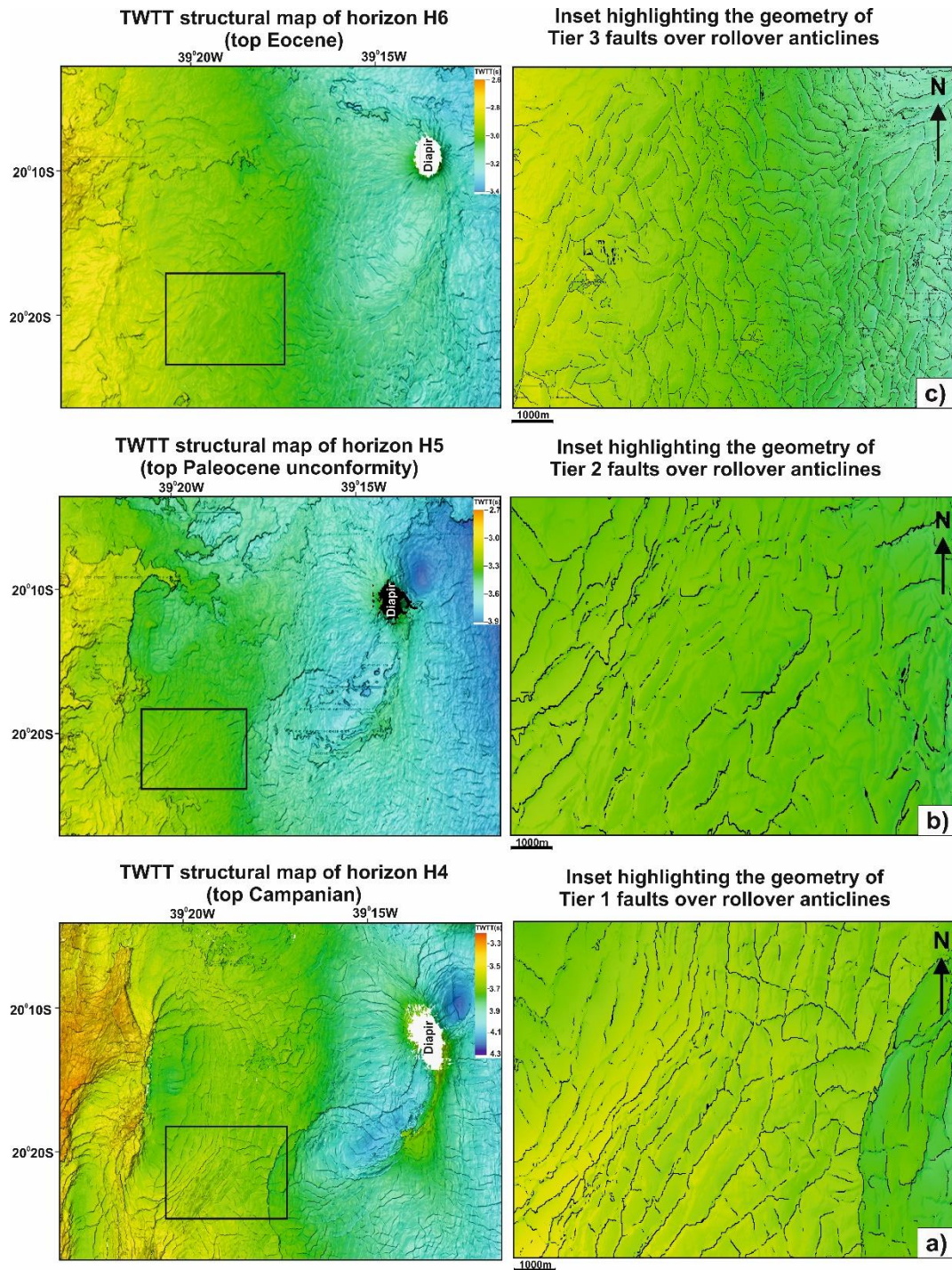
Fig. 4.6. TWTT structural maps for representative intervals in the study area highlighting variations in the geometry of distinct fault tiers over rollover anticlines (i.e., spacings, orientation, intersection relationships and linearity of fault segments). a) Tier 1 faults show curved polygonal plan-view geometries, b) Tier 2 faults show rectangular polygonal plan-view geometries, and c) Tier 3 faults show irregular polygonal geometries in plan view.
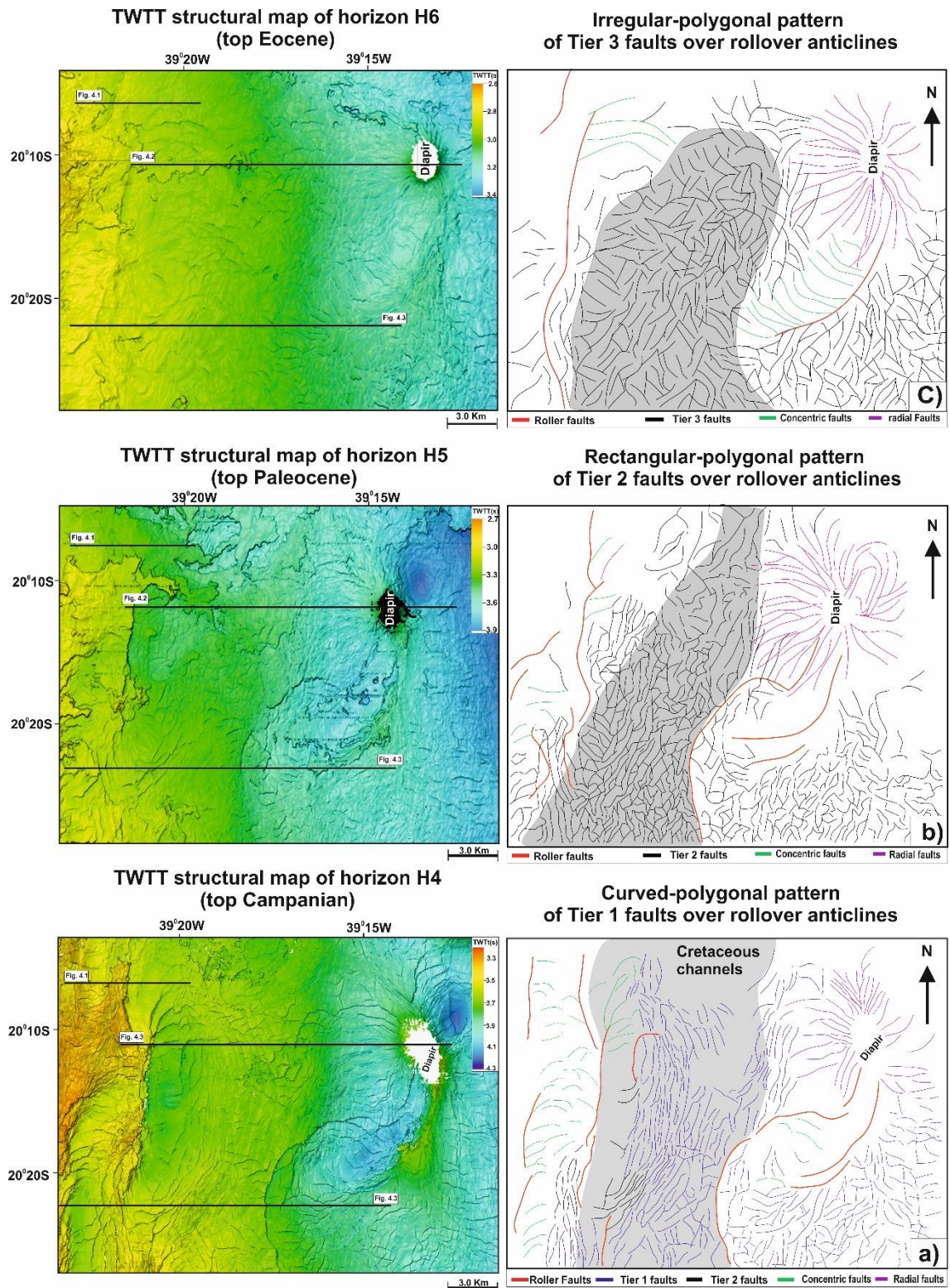
Fig. 4.7. TWTT structural map and interpreted diagrams highlighting the geometry of distinct fault tiers over N–S trending rollover anticlines (grey panel). a) Tier 1 faults: curved polygonal pattern, b) Tier 2 faults: rectangular polygonal pattern, and c) Tier 3 faults: irregular polygonal pattern.

4.7. Modes of fault reactivation

Fault reactivation has been described as resulting from further propagation of pre-existing faults after a significant period of dormancy (e.g., Cartwright et al., 1995; Baudon and Cartwright, 2008). The growth history for the interpreted faults in the Espírito Santo Basin was investigated using vertical throw-depth (T-Z) plots (Figs. 4.8–4.10). These faults were grouped into two main categories based on their mode of reactivation, as revealed by the throw-depth plots. These groups are: 1) reactivation by segment linkage, and 2) reactivation by upward propagation. Faults reactivated by segment linkage show throw profiles with zones of throw maxima separated from pre-existing faults by a region with throw minima and steepening throw gradients (Figs. 4.8–4.10). Faults reactivated by upward propagation present throw-depth plots that maintain vertical, positively stepped gradients (Baudon and Cartwright, 2008) (Fig. 4.11).

4.7.1. Reactivation by segment linkage

The throw-depth (T-Z) plots in Tier 1, 2 and 3 faults show a typical mode of reactivation by segment linkage (Figs. 4.8-4.10). This mode of reactivation is recognised by zones of throw maxima separated from pre-existing faults by areas with throw minima and steepening of the throw gradients (Figs. 4.8-4.10). The throw profiles of these faults do not always have single positive gradients and are characterised by throw profiles resembling C-type or M-type patterns between the upper-tip point and immediate throw minima (Baudon and Cartwright, 2008) (Figs. 4.8-4.10a). The presence of alternating zones of pre-existing throw maxima and minima in the throw distribution contour also point out to faults reactivating via the linkage of individual segments (Figs. 4.8-4.10b).

4.7.1.1. Fault reactivation in Tier 1

Tier 1 faults are localised and restricted to the top Cretaceous rollover anticlines, i.e. Unit S4 (Figs. 4.2 and 4.3). The throw-depth plots of these faults show truncation at horizon H4, terminating downwards within Unit S4; they never cross-cut horizon H3 (Fig. 4.8a). The vertical throw-depth plots of these faults resemble a C-type pattern between the upper-tip point and immediate throw minima (Fig. 4.8a). The lack of near zero throw values at horizon H4 confirms erosion of the fault tips by Late Santonian to Maastrichtian channel systems (Fig. 4.8a).

The mode of reactivation in Tier 1 faults is illustrated with reference to the throw distribution plots in Fig. 4.8. Segments A, B and C are pre-existing fault segments with throw maxima. Each fault segment coalesces with other segments that are similar in dip and strike directions to form a larger fault (Fig. 4.8). Segment A propagates and links with Segment C (plots 1, 2, 4 and 5; Fig. 4.8a). In a similar fashion, Segment B was reactivated to link with Segments A and C (plot 3; Fig. 4.8a). Segment C is truncated upwards at horizon H4. This fault segment appears to be eroded by the incision of Late Santonian to Maastrichtian channel systems (Vieira et al., 2007). Thus, the throw-depth plots of these faults reveal fault segment linkage as multiple peaks of throw maxima separated by throw minima (Fig. 4.8a).

Throw distribution contours provide additional information regarding segment linkage in Tier 1 faults (Fig. 4.8b). Segments with throw maxima A, B and C are pre-existing fault segments that were initiated at different depths. Each segment is separated from each other by a zone of throw minima and steepening of throw gradients as expected for faults reactivating by segment linkage (Fig. 4.8b). Similarly, the throw-distance (T-X) plots in Fig. 4.8c suggest modes of reactivation by segment linkage. The throw-

distance plots have two segments of throw maxima A and C separated by a throw minimum, as expected when growing faults by segment linkage. In other words, Segment A was reactivated and linked with Segment C (Fig. 4.8c).

4.7.1.2. Fault reactivation in Tier 2

Tier 2 faults typically offset Late Cretaceous strata (Unit S5). Some of these faults appears to overlap and link with faults from Tiers 1 and 3 (Fig. 4.3). The throw-depth plots of these faults tip out upwards just above horizon H6, and downwards into Unit S4 (Fig. 4.9a). Their vertical throw profiles are characterised by M-type and or C-type patterns between the upper-tip point and immediate throw minima (Fig. 4.9a).

The throw-depth plots of Tier 2 faults indicate a mode of reactivation dominated by segment linkage (Fig. 4.9). Along horizon H4 there is a throw maximum leading to decrease in throw at horizon H5, followed by a further increase in throw upwards (Fig. 4.9a). This character reflects reactivation by segment linkage, where two separate faults have propagated towards each other. Multiple throw peaks on throw-depth plots show that fault segment linkage is a common process (Fig. 4.9a and b). Towards the south, Segment A was reactivated to link with Segment B (plots 1, 2 and 3; Fig. 4.9a and plot 1; Fig. 4.9b).

4.7.1.3. Fault reactivation in Tier 3

Tier 3 faults are dominantly localised within Paleogene strata (Unit S6) (Fig. 4.3). These faults tip out upwards just above horizon H6, and downwards just below horizon H5. Thus, their throw profiles resemble M-type patterns (Fig. 4.10a). Tier 3 faults show a mode of reactivation by segment linkage (Fig. 4.10). Segments A, B, C and D are pre-existing fault segments with throw maxima (Fig. 4.10). Each segment is separated by a throw minimum, as expected for reactivation by segment linkage.
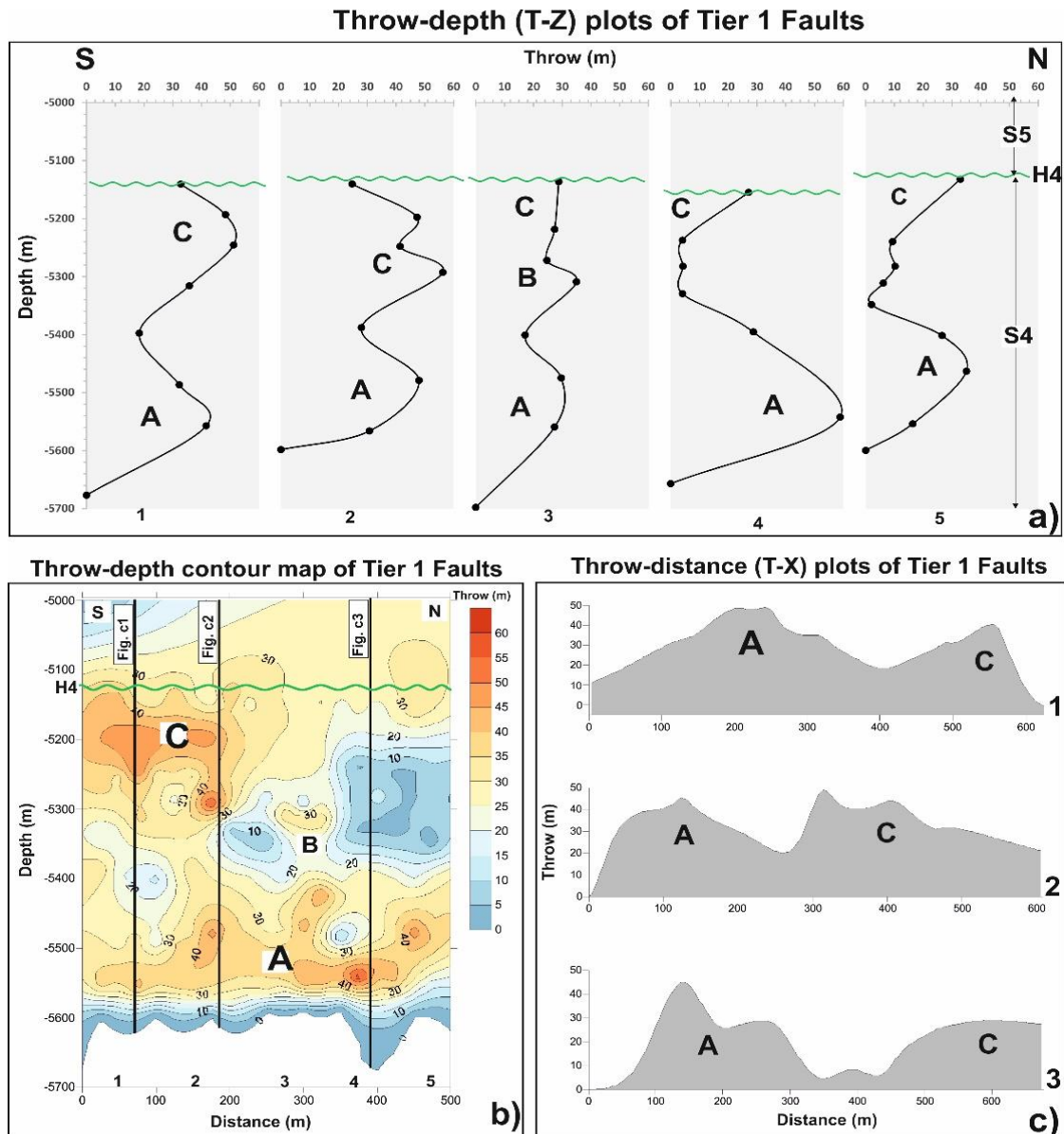
Fig. 4.8. a) Representative vertical throw-depth (T–Z) plots of Tier 1 faults, b) Throw contour map of the Tier 1 faults showing throw distributions and, c) Throw-distance (T–X) plots through the contour map (see Fig. 4.8b for profile line's location). A, B and C are individual fault segments separated by throw minima. H4, S4 and S5 relate to main horizons and seismic units.
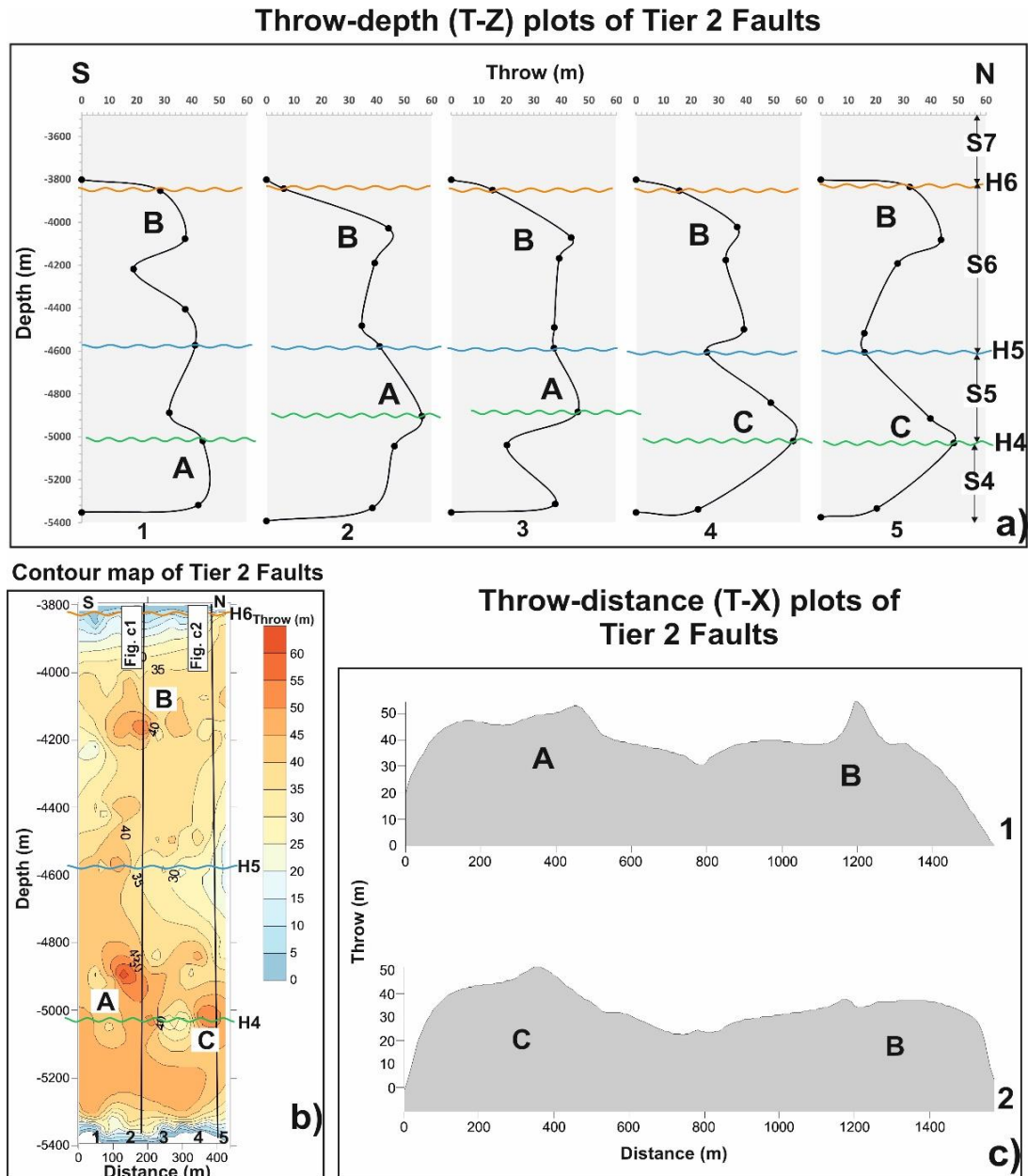
Fig. 4.9. a) Representative vertical throw-depth (T–Z) plots of Tier 2 faults, b) Throw contour map of the Tier 2 faults showing throw distributions and, c) Throw-distance (T–X) plots through the contour map (see Fig. 4.9b for profile line's location). A, B and C are individual fault segments separated by throw minima. H4, H5, and H6 are seismic horizons, while S5, S6 and S7 are seismic units.
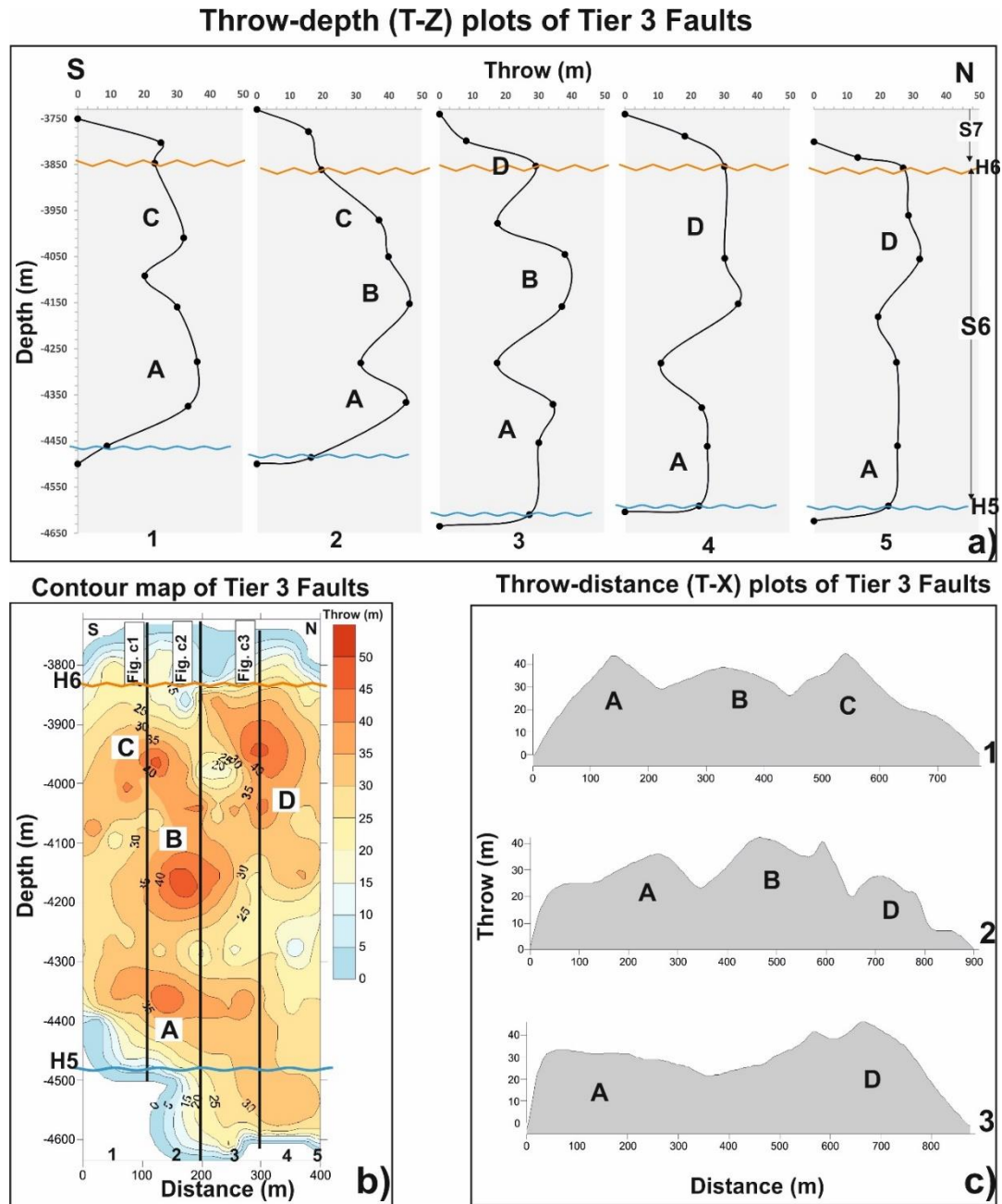
Fig. 4.10. a) Representative of vertical throw-depth (T–Z) plots of Tier 3 faults, b) Throw contour map of the Tier 3 faults showing throw distributions and, c) Throw-distance (T–X) plots through the contour map (see Fig. 4.10b for profile line's location). A, B and C are individual fault segments separated by throw minima. H5 and H6 are seismic horizons, while S6 and S7 are seismic units.

Towards the south, Segment A is reactivated by dip linkage with Segment C (plot 1; Fig. 4.10a). Further north, Segment A switches and links with Segment D (plots 4 and 5; Fig. 4.10a). Segment B was reactivated to link with Segments A and C (plot 2; Fig. 4.10a). These sharp changes in throw values are interpreted to be a consequence of reactivation by segment linkage of individual fault segments. Moreover, the throw-distance plots in Fig. 4.10c indicate a mode of reactivation by segment linkage; they show multiple peaks of throw maxima separated by a sharp change in throw gradients (Fig. 4.10c).

4.7.2. Reactivation by upward fault propagation

Large listric (roller) faults that bound the distinct fault tiers and wide rollover anticlines exhibit a typical vertical, positive stepped throw gradient (Fig. 4.11). These faults show major breaks in throw gradients around horizons H4 and H5, i.e. the Campanian and Paleocene unconformities (Fig. 4.11a, c). Throw-depth plots for these faults can be divided into three parts: lower, central, and upper parts. The lower part contains Unit S4 and shows throw maxima between 400 m and 530 m (Fig. 4.11a, c)

The central part contains Unit S5 and reveals an abrupt step in throw profiles, with throws between 150 m and 300 m (Fig. 4.11a, c). The upper part contains Unit S6 and shows almost constant positive throw gradients with no significant variations. It records fault throws between 2 m and 120 m (Fig. 4.11a, c). The decrease and vertical positive step in throw gradients recorded by the roller faults can be related to the effects of reactivation by upward propagation from parent faults above a detachment surface (Unit S2) (Baudon and Cartwright, 2008).
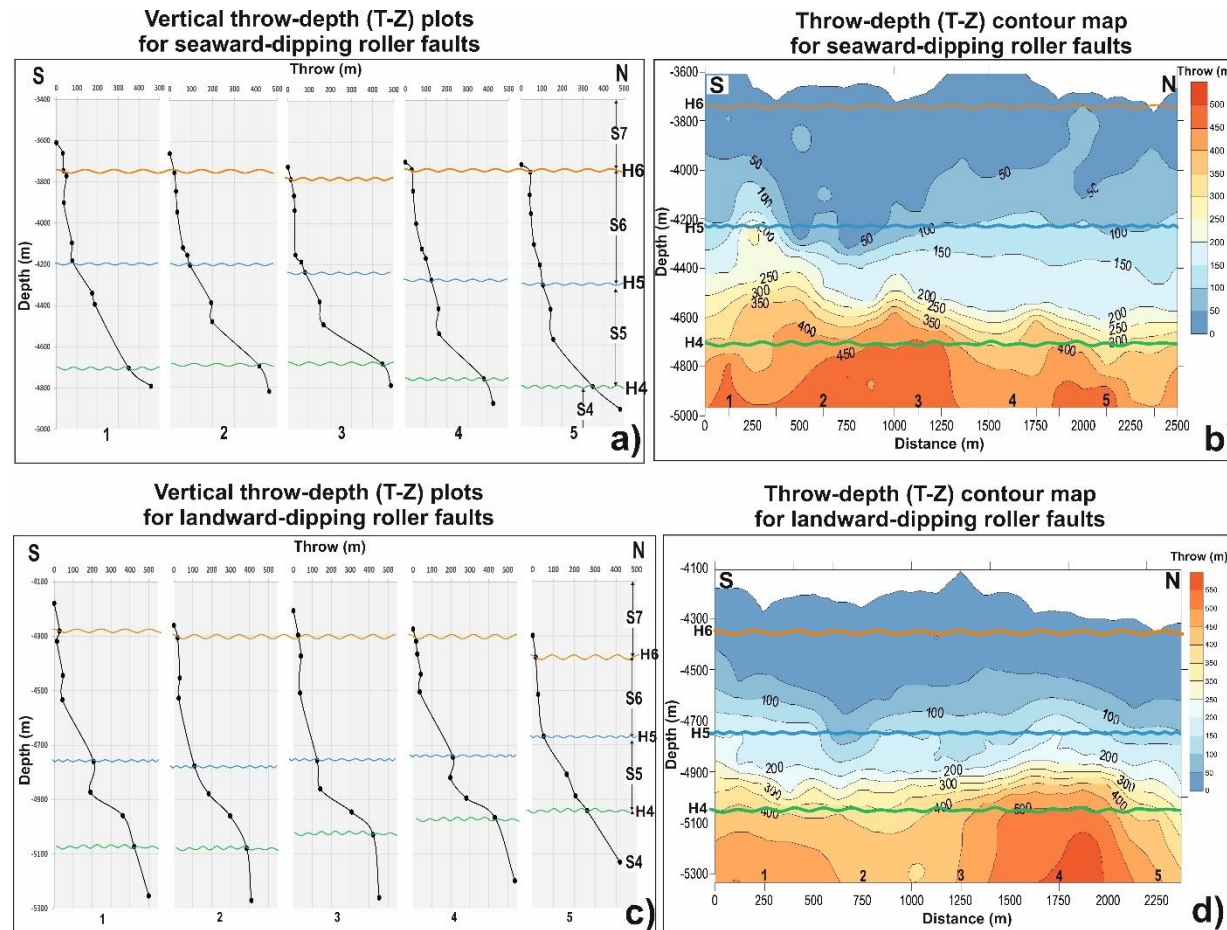
Fig. 4.11. a, c) Representative vertical throw-depth (T–Z) plots for seaward- and landward-dipping roller faults. H4, H5 and H6 are seismic horizons, while S4, S5, S6 and S7 are seismic units, b) and d) Throw-depth (T–Z) contour maps of roller faults showing their corresponding throw distributions.

Table 4.1. Summary of statistical data on the distinct fault tiers over rollover anticlines mapped in the study area.

Fault families	Maximum length (m)	Minimum length (m)	Average length (m)	Average spacing (m)	Maximum Throw (m)	Average Throw (m)
Rollover faults (Tier 1)	620	220	410	250	58	47
Reactivated faults (Tier 2)	650	280	430	310	55	48
Reactivated faults (Tier 3)	550	120	390	210	50	46
Roller faults	12,522	5,340	8,560	4,500	530	470
Concentric faults	4,562	1,860	2,650	1,250	54	50

Also, the absence of alternating zones of pre-existing throw maxima (and minima) in throw contour maps, and the observed uniform lateral continuity in throw gradients, relate to the reactivation of roller faults by upward propagation (Fig. 4.11b, d).

4.8. Discussion

4.8.1. Tiered faulting vs. distinct tectonic episodes of gravitational gliding

The continental margin of southeast Brazil is primarily associated with the continental break-up of Gondwana in the Late Jurassic to Early Cretaceous, and subsequent opening of the South Atlantic Ocean (Chang et al., 1992; Davison, 1999; Meisling et al., 2001). After rifting ceased, gravity tectonics became the primary deformational process in the Espírito Santo Basin, triggered by differential sediment loading, gravitational spreading and gliding of the supra-salt overburden. Uplift and tilting of the continental margin have been an intermittent, but important factor impacting these latter phenomena (Demercian et al., 1993; Alves et al., 2009; Fiduk et al., 2004).

On the continental slope of southeast Brazil, gravitational gliding induced a continuum of deformation and contributed significantly to shaping the supra-salt overburden - as expressed by complex structures such as listric (roller) faults, wide rollover anticlines, closely spaced collapsed growth fault crests, reactivated faults and folds, salt rollers and tectonic rafts (Figs. 4.2 and 4.3).

Three distinct Late Cretaceous to Paleogene tectonic stages of gravitational gliding are recognised in the study area; initial, renewed, and late stages of gravitational gliding (Fig. 4.14). The initial stage (post-Albian to Coniacian) caused the supra-salt strata (Unit S3) to be fragmented into discrete blocks of strata or rafts separated by large listric (roller) faults and associated minibasins (Fig. 4.14a). This stage is characterised by

downslope movement of rafts, the development of large listric (roller) faults controlling seafloor topography during extension, significant subsidence in half-grabens adjacent to roller faults, development of rollover anticlines above rafts, and initiation of normal faults on top of rollover anticlines to accommodate the buckling of the post-raft overburden. (Figs. 4.13 and 4.14a).

The renewed stage (Early Santonian to Early Paleogene) caused the rafts (Unit S3) to be translated downslope until salt welds were formed, i.e., rafts became grounded over sub-salt units. The grounding (welding) of rafts over the sub-salt strata was progressive and accompanied by moderate translation of blocks during the Early Paleogene (Alves, 2012) (Fig. 4.14b). This stage is characterised by discrete blocks of strata (rafts), seaward- and landward-dipping listric (roller) faults, wide rollover anticlines, rollover faults, reactivated faults, salt rollers and growth strata infilling minibasins (Figs. 4.13c and 4.14b).

The late stage of gravitational gliding (Mid Paleogene to Holocene) caused the diachronous grounding of rafts, thus promoting significant fault reactivation and stratal shortening in the Late Cretaceous to Paleogene strata (Fig. 4.14c). This stage is characterised by large blocks of grounded strata (rafts), wide rollover anticlines whose axes are sub parallel to the strike of rafts, seaward- and landward-dipping listric (roller) faults, normal faulting over rollover anticlines, fault reactivating, reactivated pop-up structures, drag folds, salt rollers, salt diapir and growth strata infilling minibasins (Figs. 4.2, 4.3, 4.13d and 4.14c).

4.8.2. Impact of the gravitational gliding of tectonic rafts on fault geometry

The Late Cretaceous to Paleogene gravitational gliding of tectonic rafts induced a continuum of supra-salt overburden deformation that controlled fault geometry over-
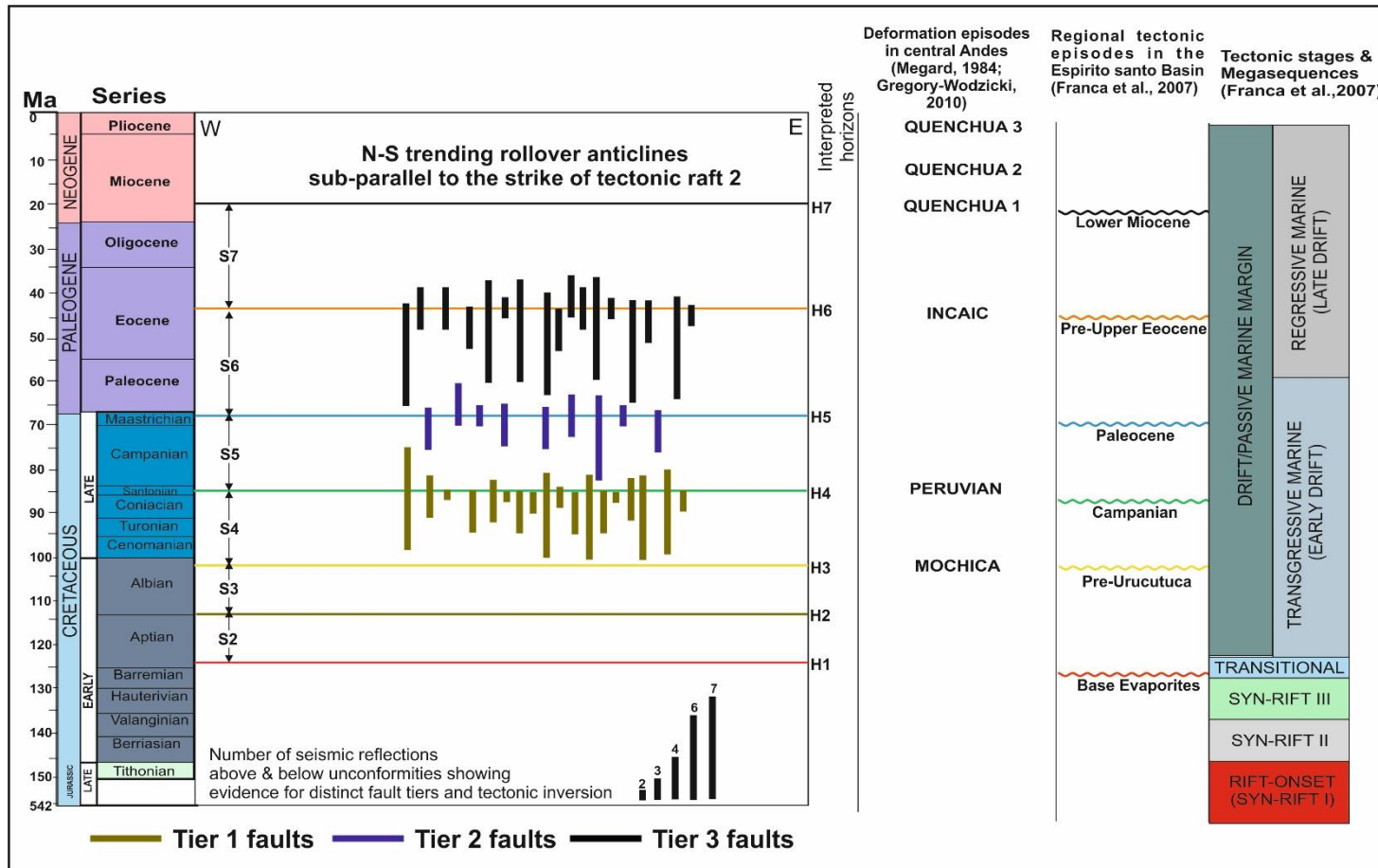
Fig. 4.12. Schematic illustration of the relative age and time-span of distinct fault tiers mapped over a N–S trending rollover anticlines that are sub-parallel to Raft 2. Plotted in the diagram is the number of reflections above and below main unconformities related to regional tectonic episodes in the Espirito Santo basin. Tier 1, 2 and 3 faults dominantly cross-cut Campanian (H4), Paleocene (H5) and Pre-Upper Eocene (H6) unconformities, respectively. S2 to S7 refer to interpreted seismic units.
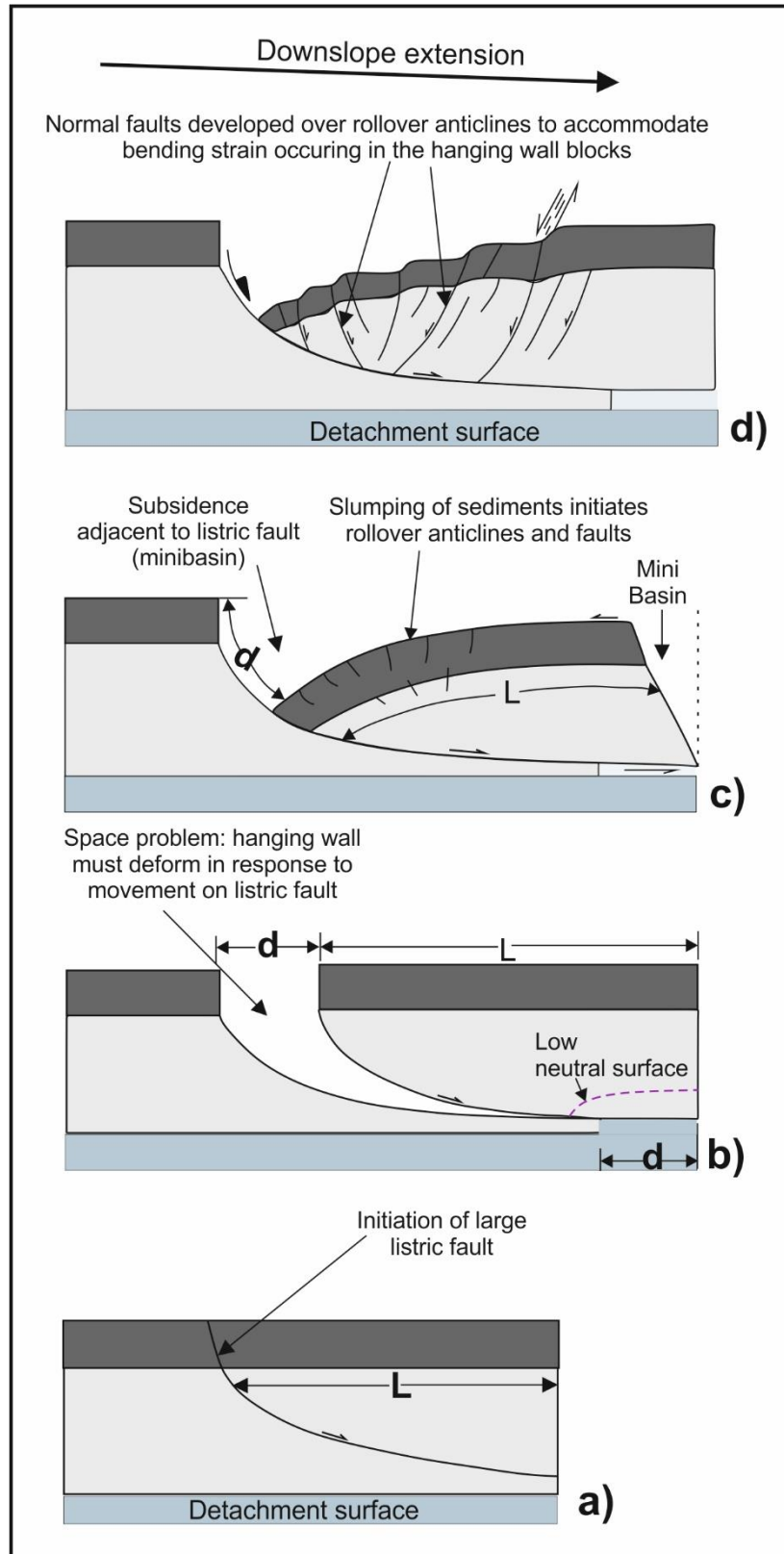
Fig. 4.13. Schematic model for the development of rollover anticlines and associated normal faults.

rollover anticlines, generating three distinct tiers (Figs. 4.3, 4.6, 4.7 and 4.12). Each fault tier has distinct fault spacings, geometries, fault trace shapes and fault strike orientations (Figs. 4.3, 4.6 and 4.7). These fault tiers include; Tiers 1, 2 and 3. Each fault tier geometry is associated with distinct tectonic episodes of gravitational gliding (Fig. 4.14).

Tier 1 faults (Cenomanian to Campanian) comprise closely spaced normal faults that resulted from the outer-arc stretching of the Late Cretaceous strata (Unit S4) overlaying tectonic rafts (Unit S3). These faults accommodate a significant part of the bending strain occurring in the hanging-wall blocks of listric (roller) faults during the initial tectonic stage of gravitational gliding (Fig. 4.14a). The faults are aligned concentrically in front of listric (roller) faults, generating large half-moon structures and curved-polygonal fault patterns over rollover anticlines (Figs. 4.6a and 4.7a). A significant part of these faults overlies tectonic rafts offshore Espírito Santo (Alves, 2012).

Tier 2 faults (Late Santonian to Maastrichtian) comprise closely spaced normal faults with a diverse range of fault strikes that form a rectangular-polygonal pattern over rollover anticlines (Figs. 4.6b and 4.7b). The progressive bending of rollover anticlines above tectonic rafts during the renewed stage of gravitational gliding led to the progressive faulting of the overburden strata by these faults. Tier 2 faults accommodate some of the bending strain and supra-salt extension in overburden strata during the renewed stage of gravitational gliding (Fig. 4.14b).

Tier 3 faults (Paleocene to Eocene) comprise densely spaced set of normal faults with a discrete range of fault strikes revealing an irregular polygonal pattern over rollover anticlines (Figs. 4.6c and 4.7c). Differences in the timing of (diachronous) grounding of tectonic rafts are responsible for the development of these faults, as well as -
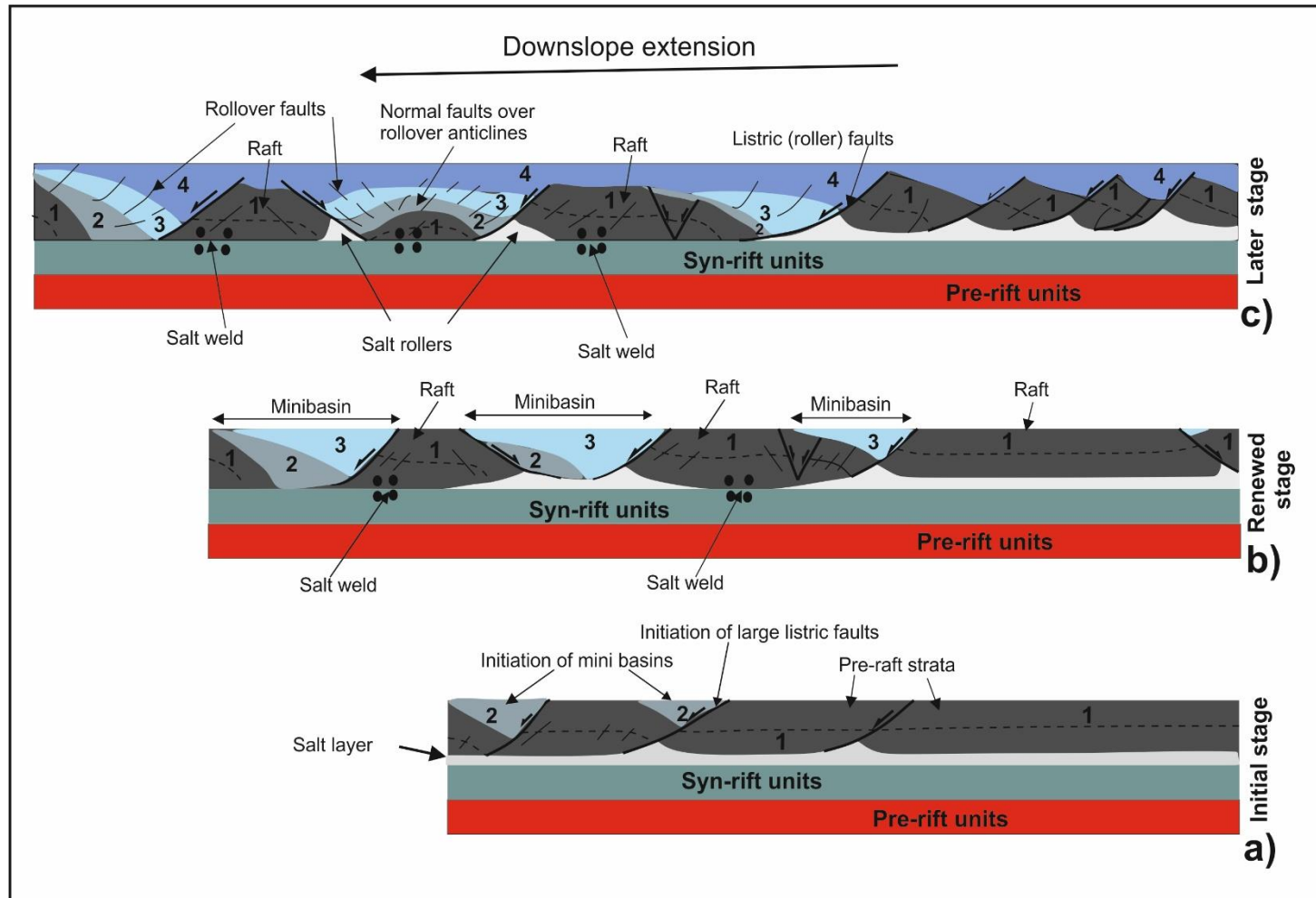
Fig. 4.14. Schematic model explaining the gravitational gliding of tectonic rafts and their relationship with local structures (listric faults, rollover anticlines and normal faults.

reactivated local popup structures and drag folds formed adjacently to roller faults (Fig. 4.3). Tier 3 faults are associated with the later tectonic stages of gravitational gliding in the Espírito Santo Basin (Fig. 4.14c). The geometric variations recognised in the distinct fault tiers, i.e. from curved to rectangular and then irregular polygonal patterns, reflect the effect of distinct episodes of gravitational gliding in the underlying tectonic rafts (Fig. 4.14).

4.8.3. Impact of the gravitational gliding of tectonic rafts on fault reactivation and growth

Fault reactivation has been described as the growth of pre-existing faults by further propagation after a significant period of quiescence (e.g. Cartwright et al., 1995; Baudon and Cartwright, 2008). Two distinct modes of faults reactivation were identified in the study area: segment linkage and upward propagation. Both modes of fault reactivation are recognised by typical stepped profiles in throw gradients. Differences in the throw-distribution provide insights into the recognition of either mode (Figs. 4.8-4.11).

Tier 1, 2 and 3 faults were reactivated by segment linkage, i.e. by fault growth through coalescence of multiple fault segments. This mode of fault reactivation is recognised by a zone of throw maxima that is separated from the pre-existing parts by a zone of throw minima and steepening of the throw gradients (Figs. 4.8-4.10). Their throw-depth plots do not always show single positive gradients and are mostly characterised by throw profiles that resemble C-type or M-type patterns between the upper-tip point and immediate throw minima (Baudon and Cartwright, 2008). These distinct fault tiers are in line with the proposed coherent fault model (e.g., Cartwright et al., 1995) as their preferential mode of growth was in both the vertical and horizontal directions.

The listric (roller) faults that bound the distinct fault tiers were reactivated by upward propagation. This mode of reactivation is recognised by vertical positive steps in throw gradients (Fig. 4.11). The faults are characterised by breaks in throw gradients corresponding to horizons H4 and H5, i.e. the Campanian and Paleocene unconformities (França et al., 2007) (Fig. 4.11a, c). These breaks in throw gradients are attributed to lithological changes during fault propagation through mechanical barriers. Contrasts in impedance above and below these boundaries are enough to cause this type of changes in throw gradients. The significant reduction in fault throws above horizon H4 is due to the presence of weak Turonian to Paleocene shales (Unit S5) above a high impedance (i.e., competent) carbonate platform (Unit S4) (Ojeda, 1982; França et al., 2007). Therefore, abrupt decreases in throw, and the vertical positive steps in throw gradients recorded by the roller faults, can be attributed to be the effects of reactivation by upward propagation from parent faults above a detachment surface, or decollement (Baudon and Cartwright, 2008) (Fig. 4.11).

4.8.4. Tiered faulting vs. discrete tectonic episodes on the southeast Brazilian margin

Early Cretaceous to Pliocene tectonic episodes, i.e. those related to the Andean Orogeny and the emplacement of the Abrolhos Plateau, caused episodic margin uplift and tilting, as reflected by the rise of coastal mountain ranges in the Santonian (Megard, 1984; Megard et al., 1984; Bueno, 2004; Fiduk et al., 2004). These discrete tectonic episodes, which include the Mochica (Late Albian), Peruvian (Late Cretaceous), the Incaic (Eocene) and Quenchua 1 (Early Miocene), Quenchua 2 (Upper Miocene), Quenchua 3 (Pliocene), as well as the emplacement of the Abrolhos Plateau in the Eocene, are the main events that influenced the regional stress regimes in southeast Brazil (Gregory-Wodzicki, 2010; Megard, 1984; Lima, 1999; Cobbold et al., 2007) (Figs. 4.1 and 4.12).

During specific tectonic episodes, sediment progradation was triggered by the uplift of coastal ranges, following the reactivation of segments of the Brazilian margin (Cobbold et al., 2010). Cobbold et al. (2010) argue that because post-rift inversion episodes are synchronous with phases of orogenesis in the Andes, a likely cause of inversion structures offshore Brazil is plate-wide horizontal compression.

In the study area, reactivated structures (pop-up anticlines, drag folds, reactivated faults; Figs. 4.3 and 4.12) formed between horizons H4 (Late Santonian) and H6 (Early Eocene), with the bulk of inversion occurring below horizon H6 (Eocene), i.e. prior to the Incaic tectonic phase (Figs. 4.1 and 4.12). These structures were controlled locally by prolonged overburden faulting, and by the continued movement of deeply buried rafts. In particular, local pop-up structures are, in the study area, invariably associated with laterally shortened anticlines formed upslope or above grounded rafts, or to the flip-flop reactivation of roller faults as thrusts by moving rafts (Alves, 2012) (Fig. 4.3). Thus, grounded rafts acted as hard and soft buttresses during renewed gravity gliding as the margin was uplifted and exhumed. In contrast, downslope moving rafts shortened inter-raft extensional basins as pop-ups. In fact, intra-raft salt structures (rollers) were able to localise strain downdip from rafts, whilst grounded, or slower-moving, rafts acted as buttresses to focus shortening on their updip flanks.

Tectonic tilting and uplift of the margin, and subsequent downslope movement of tectonic rafts, is a possible regional trigger to the reactivation of earlier extensional features as inversion structures for the more recent tectonic phases, i.e. the Incaic (Eocene) and Quenchua 1 (Early Miocene), Quenchua 2 (Upper Miocene) and Quenchua 3 (Pliocene) phases (Demercian et al., 1993; Cobbold et al., 2001). However, tectonic reactivation of tectonic rafts offshore Espírito Santo (Late Cretaceous to

Paleocene) clearly predates the Incaic (Eocene) and Quenchua (Neogene) phases (Figs. 4.1 and 4.12). Alves (2012) postulated that the principal phase of crustal shortening in Espírito Santo Basin reflects the early stages of Andean convergence, i.e. the Mochica (Late Albian) and Peruvian (Late Cretaceous) phases, but that fault and anticline reactivation can be significantly diachronous when considering distinct structures, and zones, of the Espírito Santo Basin.

4.9. Chapter-specific conclusions

The detailed mapping of stratigraphic horizons and faults, statistical analyses of fault displacement using high-quality 3D seismic reflection data from the proximal region of the Espírito Santo Basin, southeast Brazil provided us with important insights into the geometry and growth history of normal faults formed over rollover anticlines. These normal faults were reactivated during gravitational gliding of tectonic rafts. The main conclusions of this chapter are as follows:

1. In the proximal extensional parts of the southeast Brazilian margin, Late Cretaceous to Paleogene gravitational gliding of tectonic rafts, intermittent uplift and tilting of the continental slope during the Andean orogeny, and emplacement of the Abrolhos Plateau, induced a continuum of internal deformation that is expressed in the form of complex structures, including; listric (roller) faults, wide rollover anticlines, closely spaced set of normal faults, reactivated faults and folds, vertical salt diapirs, salt rollers and large blocks of strata (rafts).

2. The Late Cretaceous to Paleogene gravitational gliding of tectonic rafts induced a continuum of supra-salt overburden deformation that organised normal faults over rollover anticlines into three distinct fault geometries; from curved to rectangular

and later irregular polygonal fault patterns. These fault patterns are the result of distinct episodes of gravitational gliding offshore Espírito Santo, meaning that the curved, rectangular, and irregular polygonal fault patterns are related to the initial, renewed, and later stages of gravitational gliding, respectively. The cessation of the gravitational gliding of tectonic rafts depended on the complete grounding of rafts above sub-salt strata, or the gravitational stabilisation of rafts imposed by sediment loading and cessation of tectonic uplift (and tilting) of the continental slope.

3. The downslope translation and grounding (welding) of tectonic rafts on sub-salt strata controlled the degree of overburden deformation. Thus, enhanced fault reactivation relates to the degree of welding between sub- and supra-salt strata, which potentially promotes the migration of hydrocarbons from sub-salt source units into supra-salt reservoirs.

4. The rollover geometry over tectonic rafts is the inevitable result of the propagation of listric (roller) faults. Movement on such a curved fault plane will tend to generate a 'gap' between the hanging-wall and footwall, which will be accommodated by the collapse of the hanging-wall in either a ductile or brittle manner.

5. The interpreted fault tiers were reactivated, and their growth is characterised by segment linkage i.e. fault growth through the coalescence of multiple fault segments. The roller (listric) faults that bound the rollover anticlines were reactivated by upward propagation from parent faults above a detachment surface, i.e. the Aptian salt.

CHAPTER 5

Effect of tectonic inversion on supra-salt fault geometry and reactivation histories in the Southern North Sea

Co-author contributions to the paper:

Tiago Alves (Supervisor): checked for grammatical errors, ensured the scientific content and interpretation was accurate and appropriately presented.

5. Effect of tectonic inversion on supra-salt fault geometry and reactivation histories

5.1. Abstract

High-resolution 3D seismic and borehole data in the Broad Fourteens Basin, Southern North Sea, were used to investigate the relationship between lithology and fault throw distribution, as well as to discern the reactivation and growth histories of faults developed due to tectonic inversion. Two (2) distinct tiers of faults were identified, and their geometry analysed in detail. Tier 1 faults comprise closely spaced set of normal faults that resulted from the progressive buckling and stretching of Upper Mesozoic strata during Late Cretaceous to Paleogene tectonic inversion. They have been reactivated but still show net normal throw separations, even though they formed during a period of regional compression. Tier 2 faults comprise densely spaced set of normal faults in Paleogene strata with a discrete range of strikes forming a polygonal pattern. These faults relate to early diagenesis but still record the effect of the Paleogene inversion episode. Tier 1 faults are highly segmented and show differences in throw distribution between shale-rich and sandy intervals. The faults are more segmented with relatively smaller throw maxima of 14 ms (17.7 m) in shale-rich intervals, while sandy intervals are less segmented with larger throw maxima of 32 ms (40.3 m). Discrepancies in fault throw distribution and segmentation increase the chances of compartmentalisation or localised fluid flow through fault linkages presenting, at the same time, significant risks when injecting CO_2 in subsurface traps. Recognising the effect of tectonic inversion on supra-salt fault geometry, and reactivation histories, can be crucial to the characterisation of faulted hydrocarbon and carbon capture and storage (CCS) reservoirs in tectonically inverted basins such as the Southern North Sea.

5.2. Introduction

In layered successions, the mechanical stratigraphy of the host rock affects the nucleation, segmentation, geometry and the displacement distribution of tectonic faults (Peacock and Sanderson, 1991; Mansfield and Cartwright, 1996; Gross et al. 1997; Childs et al. 2009; Gabrielsen et al., 2016; Ferrill et al. 2017). This means that faults tend to localise (and be less segmented) in the harder lithologies such as limestones and sandstones, while becoming more widely distributed (and segmented) in weaker lithologies such as claystones and shales (Schöpfer et al., 2006; Libak et al., 2019). In parallel, analogue deformation experiments show that weak intervals can act as detachments that cause stress decoupling at a local scale, preventing the propagation of faults across specific intervals. This results in a preferable horizontal propagation of faults to the detriment of their vertical growth (Bahroudi et al., 2003; Withjack and Callaway 2000; Richardson et al., 2005; Gabrielsen et al., 2016). Such a horizontal shift in fault geometry across an incompetent layer can result in vertical fault segmentation whereby fault segments are hard- or soft-linked (Bahroudi et al. 2003; Mansfield and Cartwright, 1996; Maunde et al., 2021).

Late Cretaceous to Paleogene tectonic inversion in the Broad Fourteens Basin, Southern North Sea, contributed to the formation and reactivation of normal faults in supra-salt overburden rocks (Oudmayer and De Jager, 1993; Nalpas et al., 1995; Gerling et al., 1999; Wong et al., 2001; van Verweij and Simmelink, 2002; De Lugt et al., 2003; 2002; Duin et al., 2006). Broad anticlines presenting with outer-arc normal faults were formed in response to the Alpine inversion episodes affecting this part of NW Europe: the Sub-Hercynian, Laramide, Pyrenean and Savian tectonic episodes. This had mostly positive economic impacts, as tectonic movements reactivated older faults and allowed the secondary migration of hydrocarbons into shallower reservoir units (Van Balen et al.,

2000; Isaksen, 2004). Nevertheless, to understand the effect of tectonic inversion on the geometry and reactivation histories of faults in the Southern North Sea is key, as these structures add structural complexity and heterogeneity to supra-salt reservoir units Active fracturing provides a pathway for fluids where distinct fault segments interact, with the loci of fault segment linkage across seal units increasing the permeability of host rocks, thus allowing the migration of fluid out of underlying reservoirs (Curewitz and Karson, 1997; Knai and Knipe 1998). Conversely, faults can compartmentalise reservoir units when they form barriers to fluid flow, a character resulting in increasing exploration costs as more wells are needed to retrieve hydrocarbons, or sequestrate CO_2 and other gases (Hardman and Booth, 1991; Caine et al. 1996; Cartwright et al., 2007; Bentham et al., 2013).

Using 3D seismic and well data, this chapter explores the relationship amongst lithology, displacement distribution and the reactivation histories of Upper Mesozoic supra-salt faults in the Broad Fourteens Basin, Southern North Sea (Fig. 2.4). The aims of this chapter relate to the fact that hydrocarbon traps are much more likely to leak during periods of fault reactivation than when the faults are inactive, all other parameters of seal integrity being the same (Caine et al. 1996; Hooper, 1991; Gartrell et al., 2002; Wiprut and Zoback, 2000, 2002; Cartwright et al., 2007; Bentham et al., 2013; Ward et al., 2016). Hence, this work aims to address the following questions:

a) What are the geometry and reactivation styles of faults developing due to tectonic shortening?

b) What mode(s) of fault propagation and growth are observed in successions presenting differing lithologies?

c) What are the effects on reservoirs and seal intervals of faults reactivating during tectonic shortening?

5.3. Chapter-specific dataset and methods

5.3.1. Data

Three-dimensional (3D) seismic and borehole data from the Broad Fourteens Basin, Southern North Sea, are used in this work. The data were acquired in the northern end of the Broad Fourteens Basin, offshore The Netherlands, between 53.1º - 53.3ºN and 3.8º - 4.2ºE. The interpreted seismic volume covers an approximated area of about 845 km^2 at a shallow water depth of 37.7 m (Fig. 2.4).

The seismic data are stacked with a 2 ms vertical sampling interval, and a 25 x 25 m bin size, providing a maximum horizontal resolution of 25 m. The seismic volume is zero-phase time migrated and displayed with a normal positive polarity so that an increase in acoustic impedance is represented by a peak (red seismic reflection). A decrease in acoustic impedance is represented by a trough, i.e. a black seismic reflection (SEG European Convention; Brown, 2003). The vertical scale of the seismic data is in two-way travel time (TWTT), up to a recording length of about 4.0 seconds.

5.3.2. Methods

Seismic horizons and faults were mapped using Schlumberger's Petrel®. First, seven seismic units (Units S1 to S7) bounded by Upper Carboniferous to Miocene unconformities were mapped and tied them to well stratigraphic information published in Penge et al. (1999) and van Verweij and Simmelink (2002) (Fig. 5.3). Interpreted Listric faults and two distinct tiers of normal faults were then imaged and interpreted in Mesozoic to Paleogene strata. Throw data (T) for these interpreted faults were acquired by measuring differences between footwall and hanging-wall horizon cut-offs (Fig. 5.2a). These measurements were taken along the fault planes on seismic profiles

perpendicular and oblique to local fault strike, i.e. bearing in mind local changes in fault geometry and strike.

Two-dimensional (2D) contour maps and throw-depth (T-Z) profiles were produced to assess the reactivation and vertical growth styles of faults. From the 2D contour maps, throw-distance (T-X) profiles were produced to assess fault growth histories and the role of lithology on fault throw distribution. The measured fault throw values were depth converted from seconds to meters using Equation (5.1) below.

$$V = \frac{2Z}{T} \hspace{5cm} \text{Equation 5.1}$$

where (V) is the interval or average velocity in m/s, (Z) is the depth in meters, and (T) is the two-way travel time in seconds, gathered from borehole data.

The vertical seismic resolution for the target intervals in Upper Mesozoic strata is 15.8 m, based on a dominant frequency of 40 Hz and an average velocity of 2521.3 m/s. As fault-throw measurements depend on the vertical sampling interval, rather than the vertical seismic resolution (Tao and Alves, 2019), the minimum fault offset resolved on-screen during fault throw analysis varies from 2 ms (1.9 m) to 3.0 ms (3.8 m). However, uncertainty in the positions of stratal terminations does introduce a minimal error associated with the position in depth of the recorded fault throws (Fig. 5.2). This is a function of the frequency content of the seismic dataset (Mansfield and Cartwright, 1996). Errors associated with spurious velocity estimates may also affect the throw values when converted to meters. These limitations will affect the absolute value of estimated fault throws.
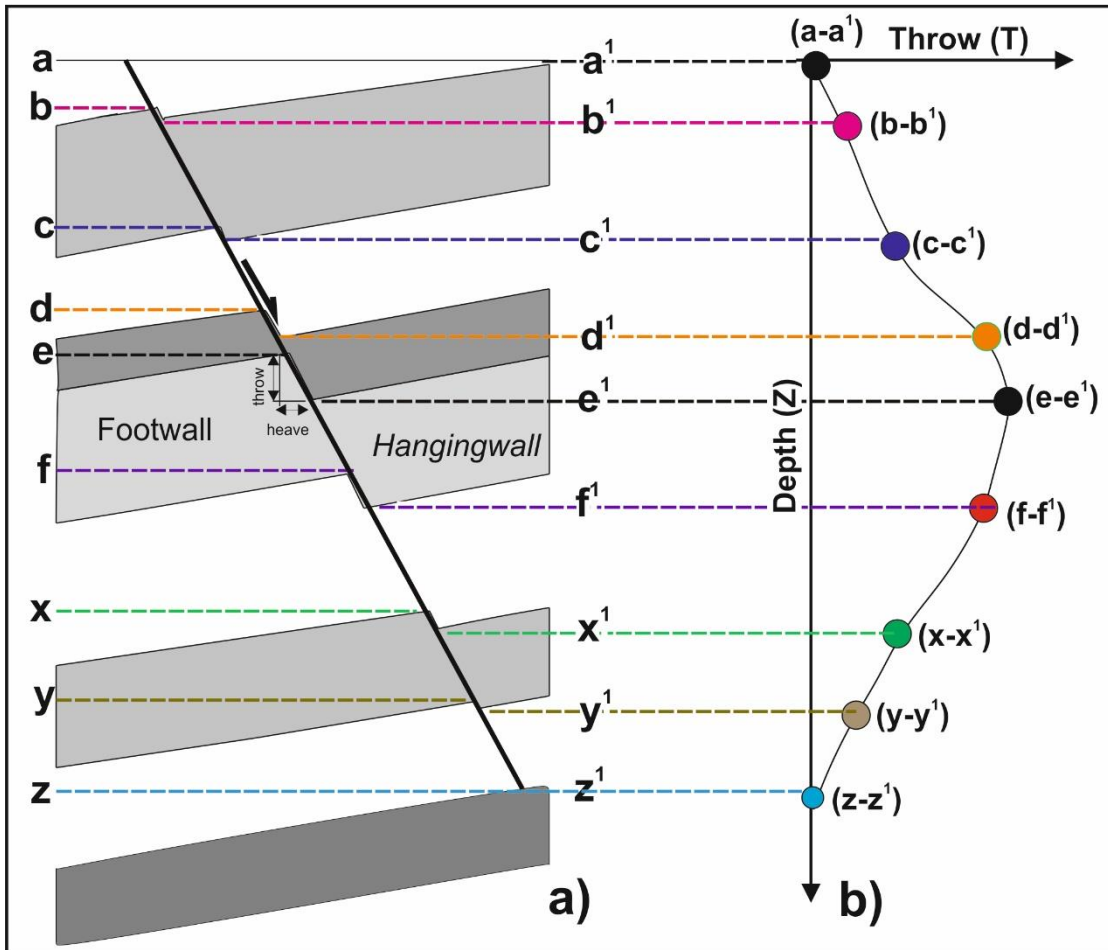
Fig. 5.2. Schematic cross-section through a simple normal fault showing the points of fault throw-depth (T-Z) measurements (a) and their corresponding throw-depth (T-Z) plots (b). Fault segment with local throw maximum in the throw-depth plot represents the interval where fault nucleate first. This segment propagates outwards until it encountered other pre-existing fault segments to link together.

Throw-depth (T-Z) profiles can offer information on multiple parameters such as fault nucleation, growth, segmentation, linkage of individual faults, and rock competence (Baudon and Cartwright, 2008; Peacock and Sanderson, 1991; Maunde et al., 2021). Discrepancies in throw gradients often result from mechanical heterogeneities, fault reactivation and fault segmentation (Childs et al., 1996; Baudon and Cartwright, 2008; Laubach et al., 2009). Therefore, analysis of the throw-depth (T-Z) profiles aimed to identify fault throw anomalies which will, in this chapter, be linked to rock properties and mechanical stratigraphy and their impact on fault segmentation.

5.4. Geological and seismic-stratigraphic settings

The Broad Fourteens Basin, part of the larger South Permian Basin, records a complex history of rifting, halokinesis and tectonic inversion (Duin et al., 2006; Nalpas et al., 1995; Van Wijhe, 1987; Verweij and Simmelink, 2002; Ziegler, 1990). The basin contains Upper Paleozoic and Mesozoic strata overlain by Cenozoic siliciclastics (Van Wijhe, 1987; Van Adrichem Boogaert and Kouwe, 1993; Gerling et al., 1999; van Verweij and Simmelink, 2002). Structural styles in the Broad Fourteens Basin are dominated by normal faulting, which reflects the predominance of an extensional regime since Late Paleozoic times (Fig. 5.4). Minor reverse structures are observed locally along major normal fault families (Alves and Elliott, 2014) (Fig. 5.4).

5.4.1. Upper Paleozoic

Towards the end of the Carboniferous a large foreland basin, the Variscan Foreland Basin, was formed in the Southern North Sea (Duin et al., 2006; Oudmayer and De Jager, 1993; Van Wijhe, 1987; Ziegler, 1990). Thick lacustrine and deltaic intervals with interbedded coal seams were deposited at this time as part of the Limburg Group

(Fig. 5.3). Included in this latter unit are the Westphalian Coal Measures, a major source of gas in the Southern North Sea (Gerling et al., 1999; Van Wijhe, 1987). Oblique-slip normal faulting predominated after the Variscan Orogeny, with the largest faults cutting through the Variscan fold belt and propagating along older NW-SE trending basement faults. The present-day structural grain of the Southern North Sea follows horst-and-graben structures bounded by the latter basement faults (Duin et al., 2006; Oudmayer and De Jager, 1993; Van Wijhe, 1987; Ziegler, 1990).

Sedimentation in the Permian was interrupted by thermal upwelling induced by doleritic magma, which intruded the basement through oblique-slip dextral normal faults. This hiatus is expressed in the form of a Saalian unconformity separating Lower from Upper Rotliegend strata (Van Wees et al., 2000) (Fig. 5.3). Subsidence was resumed in the Late Permian and, consequently, the South Permian Basin became at this time separated from the North Permian Basin by the Mid North Sea High (Duin et al., 2006). In the chapter study area, Upper Rotliegend terrestrial sandstones of the Slochteren Formation were deposited above the Saalian unconformity to become the major reservoir interval for Permian gas plays (Verweij and Simmelink, 2002) (Fig. 5.3).

The Zechstein Sea subsequently flooded the Broad Fourteens Basin in the Late Permian, depositing a thick interval of salt and relatively thin carbonate stringers (van Verweij and Simmelink, 2002; Strozyk et al., 2012) (Unit S2 in Figs. 5.3, 5.4 and 5.5). Zechstein salt caps Upper Rotliegend continental sandstones (Unit S1) and forms an effective seal rock for Permian (and older) strata (Coward, 1995). In the interpreted seismic volume, a high-amplitude seismic reflection separates the Zechstein Group (Unit S2) from the Upper Rotliegend reservoirs in Unit S1 (Figs. 5.4 to 5.6; Table 5.1).
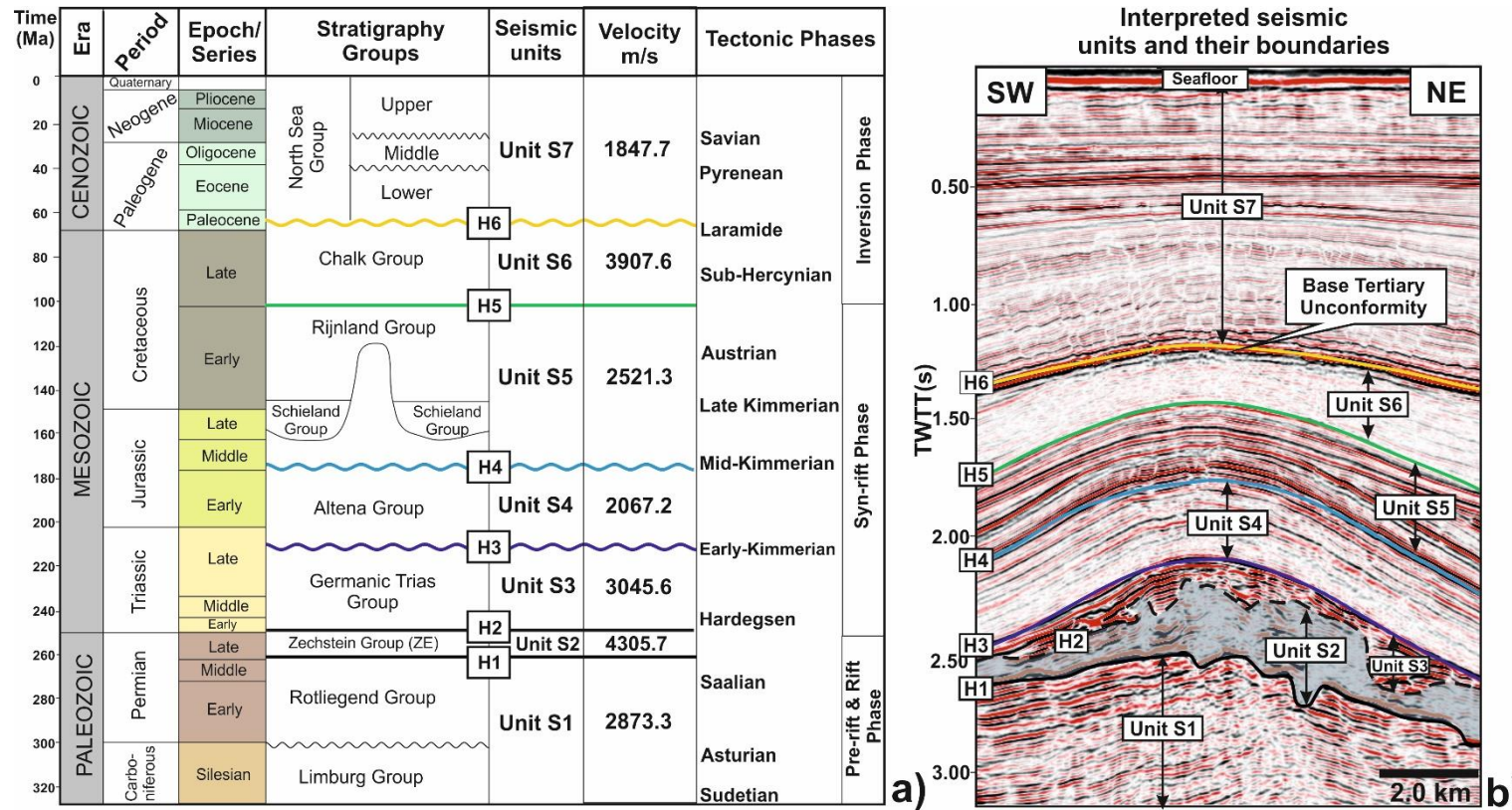
Fig. 5.3. Simplified seismic-stratigraphic correlation between the interpreted seismic units and stratigraphic column of the Dutch Sector of the Southern North Sea. Main stratigraphic groups, tectonic phases and unconformities related to regional tectonic events are based on Penge et al. (1999) and van Verweij and Simmelink (2002). Horizons H1-H6, and Units S1-S7 refer to interpreted seismic horizons and units, respectively.

5.4.2. Mesozoic

Continental rifting intensified during the Mesozoic, allowing for differential subsidence to predominate in the Southern North Sea (Alves and Elliott, 2014; Duin et al., 2006) (Fig. 5.4). In a rapidly subsiding Broad Fourteens Basin, aeolian sands and lacustrine claystones from the Lower and Upper Germanic Trias Group (Unit S3; Fig. 5.3) were conformably deposited above the Zechstein salt (Van Hulten, 2010). In seismic data, the bright reflection at the base of Germanic Trias Group correlates with a change from the high-velocity Zechstein salt (Unit S2) to the relatively low-velocity aeolian sandstones and lacustrine claystones of the Lower Germanic Trias Group in Unit S3 (Figs. 5.4 and 5.5; Table 5.1). In the chapter study area, the Germanic Trias Group (Unit S3) comprises a package with moderate frequency and moderate to high-amplitude seismic reflections (Figs. 5.4 and 5.6). Aeolian sands and lacustrine claystones of the Lower Germanic Trias Group (Buntsandstein Formation) are a prolific gas reservoir, particularly where Zechstein salt (Unit S2) has been withdrawn and welds have formed between Triassic strata (Unit S3) and the Rotliegend Group in Unit S1 (Van Hulten, 2010).

Towards the end of the Triassic, salt tectonics and reactive diapirism became concentrated along extensional boundary faults (Stewart and Coward, 1995; Ziegler, 1992). Rift-raft tectonics led to the further deepening of the Broad Fourteens Basin and the establishment of open marine conditions (Alves and Elliott, 2014; Penge et al., 1993). As a result, the deep-water Altena Shales (Unit S4) were deposited unconformably above the Germanic Trias Group, with the more bituminous Posidonia Shale Formation comprising the source interval for Jurassic oil plays following the marked segmentation of the Southern North Sea in confined sub-basins (Duin et al., 2006; Nalpas et al., 1995) (Fig. 5.3). The Altena Shales (Unit S4) comprise argillaceous

deposits, calcareous and clastic sediments (van Verweij and Simmelink, 2002), and comprise a package of high frequency, continuous and moderate to high-amplitude reflections in seismic data (Figs. 5.4 and 5.6; Table 5.1).

Deposition of the Altena Shales stopped in the Middle Jurassic during the Mid-Kimmerian upwarping tectonic event (Fig. 5.3). This upwarping event is a product of salt tectonism, reactive diapirism and thermal upwelling from dolerite intrusions (Van Wees et al., 2000), which occurred in association with the Jurassic Kimmerian tectonic phase (Fig. 5.3). In areas with the greater uplift, up to 1500 m of Jurassic strata may have been eroded (Heim et al., 2013). Despite this latter uplift event, continuing NE-SW oriented extension compartmentalised the Broad Fourteens Basin, imposing its present-day NW-SE trend (Fig. 2.4). Local erosion of Triassic, Zechstein and Rotliegend sequences above active structural highs generated thick successions of the Delfland Subgroup and Vlieland Sandstone, depositing reservoir and seal intervals for oil that was later sourced from the Posidonia Shales (Van Wijhe, 1987; Verweij and Simmelink, 2002; Duin et al., 2006).

The Rijnland Group (Unit S5) comprises coarse clastic intercalations, carbonaceous claystones and interbedded sandstones, and was deposited conformably above the Schieland Group (van Verweij and Simmelink, 2002; Van Adrichem Boogaert and Kouwe, 1993) (Fig. 5.3). Unit S5 is bounded at the top by the Base Tertiary Unconformity (H6), at which level maximum erosion takes place at the crest of a Late Cretaceous anticline (Figs. 5.4 and 5.6). In seismic data, Unit S5 forms a package of high-amplitude, high-frequency seismic reflections, deformed locally by closely-spaced normal faults (Figs. 5.4 and 5.6; Table 5.1).
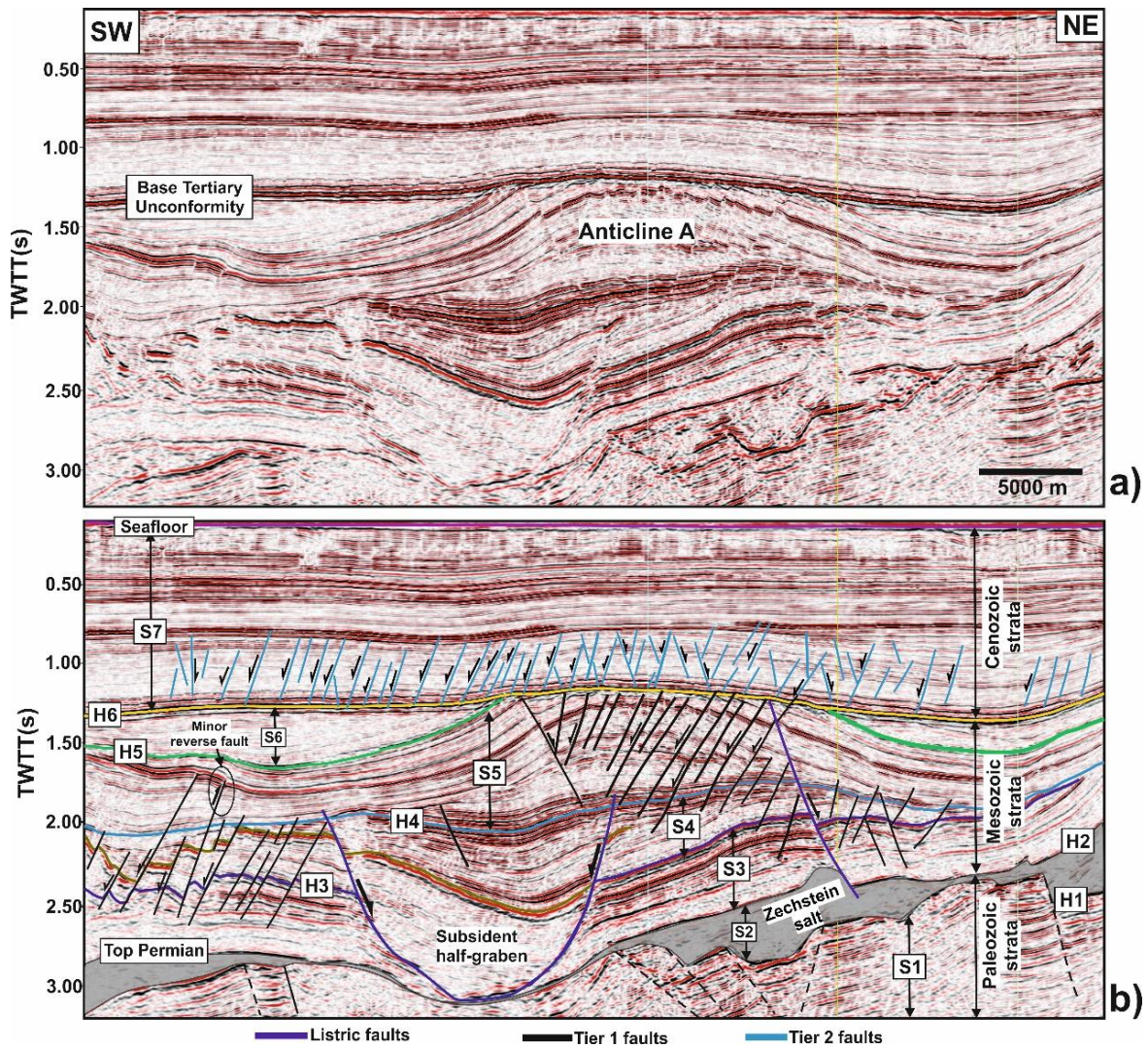
Fig. 5.4. a) Uninterpreted and b) interpreted seismic profiles revealing the distinct geometry of Upper Mesozoic (Tier 1) and Paleogene (Tier 2) faults over Anticline A. These fault Tiers are separated by the Base Tertiary Unconformity (horizons H6). Tier 1 faults responded to Late Cretaceous to Paleogene tectonic inversion episodes, whereas Tier 2 faults resulted from near-seafloor extension over growing anticlines to sudden compaction of mud-rich strata and subsequent loss of volume and fluid, forming polygonal fault geometries. The location of the seismic line is shown in Figs. 5.10a, 5.11a and 5.12a.

The Late Cretaceous records a major episode of sea-level rise, accompanied by post-rift subsidence, and led to the accumulation of the Chalk Group (Van Wijhe, 1987; Verweij and Simmelink, 2002) (Fig. 5.3). This group (Unit S6) comprises limestones, marls, calcareous claystones and glauconitic sands deposited conformably above the Rijnland Group (van Verweij and Simmelink, 2002) (Figs. 5.3 and 5.5). The onset of Alpine compression in the Late Cretaceous interrupted regional subsidence in the Broad Fourteens Basin, with the so called Sub-Hercynian tectonic phase reactivating Variscan faults with a reverse-dextral motion (De Lugt et al., 2003; Nalpas et al., 1995). Maximum erosion of ~ 700 m of strata occurred in the centre of the basin, close to the axis of inversion, herein named Anticline A, affecting the overall thickness of the Chalk Group (Nalpas et al., 1995; De Lugt et al., 2003) (Figs. 5.4 and 5.6). Later, the Laramide inversion event in the early Paleocene created a prominent Cretaceous-Tertiary boundary (H6) at the top of Chalk Group (Oudmayer and De Jager, 1993; De Lugt et al., 2003) (Figs. 5.4 and 5.6). In such a setting, the localisation of a salt (Zechstein) décollement layer to the North of the Broad Fourteens Basin accounts for the lack of connectivity between sub-salt and supra-salt faults (Van Wijhe, 1987).

5.4.3. Cenozoic

Cenozoic strata comprise sandstones, clays, silts, locally gravel or peat, and brown coal seams that are part of the North Sea Group, interpreted as Unit S7 in the seismic volume (van Verweij and Simmelink, 2002; Van Adrichem Boogaert and Kouwe, 1993). The North Sea Group directly overlies the Chalk Group (Fig. 5.5). Where maximum erosion took place around the hinge region of the Late Cretaceous Anticline A, the base of Cenozoic strata directly overlies the Rijnland Group (Unit S5; Figs. 5.4 and 5.6).

Table 5.1: Summary of principal features in the seismostratigraphic units of the Broad Fourteens Basin, Southern North Sea.

Seismic units	Stratigraphic Groups	Age of seismic units	Estimated Thickness (m)	Internal character of seismic units	Dominant lithologies (van Verweij and Simmelink, 2002)
Unit S7	North Sea Group	Paleocene to Recent	1,201	Characterised by a package of high-frequency, continuous and moderate to high-amplitude seismic reflections. Deformed by closely spaced polygonal normal faults.	Clays, sandstones, silts, locally gravel or peat, and brown coal seams.
Unit S6	Chalk Group	Late Cretaceous	684	Low amplitude and chaotic internal reflections. Erosion during the Laramide inversion event created a prominent Cretaceous-Tertiary boundary at the top of Chalk Group (H6). This boundary generated a strong, regionally mappable seismic reflector.	Limestones, marls, calcareous claystones and glauconitic sands
Unit S5	Rijnland and Schieland Groups	Late Jurassic to Early Cretaceous	505	Forms a package of high-amplitude, high-frequency seismic reflections. Deformed locally by closely-spaced normal faults around the hinge region of Anticline A.	Carbonaceous claystones, marls and thick-bedded sandstones
Unit S4	Altena Group	Late Triassic to Middle Jurassic	259	Forms a package of high frequency, continuous and moderate to high-amplitude seismic reflections.	Argillaceous deposits, calcareous and clastic sediments. Bituminous Posidonia Shale Formation comprise the source interval for Jurassic oil plays
Unit S3	Germanic Trias Group	Early to Late Triassic	335	Forms a package with moderate frequency and moderate to high-amplitude seismic reflections. On seismic profiles, the bright reflection at the base of Germanic Trias Group (Unit S3) indicates a change from the high-velocity Zechstein salt (Unit S2) to the relatively low-velocity aeolian sandstones and lacustrine claystones of the Lower Germanic Trias Group.	Marine carbonates, evaporites. aeolian sands and lacustrine claystones. Aeolian sands and lacustrine claystones of the Lower Germanic Trias Group (the Buntsandstein Formation) form a prolific gas reservoir in the study area, particularly where Zechstein salt (Unit S2) has been withdrawn and welds have formed between Triassic (Unit S3) and the Rotliegend Group (Unit S1).
Unit S2	Zechstein Group	Late Permian	668	Low amplitude, chaotic internal reflections. The bright reflection at the top (H2) indicates a change from high-velocity Zechstein salt to relatively low-velocity aeolian sandstones and lacustrine claystones.	Thick layers of salt separated by cyclic carbonate intervals. Some of which are fragmented and deformed ('Stringers')
Unit S1	Rotliegend and Limburg Groups	Early to Middle Permian	690	Forms a package of moderate frequency and moderate amplitude seismic reflections. The base of the unit is hard to identify because the overlying salt dims the internal reflections of Rotliegend strata.	Terrestrial coarse-grained sandstones (e.g. Slochteren Formation) and finer grained desert lake deposits (e.g. Silverpit Formation). Thick lacustrine and deltaic intervals with interbedded coal seams were deposited as part of the Limburg Group. Westphalian Coal Measures.

Unit S7 is characterised by a package of high-frequency, continuous and moderate to high-amplitude seismic reflections (Figs. 5.3 to 5.5; Table 5.1).

Three (3) inversion episodes affected the Broad Fourteens Basin in the Cenozoic – the Laramide, Pyrenean and Savian episodes (Fig. 5.3). The Laramide inversion (early Paleocene) reactivated Sub-Hercynian faults and created a prominent Base Tertiary Unconformity (De Lugt et al., 2003; Oudmayer and De Jager, 1993) (Horizon H6; Figs. 5.3 to 5.9). The Pyrenean inversion (Oligocene) created another unconformity at the base of the Miocene strata, separating the Lower from the Middle North Sea Group (Oudmayer and De Jager, 1993; Wong et al., 2001; Verweij and Simmelink, 2002) (Fig. 5.3). The boundary between the Middle and Upper North Sea Groups (Savian unconformity) marks a break in sedimentation that resulted from regional uplift during the Alpine Orogeny and a global sea-level lowstand (Oudmayer and De Jager, 1993; Wong et al., 2001) (Fig. 5.3).

5.5. Principal fault geometries

The seismic data show Upper Mesozoic to Paleogene strata offset by deeply-rooted listric faults, and deformed by broad anticlines associated with normal faults (Figs. 5.4 to 5.6). The TWTT structural maps in Figs. 5.10 to 5.12 highlight the main structures interpreted in the chapter study area.

5.5.1. Listric faults

In the interpreted dataset, listric faults are detached in the Zechstein salt (Unit S2) and accommodated the gravitational gliding of the overburden strata.
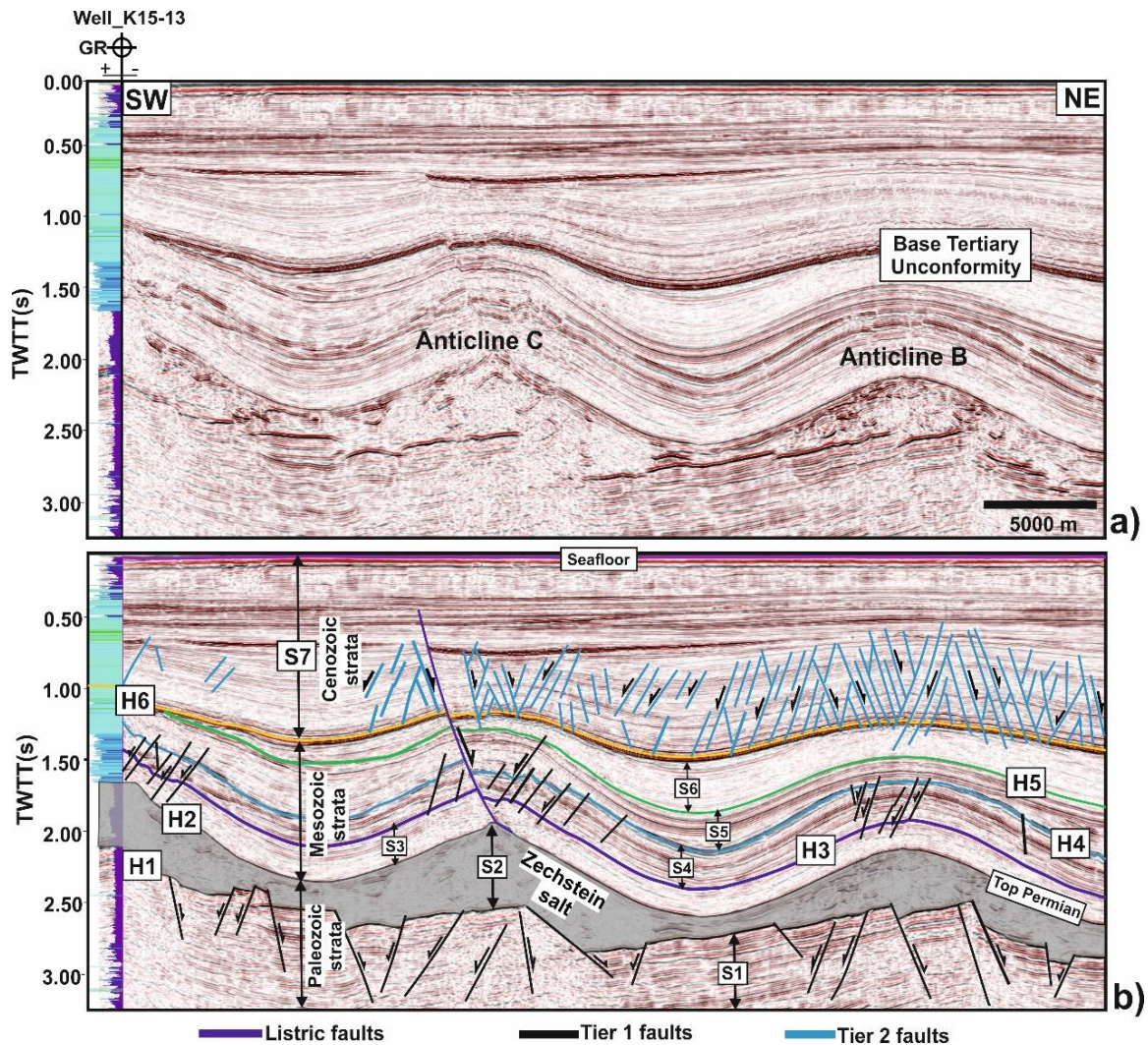
Fig. 5.5. a) Uninterpreted and b) interpreted seismic profiles showing the distinct geometry of Late Mesozoic (Tier 1) and Paleogene (Tier 2) faults over Anticlines B and C. These two fault tiers are separated by the Base Tertiary Unconformity (horizon H6). However, some of the Tier 2 faults propagate downward and offset horizon H6. The location of the seismic line is shown in Figs. 5.10a, 5.11a and 5.12a.

At the same time, significant subsidence occurred in adjacent hanging-wall blocks (Penge et al., 1999; Alves, 2012; Alves and Elliott, 2014) (Figs. 5.4, 5.5 and 5.8). Variations in thickness between the footwall and the hanging-wall blocks of listric faults reveal they are syn-sedimentary growth faults propagating upwards from the Zechstein salt (Unit S2; Figs. 5.4 to 5.6).

Listric faults offset Units S3, S4 and S5 (Lower and Middle Mesozoic strata), with some propagating vertically into Paleogene strata in Unit S7 (Figs. 5.5 and 5.8). They are characterised by a broadly spaced curvilinear pattern in map view, striking in a NW-SE direction that is sub-parallel to the trend of Anticline A (Figs. 5.10b and 5.12). Listric faults show trace lengths of 7.2-13.5 km, with a maximum fault throw of 440 m (Figs. 5.4, 5.8 and 5.12).

5.5.2. Tiers of normal faults

Normal faults are closely-spaced in Upper Mesozoic and Paleogene strata (Figs. 5.4 to 5.6). In this chapter, normal faults are grouped into two distinct tiers: Tier 1 (Upper Mesozoic) and Tier 2 (Paleogene). In the interpreted dataset, periods of fault reactivation below and above the Base Tertiary Unconformity (horizon H6) can be relatively dated. Horizon (H6) forms a high-amplitude, regionally mappable seismic reflector and represents a major change in from the soft Paleogene Lower North Sea clays and silts above (Unit S7) to the harder limestones of the Chalk Group below (Unit S6; Figs. 5.3 to 5.5 and 5.12).

5.5.2.1. Tier 1 faults: Late Mesozoic

Tier 1 faults comprise closely spaced normal faults formed around the hinge of Anticline A (Figs. 5.4 and 5.6). These faults predominantly offset Upper Mesozoic strata in Units S5 and S6 (Figs. 5.4 and 5.6).
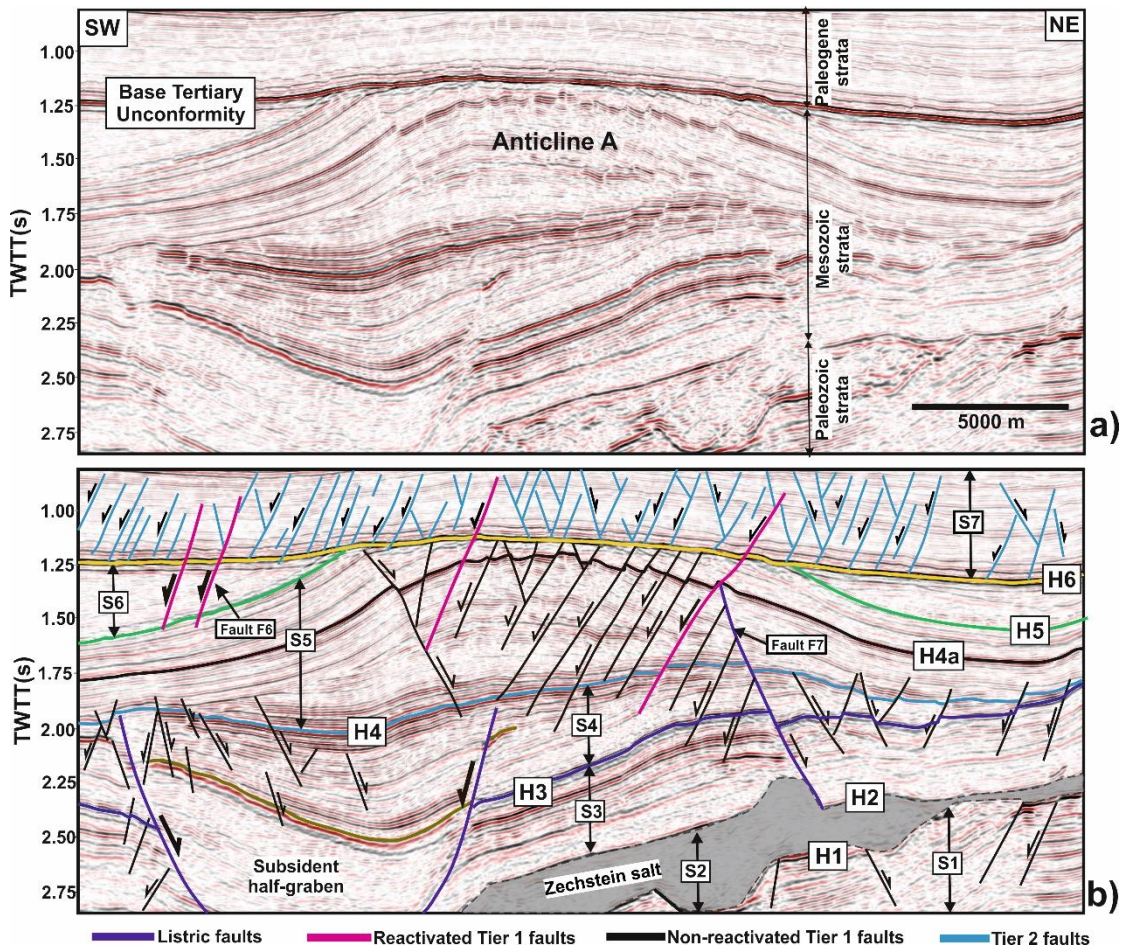
Fig. 5.6. a) Uninterpreted and b) interpreted seismic profiles revealing the geometry of Upper Mesozoic (Tier 1) and Paleogene (Tier 2) faults over Anticline A. Tier 1 faults were generated by the local buckling and stretching of the anticline's outer-arc strata during the Late Cretaceous-Paleogene tectonic inversion episodes. These faults were eroded and truncated at the Base of Tertiary Unconformity (horizon H6), with some reactivating upward into Paleogene strata (Unit S7), linking with the overlaying Paleogene Tier 2 faults. The location of the seismic line is shown in Figs. 5.10a, 5.11a and 5.12a.

The upper tip of Tier 1 faults are eroded and truncated by the Base Tertiary Unconformity (horizon H6), with some faults reactivating and extending into Paleogene strata (Figs. 5.6 to 5.8). The location of Tier 1 faults around the hinge of Anticline A suggests they are created by outer-arc stretching during buckling and, thus, do not normally accommodate regional extension (see Rowan et al., 1999) (Figs. 5.4 and 5.6). Tier 1 faults are grouped into non-reactivated (eroded) and reactivated faults based on their upper tip terminations, as revealed by the seismic sections and throw-depth (T-Z) profiles in Figs. 5.6, 5.13 and 5.14.

5.5.2.1.1. Non-reactivated (eroded) Tier 1 faults

Non-reactivated Tier 1 faults are restricted to the hinge of Anticline A (Figs. 5.6, 5.13 and 5.14). Their upper tip lines are eroded and truncated at the Base Tertiary Unconformity (horizon H6), without faults propagating upwards into Paleogene strata (Figs. 5.13 and 5.14). The relatively large throw values recorded just below horizon H6 confirm the erosion of their upper tips (Figs. 5.15 to 5.17), suggesting that these faults were active, and offsetting Unit S6, before the erosional event responsible for the Base Tertiary Unconformity (Figs. 5.3 and 5.6).

Non-reactivated Tier 1 faults are characterised by their closely spaced, linear to curvilinear conjugate pattern and strike predominantly in a NW-SE direction, roughly parallel to the strike of Anticline A (Fig. 5.10). Thus, their plan-view geometry is controlled by this latter structure (Fig. 5.10b). Non-reactivated Tier 1 faults show a maximum throw of 34.5 m, a spacing ranging from 560 to 2,300 m, and trace lengths of 1,100-11,250 m (Fig. 5.10).
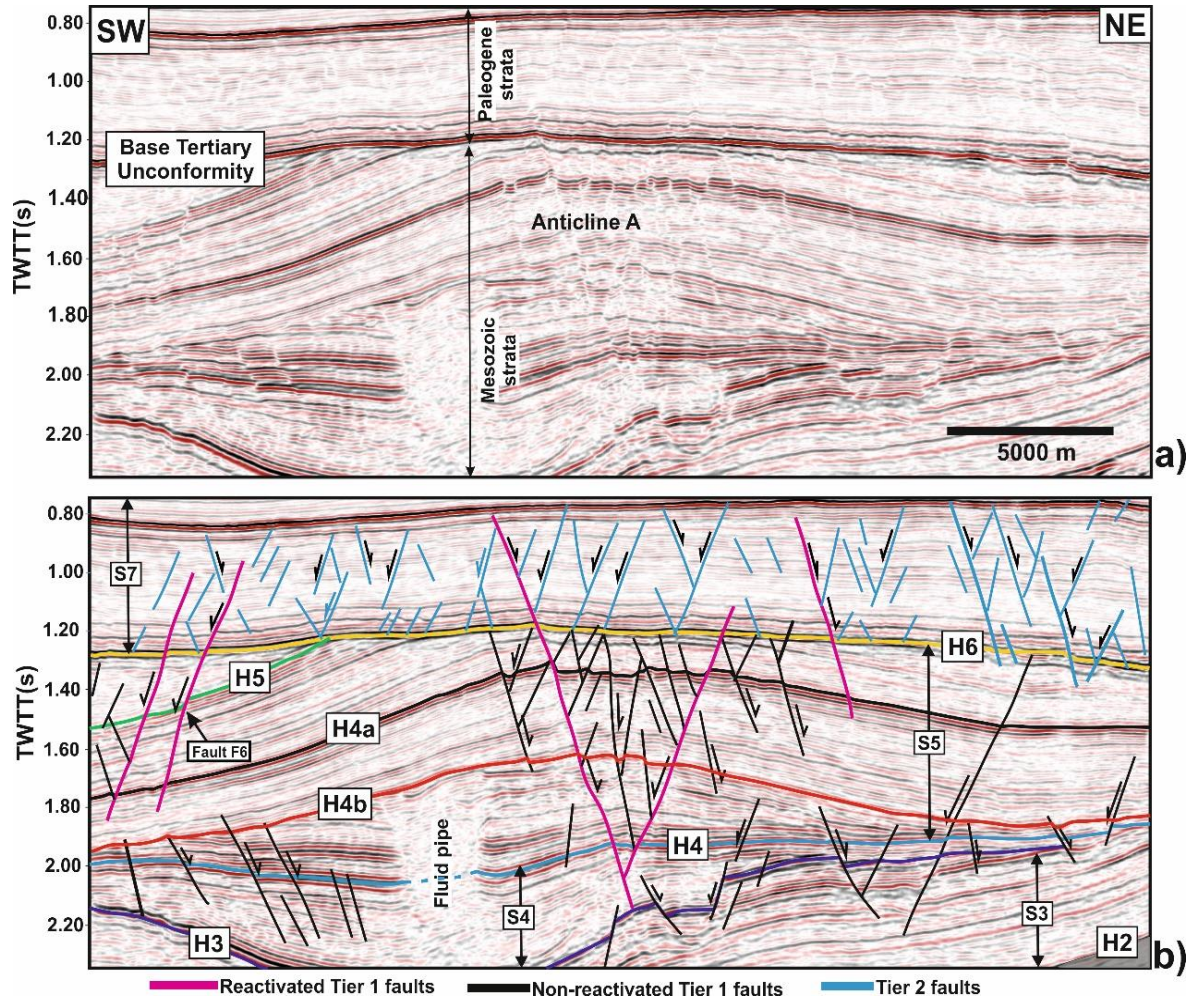
Fig. 5.7. a) Uninterpreted and b) interpreted seismic profiles highlighting the geometry of Upper Mesozoic (Tier 1) and Paleogene (Tier 2) faults over Anticline A. The imaged fault tiers are separated by the Base of Tertiary Unconformity (horizon H6), with some of the Tier 1 faults reactivating upward into Paleogene strata (Unit S7), linking with Tier 2 faults. The location of the seismic line is shown in Figs. 5.10a, 5.11a and 5.12a.
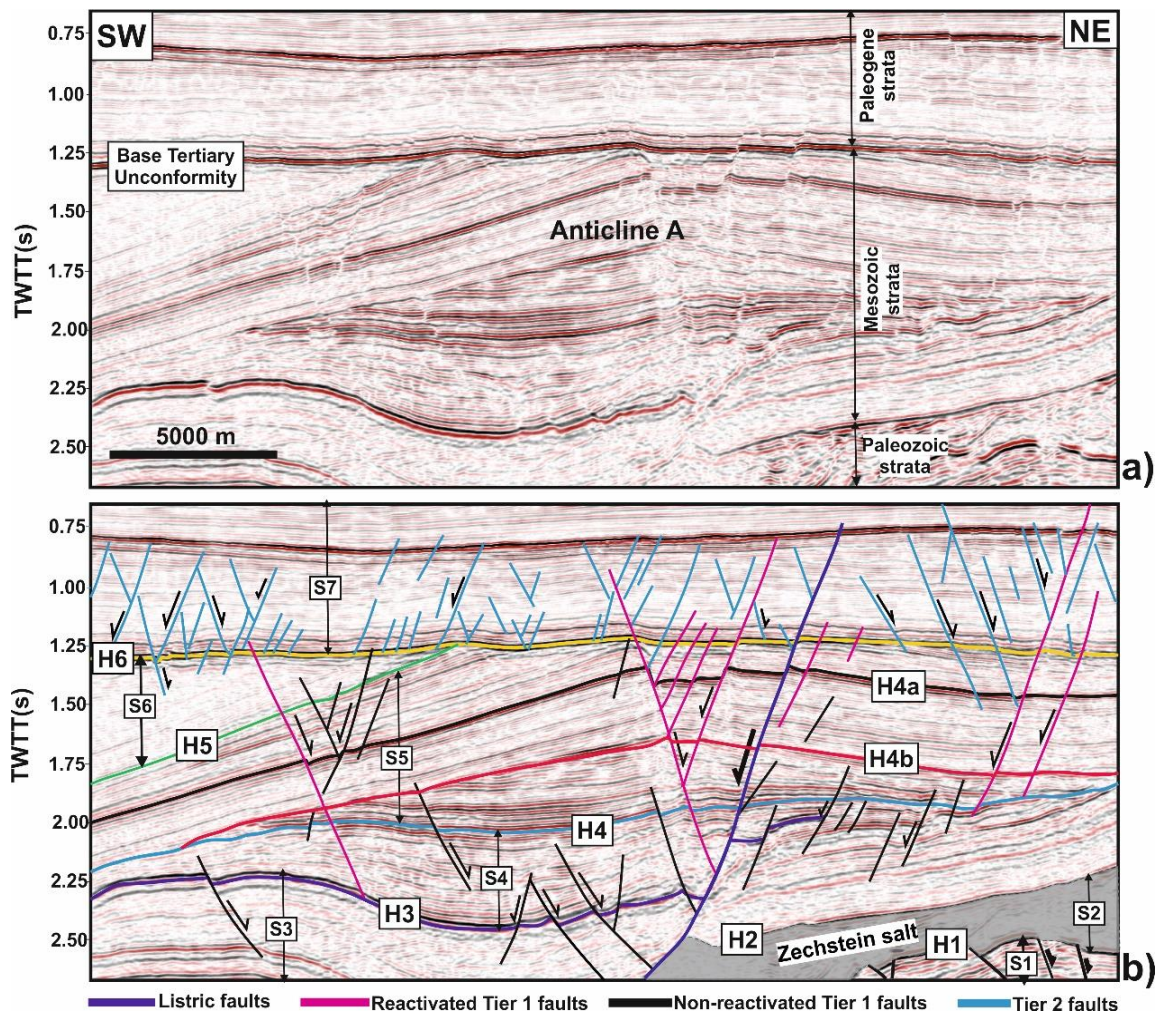
Fig. 5.8. a) Uninterpreted and b) interpreted seismic profiles highlighting the geometry of Upper Mesozoic (Tier 1) and Paleogene (Tier 2) faults over Anticline A. Distinct fault tiers are separated by the Base Tertiary Unconformity (H6), but with some of the Tier 1 faults reactivating upward into the Paleogene strata (S7) to link with Tier 2 faults. A deeply-rooted listric fault that detaches on top Zechstein salt (H2) propagates vertically into Paleogene strata (S7). Some of the Tiers 1 and 2 faults intersect this latter listric fault. The location of the seismic line is shown in Figs. 5.10a, 5.11a and 5.12a.

5.5.2.1.2. Reactivated Tier 1 faults

Fault reactivation has been described as reflecting the further propagation of pre-existing faults (Holdsworth et al., 1997; Nicol et al., 2005). Tier 1 faults that offset the Base Tertiary Unconformity (horizon H6) and propagate upwards in Paleogene strata are interpreted as reactivated Tier 1 faults (Figs. 5.6, 5.13 and 5.14). Their throws die out upwards into Paleogene strata, contrasting with non-reactivated (eroded) Tier 1 faults that are truncated at level of horizon H6, or just below this latter (Figs. 5.6, 5.13 and 5.14).

Reactivated Tier 1 faults are characterised by their linear to curvilinear pattern, and were predominantly reactivated above Anticline A in the southern part of the chapter study area (Fig. 5.12). The faults have a maximum throw of 40.2 m, a spacing of 840-5,200 m, and trace lengths of 1,200-12,250 m (Fig. 5.12). Some reactivated Tier 1 faults intersect the relatively deep listric faults, thus potentially forming secondary migratory pathways for hydrocarbons into shallower Paleogene units (Figs. 5.6, 5.8 and 5.14).

5.5.2.2. Tier 2 faults: Paleogene

Tier 2 faults comprise densely spaced sets of normal faults with a discrete range of strikes and reveal an irregular polygonal geometry in map view (Figs. 5.5, 5.6, 5.9 and 5.11). The upper and lower tip lines of these faults die out in Paleogene strata, with some faults propagating downward and offsetting the Base Tertiary Unconformity (horizon H6) around the hinge of Anticlines B and C, a character particularly observed towards the northern part of the chapter study area (Fig. 5.12). These faults were initially formed as polygonal faults and were reactivated to form new fault segments, or lengthen their sizes, due to later tectonic deformation (Figs. 5.5, 5.9 and 5.11).
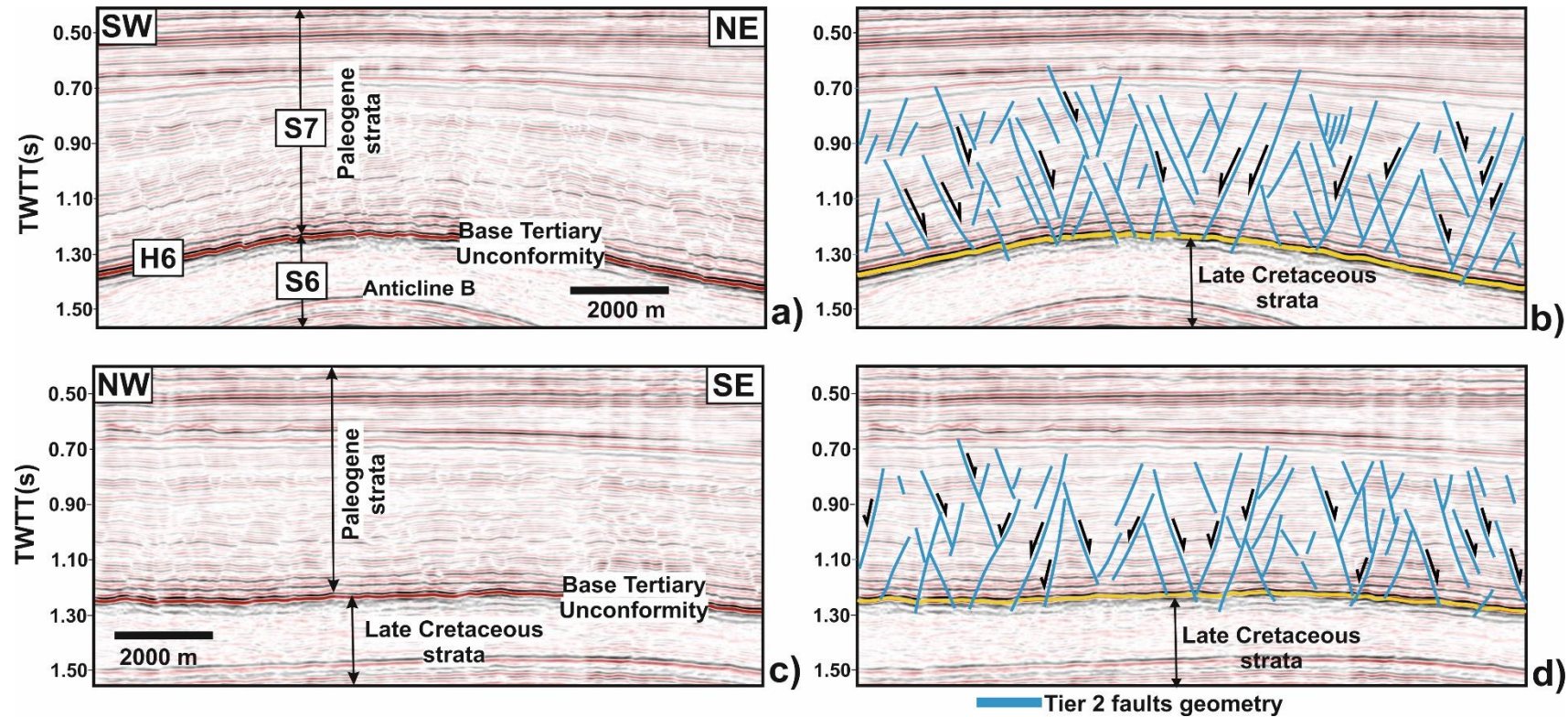
Fig. 5.9. a) Uninterpreted and b) Interpreted inline seismic sections revealing the geometry of Tier 2 faults in Paleogene strata (Unit S7: Lower North Sea Group), c) Uninterpreted and d) Interpreted crossline seismic sections also highlighting the geometry of Tier 2 faults in Paleogene strata. These faults are closely spaced, with some being also segmented. They result from near-seafloor extension over growing anticlines and sudden compaction of mud-rich strata with the subsequent loss of volume and fluid, forming polygonal fault geometries. The location of the seismic line is shown in Figs. 5.10a, 5.11a and 5.12a.
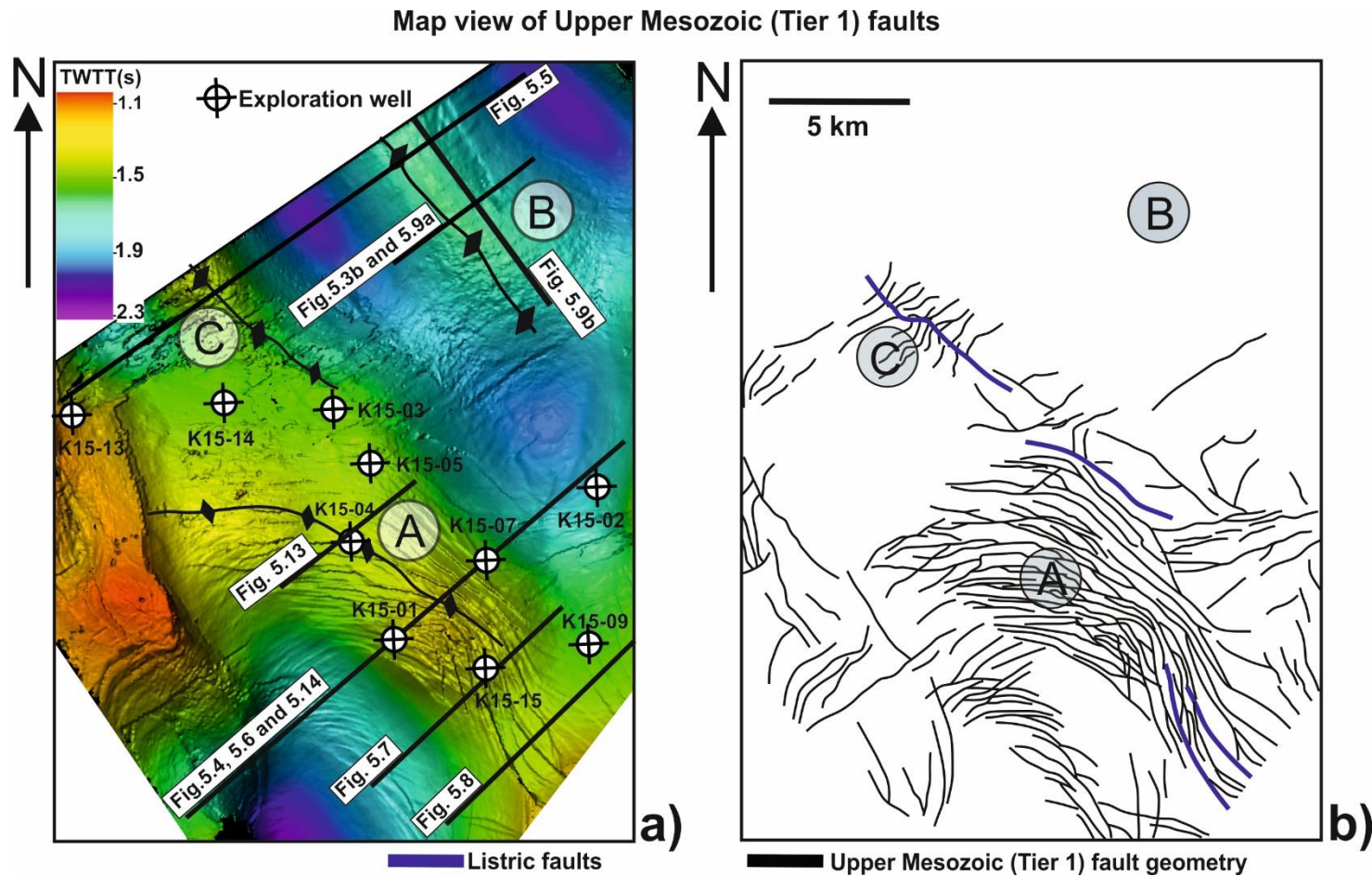
Fig. 5.10. a) TWTT structural map of a representative interval in Upper Mesozoic strata (H4a) highlighting the map view geometry of Tier 1 faults, the location of industry boreholes and key seismic lines, b) Interpreted sketch highlighting the map view geometry of Tier 1 faults over NW-SE trending Anticline A. These faults show a linear to curvilinear pattern in map view. A, B and C are interpreted anticlines responding to the effect of tectonic inversion in the Southern North Sea.

Tier 2 faults have a maximum throw of 9.8 m, a spacing of 320-680 m, and trace lengths of 950-2,000 m. They also accommodate a significant part of the local stretching affecting the Paleogene overburden (Figs. 5.9 and 5.11). The geometry of Tier 2 faults likely resulted from near-seafloor extension over growing anticlines, which affected compacting mud-rich strata (Lonergan et al., 1998; Cartwright et al., 2003).

5.6. Effect of lithology on fault throw distribution

The interpreted faults F1 to F6 are characterised by their maximum throw of 32 ms (40.2 m), an average spacing of 560 m, and trace lengths ranging from 1,100-11,250 m. These faults offset a layered succession comprising sands and shales (Figs. 5.15 to 5.20). Importantly, differences in fault throw are observed when the fault strands in the sand-rich intervals are compared to fault segments in the shale-rich intervals. In the sand-rich intervals, fault throws are larger (average 32 ms, or 40.3 m) compared to the smaller fault throws (average 13.5 ms, or 17.7 m) documented in the shale rich-intervals (Figs. 5.15 to 5.20).

A decrease in fault throw is observed as the faults propagate from sand-rich into shale-rich intervals (Figs. 5.15 to 5.20). Hence, the propagation of fault segments, first grown in sand-rich strata, into shale intervals can result in vertically segmented fault arrays, as revealed by the throw-depth (T-Z) data in Figs. 5.15 to 5.20. Nevertheless, further propagation of two hard-linked fault segments after growth can attenuate the throw variations recorded on T-Z profiles, and thus obscure differences in the throw distribution with depth.
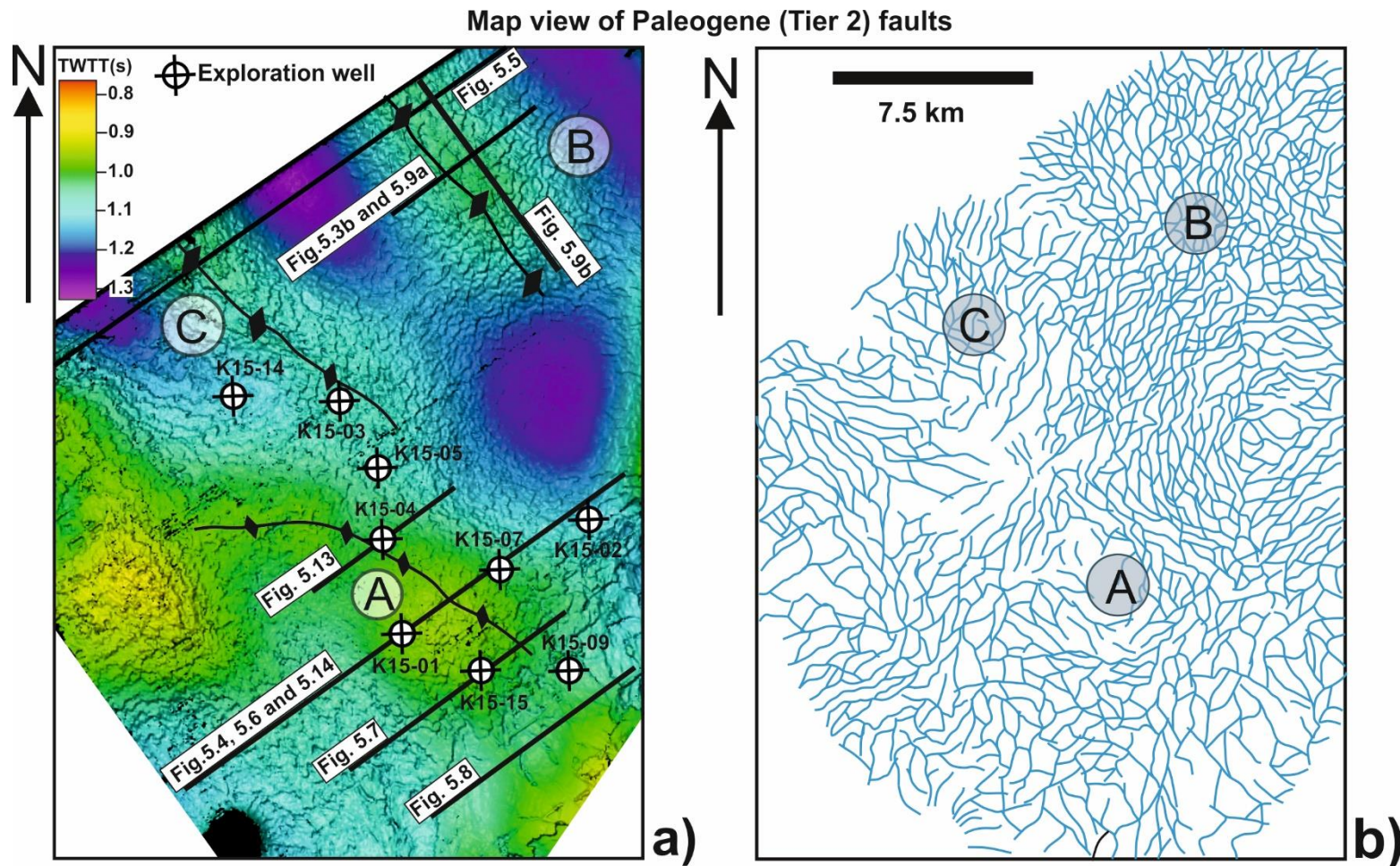
Fig. 5.11. a) TWTT structural map for representative interval in Paleogene strata highlighting the map view pattern of Tier 2 faults, the location of industry boreholes and key seismic lines, b) Interpreted sketch highlighting the geometry of Tier 2 faults. A, B and C are interpreted anticlines responding to the effect of tectonic inversion in the Southern North Sea.
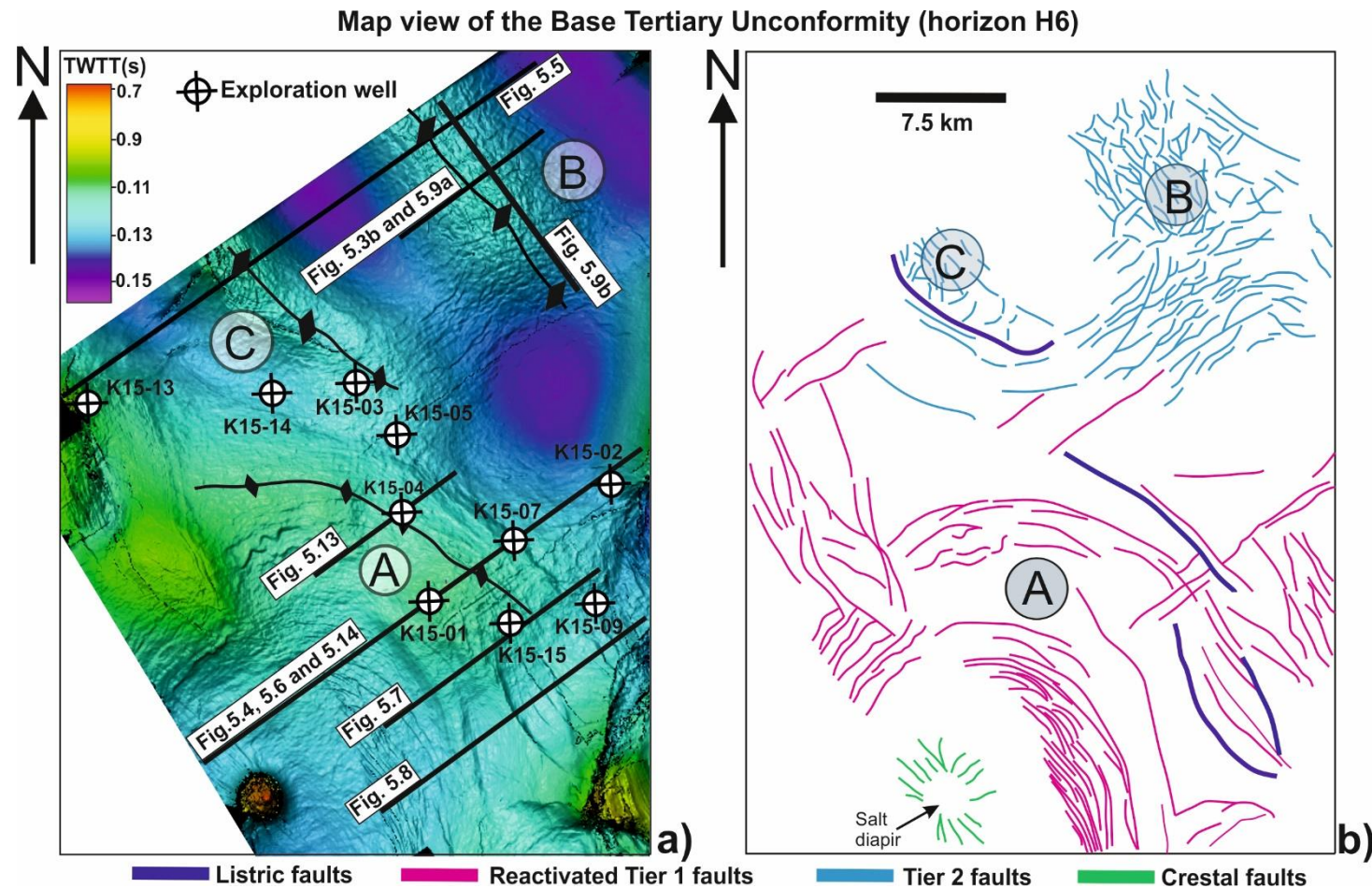
Fig. 5.12. a) TWTT structural map of the Base Tertiary Unconformity (horizon H6) showing its map view, the location of industry boreholes and key seismic lines. A, B and C are interpreted anticlines responding to the effect of tectonic inversion in the Southern North Sea, b) Interpreted sketch highlighting the geometry of reactivated fault families affecting the Base Tertiary Unconformity (horizon H6). Reactivated Tier 1 faults show linear to curvilinear distributions around Anticline A. Tier 2 faults show irregular polygonal geometries over Anticlines B and C.

5.7. Propagation and growth history of faults

5.7.1. Fault nucleation

The relative nucleation of representative faults F1 to F6 in the chapter study area is illustrated with reference to the throw-depth (T-Z) profiles in Figs. 5.15 to 5.20. Fault segments with local throw between 16 ms and 32 ms (20.2 m and 40.3 m) are early-stage fault segments and represent regions where faults nucleated first in competent sand and limestone intervals (Figs. 5.15 to 5.20). Each segment of these early-stage faults propagated outwards until they encountered other fault strands to link with. Linkage points are located where local throw minima between 2 ms and 14 ms (2.5 m to 17.7 m) are recorded in less competent shale-rich intervals (Figs. 5.15 to 5.20) (Ellis and Dunlap, 1988; Mansfield and Cartwright, 1996). Hence, regions with local throw maxima in the throw-depth (T-Z) profiles are interpreted as the first loci of fault growth, which dominantly occurred in competent sand and limestone intervals (Figs. 5.15b to 5.20b).

5.7.2. Modes of fault growth

Two (2) distinct modes of fault growth were recognised in the area, as revealed by the throw-depth profiles in Figs. 5.15 to 5.22. These modes include fault growth via upward propagation and segment linkage. Listric faults that reflect the early-stage deformation of Mesozoic strata grew via the upward propagation from a parent fault above the Zechstein salt (Unit S2; Figs. 5.4 to 5.6). These faults exhibit a typical vertical, positive stepped throw gradient (Fault F7; Fig. 5.21). They show major breaks in throw gradients around the top of Jurassic strata. The fault strands below the top Jurassic marker (horizon H4a) offset Triassic-Jurassic strata and show throw maxima between 42 ms and 85 ms (52.9 m to 129 m) (Fig. 5.21).
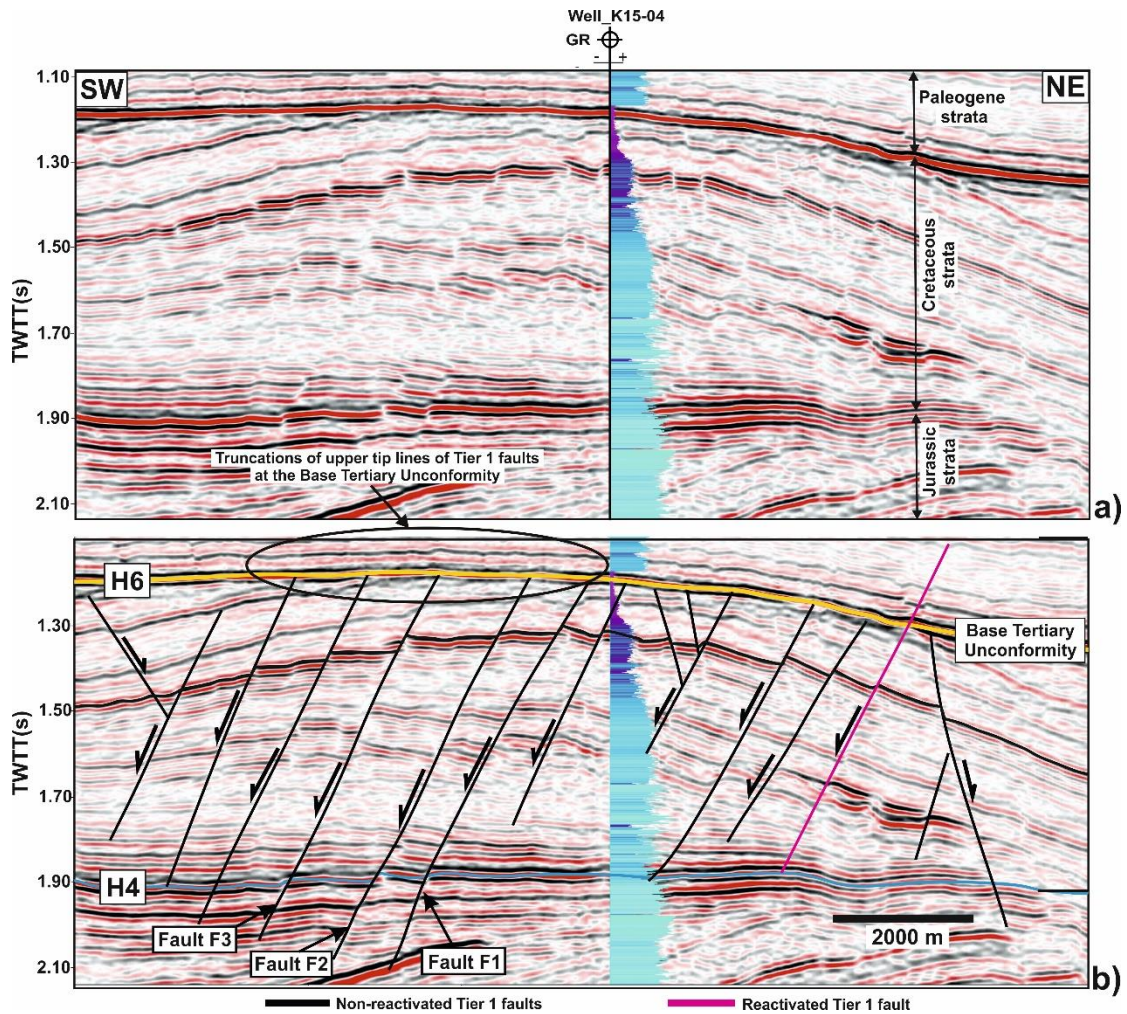
Fig. 5.13. a) Uninterpreted and b) interpreted seismic profiles revealing the geometry of representative Upper Mesozoic (Tier 1) faults over Anticline A. These faults were eroded and truncated at the Base of Tertiary Unconformity (Non-reactivated Tier 1 faults), with some reactivating and propagating upward into the Paleogene strata (Reactivated Tier 1 faults). The location of the seismic line is shown in Figs. 5.10a, 5.11a and 5.12a.
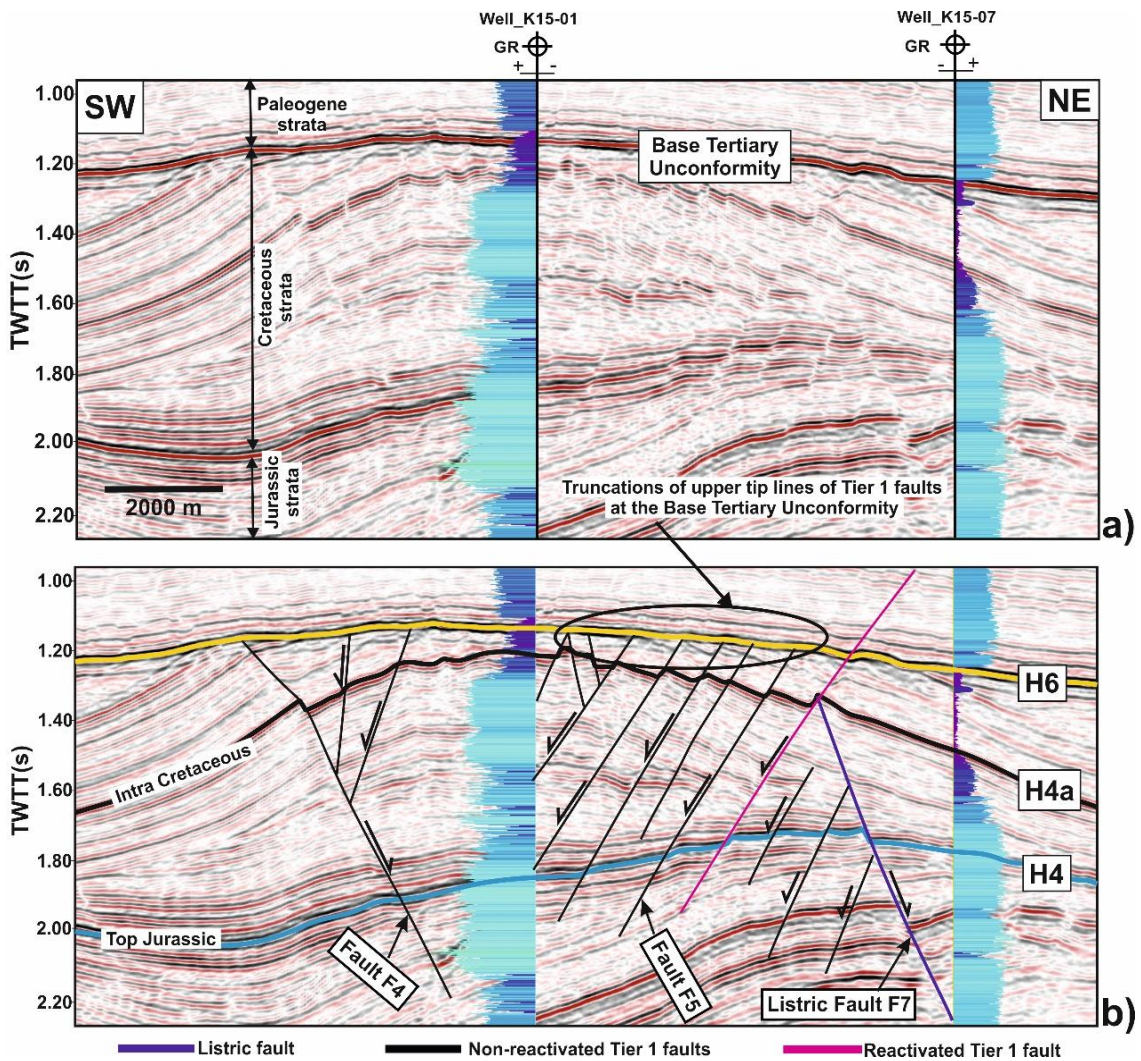
Fig. 5.14. a) Uninterpreted and b) interpreted seismic profiles revealing the geometry of representative Upper Mesozoic (Tier 1) faults over Anticline A. These faults were eroded and truncated at the Base of Tertiary Unconformity (Non-reactivated Tier 1 faults), with some reactivating and propagating upward into the Paleogene strata (Reactivated Tier 1 faults). Some of the Tier 1 faults intersect a deeply-rooted listric fault that detaches on the top of Zechstein salt.

The strands above the top Jurassic marker offset Cretaceous strata and reveal abrupt steps in throw profiles, with throws between 15 ms and 32 ms (18.9 m to 40.3 m) (Fig. 5.21).

The upward decrease in throw values, and the vertical positive step in throw gradients recorded by listric fault F7, are related to fault growth by upward propagation from parent faults above the Zechstein salt (Unit S2; Figs. 5.4 to 5.6). The absence of alternating local throw maxima and minima on the throw distribution profiles reflects the growth of listric faults by upward propagation (Fig. 5.21). Also, thickness variations between the footwall and the hanging-wall blocks of listric faults show these are syn-sedimentary faults, and propagated vertically during their growth (Figs. 5.4 to 5.6).

The representative vertical throw-depth (T-Z) profiles in Figs. 5.15b to 5.20b and 5.22c show a distinct mode of growth dominated by segment linkage. This mode of fault growth is recognised by its stepped vertical throw-depth (T-Z) profiles with a break in throw gradients (Figs. 5.15b to 5.20b and 5.22c). Sharp changes in throw values are interpreted to be a consequence of reactivation and growth by segment linkage, where two separate faults have propagated towards each other. Segments with local throw maxima are early-stage fault-segments formed in regions where faults nucleated first in more competent (sand-rich) intervals. Each fault segment is separated by a local throw minimum in less competent (shale-rich) intervals, as expected for this type of growth by segment linkage (Figs. 5.15b to 5.20b and 5.22c).

Abrupt changes in fault throw are interpreted as a characteristic of fault reactivation and can be attributed to lithological effects during fault propagation through mechanical barriers (Figs. 5.15b to 5.20b). Contrasts in acoustic impedance of the sediments along the fault planes are sufficient to infer such major change in throw gradients.
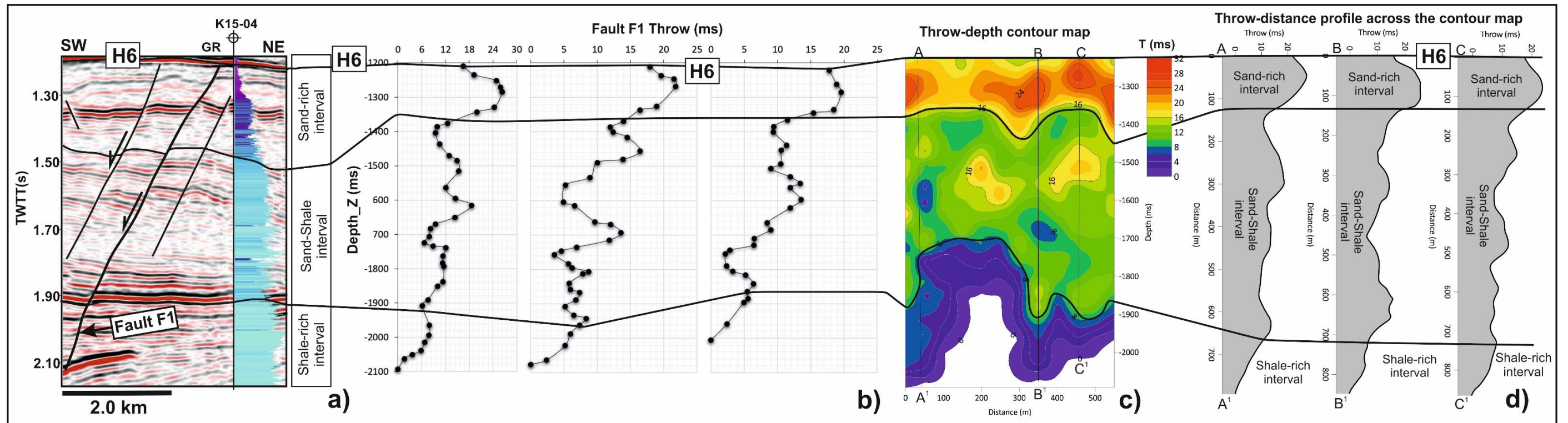
Fig. 5.15. Representative throw-depth (T-Z) profiles stressing the influence of mechanical stratigraphy and lithology on throw distribution and growth on fault F1. a) Interpreted seismic section and well log. b) Representative throw-depth (T-Z) profiles revealing fault reactivation and growth by segment linkage, where two separate pre-existing faults with throw maxima in sand-rich competent intervals have propagated towards each other and linked in shale-rich intervals where local fault throw minima are recorded. c) Throw-depth contour map showing anomalous throw distributions and, d) Throw-distance (T-X) plots through the contour map. See Fig. 5.13 for a full seismic section of the interpreted fault F1.
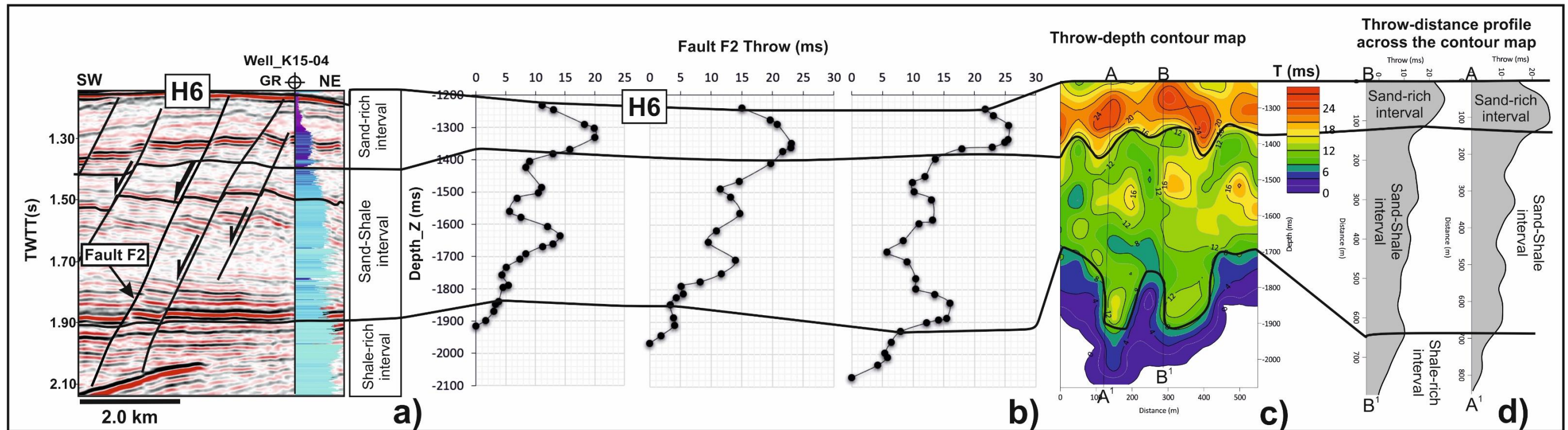
Fig. 5.16. Representative throw-depth (T-Z) profiles revealing the effect of mechanical stratigraphy and lithology on throw distribution and growth on fault F2. a) Interpreted seismic section and well log. b) Representative throw-depth (T-Z) profiles showing fault reactivation and growth by segment linkage. Where two separate faults with local throw maxima between 15 and 30 ms (18.2-37.8 m) in sand-rich (competent) intervals have propagated towards each other and linked in shale-rich (incompetent) interval where local throw minima between 2 and 15 ms (2.5-19.2 m) are recorded. c) Throw-depth contour map showing anomalous throw distributions. d) Throw-distance (T-X) plots through the contour map stressing fault growth via segment linkages. See Fig. 5.13 for a full seismic section of the interpreted fault F2.

Fault growth via segment linkage has wider implications for reactivation processes in fault systems, particularly where more competent (strong) mechanical layer favours nucleation of new faults in distinct mechanical intervals (Peacock and Sanderson, 1992; Childs et al., 1996) (Figs. 5.15 to 5.20).

5.8. Discussion

5.8.1. Impact of tectonic shortening on the geometry and reactivation of supra-salt faults

Fault reactivation has been described as reflecting the further propagation of pre-existing faults after a significant period of inactivity (Holdsworth et al., 1997; Nicol et al., 2005). The ability for a fault to repeatedly reactivate is directly related to the orientation of the fault planes with respect to the principal stresses (White et al., 1986; Richard and Krantz, 1991), and the mechanical properties of the fault surface or zone itself, including the cohesion and coefficient of friction that hinder slip on the fault surface, fluid pressure and regional kinematics or tectonic regime (Ward et al., 2016; Ferrill et al., 2017).

The Late Cretaceous to Paleogene tectonic inversion episodes (i.e., Sub-Hercynian, Laramide, Pyrenean and Savian episodes; Figs. 5.3 and 5.23), have induced a continuum of deformation in the Broad Fourteen Basin, Southern North Sea, and contributed significantly to the formation and subsequent reactivation of Upper Mesozoic to Paleogene supra-salt faults (Figs. 5.4, 5.5 and 5.23). In the chapter dataset, two distinct tiers of faults are recognised according to their geometry: a) Tier 1 faults (Upper Mesozoic), and b) Tier 2 faults (Paleogene) (Figs. 5.4 to 5.6).

Correlation panel amongst fault throw distribution, lithology, and growth history for fault F3
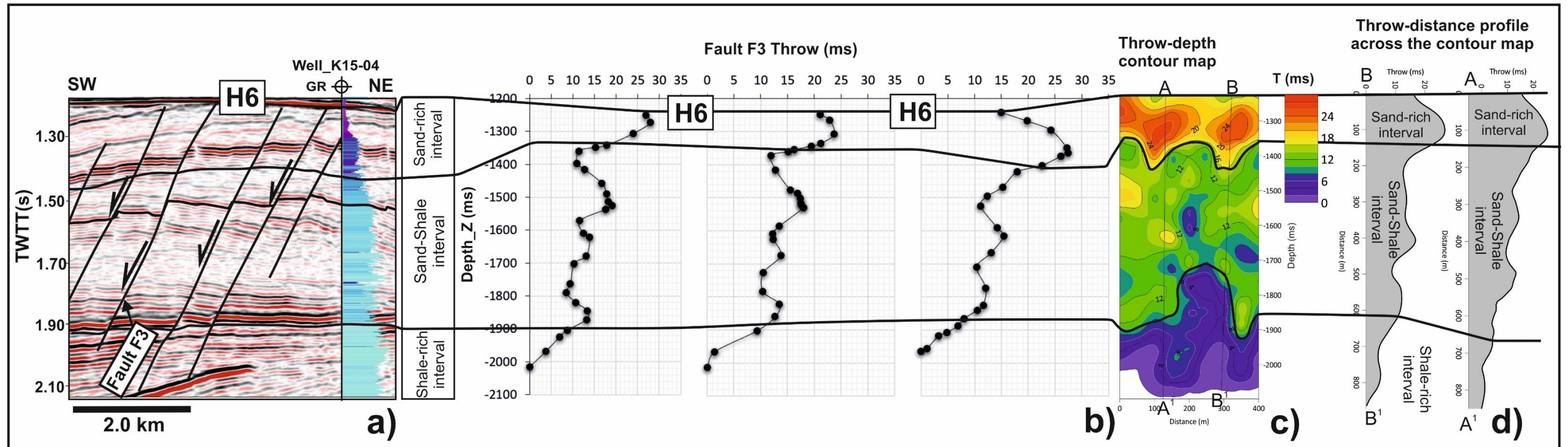
Fig. 5.17. Representative throw-depth (T-Z) profiles revealing the effect of mechanical stratigraphy and lithology on throw distribution and growth on fault F3. In sand-rich intervals, fault throws are usually larger - between 14 and 30 ms (17.7-37.8 m) - compared to the smaller fault throws between 2 and 14 ms (2.5-17.7 m) recorded in shale rich-intervals. These changes in throw values are interpreted to be a consequence of mechanical stratigraphy and lithological changes in the host rock. a) Interpreted seismic section and well log. b) Representative throw-depth (T-Z) profiles showing fault reactivation and growth by segment linkage. c) Throw-depth contour map showing throw distributions. d) Throw-distance (T-X) plots through the contour map. See Fig. 5.13 for a full seismic section of the interpreted fault F3.

Tier 1 faults resulted from the progressive buckling and stretching of outer arc Mesozoic strata during the Late Cretaceous inversion episode, i.e. during Sub-Hercynian tectonics (Figs. 5.3, 5.4 and 5.24c,d).

The Laramide inversion episode (Early Paleocene) reactivated Sub-Hercynian Tier 1 faults and created a prominent Late Cretaceous-Tertiary unconformity (horizon H6) (De Lugt et al., 2003; Oudmayer and De Jager, 1993). Horizon H6 is a strong, regionally mappable seismic reflector and represents a major change in rock strength from softer Tertiary clays and silts of the North Sea Group (Unit S7) to stiffer Upper Cretaceous limestones deposits of the Chalk Group below (Unit S6; Figs. 5.3, 5.4, 5.23 and 5.24e). The upper tip lines for these Tier 1 faults were eroded by the Paleocene Laramide erosional event at the Base Tertiary Unconformity (H6; Figs. 5.13 and 5.14). The truncation of these faults suggest that they were active in the Upper Mesozoic strata before the onset of the Laramide erosional event (Fig. 5.24c and d). Subsequently, the Pyrenean (Oligocene) and Savian (Miocene) inversion episodes reactivated some of these faults upward into the Paleogene strata (Unit S7), where they link with the overlaying Paleogene Tier 2 faults (Figs. 5.6, 5.23 and 5.24e).

The TWTT structural maps in Fig. 5.12 highlight the map view of these fault tiers. Tier 1 faults largely reactivated around the hinge of Late Mesozoic Anticline A, whereas the overlying Tier 2 faults were selectively reactivated around the hinges of Anticline B and C (Fig. 5.12). This observation perhaps suggests that in addition to the fault's orientation and geometry (Richard and Krantz, 1991; Baudon and Cartwright, 2000) other controls, such as the location of the underlying anticlines, affected fault reactivation in the chapter study area, as observed in the TWTT map in Fig. 5.12.

Correlation panel amongst fault throw distribution, lithology, and growth history for fault F4
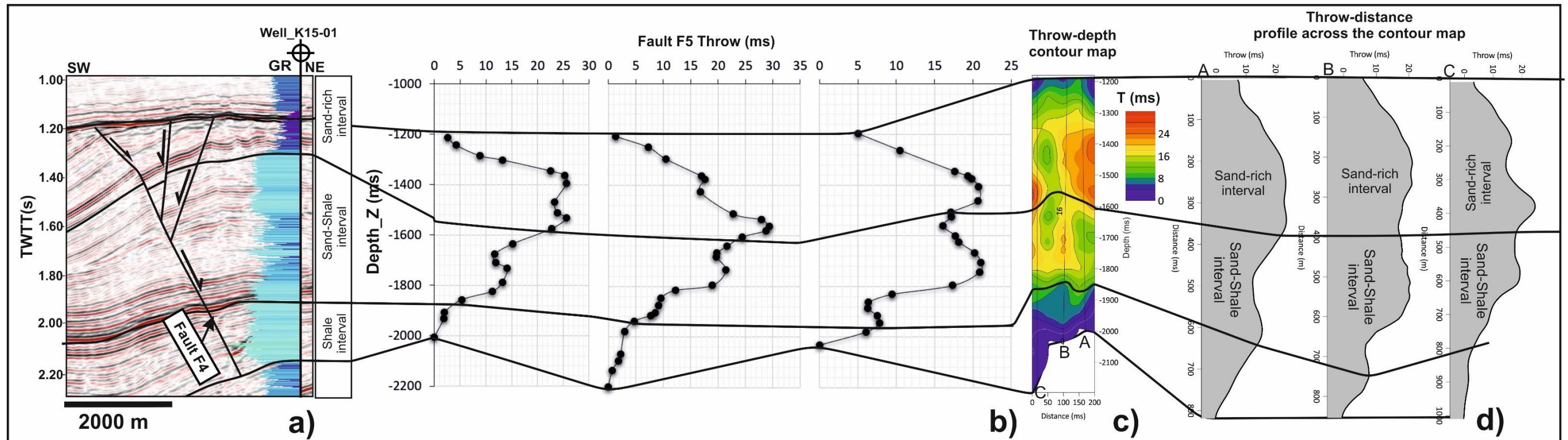
Fig. 5.18. Representative throw-depth (T-Z) profiles stressing the influence of mechanical stratigraphy and lithology on throw distribution and growth on fault F4. A reduction in throw values is observed over the fault planes, as faults propagate from sand-rich intervals into shale-rich intervals. a) Interpreted seismic section and well log. b) Representative throw-depth (T-Z) profiles showing the fault reactivation and growth by segment linkage, where two separate pre-existing faults with throw maxima in sand-rich competent intervals have propagated towards each other and linked in shale-rich intervals where local fault throw minima are recorded. c) Throw-depth contour map showing throw distributions. d) Throw-distance (T-X) plots through the contour map. See Fig. 5.14 for a full seismic section of the interpreted fault F4.

The distinct geometries observed in Tier 1 and 2 faults can be attributed to the mechanical differences in different lithological intervals and deformation mechanisms (Figs. 5.10 and 5.11). The tectonic shortening and brittle deformation in the more competent carbonate and sand-rich strata of the Chalk and Rijnland Groups led to a more localised linear-curvilinear faults pattern in Tier 1 faults (Fig. 5.10), whereas compactional loading (diagenesis) and the relatively ductile deformation of the incompetent mud-rich strata of the Lower North Sea Group resulted in diffuse strain and the generation of a polygonal pattern in Tier 2 faults (Figs. 5.11). The polygonal pattern in Tier 2 faults was likely formed from near-seafloor extensional stresses predominating over growing anticlines, accompanied by the sudden compaction of mud-rich strata and subsequent loss of volume and fluid (Lonergan et al., 1998; Cartwright et al., 2003) (Fig. 5.11). Nevertheless, some of the Tier 2 faults still record the effect of Miocene inversion episode (Savian phase) which largely reactivated and lengthen some of these latter faults downwards around the hinge of Anticlines B and C (Figs. 5.5, 5.9 and 5.12).

According to the analogue sandbox experiments presented in Gabrielsen et al. (2016), incompetent layers or intervals with ductile behaviour can prevent fault propagation or lead to vertical segmentation (decoupling) when fault segments are subjected to various types of linkage across ductile layers. In the study area, vertical fault segmentation is observed in both seismic and throw-depth (T-Z) profiles (Figs. 5.9, 5.15b, 5.16b, 5.17b and 5.22c). Several fault segments with relatively smaller throws are observed in shale-rich intervals, while faults in the sand-rich intervals appear as discrete, isolated faults recording the largest throws (Figs. 5.15b to 5.17b, 5.19c and 5.22c).
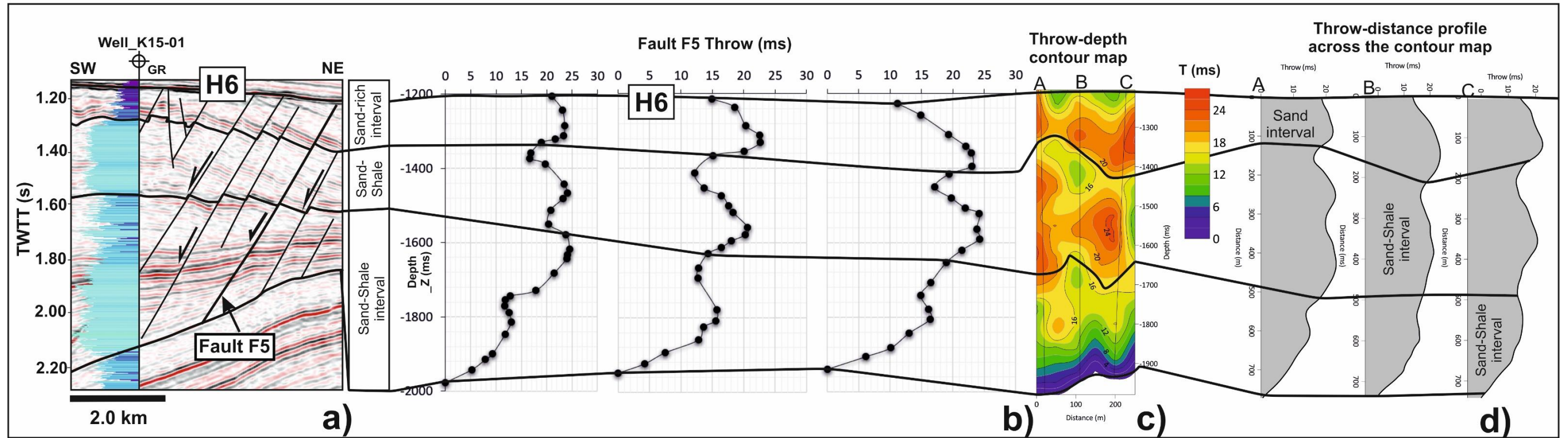
Fig. 5.19. Representative throw-depth (T-Z) profiles revealing the effect of mechanical stratigraphy and lithology on throw distribution and growth on fault F5. a) Interpreted seismic section and well log. b) Representative throw-depth (T-Z) profiles showing the fault reactivation and growth by segment linkage. c) Throw-depth contour map showing anomalous throw distributions. d) Throw-distance (T-X) plots through the contour map stressing fault growth via segment linkages. See Fig. 5.14 for a full seismic section of the interpreted fault F5.

The effect of incompetent layers on the segmentation of faults has been studied at outcrop and using seismic data (Soliva et al. 2005; Schöpfer et al. 2006; Libak et al., 2019; Ferrill et al. 2017). For instance, Libak et al. (2019) recently interpreted seismic data from the Norwegian Barents Sea to show that fault zones are more segmented and wider in claystones, while faults in sandy intervals are narrower and more localised, thus less segmented. Deformation tends to be more localised (less segmented) to reveal local throw maxima in competent lithologies such as sandstones and carbonates, and more distributed (segmented) in incompetent lithologies such as claystones and shales, where throw minima are recorded (Schöpfer et al. 2006).

Research has also shown that faults are often steep in competent lithologies, while faults have more gentle dips in relatively incompetent lithologies (Peacock 2002; Ferrill et al. 2017). Such differences in fault dip along a fault segment can locally lead to fault refraction, which may generate extensional (dilatational) jogs (Peacock and Sanderson 1991; Ferrill et al. 2017). In the chapter study area, no evidence exists for changes in fault dip geometries, as faults propagate from competent intervals into incompetent intervals, due to intricate nature of the fault geometries and limited resolution of the seismic datasets i.e. the faults are not resolved by the seismic data. This interpreted as reflecting the deformation of the original segment dip-linkage structures during post-linkage slip of the faults, with any original topological irregularities having been largely eliminated during fault reactivation.

5.8.2. Propagation and growth history of faults in layered successions

Interpreted faults F1 to F6 and F8 to F11 reveal a break in throw gradients, and a progressive decrease in throw towards the fault tips, a characteristic of reactivation and growth during fault propagation through mechanical barriers (Gross et al., 1997;

Wilkins and Gross, 2002) (Figs. 5.15b to 5.20b and 5.22c). Research has shown that, as strain accumulates in a layered sedimentary sequence, competent (brittle) lithologies such as limestones and sandstones accommodate smaller amounts of pre-failure strain and are able to fracture first, whereas incompetent (ductile) lithologies such as claystones and shales accommodate higher prefailure strain prior to faulting and usually fracture later (Ferrill and Morris, 2003, 2008; Welch et al., 2009). Hence, faults would be expected to nucleate first in competent lithologies with the larger throws, and this chapter show this to be the case (Figs. 5.15 to 5.20).

The results in this work show differences between the throw magnitudes of faults in sand-rich intervals (with a throw maximum of 32 ms, or 40.3 m) compared to the shale-rich intervals (with a throw maximum of 14 ms, or 17.7 m) (Figs. 5.15 to 5.20). This difference can be related to the predominance of brittle deformation in the competent sand-rich intervals, resulting in a less segmented zones of fault deformation with local throw maxima, while ductile deformation in incompetent shale-rich interval led to a more segmented zone of deformation, with local throw minima (Figs. 5.15b to 5.20b and 5.22c). Thus, fault segments with local throw maxima in the throw-depth (T-Z) profiles are interpreted to be the loci where faults nucleated first, with this occurring predominantly in competent sand-rich intervals (Figs. 5.15 to 5.20). These fault segments drove displacement into shale-rich intervals where smaller fault throws are accommodated by more ductile deformation (Figs. 5.15 to 5.20).

In throw-depth (T-Z) profiles, evidence for vertical fault segmentation is observed, where the fault segments with local throw minima in the shale-rich intervals were linked to pre-existing fault segments with local throw maxima in the sand-rich intervals (Figs. 5.15b to 5.20b).

Correlation panel amongst fault throw distribution, lithology, and growth history for fault F6
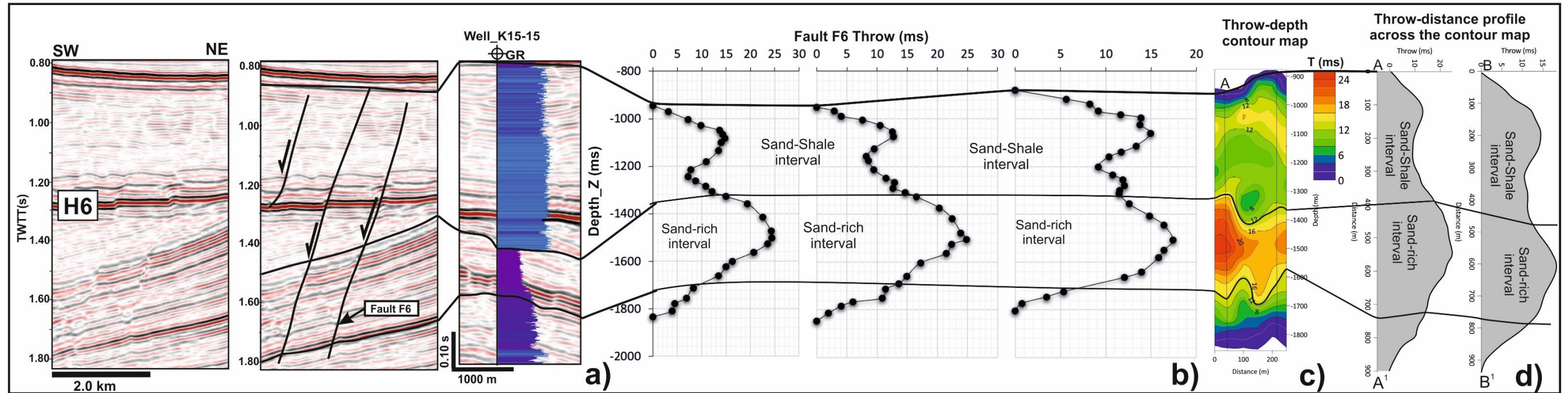
Fig. 5.20. Representative throw-depth (T-Z) profiles revealing the effect of mechanical stratigraphy and lithology on throw distribution and growth on fault F6. a) Interpreted seismic section and well log. b) Representative throw-depth (T-Z) profiles showing the fault reactivation and growth by segment linkage, where two separate pre-existing faults with throw maxima in more competent intervals have propagated towards each other and linked in less competent intervals. c) Throw-depth contour map showing throw distributions. d) Throw-distance (T-X) plots through the contour map. See Figs. 5.6 and 5.7 for a full seismic section of the interpreted fault F6.
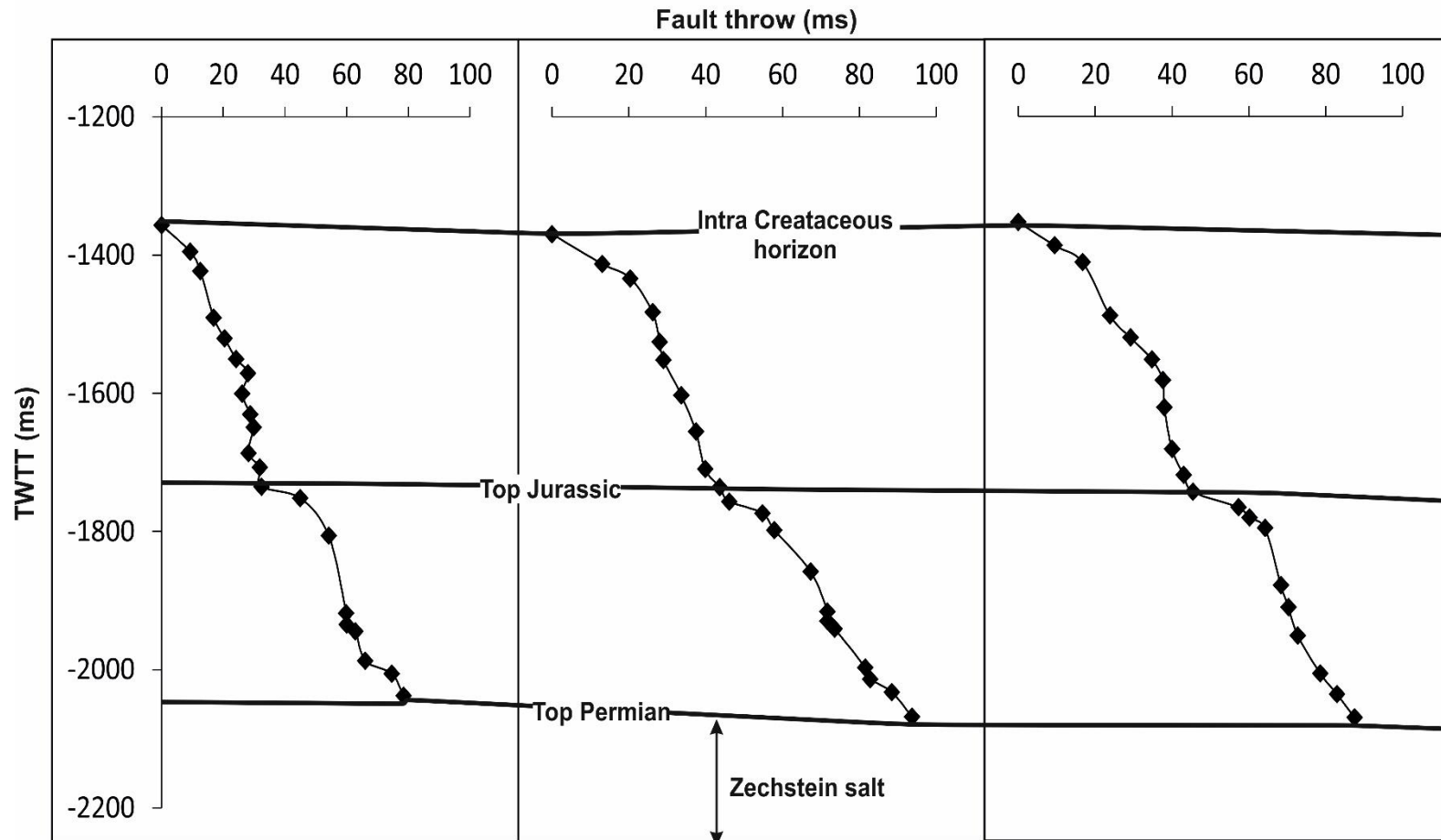
Fig. 5.21. Representative throw-depth (T-Z) profiles for a listric fault showing typical growth by upward propagation, i.e. a vertical, positive stepped throw gradient. The decrease and vertical positive step in throw gradients recorded by the listric fault can be related to the effects of reactivation by upward propagation from parent faults above a detachment surface, i.e. Zechstein salt in Fig. 5.6.

Thus, the propagation of slip from fault segments with local throw maxima (in the sand-rich intervals) into the shale-rich interval can describe the vertically segmented fault arrays observed in the throw-depth (T-Z) profiles in Figs. 5.15b to 5.20b and 5.22c. The results of throw-depth (T-Z) interpretation support the view that vertically segmented fault arrays initially nucleated in the competent, and brittle, lithologies (sandstones and limestones) with less segmented maximum throws and are later linked by faults in the incompetent, ductile, lithologies (shales) with more segmented minimum throws (Peacock and Sanderson, 1992; Childs et al., 1996) (Figs. 5.15b to 5.20b).

Differences in the throw distribution provide insights into the recognition of two (2) distinct modes of fault growth: fault growth via upward propagation vs. fault segment linkage. The listric fault F7 (Fig. 5.21) shows a regular upward decrease in throw values and maintains vertical, positively stepped gradients, revealing the classical model for fault growth by upward propagation from pre-existing faults above thick salt (Richard and Krantz, 1991; Baudon and Cartwright, 2008; Maunde and Alves, 2020) (Fig. 5.21). The maximum throw value on the throw profile marks the onset of faulting; thus, faulting started above the Permian Zechstein salt (Figs. 5.6 and 5.21).

The interpreted faults F1 to F6 and F8 to F11 present throw-depth (T-Z) profiles with multiple local throw maxima separated by local throw minima, revealing fault growth via segment linkage (Baudon and Cartwright, 2008; Kim and Sanderson, 2005) (Figs. 5.15b to 5.20b and 5.22c). Fault segments with local throw maxima represent the intervals where faults nucleate first in more competent sand-rich intervals. Each of these fault segments propagated outwards until they encountered other pre-existing fault segments to link together.

198
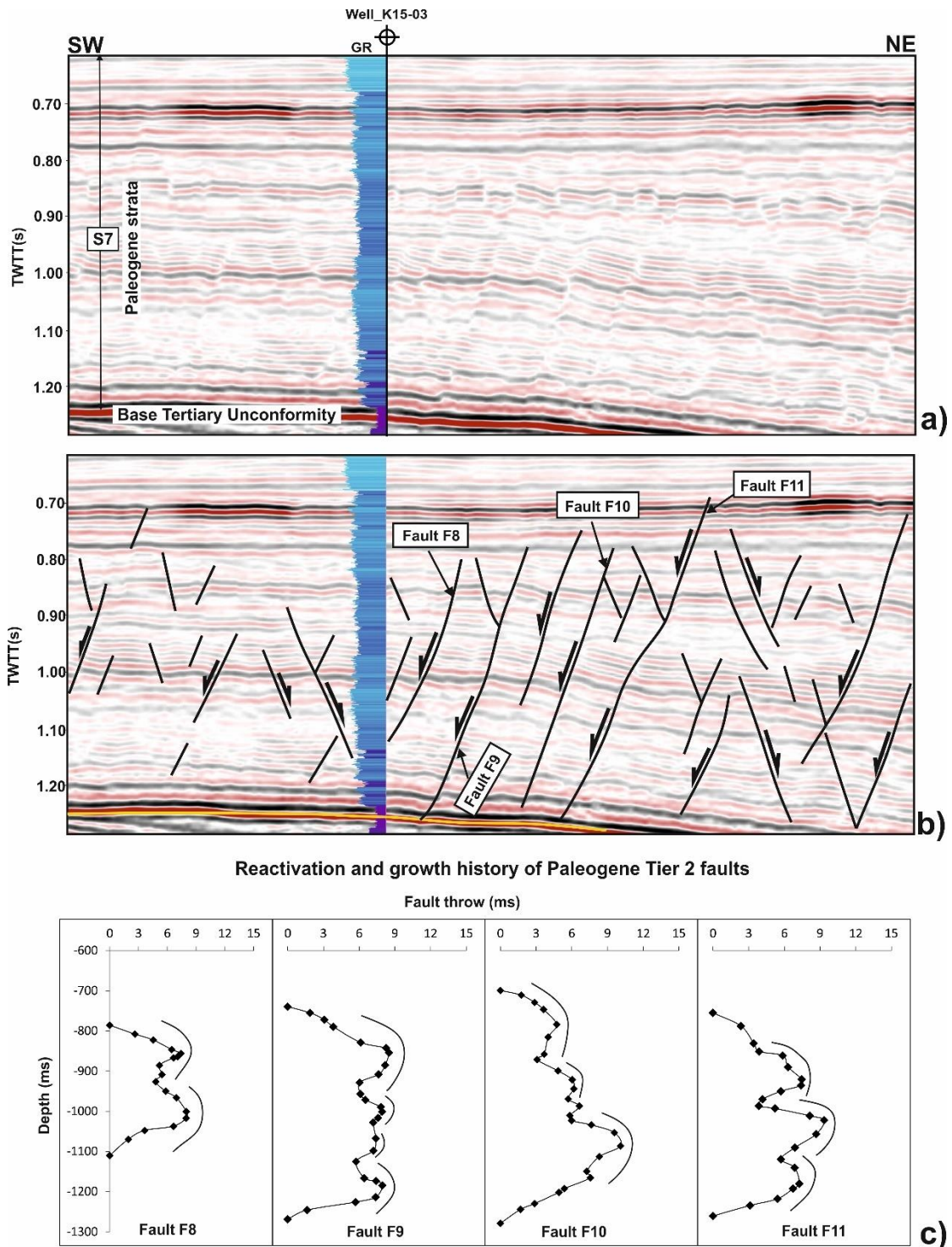
Fig. 5.22. a) Uninterpreted and b) interpreted seismic profiles showing the geometry of Tier 2 faults in Paleogene strata (Unit S7; Lower North Sea Group). c) Representative throw-depth (T-Z) profiles highlighting the reactivation and growth history on Tier 2 faults. The sharp changes in throw values are interpreted to relate to fault reactivation and growth by segment linkage, where multiple throw maxima are separated by throw minima.

The zone of linkage between two originally individual segments that are linked is recognisable by a zone of local throw minima and steepening of the throw gradients (Cartwright et al., 1995; Lohr et al., 2008). (Figs. 5.15b to 5.20b). However, further propagation of the two hard-linked fault segments after growth might attenuate the throw variations and obscure differences in the throw distribution (Figs. 5.18b and 5.20b).

The interpreted fault tiers are largely segmented and may present an important limitation for the implementation of carbon capture and storage (CCS) in the Broad Fourteens Basin (Figs. 5.15b to 5.20b and 5.22c). For example, the locus of fault segment linkage may increase the permeability of the rocks. Where the fault segments interact, active fracturing provides a pathway for fluids, as well as increasing the chances of compartmentalisation or localised fluid flow through the fault linkages (Curewitz and Karson, 1997; Ward et al., 2016), thus revealing significant risks when injecting CO_2 into the subsurface. In the Broad Fourteens Basin, listric faults control and transmit fluids within, and between Mesozoic strata (Penge et al., 1999; Alves and Elliott, 2014). The reactivated Tier 1 faults intersecting these deeply rooted listric faults potentially allow secondary migration of hydrocarbons into shallower Paleogene reservoirs (Figs. 5.8 and 5.24e).

The models for the evolution of interpreted faults in Fig. 5.24 provide insights into the timing of fault activity, with a direct application to hydrocarbon migration and sealing of faults in petroleum reservoirs. For instance, accurate timing of any reactivation phases with reference to constraints on the filling of hydrocarbon traps would be critical for an evaluation of seal risk (Cartwright et al., 2007).
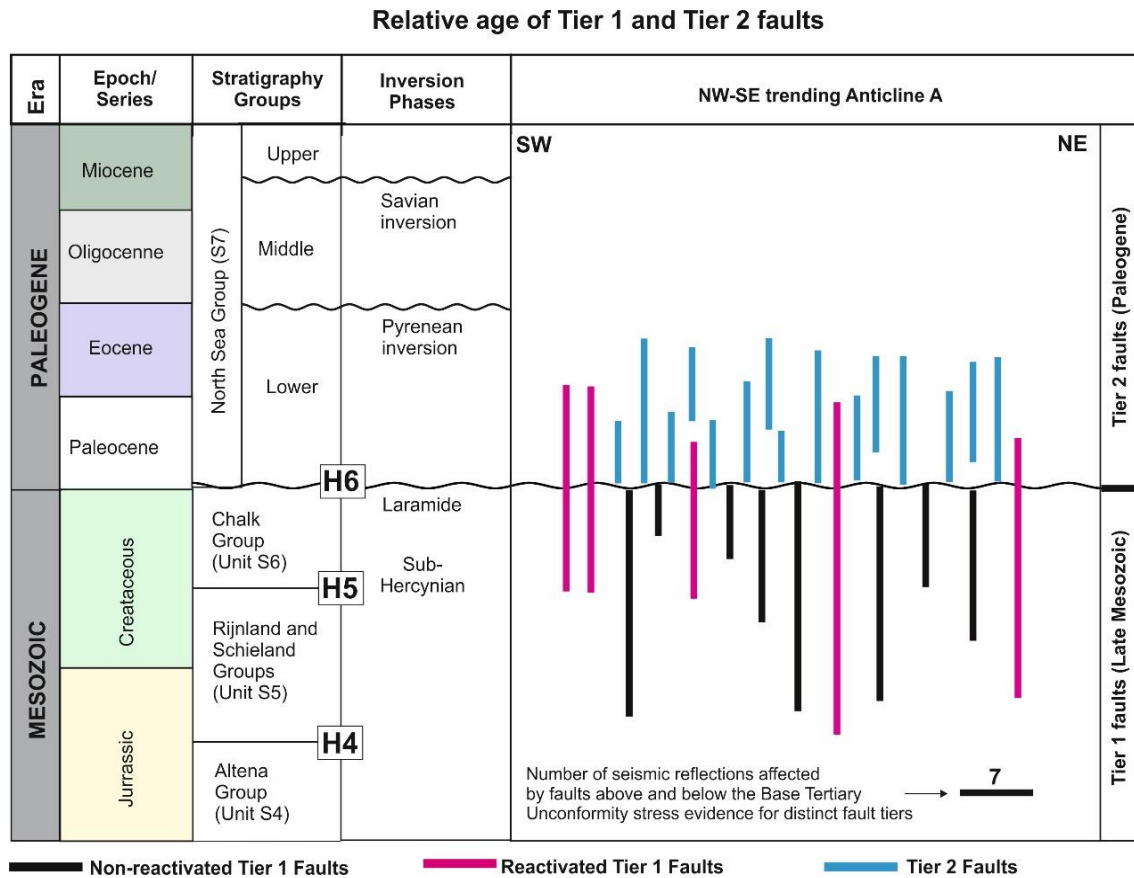
Fig. 5.23. Schematic illustration of the relative age and timespan of representative distinct fault tiers mapped over a NW-SE trending Anticline A. Plotted in the diagram is the number of reflections affected by faults above and below the Base Tertiary Unconformity (H6). Tier 1 faults dominantly offset Upper Mesozoic strata and truncated/eroded at the Base Tertiary Unconformity (Non-reactivated Tier 1 faults), with some faults reactivating upward into Paleogene strata (Reactivated Tier 1 faults). Tier 2 faults dominantly offset Paleogene strata. They are related to early diagenesis but still record the effect of the Paleogene inversion episode. Main stratigraphic groups, tectonic phases and unconformities related to regional tectonic events are based on Penge et al. (1999) and van Verweij and Simmelink (2002).
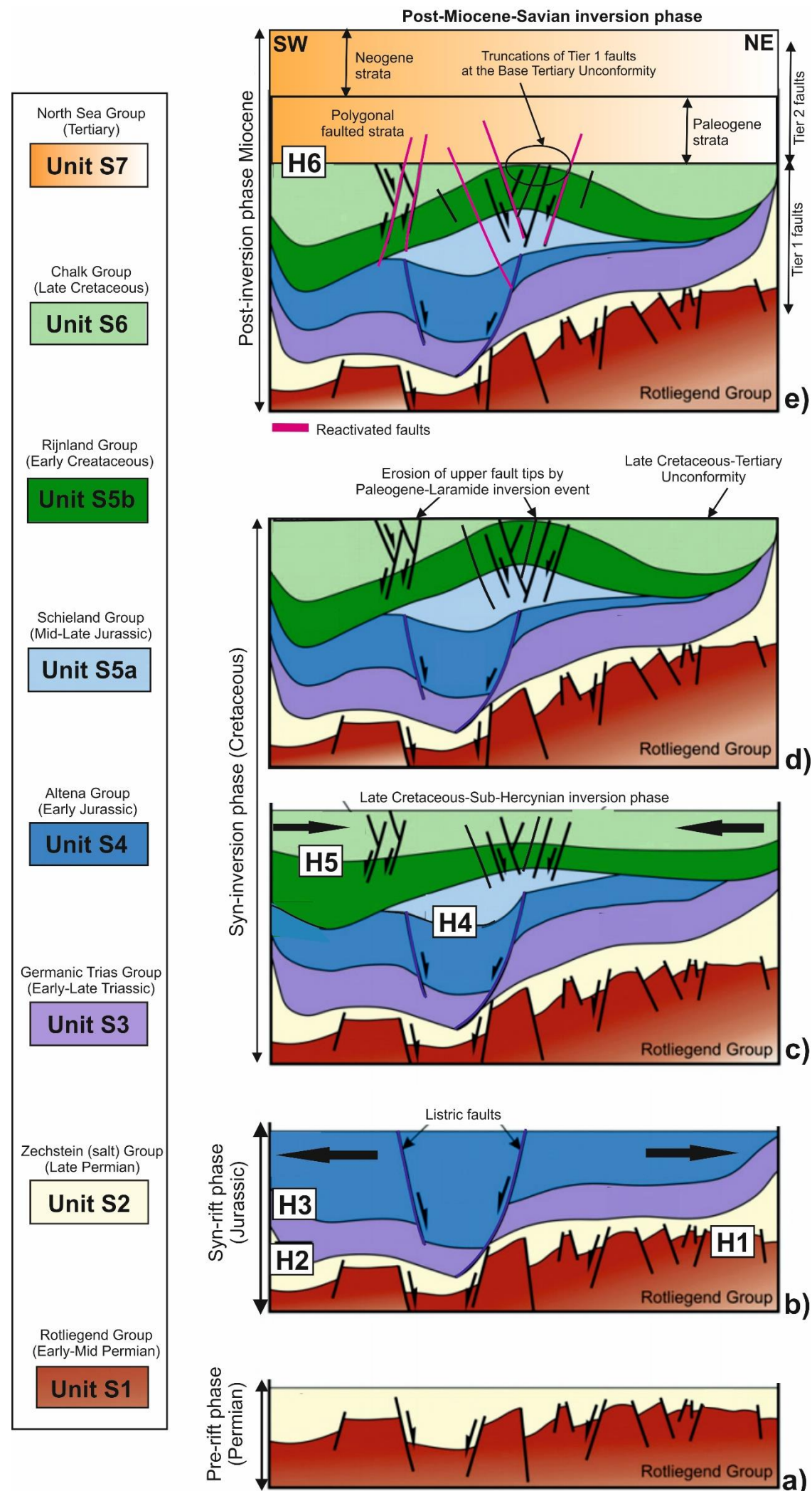
Fig. 5.24. Schematic model for the geological evolution of the study area highlighting the age and reactivation of fault families. a) Pre-rift to rift phase. Listric faults active in during the Jurassic syn-rift phase in association with rift-raft tectonics, b). c) Tier 1 faults occurred during Late Cretaceous Sub-Hercynian inversion, i.e., the time of the formation of major anticlines and deposition of the Chalk Group. d) Period of reactivation of Sub-Hercynian faults (Tier 1 faults) and erosion of their upper fault tips by Paleocene-Laramide erosional event, creating a prominent Late Cretaceous-Tertiary Unconformity (horizon H6). e) Phase of reactivation of some Tier 1 faults into the Paleogene strata during Oligocene-Pyrenian inversion and formation of Tier 2 faults in Paleogene strata. The present-day, post-inversion phase comprises two distinct fault tiers: Tier 1 (Late Mesozoic) and Tier 2 (Paleogene) faults.

A further understanding of reactivation processes will greatly improve petroleum prediction of seal integrity, trap geometry and fluid migration into shallower reservoirs in the Broad Fourteens Basin, Southern North Sea.

5.9. Chapter specific conclusions

Detailed mapping and geometric analyses of normal faults using high-quality 3D seismic and borehole data from the Broad Fourteens Basin, offshore The Netherlands, provided us with insights into the geometry and reactivation histories of Upper Mesozoic to Paleogene supra-salt faults. The key conclusions of this chapter are as follows:

1. In the Broad Fourteen Basin, Southern North Sea, the Late Cretaceous to Paleogene tectonic inversion episodes induced a continuum of internal deformation and contributed significantly to the formation and subsequent reactivation of supra-salt faults. Such a phenomenon had a positive economic impact, as reactivated faults potentially allowed the secondary migration of hydrocarbons into shallower reservoir units.

2. Two distinct tiers of fault geometry are recognised in the chapter study area: a) Tier 1 faults (Late Mesozoic) resulted from local buckling and stretching of outer arc Mesozoic strata during the Late Cretaceous-Paleogene tectonic inversion episodes (i.e. Sub-Hercynian, Laramide, Pyrenean and Savian phases), b) Tier 2 faults (Paleogene) relate to early diagenesis but still record the effect of a Paleogene inversion episode. The geometry and location of underlying anticlinal structures affect the selection of reactivation and growth histories of the interpreted fault tiers.

3. The truncation and lack of near-zero throw values at the Base Tertiary Unconformity, revealed by Tier 1 faults, confirm the erosion of the upper fault tips by a Paleocene-Laramide erosional event. This truncation suggest that Tier 1 faults were active in the Upper Cretaceous Chalk Group before the onset of a Paleocene erosional event in the Southern North Sea.

4. Notable differences in fault throw values are observed between sand- and shale-rich intervals. In sand-rich intervals, fault throws are larger (32 ms or 40.3 m) compared to shale-rich intervals (14 ms or 17.7 m). Hence, families of vertically segmented fault arrays are observed in the throw-depth profiles, as faults propagated through alternating sand-shale intervals.

5. The interpreted fault tiers are segmented, increasing the chances of compartmentalisation or localised fluid flow through fault linkages. In the Broad Fourteens Basin, listric faults provide significant pathways for fluid migrating from pre-Zechstein salt units into Mesozoic strata. Consequently, Tier 1 faults intersecting these deeply-rooted listric faults will potentially allow secondary migration of hydrocarbons into shallower reservoir units.

CHAPTER 6

Shallow fault systems of thrust anticlines responding to changes in accretionary prism lithology (Nankai, SE Japan)

Co-author contributions to the paper:

Tiago Alves (Supervisor): checked for grammatical errors, ensured the scientific content and interpretation was accurate and appropriately presented.

Gregory F. Moore – checked for any errors in the theme of tectono-stratigraphic setting and provided feedback on paper.

6. Shallow fault systems of thrust anticlines responding to changes in accretionary prism lithology (Nankai, SE Japan)

6.1. Abstract

Three-dimensional (3D) pre-stack depth migrated seismic data are used to analyse the geometry and growth of shallow faults associated with tectonic shortening in four (4) prominent thrust anticlines off Nankai, SE Japan. The four thrust anticlines show a trenchward increase in horizontal shortening and deform the seafloor at present. They shortened the overburden strata by 7143 m in the Late Quaternary, reflecting a horizontal shortening of 32.9% in response to plate subduction. A significant number of closely spaced and segmented fault arrays is observed in their hinge regions. Vertically segmented fault arrays with local throw maxima between 5 and 14 m relate to the existence of more competent (strong) intervals, or layers. Incompetent (weak) intervals record relatively small throw values between 2 and 5 m. The presence of closely spaced, segmented fault arrays at shallow stratigraphic levels can have a significant impact on local stress distribution, controlling near-seafloor strain in accretionary prisms as Nankai's. The observed mechanical layering is likely to continue at depth to control the accumulation of tectonic stress in faults posed to reactivate during seismic events.

6.2. Introduction

Offshore SE Japan, the subduction of the Philippine Sea Plate beneath the southeast margin of Eurasia occurs at a variable convergence rate of 4.0 to 6.5 cm/year (Seno et al., 1993; Miyazaki and Heki, 2001; DeMets et al., 2010). This process has caused, since the Pliocene-Pleistocene, large-scale tectonic shortening and uplift of overburden strata above a subducted oceanic slab to form the Nankai accretionary prism, i.e. a

volume of strata that has been scrapped off from the subducting Philippine Sea Plate and accreted together with sediment derived from SE Japan (e.g., Taira, 2001; Miyazaki and Heki, 2001; Bird, 2003; Kimura et al., 2011, 2018). The continuous movement of the subducted Philippine Sea Plate has induced a continuum of internal deformation in the study area that is expressed in the form of imbricate thrust faults, thrust anticlines, pop-up structures, megasplay faults, strike-slip faults and dip-slip faults (e.g., Kimura et al., 2011; Moore et al., 2013; Alves et al., 2014; Lin et al., 2015; Van Tuyl et al., 2015; Azevêdo et al., 2018).

Several studies have shown how local stress fields can control faulting and accretionary prism deformation off Nankai (e.g., Wu et al., 2013; Moore et al., 2013; Van Tuyl et al., 2015; Lin et al., 2015; Chang and Song, 2016). For instance, Moore et al. (2013) and Van Tuyl et al. (2015) suggested that stress decoupling occurs between a shallow regime of extensional normal faulting and a deeper regime of strike-slip faulting and thrusting in both the inner and outer wedge regions of the Nankai accretionary prism. Authors such as Chang and Song (2016) have recently postulated that structures in the inner wedge region of Nankai reflect strike-slip and normal faulting stress regimes as horizontal and vertical stresses show similar magnitudes. In fact, strike-slip and extensional structures are found in both core and regional seismic data from the inner wedge of Nankai. In the outer wedge region, Azevêdo et al. (2018) and Lackey et al. (2020) showed that strike-slip, together with thrusting, are the two major styles of deformation. The outer wedge region of the Nankai accretionary prism thus comprises closely spaced, synthetic forethrusts, antithetic backthrusts and corresponding anticlines that occur, near the seafloor, in association with shallow fault systems.

Despite the growing number of articles addressing the relationship between regional tectonic stresses and SE Japan's structural evolution, the published literature has thus far overlooked the effect of mechanical stratigraphy on fault geometry and growth off Nankai, in great part due to the relative lack of borehole data acquired in its outer wedge region. This results in a relative underrepresentation of the true structural evolution of the Nankai Trough as a whole; outcrop and seismic data in other regions of the world often relate the styles and geometries of faults with mechanical-stratigraphic differences in the host rocks (Childs et al., 1996; Ferrill and Morris, 2003, 2008; Childs et al., 2009; Ferrill et al., 2014; Tvedt et al., 2013; Ferrill et al., 2017; Libak et al., 2019). This is an important caveat, as the relationship between faulting and mechanical stratigraphy can be used either to predict fault style and geometry or, conversely, interpret mechanical stratigraphy based on characterisation of the fault styles and geometries (Ferrill and Morris, 2003, 2008; Ferrill et al., 2017). This chapter explores a set of shallow fault systems from areas dominated by thrust anticlines in the outer wedge region of the Nankai accretionary prism (SE Japan), aiming to address the following questions:

a) What are the geometries and styles of shallow fault populations in areas dominated by tectonic shortening such as the Nankai accretionary prism?

b) What mode(s) of fault propagation and growth are observed in the successions blanketing the outer wedge region of Nankai?

c) Can the geometry and distribution of shallow fault populations in the uppermost strata of the Nankai accretionary prism provide information about the mechanical stratigraphy of strata in this region?

In this chapter, the terms incompetent (weak) and competent (strong) were use to describe the local mechanical stratigraphy. Incompetent (weak) intervals, or layers, are

ductile and can accommodate greater amounts of pre-failure strain than competent (strong) intervals under the same conditions. The latter (stronger) intervals tend to resist deformation and accommodate little deformation before brittle failure (Ferrill and Morris, 2008; Ferrill et al., 2017). Moreover, incompetent intervals can act as detachments that cause decoupling and prevent propagation of faults across specific intervals, resulting in a preferable horizontal propagation of faults to the detriment of their vertical growth (Pascoe et al., 1999; Bahroudi et al., 2003; Withjack and Callaway, 2000; Richardson et al., 2005; Gabrielsen et al., 2016).

6.3. Chapter specific dataset and methods

6.3.1. Seismic data

Three-dimensional (3D) pre-stack depth migrated seismic data were used in this chapter. The data were acquired in the outer wedge region of the Nankai accretionary prism, SE Japan, between 33.0o -33.2o N and 136.5o -136.8∘E (Fig. 2.6). The survey area is oriented at N150o and covers an area of approximately 12 km by 23 km in water depths ranging between 2500 m and 5000 m. The seismic data were acquired using dual airguns and an array of four 4500 m-long streamers deployed with a spacing of 150 m. This configuration provided a 30-fold coverage and a maximum lateral resolution of 12.5 m. Data were recorded with a 2 ms vertical sampling interval and a 12.5×18.75 m bin size. After being processed, seismic data is displayed on interpretation workstations with a 5 m vertical sampling - the minimum fault offset resolved on-screen varies from 2 m to 5 m. The seismic data was zero-phase, pre-stack depth migrated and displayed with a normal positive polarity (i.e., following SEG's European convention), so that an increase in acoustic impedance is represented by a red seismic reflection (Moore et al., 2009).

In the interpreted seismic volume, shallow faults and thrust-related anticlines are well preserved in accretionary prism sediments (Unit II). Vertical seismic resolution approaches 6 m in shallow slope basin sediments (Unit I) based on the dominant wavelength of approximately 24 m (Alves et al., 2014). As previously mentioned, fault offsets between 2 m and 5 m can be distinguished using the interpreted seismic volume. Vertical resolution in Unit II approaches 14 m based on the dominant frequency of 40 Hz and velocity of 2200 m/s. Fault offsets of 4–5 m can be recognised at this level. The overall quality of the seismic dataset is good; however, some of the reflections are weak in the deepest parts of Unit II, where complex thrust fault planes occur.

6.3.2. Seismic interpretation

Shallow faults and associated thrust anticlines were identified and mapped using Schlumberger's Petrel®. The seafloor horizon was mapped throughout the 3D seismic volume. From the seafloor structural map and seismic sections, Four (4) major thrust anticlines (A to D) were identified. In addition, three (3) horizons (H1 to H3) were mapped across the thrust anticlines to quantify any variations in the spatial and temporal horizontal shortening of these same anticlines.

Faults occurring at a stratigraphic depth interval between 20 and 1000 m below the sea floor (mbsf) were interpreted and assessed their vertical growth styles via the collection of fault throws along their strikes. The measured throw values were plotted against depth to assess their nucleation points, and vertical growth styles, as well as gather information about the competence of sediments they had affected. Throw-depth (T-Z) profiles offer information on the rock competence, nucleation, growth, segmentation, and linkage of individual faults (Baudon and Cartwright, 2008; Peacock and Sanderson, 1991; Maunde and Alves, 2020). Discrepancies in throw gradients commonly result

from mechanical heterogeneities, fault reactivation and fault segmentation (Childs et al., 1996; Baudon and Cartwright, 2008; Laubach et al., 2009).

6.3.3. Shortening and strain measurements

Horizontal shortening (Sh) and strain (e) experienced by accretionary prism strata were measured by line-length balancing (Dahlstrom, 1969) on a series of dip-line sections spaced approximately 500 m along the strike of Thrust Anticlines A to D. Horizontal shortening was measured by considering the length of the folded and faulted horizon (Lo) between the section pinpoints minus the present-day bed length (Lf) between the same pinpoints (Fig. 6.1). It is worth noting, however, that the absolute value of shortening depends on the depth of reference chosen for the measurement, which may change along the length of the thrust anticlines. The strain values associated with the horizontal shortening were also computed using Equation 6.1 below:

$$e = (Lf - Lo)/Lo \qquad\qquad \text{Equation 6.1}$$

where (e) is the strain, (Lf) is the present-day bed length after deformation, and (Lo) is the initial bed length before deformation (Fig. 6.1).

Strain (e) measurements were completed for the four (4) seismic horizons mapped in the study area through thrust anticlines A to D. The measured strain values were plotted against distance, i.e. strain distance (e-x) plots, as routinely used for extensional fault systems, e.g. in throw-distance (T-x) plots (Baudon and Cartwright, 2008; Maunde and Alves, 2020). From the measured strain, cumulative strain and shortening for the horizons mapped in Thrust Anticlines A to D could be computed.
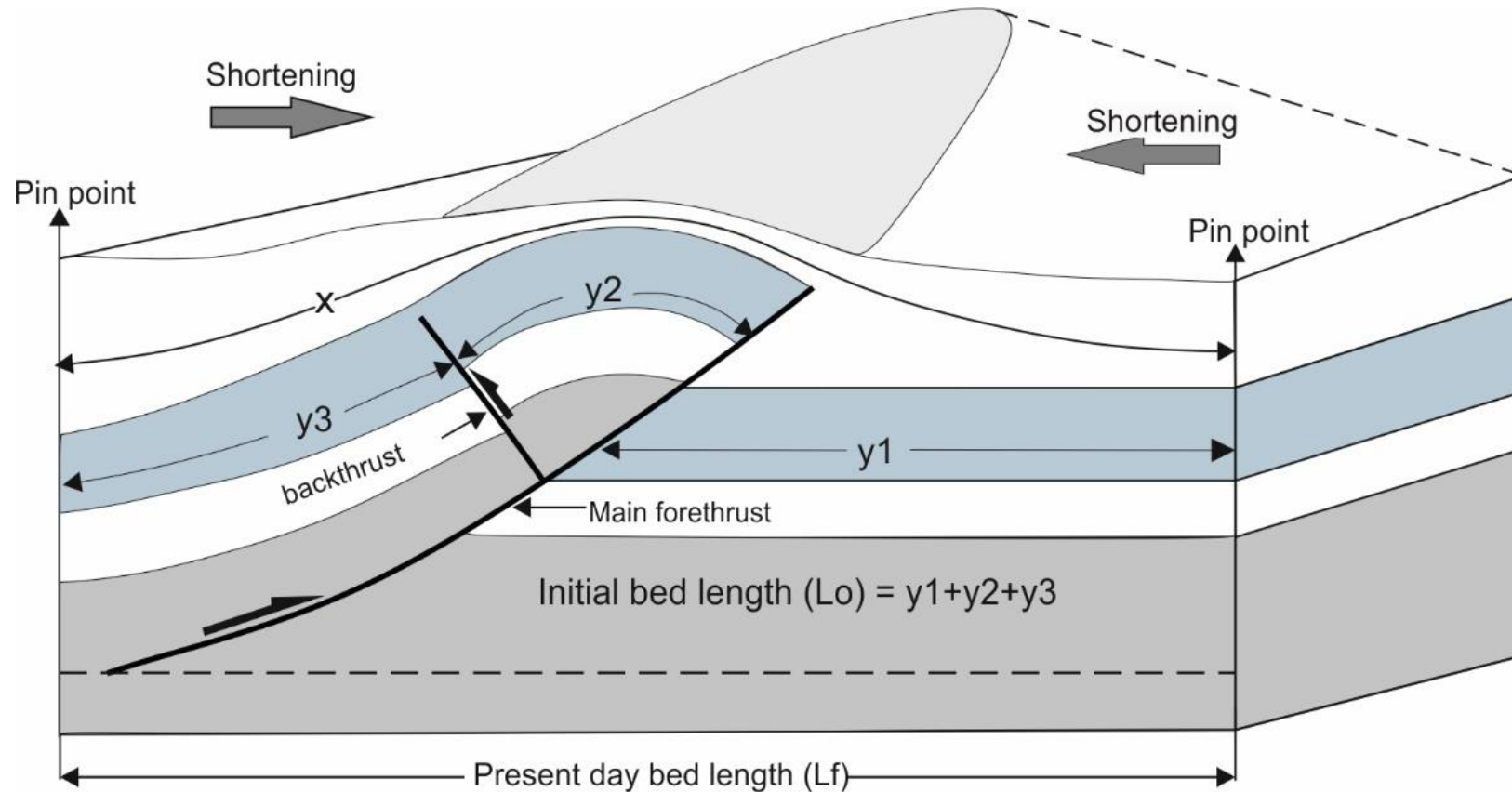
Fig. 6.1. Schematic section highlighting strain-distance (e-x) measurements through folded and faulted strata using line-length balancing techniques. Initial bed length, Lo, in thrusted strata is expressed as Lo = y1 + y2 + y3, while in the overlapping strata is Lo = x. Lf is the present-day bed length after deformation.

The seismic signal is often weak in the vicinity of thrust faults, creating uncertainty in the location of fault planes and, hence, in the position of horizon cut-offs. In the Nankai seismic volume, a single fault plane was usually interpreted by positioning it mid-way through the region of poor data quality. Mapped seismic horizons were extrapolated to intersect the fault plane.

Errors are associated with the digitisation of the horizon upon which shortening, and strain are measured, either by slightly increasing or decreasing the bed length, affecting the calculated values of strain, and shortening across the interpreted thrust anticlines. Uncertainty associated with the measurement of fault-throw values may arise from the vertical sampling rate. The sampling interval, rather than the vertical stratigraphic resolution, determines accuracy when matching two correlative seismic reflection peaks or troughs (Baudon and Cartwright, 2008).

Uncertainties associated with the measurement of fault-throw values may arise either by slightly increasing or decreasing the position in depth of the recorded displacements. Errors associated with spurious velocity estimates may also affect the throw values when converted to meters. These limitations will affect the absolute value of estimated thrust anticlines shortening and fault displacements. However, the approach used in this chapter to quantify the variations in thrust anticlines shortening and fault displacements is robust considering the high resolution (and quality) of the seismic dataset.

6.4. Interpreted seismic units

The Nankai accretionary prism consists of slope basin sediments, accreted and underplated trench-fill turbidite facies transported axially along the Nankai Trough because of subduction of the Shikoku Basin crust during the Pliocene-Pleistocene (e.g., Kinoshita et al., 2010; Kopf et al., 2010). Two (2) seismic units that comprise slope

basin sediments (Unit I) and accretionary prism strata were interpreted in this Chapter (Unit II; Fig. 6.3).

6.4.1. Unit I: Slope basin sediments

Unit I comprises fine-grained turbidites dated as latest Pliocene to Recent and deposited in slope aprons (Kimura et al., 2011; Alves et al., 2014) (Fig. 6.3). The unit is discontinuous in the outer wedge of the Nankai accretionary prism, being bathymetrically confined by thrust anticlines (Fig. 6.3b). In seismic data, it forms a package of high frequency, continuous and moderate- to high-amplitude reflections accumulated above an angular unconformity that separates it from the underlying Unit II. This latter unit comprises strata belonging to the upper part of the accretionary prism (Kimura et al., 2011) (Fig. 6.3b). Three sub-units including Units Ia, Ib and Ic are recognised in the study area (Fig. 6.3ciii).

Silty mud and turbidites with multiple ash layers comprise the first of the sub-units, Unit Ia (Kimura et al., 2011). They are imaged in seismic data as successions of continuous high-amplitude reflections (Fig. 6.3ciii). The base of Unit Ia coincides with a relatively thick mass-transport deposit (MTD 6) at IODP Site C0018A (Fig. 6.3cii). Unit Ib comprises coarse turbidite and ash layers with interbedded silty mud and clay (Expedition 333 Scientists, 2012; Kimura et al., 2011; Strasser et al., 2012; Alves et al., 2014). It comprises a succession of low-amplitude reflections of poor to moderate continuity in seismic data (Fig. 6.3ciii). Lastly, Unit Ic consists of greenish/grey silty clay with beds of sand, sandy silt, silt, and volcanic ash layers (Kimura et al., 2011; Strasser et al., 2012). On seismic data, Unit Ic comprises a low- to moderate-amplitude package (Fig. 6.3ciii).
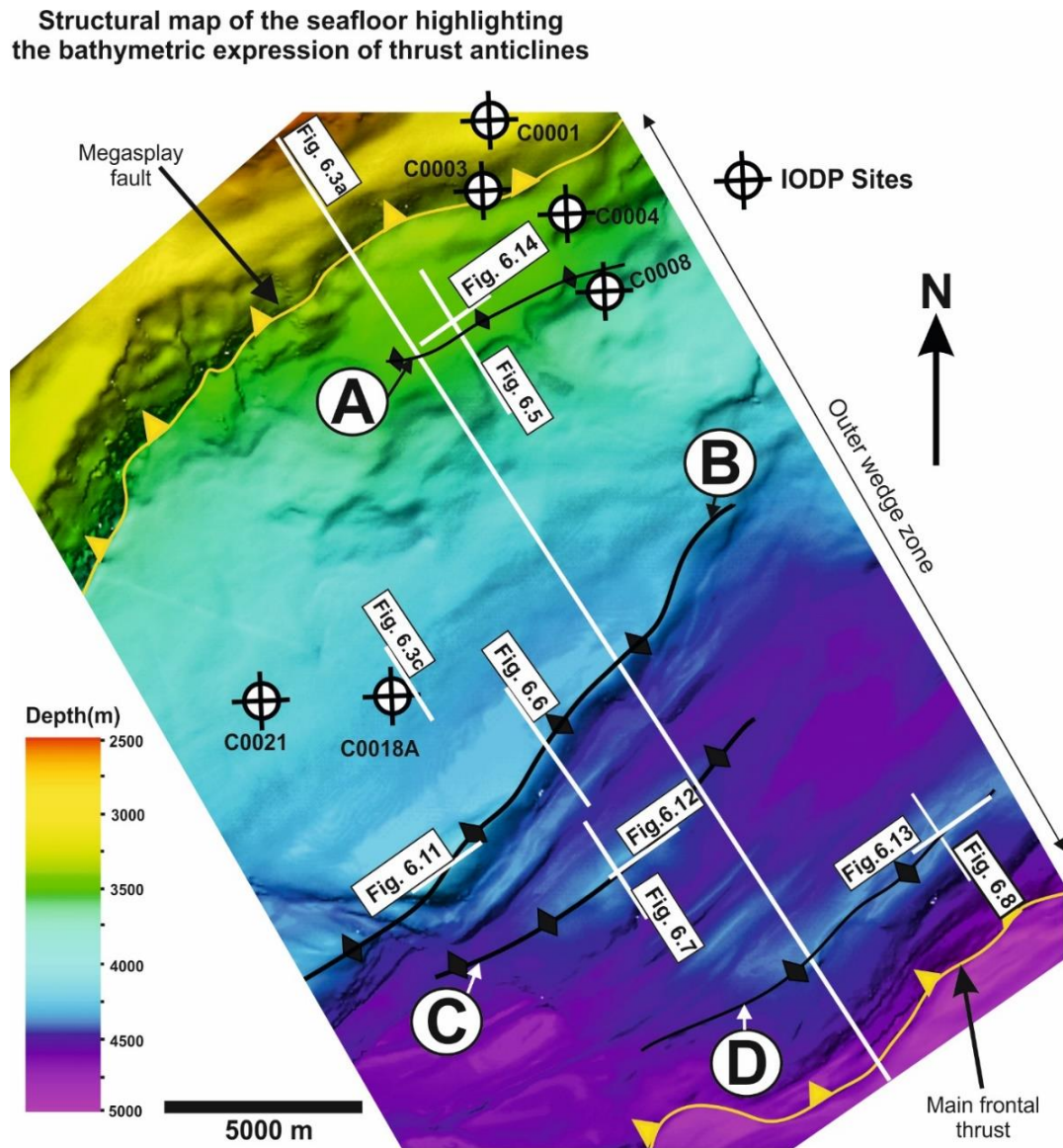
Fig. 6.2. Structural map of the seafloor highlighting the bathymetric expression of thrust anticlines, trending perpendicular to the regional bathymetric slope. Seismic profile lines and key Integrated Ocean Drilling Programme (IODP) Sites are shown on the map. Letters A, B, C and D on the map represent Thrust Anticlines A to D.

6.4.2. Unit II: Accretionary prism sediments

Unit II forms the upper part of the accretionary prism (Fig. 6.3b). It comprises thrusted hemipelagic mudstones and sands interbedded with volcanic ash and tuffs (Expedition 316 Scientists, 2009; Park et al., 2010). The unit is imaged as an interval of discontinuous and moderate amplitude reflections, showing moderate to low frequency, that are highly deformed by thrust faults and folds (Figs. 6.3b). The upper part of Unit II comprises high-velocity overthrusted sediments (e.g., Unit A of Park et al., 2010), while the lower part comprises of low-velocity sediments deposited above underthrusted marine sediments (e.g., Unit B of Park et al., 2010).

6.5. Geometry and shortening of thrust anticlines

6.5.1. Geometry of thrust anticlines

Seismic imaging shows that the outer wedge region of the Nankai accretionary prism is characterised by its closely spaced, NW dipping synthetic forethrusts, SE dipping antithetic backthrusts and SE-verging thrust anticlines with a linear NE-SW trend (Figs. 6.2 and 6.3b).

The latter thrust anticlines were formed orthogonally to the regional bathymetric slope (Figs. 6.2 and 6.4). On the seafloor structural map in Figs. 6.2 and 6.4, these thrust anticlines can be traced along strike, having well-developed bathymetric expression, an evidence for their active growth at present. Thrust anticlines have a relatively simple bathymetric expression on the seafloor, but more complex thrusting occurs at depth (Fig. 6.3b). The crests of the anticlines are separated by 3.2–5.5 km, and synclinal basins (i.e. synclines located between the thrust anticlines) contain up to 350 m of growth strata with significant thinning and onlap onto the crests of the anticlines.
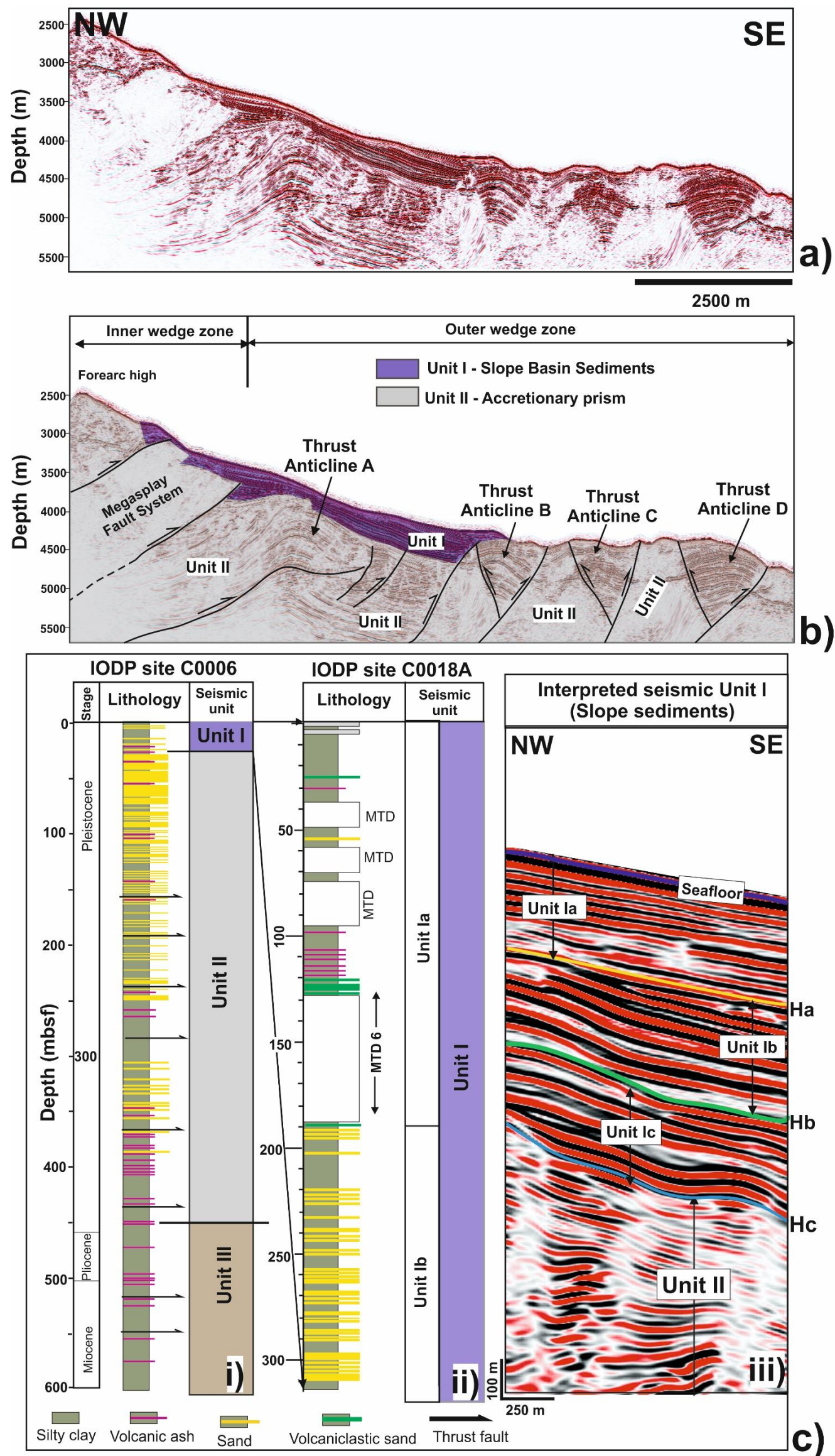
Fig. 6.3. a) Uninterpreted and **b)** interpreted seismic section across the deep-water Nankai accretionary prism highlighting the structural styles, interpreted seismic units (Units I and II) and the four Thrust Anticlines A to D studied in this chapter. c) Seismic-stratigraphic correlation amongst the interpreted seismic units, stratigraphic ages and lithologies in the Nankai accretionary prism, SE Japan. Unit I represent relatively undeformed slope sediments (Expedition 333 Scientists, 2012; Kimura et al., 2011; Alves et al., 2014; Strasser et al., 2014). Unit II are overthrusted sediments (Park et al., 2010). IODP well C0018A highlights the subdivision of Unit I into Units Ia, Ib and Ic based on Strasser et al. (2014) and Alves et al. (2014). IODP Site C0006 (Expedition 316 Scientists, 2009) which is ~4 km SE from the seismic profile (see Fig. 2.6c) was correlated with the seismic unit II interpreted in this chapter.

Four major thrust anticlines (A to B) were investigated in the study area (Figs. 6.2, 6.3b and 6.4).

6.5.1.1. Thrust Anticline A

Thrust Anticline A is the most landward of the thrusts in the study area. Compared to Thrust Anticlines B to D, it comprises a much broader, longer wavelength anticline with a moderate-displacement curved forethrust in its front limb and anticline core (Figs. 6.3b and 6.5). Thrust Anticline A forms the landward boundary of the outer wedge region of Nankai, near the Megasplay Fault Zone (Figs. 6.2, 6.3b and 6.4). Thrust Anticline A is presently covered by slope-basin sediments (Unit I; Figs. 6.3b and 6.5), and does not have a bathymetric expression, compared to Thrust Anticlines B to D (Figs. 6.2, 6.3b and 6.4).

6.5.1.2. Thrust Anticline B

Thrust Anticline B extends outside of the study area towards the southwest (Figs. 6.2 and 6.4). It is linear in plan view and formed above a seaward-verging forethrust. The forethrust terminates upwards, with some segments forming seafloor scarps (Figs. 6.2, 6.3b and 6.4). An antithetic backthrust, which intersects the forethrust, deforms the back limb of the anticline and dies out near the seafloor (Figs. 6.3b and 6.6

Thrust Anticline B can be traced along strike on the seafloor for at least 10 km, developing a bathymetric high up to 102 m in relief, and thus revealing active growth (Figs. 6.4 and 6.6). The thrust anticline is at least 1.4 km wide and forms a linear NE-SW trend that is perpendicular to the bathymetric slope (Figs. 6.2 and 6.4).
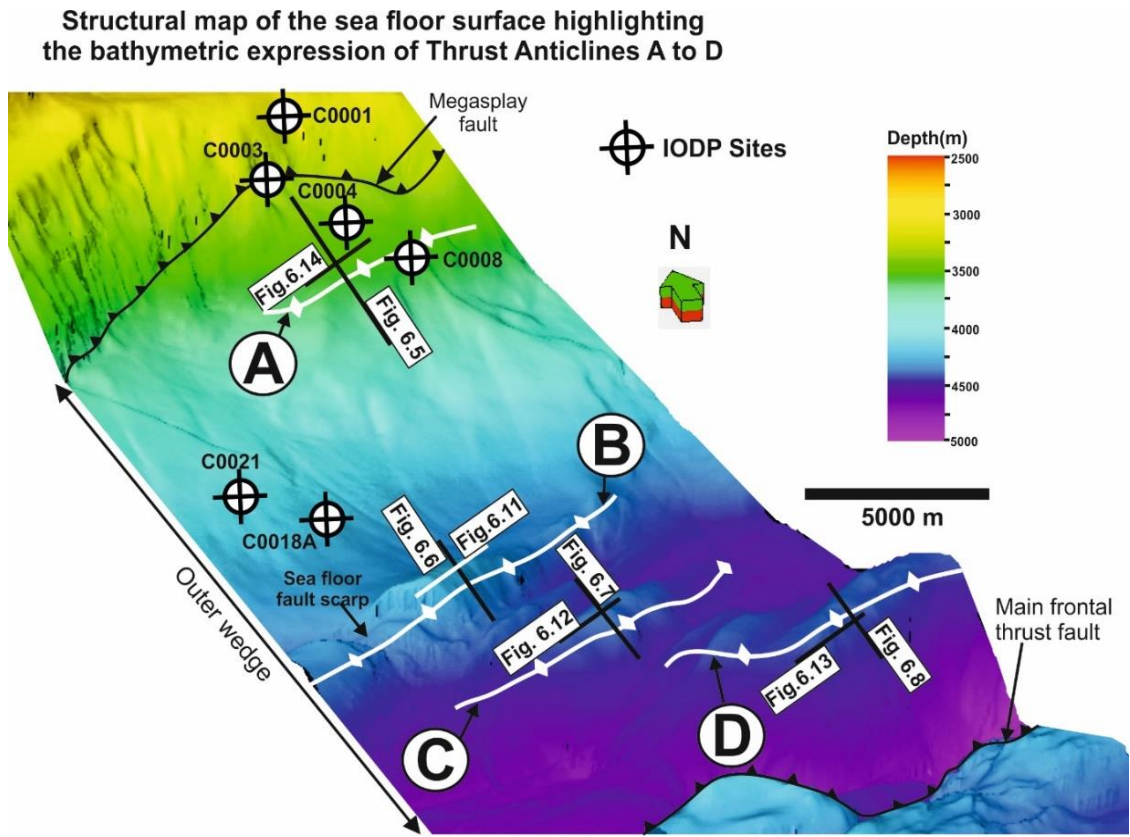
Fig. 6.4. 3D seafloor structural map of the study area highlighting the bathymetric expression of the four studied thrust anticlines (A to D) with a linear NE-SW trend, perpendicular to the regional bathymetric slope. Thrust Anticlines B, C and D deform the modern seafloor and develop corresponding bathymetric highs that are up to 102 m, 113 m, and 182 m in relief. Thrust Anticline B developed a seafloor fault scarp. Seismic profile lines and key Integrated Ocean Drilling Programme (IODP) Sites are shown on the map. The letters A, B, C and D on the map represent Thrust Anticlines A to D.
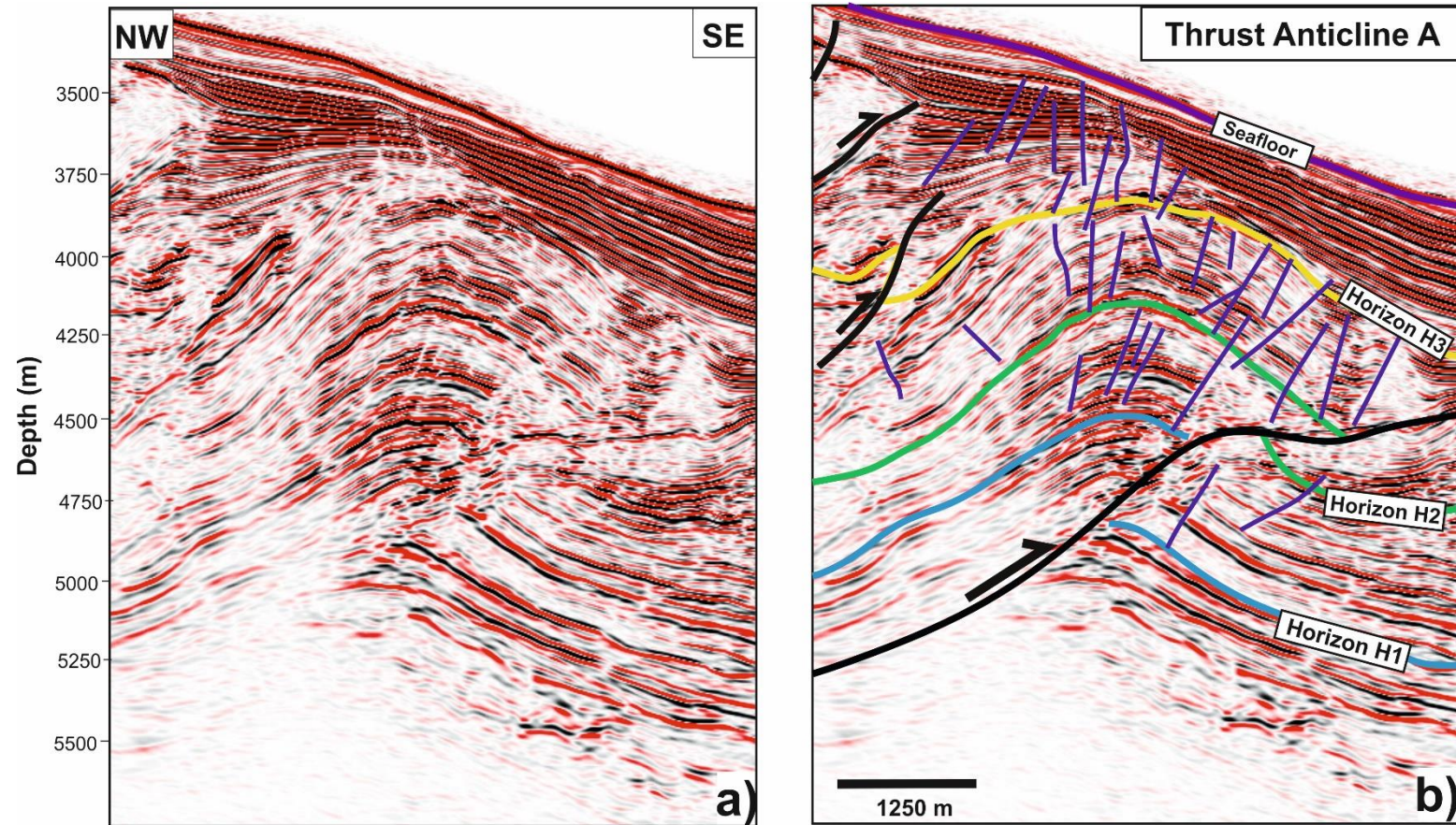
Fig. 6.5. Uninterpreted and interpreted seismic section across the most landward Thrust Anticline A highlighting the interpreted horizons, shallow faults and major (curved) forethrust on the front limb and in the anticline core. The shallow faults are in the uppermost part of the accreted (Unit II) and slope (Unit I) sediments. The location of the seismic section is shown in Figs. 6.2 and 6.4.

6.5.1.3. Thrust Anticline C

Thrust Anticline C can be traced for at least 6.0 km along strike, is 1.1 km wide, and creates bathymetric relief of up to 113 m (Figs. 6.2, 6.4 and 6.7). It consists of two closely spaced thrusts. The seaward-verging forethrust dominates the structure. A second backthrust cuts the backlimb of the frontal thrust and dies out upwards, with no faults reaching the seafloor (Figs. 6.3b and 6.7). Thrust Anticline C is linear in plan view and shows a dominant NE trend.

6.5.1.4. Thrust Anticline D

Thrust Anticline D is the most distal of thrusts and extends outside the seismic dataset towards the northeast (Figs. 6.2 and 6.4). It forms the oceanward boundary of the outer wedge of Nankai accretionary prism, i.e. the boundary of the main frontal thrust, which is at least 1.7 km wide on the seafloor (Figs. 6.2 and 6.4). Thrust anticline D is also a composite structure consisting of two closely-spaced thrusts. The seaward-verging forethrust dominates Thrust Anticline D. An antithetic backthrust deforms the back limb of the anticline and dies out upwards, with no faults offsetting the seafloor (Figs. 6.3b and 6.8). Thrust Anticline D can be traced along strike for at least 6.0 km, forming a bathymetric high of up to 182 m (Figs. 6.3, 6.4 and 6.8).

6.5.2. Spatial variations in anticline shortening

The along-strike variations in the shortening of thrust anticlines are illustrated with reference to the strain-distance (e-x) profiles in Fig. 6.9. Strain distribution in Thrust Anticlines A and C decreases towards their tips, showing a broadly bell-shaped distribution profile that reflects a key characteristic of structures that grow by lateral propagation (Jolly et al., 2016) (Fig. 6.9a, c). For Thrust Anticlines B and D, strain distribution extends outside of the interpreted seismic volume (Fig. 6.9b, d).
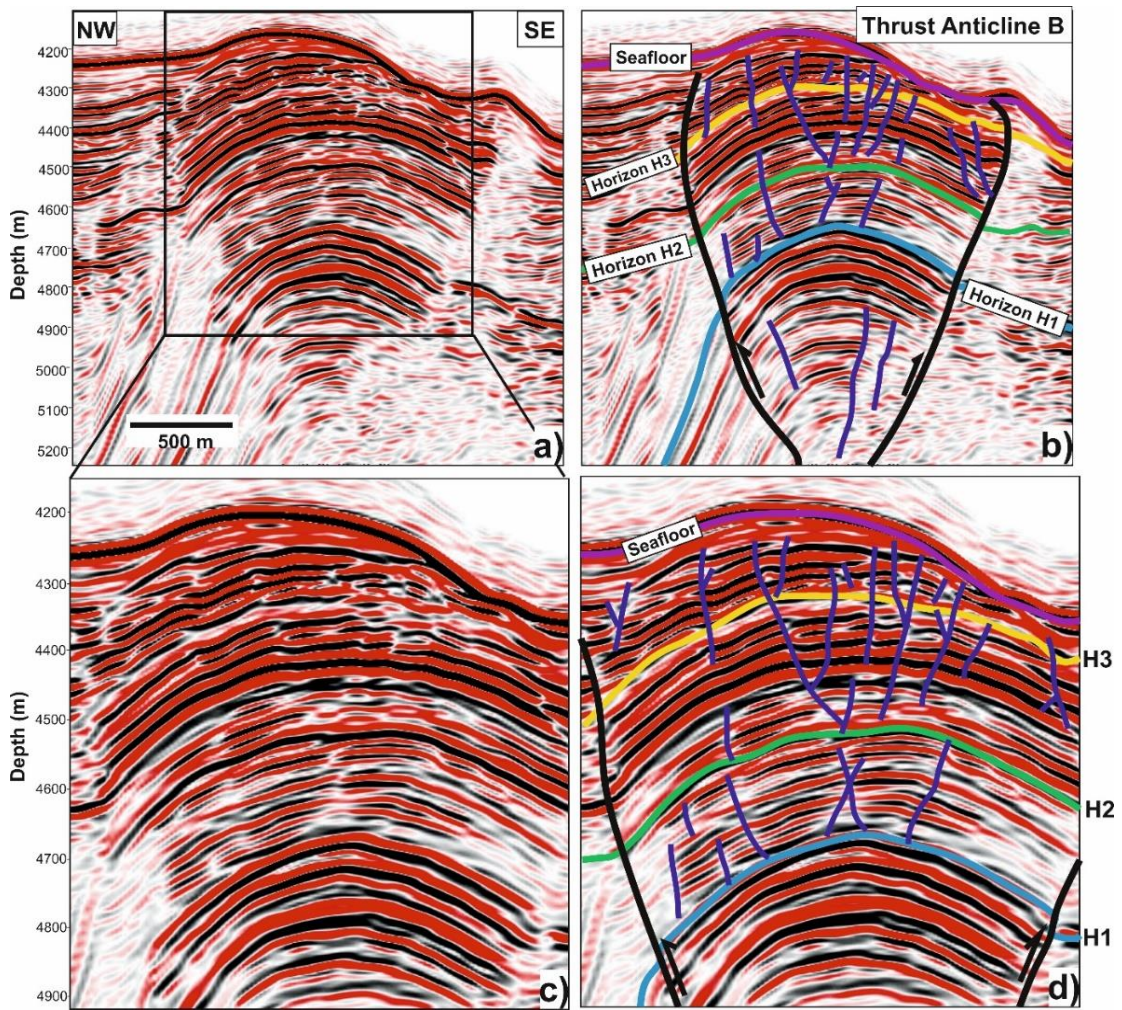
Fig. 6.6. Uninterpreted and interpreted seismic sections across Thrust Anticline B highlighting the geometry of major thrust and shallow fault populations. The shallow faults are in the hinge region of the thrust anticline. These faults are closely spaced and vertically segmented, with some propagating and linking with other faults. The location of the seismic sections is shown in Figs. 6.2 and 6.4.
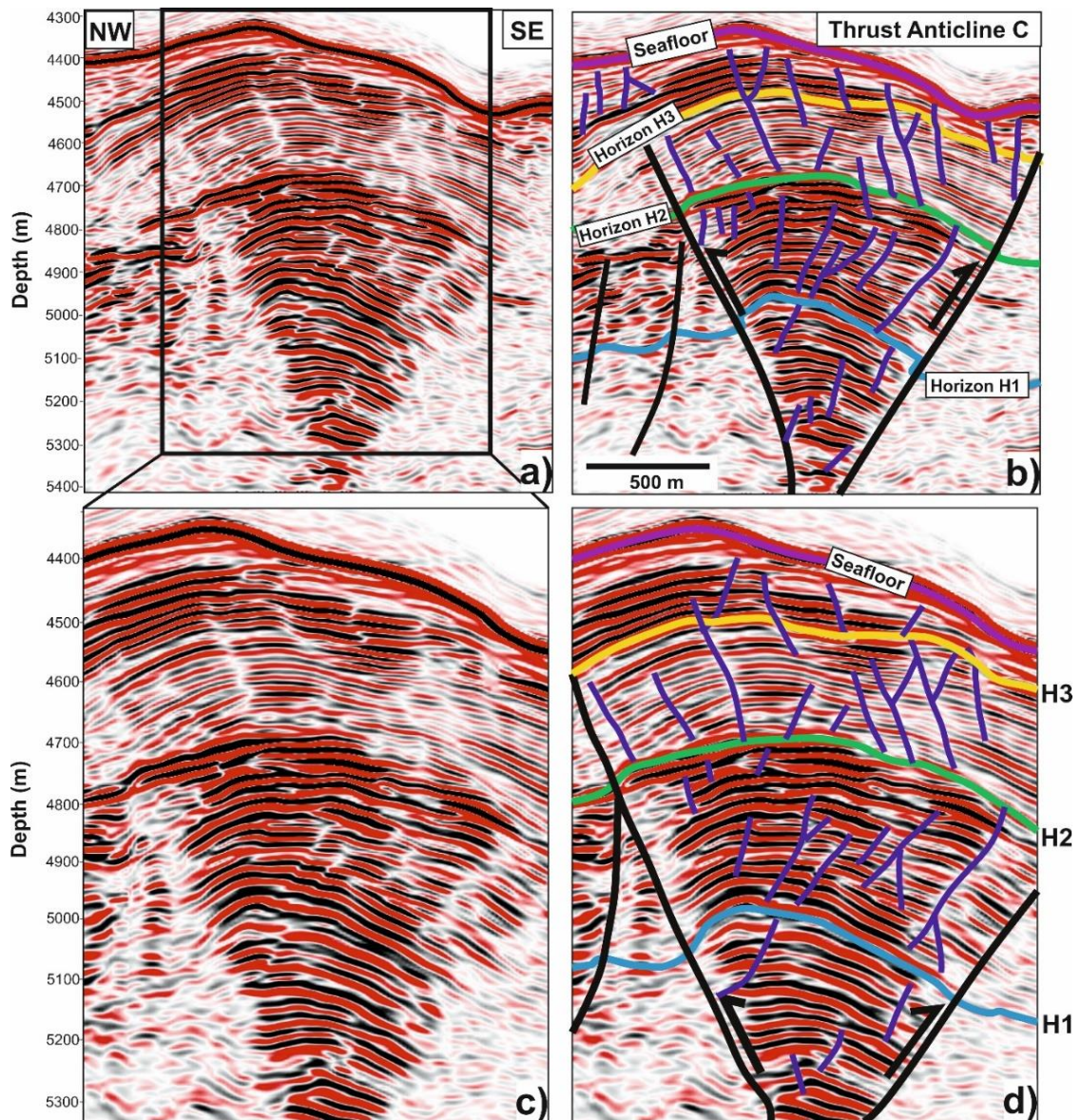
Fig. 6.7. Uninterpreted and interpreted seismic sections across Thrust Anticline C highlighting the interpreted horizons, major thrust faults, and shallow faults. The shallow faults are chiefly located in the hinge region of the thrust anticline. These faults are vertically segmented and offset strata at shallow stratigraphic levels, with some propagating and linking with other faults. The location of the seismic sections is shown in Figs. 6.2 and 6.4.
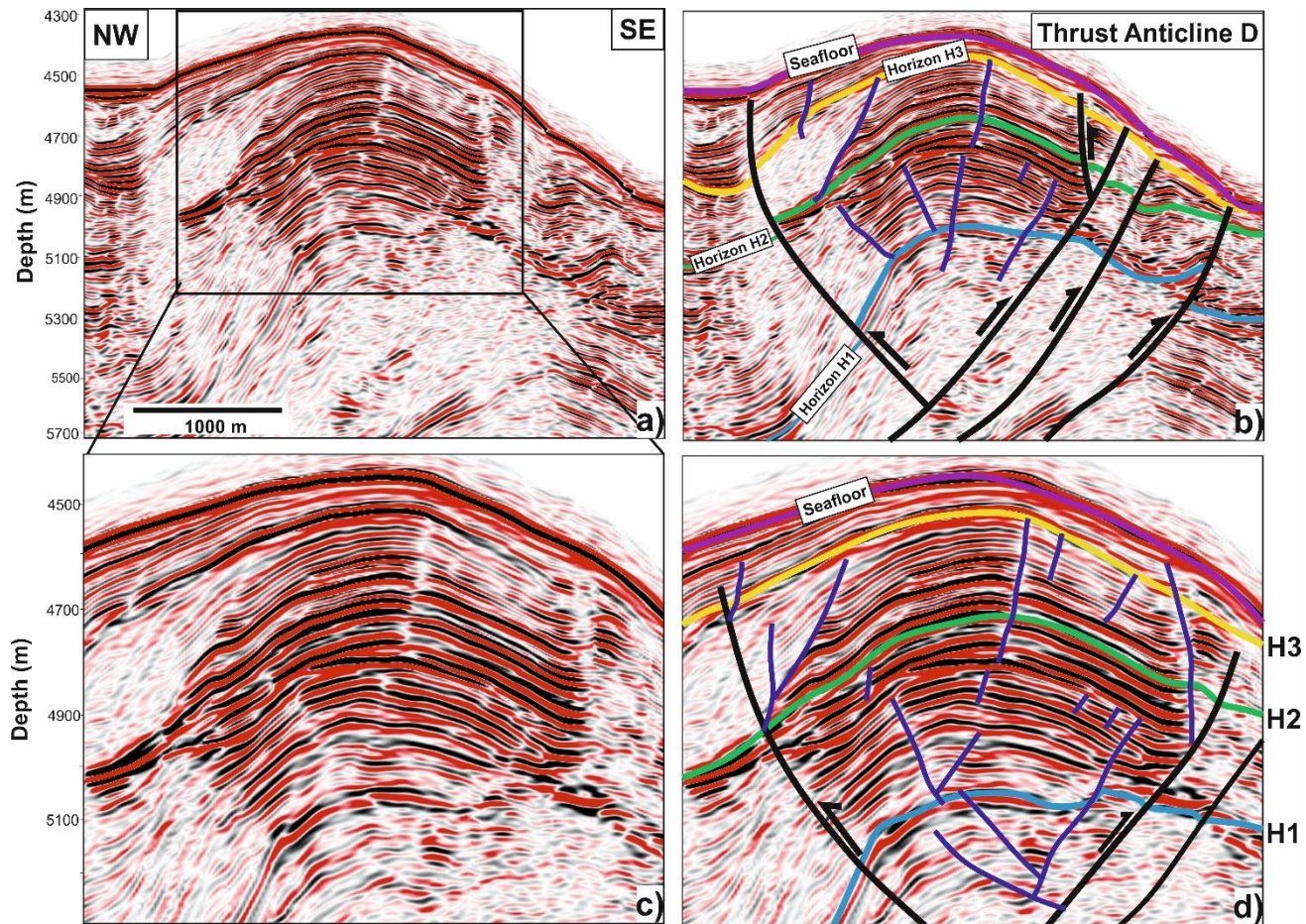
Fig. 6.8. Uninterpreted and interpreted seismic sections across the most seaward Thrust Anticline D highlighting the interpreted horizons, major thrust faults, and shallow faults. The shallow faults are in the uppermost part of the accreted sediments (Unit II), in the hinge region of the thrust anticline. These faults are closely spaced and segmented, with some propagating and linking with other faults. The location of the seismic sections is shown in Figs. 6.2 and 6.4.

Strain distribution in the mapped horizons increases with depth – values are larger in the older horizons and smaller in the younger horizons, reflecting growth of the Thrust Anticlines A to D through time (Fig. 6.9).

Local strain minima are observed between regions of strain maxima (Fig. 6.9). Such local minima in fault systems are typically interpreted as the signature of fault segment linkage (Baudon and Cartwright, 2008; Maunde and Alves, 2020). The relatively smaller strain values for Thrust Anticline B at 8.0 km along strike coincide with the position where the main thrust fault offsets the seafloor (Figs. 6.2 and 6.4). Shortening is always at a minimum at this location in Thrust Anticline B (Fig. 6.9b). In addition, the strain (e) is always at a maximum around 6.0 km along strike, including at the level of the present-day seafloor (Fig. 6.9b).

Strain maxima and minima are not always in the same location for each mapped seismic horizon (Fig. 6.9). For example, strain maxima in H1 and H2 horizons correlate with strain minima at the seafloor at 1.0 km along the strike of Thrust Anticline B (Fig. 6.9b). Furthermore, at 3.0 km along this same thrust anticline, strain maxima in horizon H1 correlate with strain minima in horizons H2, H3 and near the seafloor. At 4.0 km, a broad strain minimum in the older horizon H1 corresponds with a strain maximum in horizons H2, H3 and at the seafloor (Fig. 6.9b). In Thrust Anticlines C and D, along-strike variations in strain show local strain minima between regions of strain maxima (Fig. 6.9c, d). This character clearly indicates linkage between fold segments (see Jolly et al., 2016).

6.5.3. Temporal variations in anticline shortening

Temporal variations in the shortening of thrust anticlines are illustrated with reference to the cumulative strain-distribution profiles in Fig. 6.10.
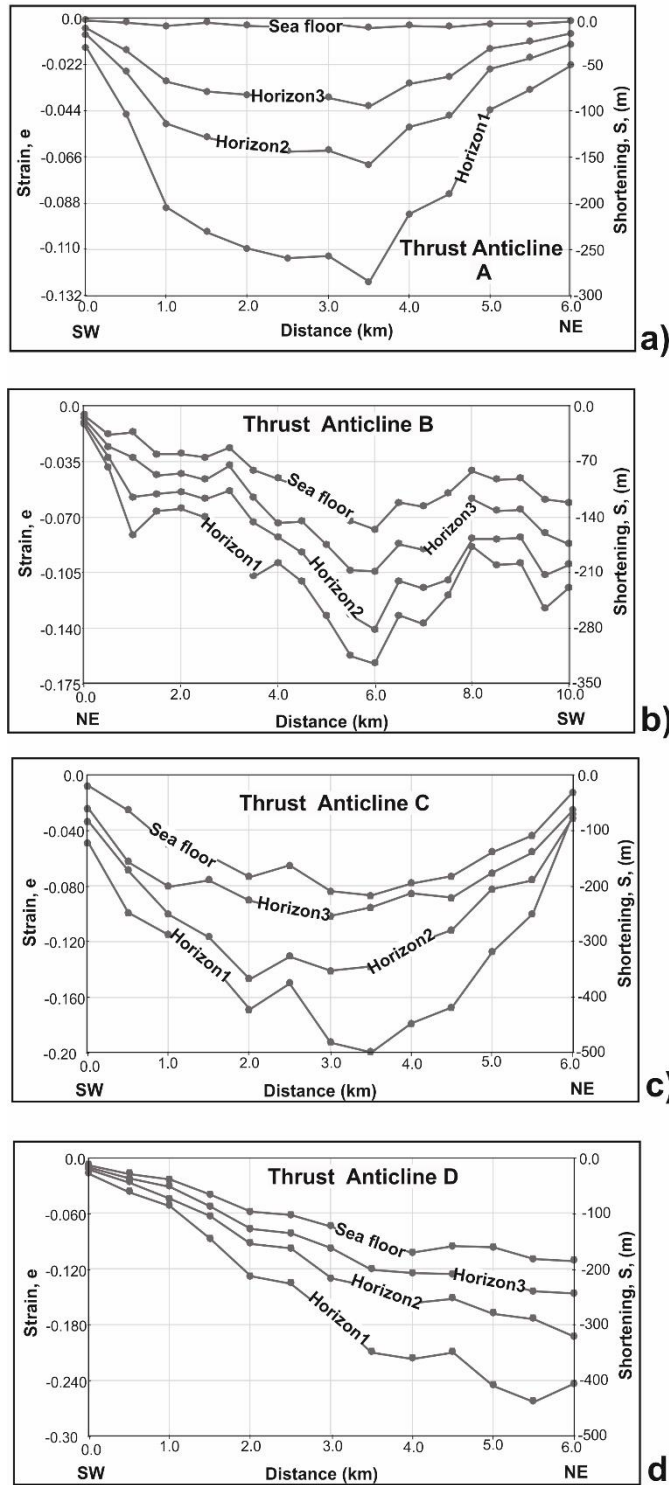
Fig. 6.9. Strain–distance (e-x) plots illustrating the along-strike variations in the shortening of thrust anticlines at the level of the mapped horizons. Strain distribution in the mapped horizons increases with depth (i.e., it is higher in the older horizons and lower in the younger horizons), reflecting growth of the interpreted thrust anticlines through time.

The relatively poor seismic signal below horizon H1 makes it difficult to identify and map additional seismic horizons to precisely constrain the onset of tectonic shortening in the Nankai accretionary prism (Fig. 6.3b). Thus, this chapter focused on calculating shortening for strata at H1 level or above, i.e. for strata that are upper Quaternary in age. Based on the mapped horizons, shortening started prior to horizon H1 as revealed by the greater shortening values recorded at this level across all the thrust anticlines (see Lackey et al., 2020) (Figs. 6.9 and 6.10).

Thrust anticlines B and C record cumulative shortenings of 1524 m and 1902 m, generating relatively moderate bathymetric highs of 102 m and 113 m, respectively (Figs. 6.6, 6.7 and 6.10b, c). The most seaward Thrust Anticline D records the greatest cumulative shortening of 2478 m and developed bathymetric relief up to 182 m in height (Figs. 6.8 and 6.10d). The most landward Thrust Anticline A has shortened the seismic section by 1239 m and is presently buried by slope-basin sediments (Unit I; Figs. 6.3b and 6.5). Hence, it records the least cumulative shortening when compared with Thrust Anticlines B to D (Fig. 6.10). Thrust Anticline A consists of a single thrust (forethrust), so the accumulated shortening is expected to be relatively low compared to the more seaward Thrust Anticlines B to D, which generated both forethrust and backthrusts (Figs. 6.3b, 6.5, 6.6, 6.7 and 6.8).

The four studied thrust anticlines (A to D) have shortened the overburden strata by 7143 m during the late Quaternary, reflecting a horizontal shortening of 32.9% in response to plate subduction at Nankai. When compared with the results in Lackey et al. (2020), these values indicate that ~ 40% of the tectonic shortening accommodated in the outer accretionary prism is relatively young, postdating the already Late Quaternary Horizon H1.
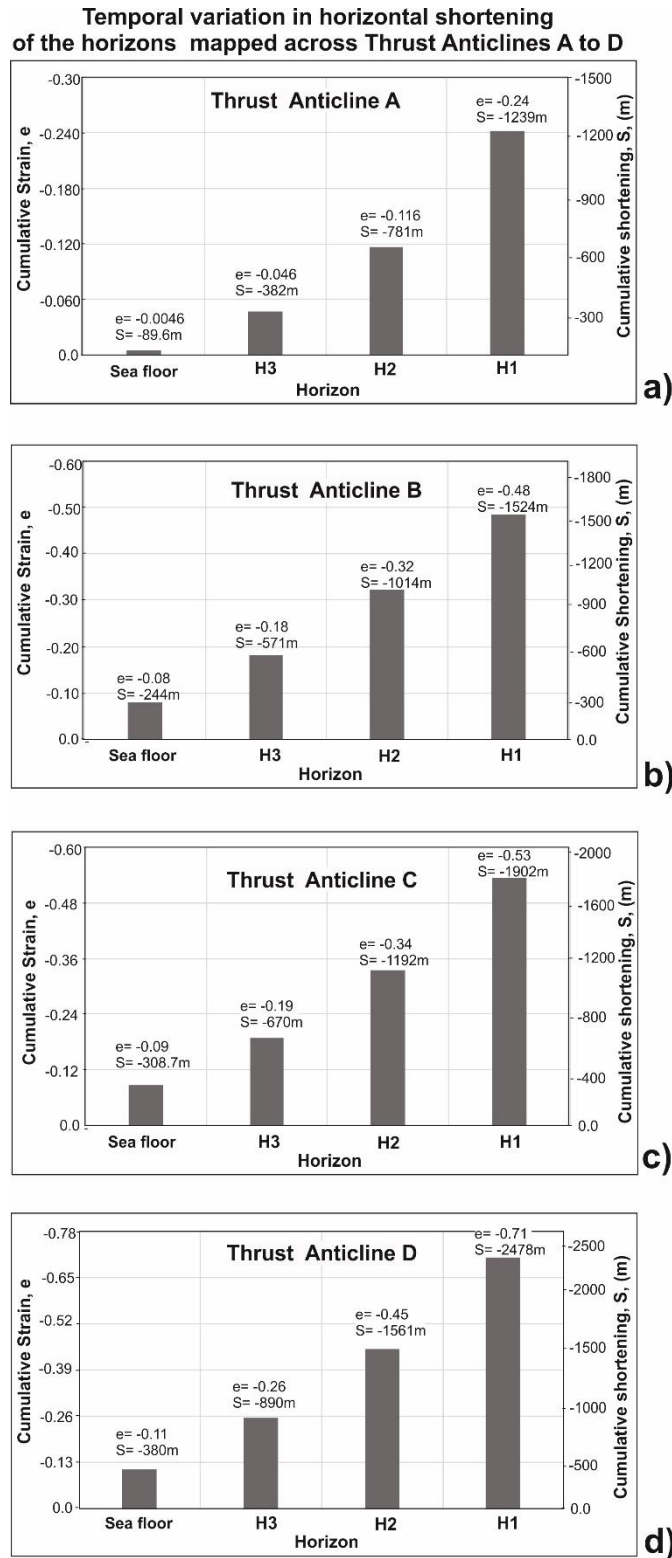
Fig. 6.10. Cumulative strain plots illustrating the variations in the shortening of the thrust anticlines at the level of the mapped seismic horizons. The maximum cumulative shortening recorded by the most landward Thrust Anticline A (1239 m), is approximately half of the maximum cumulative shortening recorded for the most seaward Thrust Anticline D (2478 m), indicating a trenchward increase in horizontal shortening of the outer wedge region of Nankai.

228

6.6. Geometry and growth of shallow faults on thrust-anticline crests

6.6.1. Geometry of shallow faults

A significant part of shallow faults is confined to Unit II. They are often observed in the hinge region of thrust anticlines A to D (Figs. 6.5–6.8). In Nankai, shallow faults following the trend of strike-slip faults have been classified as normal as they show minor throws without clear evidence for horizontal movement (e.g., Kimura et al., 2011; Azevêdo et al., 2018). However, these shallow faults can also comprise oblique slip faults with their horizontal displacement below the horizontal resolution of the seismic data.

Shallow faults dissect the uppermost part of the accretionary wedge, between a stratigraphic interval of 20 and 1000 mbsf. They are very small features with fault throw ranging between 2 m and 14 m, compared to the larger thrust faults that detach at underthrusted sediments, showing displacements larger than 450 m (Figs. 6.5–6.8). Shallow faults primarily result from bending and stretching of overburden strata in response to ongoing tectonic shortening offshore Nankai. Thus, they accommodate a significant part of the bending strain occurring during thrust-anticline development and associated seismic events (Figs. 6.5–6.8).

The seismic sections in Figs. 6.11–6.14 highlight some of the features of shallow faults in the uppermost part of the outer wedge region of Nankai accretionary prism. These faults are closely spaced and vertically segmented, with some appear to propagate and link with other faults. Throws die out at different stratigraphic intervals, with no faults offsetting the seafloor (Figs. 6.11–6.14).
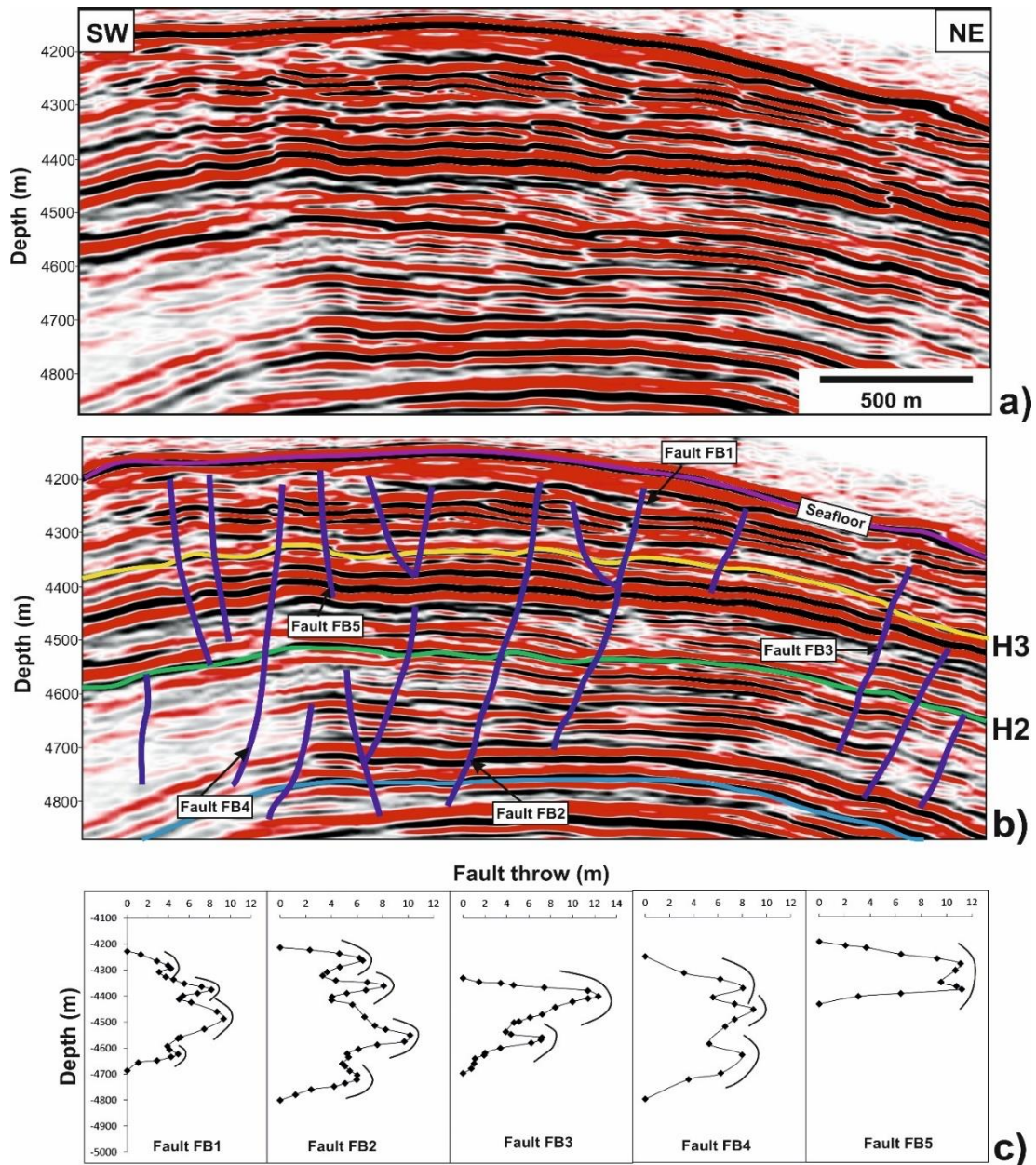
Fig. 6.11. a) Uninterpreted and b) interpreted seismic section highlighting some of the features of shallow fault populations around the hinge region of Thrust Anticline B. The faults are vertically segmented, with some propagating and linking with other faults, c) Representative vertical throw distribution of the shallow faults. Multiple throw maxima separated by throw minima on the throw distribution profiles show that fault segment linkage is a common process. The location of the seismic section is shown in Figs. 6.2 and 6.4.

Fig. 6.12. a) Uninterpreted and b) interpreted seismic section highlighting the geometry of shallow fault populations around the hinge region of the Thrust Anticline C. These faults are closely spaced and vertically segmented, with some propagating and linking with other faults, c) Representative vertical throw distribution of shallow faults. These faults are vertically segmented with relatively larger fault throw maxima. Fault segments with throw maxima nucleate first in more competent (stronger) intervals and are later linked by throw minima in less competent (weaker) intervals. The location of the seismic section is shown in Figs. 6.2 and 6.4.

6.6.2. Growth of shallow faults

The growth of shallow faults in the study area was investigated using the throw distribution profiles in Figs. 6.11c-6.14c. These profiles show a typical mode of fault growth that is dominated by segment linkage, i.e. multiple throw maxima separated by throw minima in the throw distribution profiles. The throw profiles of these faults do not always have single positive gradients and are characterised by throw profiles resembling M-type patterns between their upper-tip points and immediate throw minima (e.g., Baudon and Cartwright, 2008).

Fault segments with local throw maxima between 5 and 14 m are pre-existing fault segments, representing intervals where faults nucleate first. Each segment of these pre-existing faults propagates outwards until they encounter other pre-existing fault segments to link together. Linkage points of these pre-existing fault segments occur where local throw minima between 2 and 5 m are recorded (Figs. 6.11c-6.14c).

The fault segments revealing local throw maxima develop in more competent (stronger) intervals. These fault segments drive displacement into less competent (weaker) intervals where throw minimum is accommodated by ductile deformation. Thus, propagation of slip from fault segments with local throw maxima in more competent (stronger) intervals into less competent (weaker) intervals can result in the vertically segmented fault arrays observed in the seismic dataset and throw-depth (T-Z) profiles (Figs. 6.11–6.14). Such a character reflects fault propagating and growing by segment linkage, where by two separate fault segments with throw maxima have propagated towards each other and linked to form a larger fault (Baudon and Cartwright, 2008; Maunde and Alves, 2020).
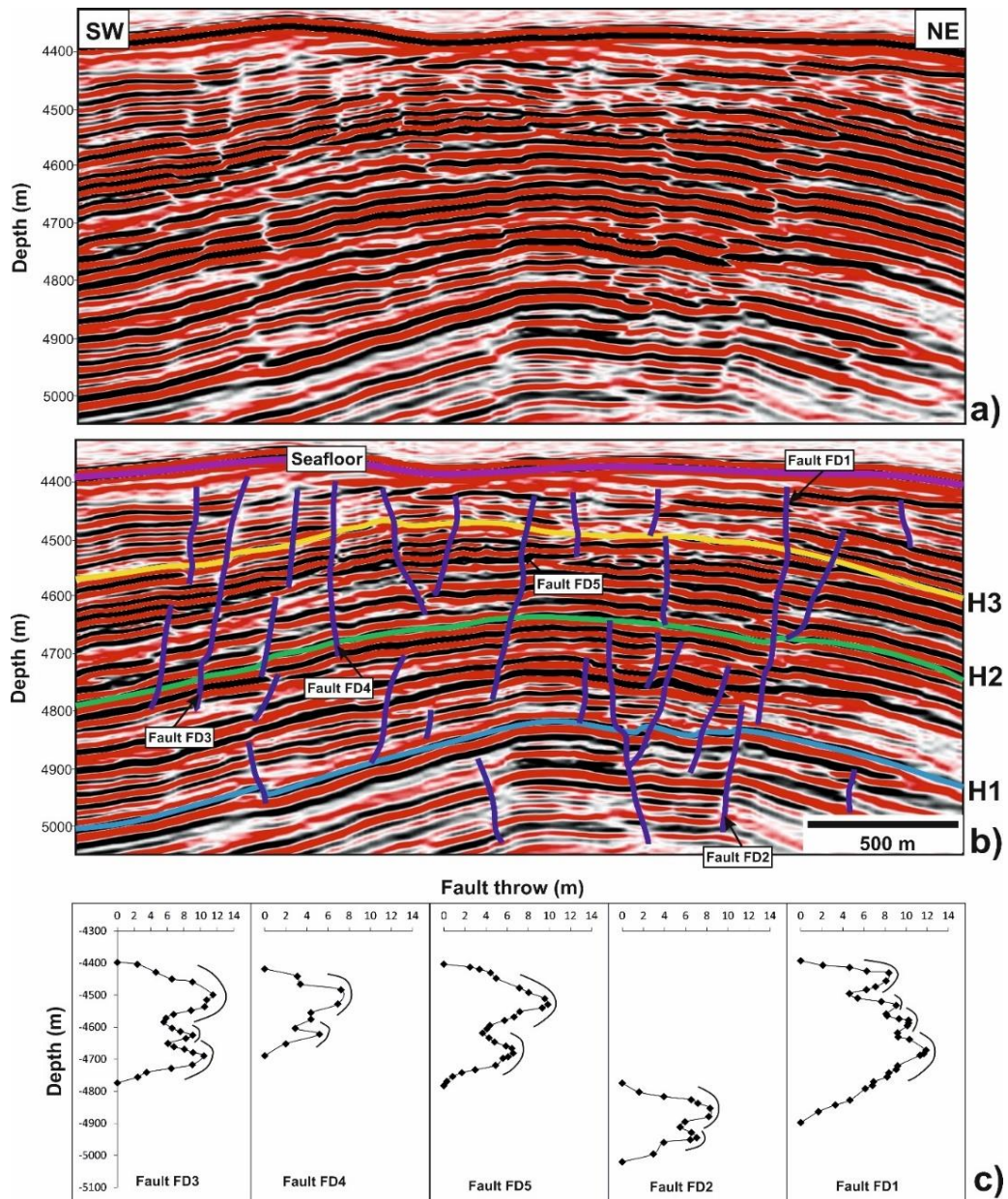
Fig. 6.13. a) Uninterpreted and b) interpreted seismic section highlighting some of the features of shallow fault populations around the hinge region of Thrust Anticline D. The faults are vertically segmented, with some propagating and linking with other faults, c) Representative vertical throw distribution of the shallow faults. Multiple throw maxima separated by throw minima on the throw distribution profiles show that fault segment linkage is a common process. The location of the seismic section is shown in Figs. 6.2 and 6.4.
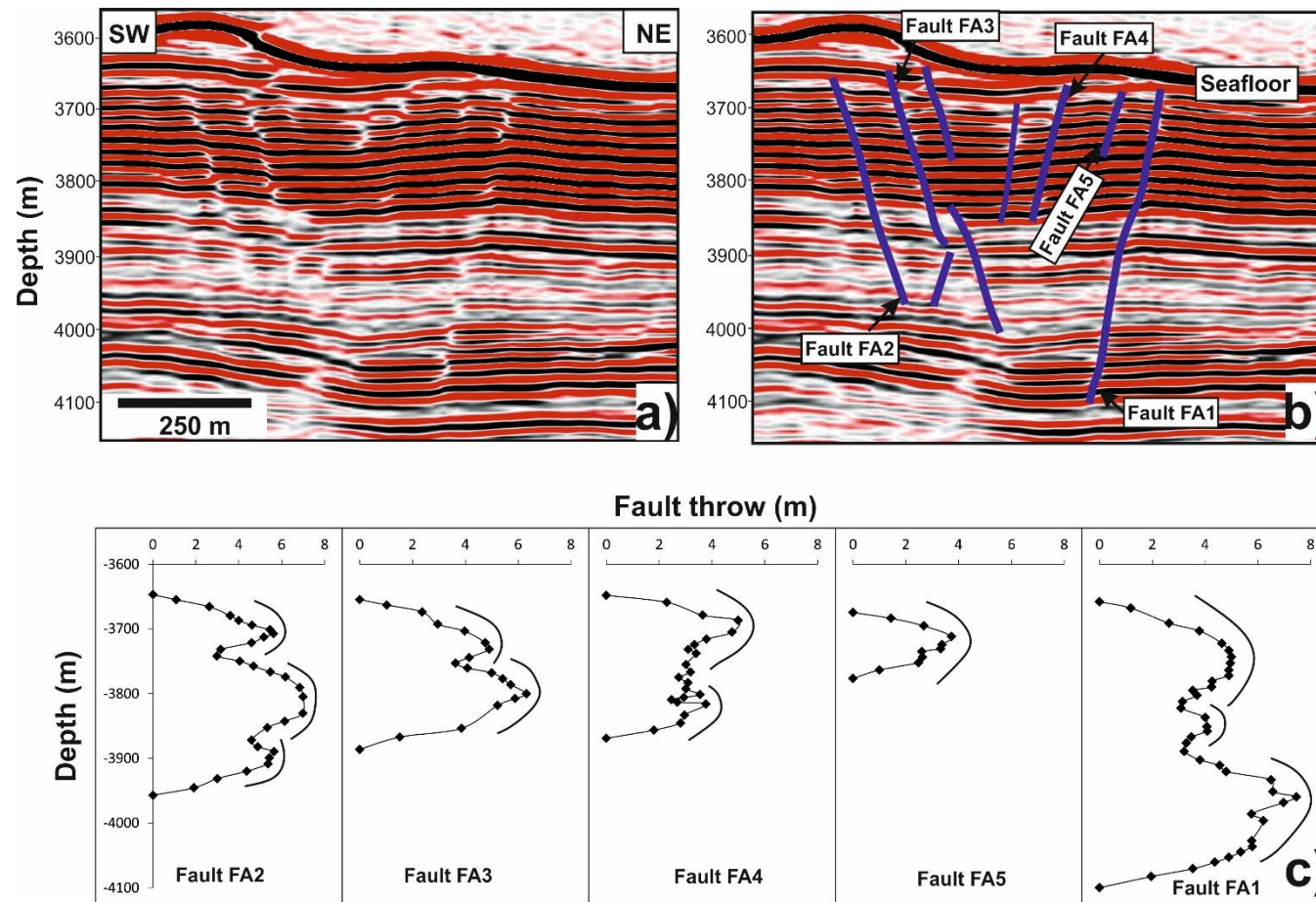
Fig. 6.14. a) Uninterpreted and b) interpreted seismic section highlighting the typical geometry of shallow fault populations in the slope basin sediments (Unit I). These faults are segmented, with some propagating and linking with other faults, c) Representative vertical throw-depth (T–Z) profiles of the shallow faults. The profiles highlight fault propagating and growing by segment linkage, whereby two separate fault segments with throw maxima in more competent (strong) intervals have propagated towards each other and linked in less competent (weak) interval with throw minima. The location of the seismic section is shown in Figs. 6.2 and 6.4.

6.7. Discussion

6.7.1 Impact of tectonic shortening offshore Nankai

Accretionary prims such as the Nankai Trough in SE Japan record large-scale tectonic shortening and uplift driven by plate subduction (Miyazaki and Heki, 2001; Bird, 2003; DeMets et al., 2010; Tsuji et al., 2014). Previous studies have suggested predominant compressional tectonics operating on this prism (Kimura et al., 2011; Lin et al., 2015). However, complex sets of thrust-related anticlines associated with segmented shallow faults are observed on seismic data across the outer wedge of Nankai, hinting at a complex strain distribution between a shallow regime of dip-slip faulting and a deeper regime of thrusting (Figs. 6.3b, 6.6, 6.8, 6.11 and 6.12). Thrust faults form the larger structural framework that accommodates regional compression and tectonic shortening of overburden strata in response to ongoing down-dip subduction of the Shikoku Basin crust (e.g., Kimura et al., 2011; Moore et al., 2015) (Fig. 6.3b). Against this backdrop, the shallow faults observed in the study area accommodate a significant part of the bending and stretching strain occurring during the development of thrust anticlines and subsequent local stress redistribution during seismic events (Lin et al., 2015) (Figs. 6.11–6.14).

The four studied thrust anticlines (A to D) have shortened the overburden strata by 7143 m, reflecting a horizontal shortening of 32.9% in response to the down-dip subduction. Thrust Anticlines B, C and D have recorded a significant horizontal shortening of around 1524 m, 1902 m, and 2478 m respectively, and developed bathymetric relief of up to 102 m, 113 m, and 182 m in height, respectively. They deform the seafloor, proving their active growth (Figs. 6.3b, 6.4, 6.10b, c and d). The proximal Thrust Anticline A records the least shortening (1239 m) and is currently buried by slope basin

sediments (Figs. 6.3b and 6.4). This confirms a trenchward increase in horizontal shortening in the outer wedge region Nankai accretionary prism (Fig. 6.10). This active trenchward increase in horizontal shortening of thrust anticlines may be due to an overall increase in deformation rates on the entire Nankai accretionary prism. In fact, Kinoshita et al. (2010) and Kopf et al. (2010) suggest an increase of deformation rate in the outer wedge region of the Nankai accretionary prism due to subduction of the Shikoku Basin crust during the Pliocene-Pleistocene. An important question revealed in this chapter, however, is how tectonic shortening translates into seafloor bathymetric features in the seaward Thrust Anticlines B to D (Figs. 6.3b and 6.4).

As highlighted in Equations 6.2 and 6.3 below, horizontal shortening of overburden rocks often generates vertical uplift (Hardy and Poblet, 2005). This uplift continues as the shortening progresses, except for the case of a simple fault bend fold, where the fold broadens (increases in width) without generating any further vertical relief once the lowest unit in hanging-wall reaches the upper footwall flat (Poblet and Hardy, 1995). However, tectonic shortening and uplift on continental margins is frequently associated with seafloor expression and gully erosion atop active anticlines (Alves et al., 2014; Mountjoy et al., 2009), a process further emphasised by climatic and oceanographic phenomena (Lewis et al., 1994; Micallef and Mountjoy, 2011).

The conceptual models in Fig. 6.15 illustrate the relationship between structural uplift rate, sediment accumulation rate and development of seafloor bathymetric expression. In this relationship, the ratio between the amount of sediment accumulated and the rate of structural uplift (or shortening) determines whether a structure develops a bathymetric expression on the seafloor (Shaw et al., 2004, 2006; Ford et al., 1997), following Equations 6.2 and 6.3 below:

$$s = \frac{sh}{t cos \emptyset} \qquad \text{Equation 6.2}$$

$$u = 2sSin\emptyset \qquad \text{Equation 6.3}$$

where s is the slip rate, $\emptyset$ is fault dip, horizontal shortening is sh, t is the time frame of reference and u is the uplift rate.

Based on the equations above, when the structural uplift rate is greater than the sediment accumulation rate sediments will barely onlap growing structures and their bathymetric expression will be clear on the seafloor (Fig. 6.15a). Consequently, actively growing structures will affect any sediment transported downslope. Thus, downslope sediment (e.g. Unit I; Fig. 6.3b) will be expected to accumulate in a perched basin (i.e. a local syncline) created by the growing structure. In the chapter dataset, three Thrust Anticlines (B, C and D) were identified as having a clear bathymetric expression (Figs. 6.3b and 6.4). These structures record significant tectonic shortening and developed a corresponding bathymetric relief of up to 102 m, 113 m, and 182 m in height, respectively. Thus, they reflect the conceptual model in Fig. 6.15a.

When the sediment accumulation rate is greater than the uplift rate of the thrust anticline, the deposited sediments will thin over the crest of the thrust anticline, thus forming overlapping geometries that will relatively smoothen the seafloor (Fig. 6.15b). In the study area, Thrust Anticline A is identified as having a relatively smooth bathymetry. This anticline records the least shortening (1239 m) with no corresponding bathymetric expression (Figs. 6.3b, 6.4 and 6.5), a geometry lying close to the conceptual model in Fig. 6.15b.
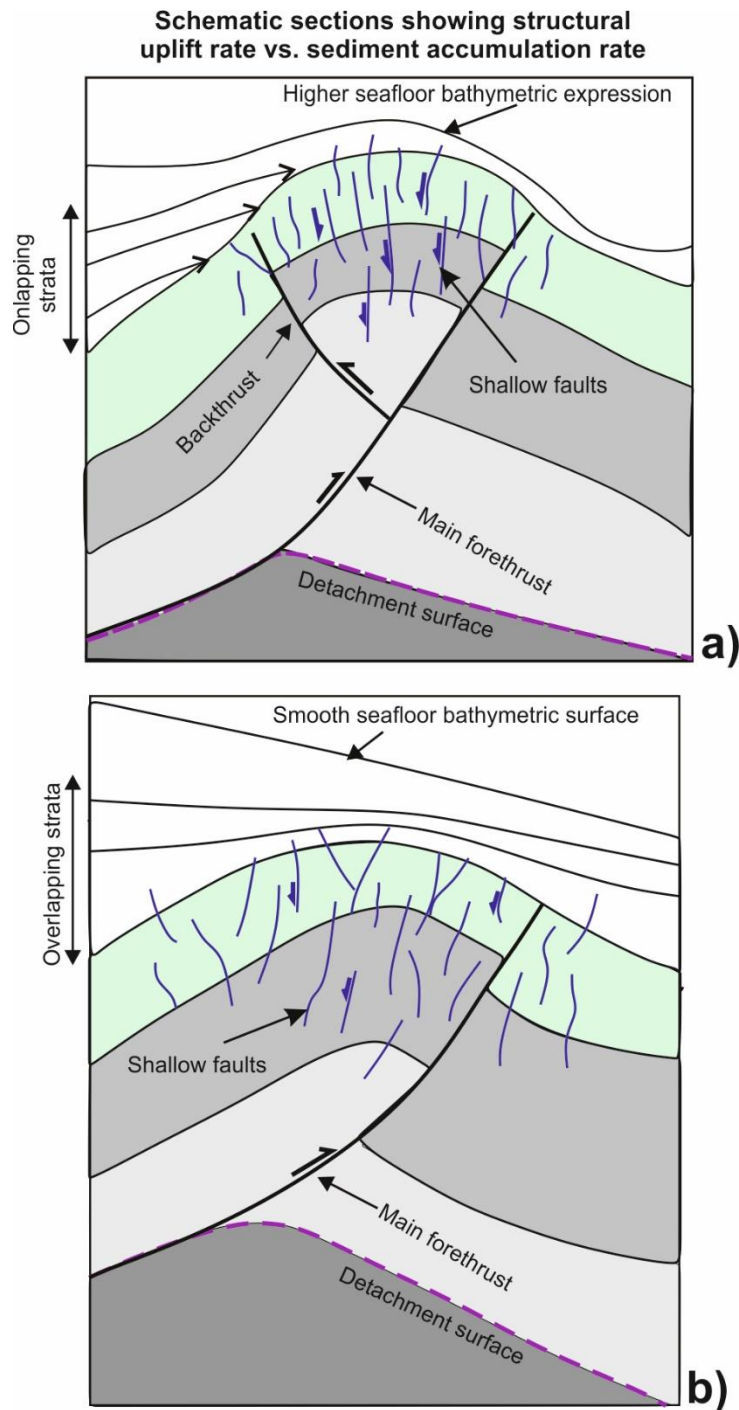
Fig. 6.15. Schematic sections depicting the relationship between structural uplift rate and sediment accumulation rate based on the interpreted seismic data. a) Higher uplift rate relative to sediment accumulation rate. Growth strata mainly onlap the growing structure, leading to development of seafloor bathymetric expression associated with the growing structure (e.g., Thrust Anticlines B, C and D). b) Higher sediment accumulation rates relative to uplift rate. Growth strata mainly overlap the growing structure, leading to a relatively smooth seafloor bathymetric expression (e.g., Thrust Anticlines A).

This Chapter stresses that geometries of strata observed on the flanks of growing structures, as shown in the conceptual models in Fig. 6.15, are not often this well-defined on seismic data - both onlapping and overlapping geometries can occur over the same growing structure, as either sediment supply or uplift rates vary through time (see Shaw et al., 2004; Jolly et al., 2016).

6.7.2. Geometry and growth of shallow faults offshore Nankai

Research has shown that, as strain accumulates in a mechanically layered sedimentary section brittle layers will fracture first, whereas ductile layers accommodate greater pre-failure strain prior to faulting (Ferrill and Morris, 2003, 2008; Welch et al., 2009). Thus, faults are expected to nucleate first in more competent layers, or intervals, with local throw maxima (Fig. 6.16a) and are later linked together in incompetent/weaker layers or intervals with local throw minima (Fig. 6.16c).

Incompetent (weak) intervals can prevent or slow propagation of faults from other layers, so that the locus of deformation can be shifted laterally across incompetent intervals. Such a shift in fault position across an incompetent layer can result in vertical fault segmentation, whereby fault segments can be hard or soft-linked (Bahroudi et al., 2003; Gabrielsen et al., 2016) (Fig. 6.16). Therefore, it is well established in the literature that the lithology and mechanical behaviour of the host rock influence fault kinematics and their related geometries.

In the study are, vertical fault segmentation with alternating local fault-throw maxima and minima is observed in the interpreted throw-depth (T-Z) profiles, a character reflecting the presence of mechanical heterogeneous successions blanketing the Nankai accretionary prism, whereby fault-throw maxima are related to more competent (strong) layers or intervals, and fault-throw minima are associated with less competent (weak)

intervals (Figs. 6.11c–6.14c). There is also strong evidence for vertical fault segmentation in the interpreted seismic dataset, a character indicating the presence of incompetent (weak) intervals (Figs. 6.11–6.14). Incompetent intervals can act as detachments that cause decoupling and prevent propagation of faults across specific intervals, resulting in a preferable horizontal propagation of faults to the detriment of their vertical growth (e.g., Richardson et al., 2005; Gabrielsen et al., 2016) (Figs. 6.11–6.14). In fact, IODP Site C0006 (Expedition 316 Scientists, 2009; Fig. 6.3ci) recognised the presence of hemipelagic mudstone to sand, mud, and silty-clay sequences interbedded with volcanic ash and tuffs in the study interval. This hints at a presence of heterogenous lithologies blanketing the Nankai accretionary prism (Fig. 6.3ci).

6.7.3. Mechanisms of formation of shallow faults off Nankai

According to data in Price and Cosgrove (1990), Lonergan et al. (1998) and Cartwright et al. (2003), shallow normal faults can be formed by a multitude of phenomena, from near-seafloor extension over growing anticlines to sudden compaction of mud-rich strata and subsequent loss of volume and fluid to form polygonal fault families. This brings to this discussion an important question: what were the mechanisms responsible for the formation of the shallow fault families imaged in Unit II, in the Nankai case study?

The interpreted data confirm the assumption that local extension occurred in Thrust Anticlines A to D above a so-called neutral surface (Price and Cosgrove, 1990; Ramsay, 1967) – a characteristic also used by Lin et al. (2015) and Wu et al. (2013) to prove that the Nankai Trough region is experiencing an intra-seismic cycle in which compression was replaced by widespread extension. Furthermore, Van Tuyl et al. (2015) showed-
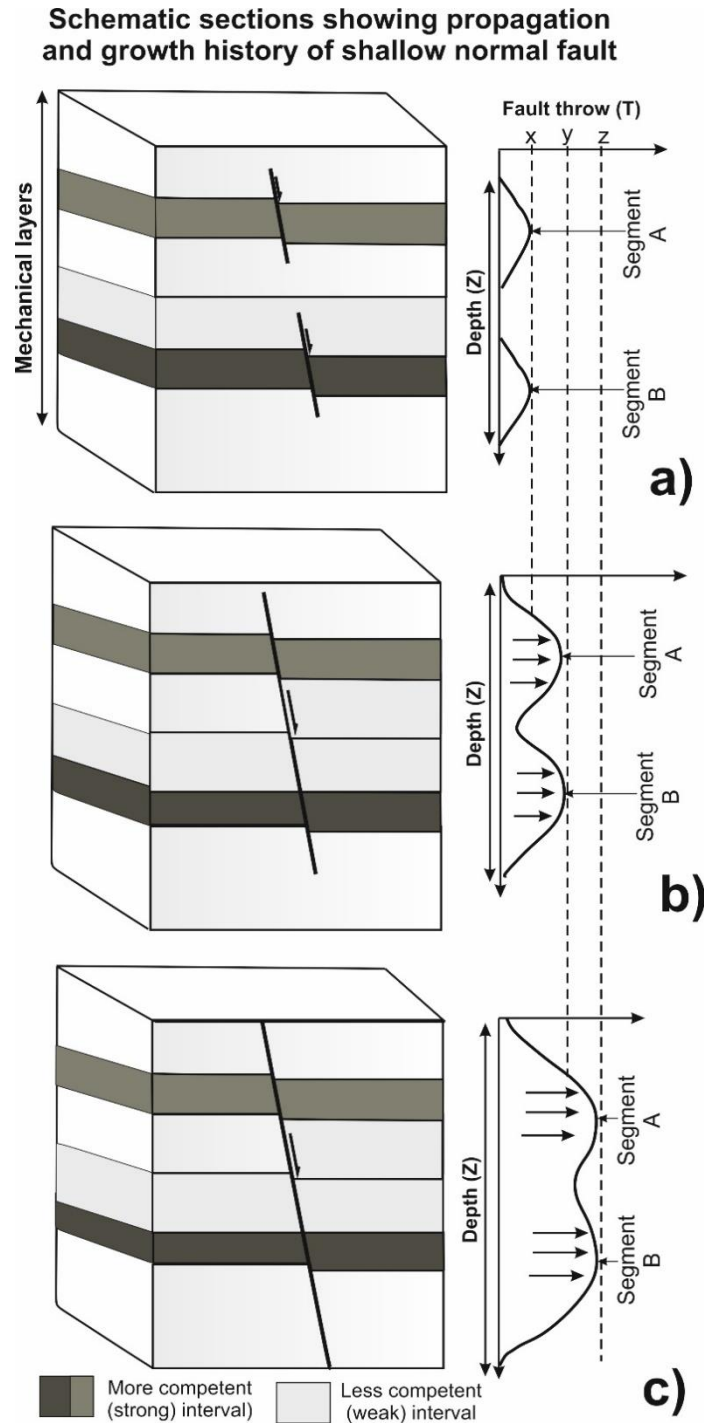
Fig. 6.16. Schematic sections illustrating the vertical growth of shallow faults by segment linkage. a) Faults nucleate first in more competent (strong) intervals with larger throw maxima, b) the nucleated faults propagate outwards into incompetent (weak) intervals. Incompetent (weak) intervals can prevent or slow faults from propagation across other layers, resulting in a preferable horizontal propagation of faults rather than vertical growth. c) a shift in fault position across an incompetent layer can result in vertical fault segmentation, where the fault segments with throw maxima in more competent (strong) intervals can be hard- or soft-linked by throw minima in less competent (weak) intervals.

that a clear limit exists throughout the outer wedge region between extension and compressional stresses across what was called the Extension-Compression Depth.

A complementary explanation to the formation of, at least, some of the shallow faults in the study area would be sudden compaction of a mud-rich succession, with localised fluid escape through the imaged fault planes. There are aspects that seem to both corroborate and rebuke this latter interpretation, as explained in the paragraphs below.

The role of sediment compaction should be considered in the study area, but features mapped do not resemble vertical gas (of water) pipes, nor any other kind of fluid flow feature. They are limited in their height, the depths in which they occur, and there are no fluid-flow features - such as pockmarks on the seafloor – associated with them. They clearly offset the imaged strata within the vertical resolution limits of the seismic data, which allows the mapping of fault offsets of up to 14 m (Figs. 6.11c–6.14c).

Compaction and fluid escape should occur in a geological setting as Nankai's, but the features mapped clearly offset the adjacent strata; they are also associated with the structural bending of the Thrust Anticlines A to D (Figs. 6.5–6.8). In addition, mechanical stratigraphy is likely to evolve through time for very 'fresh', young sediments experiencing compaction and dewatering ((Xiao and Suppe, 1989; Zoback, 2007; Ferrill et al., 2012). However, Unit II is not the youngest of intervals in Nankai and comprises sediment that has potentially been compacted in the last few million years (Ma), and later exhumed in Thrust Anticlines A and D to form broad antiform structures. In this case, Thrust Anticlines A and D are not formed by the youngest (and potentially softer) of slope basin strata; instead, they are composed of strata in Unit II that span the Early Pleistocene to Pliocene in age (Fig. 6.3ci).

In essence, the shallow faults (or discontinuities) imaged in the individual reflections' present clear offsets in seismic data – well within its vertical sampling limits - and comprise a combination of normal faults, bands of compaction or dilation, and ancillary faults and fractures responding to local strike slip motion. The stated vertical resolution is ~6 m, but the mapping of fault throws as those in this chapter depend on the vertical sampling of the seismic data. Throws were measured from the upper tip of the fault, with zero (0) throws, to the lower tip in each of the faults. Therefore, errors in measurements obey the vertical sampling rate of the seismic data (Tao and Alves, 2019) (Figs. 6.11–6.14).

6.8. Chapter specific conclusions

Detailed seismic interpretation of shallow faults in Nankai, showing throws between 2 m and 14 m, provided us with insights into the geometry and growth of shallow faults in this area, as well as the competence of sediments blanketing an active accretionary prism. The main conclusions of this chapter are as follows:

1. Offshore Nankai (SE Japan), tectonic shortening and uplift of overburden strata have induced a continuum of internal deformation that is expressed in the form of structures such as forethrusts, backthrusts and corresponding anticlines that occur, near the seafloor, in association with significant distribution of the shallow fault populations in the uppermost part of the Nankai accretionary prism. The four studied Thrust Anticlines A to D confirm a trenchward increase in horizontal shortening and have actively grown and deformed the modern seafloor. They cumulatively shortened the study area by 7143 m, representing a horizontal shortening of about 32.9% during the late Quaternary in response to the ongoing down-dip subduction of the Shikoku Basin crust in Nankai.

2. The presence of vertically segmented fault arrays dissecting the uppermost strata with local throw maxima between 5 m and 14 m relate to the existence of more competent (strong) intervals. Linkage points of these segmented fault throw maxima occur where local throw minima between 2 and 5 m are recorded in less competent (weak) intervals. Hence, multiple throw maxima separated by throw minima on the throw distribution profiles show that fault segment linkage is a common process during the growth of shallow faults in the uppermost part of the outer wedge region of Nankai accretionary prism.

3. The presence of closely spaced and vertically segmented fault arrays observed in the seismic dataset confirm the existence of incompetent (weak) lithologies. Incompetent (weak) lithologies, or layers, can act as local detachments that cause stress decoupling and prevent propagation of faults across specific layers resulting in a preferable horizontal propagation of faults to the detriment of their vertical growth.

4. d) The significant distribution of the shallow faults in the uppermost part of the Nankai accretionary prism accommodates a significant part of the bending and stretching strain occurring during thrust anticlines development, and subsequent local stress distribution and accommodation of strain during seismic events offshore Nankai.

CHAPTER 7

Summary and Discussion

7. Summary and Discussion

7.1. Introduction and summary of main results

This chapter aims at discussing the impact of distinct magnitudes of tectonic shortening on the reactivation and growth histories of normal faults formed in mechanically layered sequences, as well as the control of such faults on fluid flow. The chapter further summarises the main results in each of the result chapters presented in this thesis (Fig. 7.1) and re-examines the seismic volumes from the three (3) study areas: Espírito Santo Basin (SE Brazil), Broad Fourteens Basin (Southern North Sea) and Nankai Trough (SE Japan).

7.1.1. Chapter 4: Impact of tectonic rafts' gravitational instability on fault reactivation and geometry

Chapter 4 uses three-dimensional (3-D) seismic reflection data from the salt-rich Espírito Santo Basin (SE Brazil; Fig. 2.1) to investigate the geometry and reactivation histories of normal faults associated with the development rollover anticlines above tectonic rafts. Detailed mapping of fault geometry and throw revealed that the complex fault geometries observed above rollover anticlines are primarily due to downslope gravitational gliding of tectonic rafts. As a result, three (3) distinct tiers of normal fault geometry are recognised (Figs. 4.2 and 4.3). These fault tiers include Tiers 1, 2 and 3 which correspond to the initial, renewed (intermediate), and late stages of downslope gravitational gliding of tectonic rafts, respectively (Fig. 4.14).

Tier 1 faults comprise closely spaced normal faults that resulted from the outer-arc bending and stretching of the Late Cretaceous strata (Unit S4) during the development of rollover anticlines above tectonic rafts and are thus interpreted as rollover faults

(Figs. 4.2 and 4.3). These faults accommodate a significant part of the bending strain occurring in the hanging-wall blocks of listric (roller) faults during the initial stage of tectonic rafts gravitational gliding (Fig. 4.14a). A significant part of these faults overlies tectonic rafts offshore Espírito Santo (Alves, 2012) (Figs. 4.2 and 4.3). The faults are characterised by a linear to curvilinear patterns over rollover anticline's (Figs. 4.6a and 4.7a).

Tier 2 faults comprise closely spaced normal faults with a diverse range of fault strikes that form a polygonal pattern over rollover anticlines (Figs. 4.2, 4.3, 4.6b and 4.7b). The progressive bending of rollover anticlines above tectonic rafts during the renewed stage of downslope gravitational gliding of tectonic rafts led to the progressive faulting of the overburden strata by these faults. Tier 2 faults accommodate some of the bending strain and supra-salt extension in overburden strata during the renewed stage of tectonic rafts gravitational gliding (Fig. 4.14b).

Tier 3 faults comprise densely spaced set of normal faults with a discrete range of fault strikes revealing a polygonal pattern over rollover anticlines (Figs. 4.2, 4.3, 4.6c and 4.7c). Differences in the timing of (diachronous) grounding of tectonic rafts are responsible for the development of these faults, as well as for the reactivation of local pop-up structures and drag folds formed adjacently to roller faults (Alves, 2012) (Fig. 4.3). Tier 3 faults are associated with the later stages of downslope gravitational gliding tectonic rafts in the Espírito Santo Basin (Fig. 4.14c). Fault reactivation and growth via segment linkages characterised the mode of growth of the interpreted fault tiers, whereby two separate faults with local throw maxima propagate towards each other and linked in throw-minimum in the throw-depth (T-Z) profiles and contour maps (Figs. 4.8, 4.9 and 4.10).

246

Fig. 7.1. Diagram summarising the key results presented in this thesis. Chapter 4 investigated the geometry and reactivation histories of distinct normal fault tiers developed above the rollover anticlines. Chapter 5 investigated the effect of tectonic inversion on supra-salt fault geometry and reactivation histories. Chapter 6 explored the effect of mechanical stratigraphy on shallow fault geometry and growth histories in areas dominated by thrust anticlines in the outer wedge region of the Nankai accretionary prism.

7.1.2. Chapter 5: Effect of tectonic inversion on supra-salt fault geometry and reactivation histories

Chapter 5 uses high-quality 3-D seismic and borehole datasets from the Broad Fourteen Basin, Southern North Sea (Fig. 2.4) to investigate the effect of lithology on fault throw distribution and segmentation along the fault planes, as well as the geometry and reactivation histories of faults developed due to Late Cretaceous to Paleogene tectonic inversion (i.e. Sub-Hercynian, Laramide, Pyrenean and Savian tectonic phases; Fig. 5.3). Detailed mapping of fault geometry and throw shows that the complex Late Mesozoic normal fault geometries observed above anticlinal structures are primarily due to effect of tectonic inversion in the Southern North Sea, in which two (2) distinct tiers of fault geometries were generated (Figs. 5.4 and 5.6).

Tier 1 faults (Upper Mesozoic) comprise closely spaced normal faults that resulted from the progressive bending and stretching of outer-arc Upper Mesozoic strata during the development of anticlines in response to the effect of Late Cretaceous inversion (i.e. Sub-Hercynian episode; Fig. 5.24c). The Pyrenean (Oligocene) and Savian (Miocene) inversion episodes reactivated some of these Tier 1 faults upward into the Paleogene strata around the hinge region of Late Mesozoic anticlines (Figs. 5.4, 5.6 and 5.24e). These Tier 1 faults are characterised by a linear to curvilinear pattern, striking in a NW-SE direction roughly parallel to the strike of the underlying anticline (Fig. 5.10).

Tier 2 faults (Paleogene) comprise densely spaced sets of normal faults, with a discrete range of strikes, revealing a polygonal geometry in map view (Figs. 5.9 and 5.11). The upper and lower tip lines of these faults die out in Paleogene strata, with some faults propagating downward into Upper Mesozoic strata around the hinge of anticlines (Fig. 5.12). These faults were initially formed as polygonal faults and were later reactivated to form new segments, or lengthen their sizes, due to later Savian (Miocene) inversion

episode in the Southern North Sea (Figs. 5.5 and 5.9). The reactivation of the interpreted fault tiers largely occurred around the hinge regions of underlying anticlines (Figs. 5.5, 5.6, 5.12 and 7.4). This observation perhaps suggests that apart from the orientation of the fault planes with respect to their principal local stresses, other controls such as the location of the underlying anticlines affect the reactivation of fault, as observed in the TWTT map relationships in Fig. 5.12.

The interpreted fault tiers offset a layered succession comprising sands and shales (Figs. 5.13 to 5.20). When the fault strands in the sand-rich intervals are compared to fault segments in the shale-rich intervals, notable differences in throw values are observed. In the sand-rich intervals, fault throws are larger (i.e., maximum throw of 40.3 m) compared to the smaller fault throw (i.e., maximum throw of 17.7 m) in the shale rich-intervals (Figs. 5.15 to 5.20). The larger fault throws are early-stage fault segments and represent regions where faults localise first in competent sand and limestone intervals (Figs. 5.15 to 5.20). Each segment of these early-stage faults propagates outwards until they encounter other fault strands and link together. Linkage points are located where local throw minima are recorded in less competent shale-rich intervals (Ellis and Dunlap, 1988) (Figs. 5.15 to 5.20).

The propagation of slip from fault segments (with local throw maxima) in sand-rich intervals into the shale-rich intervals can explain the vertically segmented fault arrays observed in the throw-depth (T-Z) profiles (Figs. 5.15b to 5.20b and 5.22c). This interpretation of throw-depth (T-Z) data supports the view that vertically segmented fault arrays initially nucleate in competent, brittle lithologies (sandstones and limestones) with local throw maxima, and are later linked by faults in the incompetent,

and ductile, lithologies (shales, mudstones) with minimum throws (Peacock and Sanderson, 1992; Childs et al., 1996) (Figs. 5.15b to 5.20).

7.1.3. Chapter 6: Shallow fault systems of thrust anticlines responding to changes in accretionary prism lithology (Nankai, SE Japan)

Chapter 6 uses three-dimensional (3-D) pre-stack depth migrated seismic data to explore the effect of mechanical stratigraphy on shallow fault geometry and growth history from areas dominated by thrust anticlines in the outer wedge region of the Nankai accretionary prism (SE Japan) (Figs. 2.6 and 6.3). Accretionary prims such as the Nankai Trough in SE Japan record large-scale tectonic shortening and uplift driven by plate subduction (DeMets et al., 2010; Tsuji et al., 2014).

Complex sets of thrust-related anticlines associated with segmented shallow fault systems are observed on the seismic data across the outer wedge of Nankai, hinting at a complex strain distribution between a shallow regime of dip-slip faulting and a deeper regime of thrusting. Thrust faults form the larger structural framework that accommodates regional compression and tectonic shortening of overburden strata in response to ongoing down-dip subduction of the Shikoku Basin crust (Kimura et al., 2011; Moore et al., 2015) (Fig. 6.3b). In contrast, the shallow fault systems accommodate a significant part of the bending and stretching strain occurring during the development of thrust anticlines and subsequent local stress redistribution during seismic events (Lin et al., 2015) (Figs. 6.5-6.8 and 6.11–6.14).

A significant part of shallow fault systems is observed in the hinge regions of thrust anticlines (Figs. 6.5-6.8). These faults primarily result from the progressive bending and stretching of overburden strata in response to ongoing tectonic shortening. In Nankai, shallow fault systems following the trend of strike-slip faults have been

classified as normal as they show minor throws without clear evidence for horizontal movement (Kimura et al., 2011; Azevêdo et al., 2018). However, these shallow faults can also comprise a combination of normal faults, oblique-slip faults, bands of compaction or dilation, and ancillary faults and fractures responding to local strike slip motion. They are very small features with fault throw ranging between 2 m and 14 m compared to the larger thrust faults that detach at underthrusted sediments, showing fault throws larger than 450 m (Figs. 6.5-6.8).

The distribution of and displacements on the shallow fault systems accommodate outer-arc extension. Although the inner-arc of the anticlines may remain in a thrust faulting stress regime. Thus, the interpreted data confirm the assumption that local extension occurred in thrust anticlines above a so-called neutral surface (Price and Cosgrove, 1990; Ramsay, 1967), a characteristic also used by Lin et al. (2015) and Wu et al. (2013) to prove that the Nankai Trough region is experiencing an intra-seismic cycle in which compression was replaced by widespread extension. Van Tuyl et al. (2015) showed that a clear limit exists throughout the outer wedge region between extension and compressional stresses across what was called the Extension-Compression Depth.

In the Nankai seismic dataset, the shallow fault systems show evidence for vertical fault segmentations, a character indicating the presence of incompetent (soft) intervals dominating the Nankai accretionary prism (Figs. 6.11-6.14). Incompetent intervals can act as detachments that cause decoupling and prevent propagation of faults across specific intervals, resulting in a preferable horizontal propagation of faults to the detriment of their vertical growth (Richardson et al., 2005; Gabrielsen et al., 2016) (Figs. 6.11-6.14). Moreover, incompetent (ductile) layers can accommodate greater

pre-failure strain prior to faulting and faulted with relatively low throw maximum as observed on the shallow faults throw-depth (T-Z) profiles (i.e. 14 m) (Figs. 6.11-6.14).

7.2. Impact of tectonic shortening on fault formation and reactivation histories

The reactivation and geometry of normal faults investigated in this chapter are associated with distinct magnitudes of horizontal shortening, varying from a moderate horizontal shortening of 10.3% over rollover anticlines in the Espírito Santo Basin (SE Brazil; Fig. 7.2) to a moderately high shortening of 19.4% over broad anticlines in the Broad Fourteens Basin (Southern North Sea; Fig. 7.3) and, finally, significant horizontal shortening exceeding 40% over thrust anticlines in the Nankai accretionary prism (SE Japan; Fig. 7.4).

In the Espírito Santo Basin (SE Brazil), the downslope gravitational instability of tectonic rafts trigger the development of rollover anticlines and their associated outer-arc normal faults, as well as subsequent reactivation of these latter faults. The onset of tectonic rafting during post-Albian to Coniacian period caused the supra-salt strata to be fragmented into discrete blocks of strata or rafts separated by large listric (roller) faults and associated rollover anticlines in their hanging wall blocks. Outer-arc normal faults were formed above rollover anticlines to accommodate the initial buckling of the post-raft overburden during the development of rollover anticlines (Fig. 7.2d1).Continued evacuation of salt from upper-slope regions to the base of the continental slope during Early Santonian period promoted the progressive downslope translation of rafted strata and triggered the reactivation of rollover faults in the form of crestal fault systems associated with local extensional collapse (Fig. 7.2d2).

Subsequently, continued evacuation of salt during Middle/Late Eocene caused tectonic rafts to be translated downslope until salt welds were formed and post-salt strata became grounded over pre-salt successions. The grounding (welding) of tectonic rafts over the pre-salt successions was progressive and accompanied by moderate translation of blocks during the Cenozoic. Differences in the degree of downslope translation of un-welded rafts further enhanced the reactivation of rollover faults, a phenomenon that promoted the migration of hydrocarbons from welded sub-salt source units into supra-salt reservoirs (Fig. 7.2d3).

In the Broad Fourteens Basin (Southern North Sea), the Late Cretaceous to Paleogene tectonic inversion have induced a continuum of deformation and contributed significantly to the formation and subsequent reactivation of Late Mesozoic faults (Fig. 7.3). Late Cretaceous inversion (i.e. the Sub-Hercynian inversion episode) led to the formation of broad anticlines associated with outer-arc normal faults in Upper Mesozoic strata. The progressive bending and stretching of outer-arc Mesozoic strata during the Early Paleocene inversion episode (i.e. Laramide episode) reactivated lengthened the early formed Sub-Hercynian faults.

The erosion (truncation) of upper tip lines for these latter faults at the Base Tertiary Boundary suggest that they were active in the Upper Mesozoic strata before the onset of the Laramide erosional event (De Lugt et al., 2003; Oudmayer and De Jager, 1993) (Figs. 5.4, 5.6 and 7.3d3). In a last stage, the Pyrenean (Oligocene) and Savian (Miocene) inversion episodes reactivated some of these faults upward into Tertiary strata (Figs. 5.6 and 7.3d4).
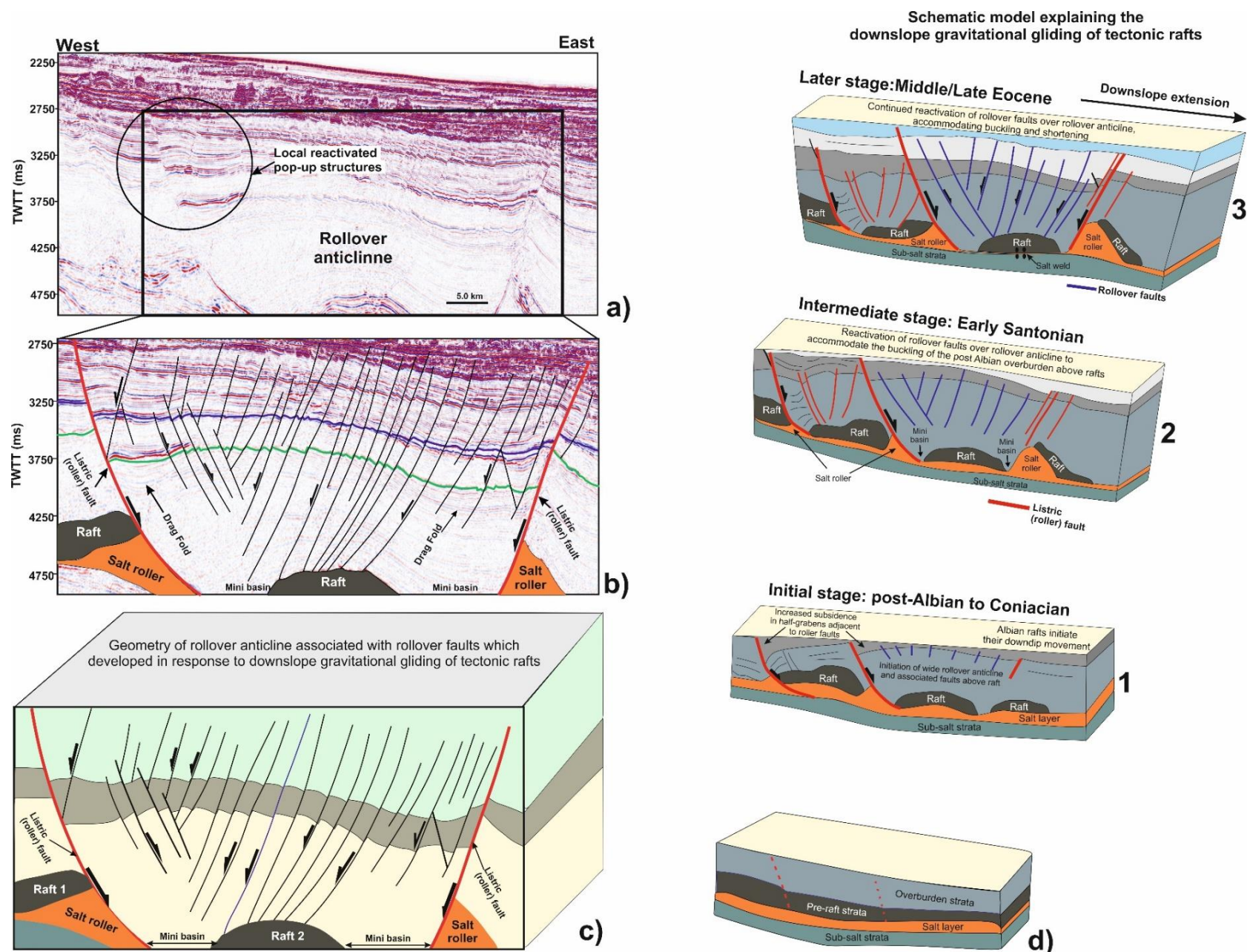
Fig. 7.2. a) Uninterpreted, b) Interpreted and c) schematic seismic sections across the Espírito Santo Basin (SE Brazil). The sections highlight large roller faults bounding Cretaceous minibasins, rollover normal faults over rollover anticline, drag folds adjacent to roller faults, tectonic rafts between and above salt rollers, and local reactivated pop-up structures. Tectonic raft forms the core of rollover anticline. The presence of reactivated pop-up structures and the drag folds adjacent to the roller fault, responded to the diachronous grounding of tectonic rafts, d) Schematic model explaining the downslope gravitational gliding of tectonic rafts and their relationship with local structures (listric faults, rollover anticline and rollover normal faults) in the Espírito Santo Basin (SE Brazil). d1) Initial stage (post-Albian to Coniacian) caused the supra-salt strata to be fragmented into discrete blocks of strata or rafts separated by large listric (roller) faults and associated wide rollover anticlines above rafts. Outer-arc rollover normal faults were initiated to accommodate the buckling of the post-raft overburden during the development of rollover anticlines. d2) In intermediate stage (Early Santonian), continued evacuation of evaporites from upper-slope regions to the base of the continental slope promoted the progressive downslope translation of rafted strata and reactivation of rollover faults in the crestal collapse systems of rollover anticlines. d3) Late-stage gravitational gliding (Middle/Late Eocene) caused tectonic rafts to be translated downslope until salt welds were formed and post-salt strata became grounded over pre-salt successions. Differences in the degree of downslope translation of un-welded rafts further enhanced the reactivation of rollover faults which potentially promotes the migration of hydrocarbons from welded sub-salt source units into supra-salt reservoirs.
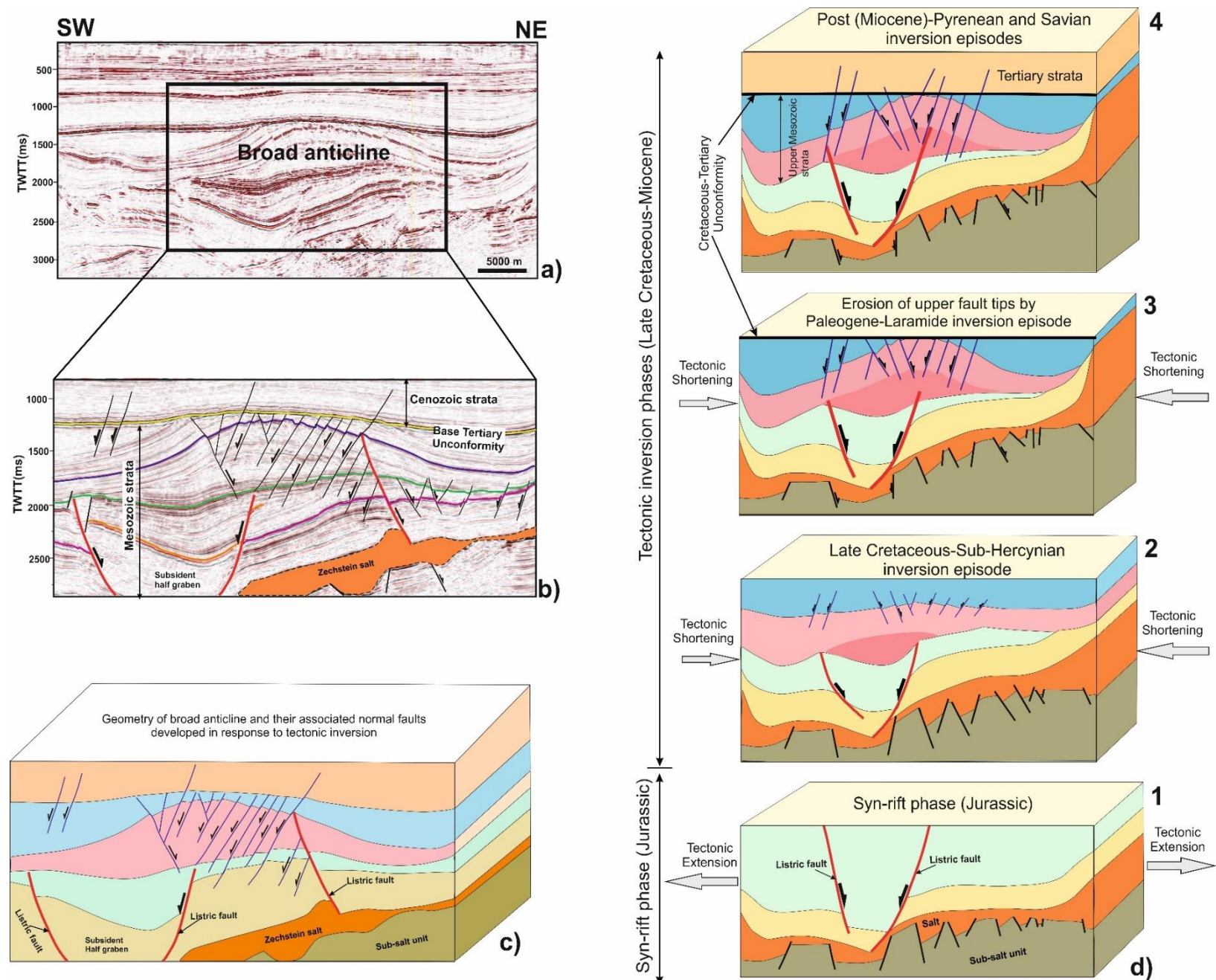
Fig. 7.3. a) Uninterpreted, b) Interpreted and c) schematic sections across the Broad Fourteens Basin (Southern North Sea) a and b) Uninterpreted and interpreted seismic sections across the Broad Fourteens Basin (Southern North Sea) showing the geometry and structural styles of faults that resulted from Late Cretaceous to Paleogene tectonic inversion. Local bending and stretching of the Upper Mesozoic strata during the Late Cretaceous-Paleogene tectonic inversion episodes produced the broad anticlines associated with outer-arc normal faults, d) Schematic model for the geological evolution of faults associated with tectonic inversion. Listric faults active in during the Jurassic syn-rift phase in association with rift-raft tectonics, d1). d2) Broad anticlines associated with outer-arc normal faults occurred during Late Cretaceous-Sub-Hercynian inversion (i.e., time of formation of major anticlines), d3) Period of reactivation of Sub-Hercynian faults and erosion of their upper fault tips by Paleocene-Laramide erosional event, creating a prominent Cretaceous-Tertiary Unconformity, d4) Phase of reactivation of some faults into the Tertiary strata during Pyrenian (Oligocene) and Savian (Miocene) inversion episodes. The present-day post inversion phase highlight geometry of broad anticline and their associated normal faults.

In the Nankai accretionary prism (SE Japan), the subduction of the Philippine Sea Plate beneath the southeast margin of Eurasia has led to large-scale tectonic shortening and uplift of overburden rocks above a subducted oceanic slab to form Nankai accretionary prism (Miyazaki and Heki, 2001; Kimura et al., 2011, 2018) (Fig. 6.3). This prism is characterised by thrust anticlines associated with shallow fault sytems in their hinge region (Figs. 6.5-6.8). Shallow fault systems are primarily resulted from the progressive bending and stretching of overburden strata in response to ongoing plate subduction offshore Nankai and thus accommodate a significant part of the bending strain occurring during thrust-anticlines development.

Shallow faults deformations in the Nankai accretionary prism are vertically segmented and distributed (Fig. 7.4) compared to fault deformations in the Espírito Santo and Broad Fourteens Basins which are more continuous and localised (less segmented) (Figs. 7.2b and 7.3b). Consequently, fault reactivation and height are limited by the thickness and differences of mechanical layers (Roche et al., 2012, 2013) rather than controlled solely by the distinct magnitudes of tectonic shortening. For instance, a moderate fault reactivation with relatively smaller throw maxima of 14 m and vertically segmented fault arrays were observed in the highly shortened (i.e. 40% horizontal shortening) and younger (softer) strata of the Nankai case study (Fig. 7.4), while significant fault reactivation with relatively larger throw maxima (between 30 m and 60 m) and more localised (less segmented) faults were observed in the least shortened (i.e. between 10.3-19.4% horizontal shortening) and stronger strata of the Espírito Santo and Broad Fourteens Basins (Figs. 7.2 and 7.3). These observations can be attributed to the effect in the differences of mechanical stratigraphy of the host rocks as discussed in the following sections.
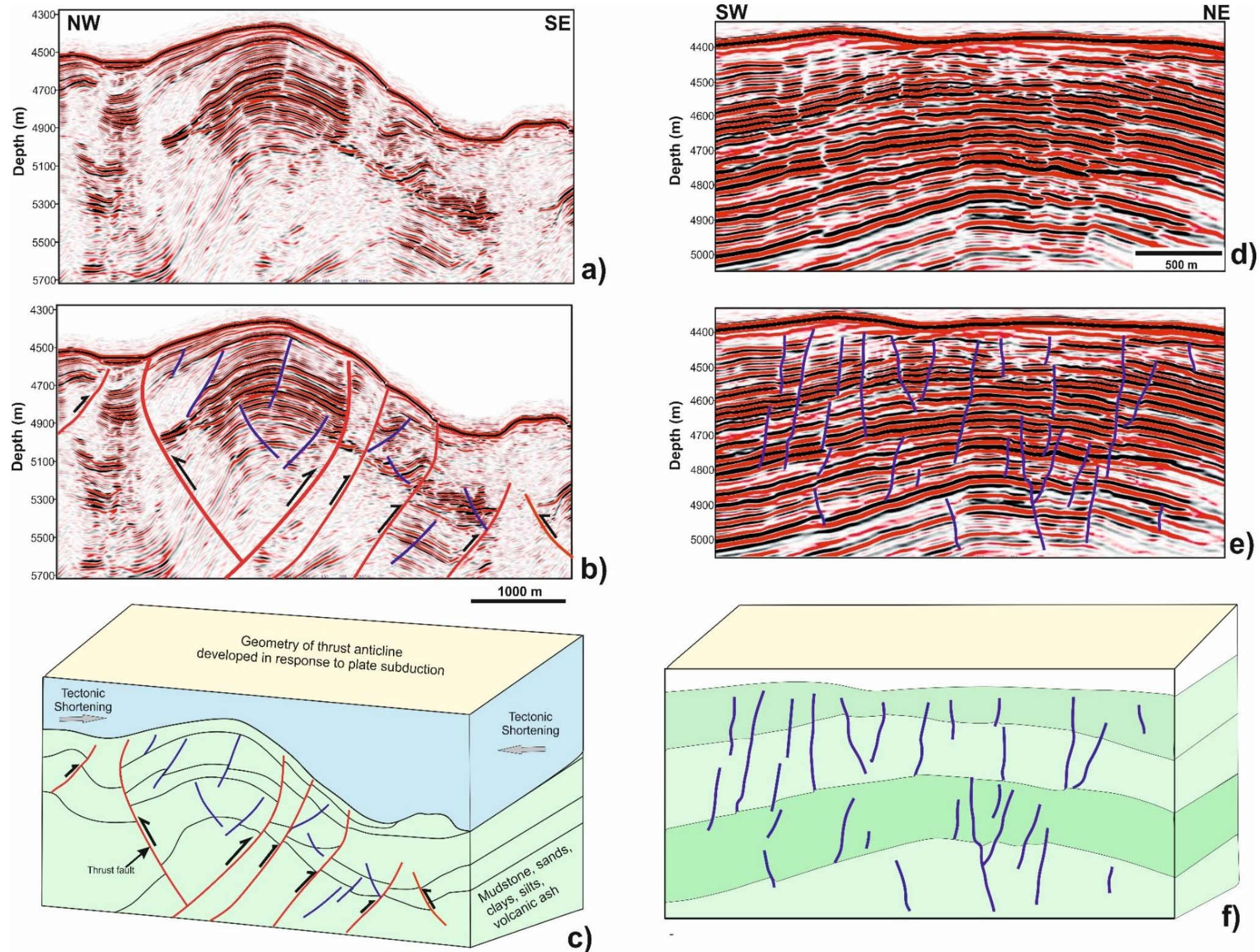
Fig. 7.4. a) Uninterpreted, b) Interpreted and c) schematic inline sections across the selected thrust anticline highlighting the major thrust faults, and shallow faults. The shallow faults are vertically segmented. d) Uninterpreted, e) Interpreted and f) schematic crossline sections highlighting some of the features of shallow fault systems around the hinge region of thrust anticline. The faults are vertically segmented, with some propagating and linking with other faults.

7.3. Impact of mechanical stratigraphy on normal faulting

Mechanical stratigraphy strongly influences fault reactivation and especially the ability of faults to reactivate across mechanical layering, the deformation mechanisms, and fault zone architecture (Wilkins and Gross, 2002; Ferrill and Morris, 2008; Welch et al., 2009; Childs et al. 2009; Libak et al., 2019). Normal faults are often seen to be vertically restricted by mechanically weak layers (Figs. 7.6 and 7.7). Therefore, fault reactivation and height are limited by the thickness and differences of mechanical layers (Roche et al., 2012, 2013) rather than controlled solely by the magnitude of tectonic shortening.

7.3.1. Impact of mechanical stratigraphy on normal fault nucleation

Research has shown that, as strain accumulates in a mechanically layered sedimentary section, competent (brittle) lithologies such as limestones and sandstones accommodate lower amounts of pre-failure strain and fracture first, whereas incompetent (ductile) lithologies like claystones and shales accommodate greater pre-failure strain prior to fracturing and fracture later (Ferrill and Morris, 2003, 2008; Welch et al., 2009). Thus, faults are expected to nucleate first in more competent (brittle) layers, or intervals, with local throw maxima and are later reactivated and linked together in incompetent (ductile) layers or intervals with local throw minima, and this study show this to be the case (Fig. 7.5a).

The relative nucleation of interpreted faults in the three study areas are illustrated with reference to the throw-depth (T-Z) profiles in Fig. 7.5. Fault segments with local throw maxima in the throw distribution profiles are early-stage fault segments and represent regions where faults nucleate first in more competent intervals. Each segment of these early-stage faults propagates outwards until they encounter other fault strands and link-

together. Linkage points are located where local throw minima are recorded in less competent intervals (Ellis and Dunlap, 1988; Mansfield and Cartwright, 1996) (Fig. 7.5). Hence, regions with local throw maxima in the throw distribution profiles are interpreted as the locus of fault nucleation, which dominantly occurs in more competent (brittle) intervals (Fig. 7.5).

7.3.2. Impact of mechanical stratigraphy on fault propagation and segmentation

Once fault nucleate, the rate of fault propagation is strongly controlled by the mechanical properties of the deforming rock. This behaviour is related to the ductility of the material - high ductility material will tend to impede fault propagation, whereas low ductility (brittle) material will tend to fault relatively easily. In brittle intervals such as massive limestone or indurated sandstone, faults tend to propagate rapidly with respect to the rate of fault displacement accumulation, and these faults tend to have relatively low displacement gradients with little or no associated folding (Ferrill and Morris, 2008; Ferrill et al., 2017) (Figs. 7.5a1). In contrast, fault propagation tends to slow or cease in incompetent (high ductility) intervals such as clay-rich shale or evaporite layers (Ferrill and Morris, 2008; Ferrill et al., 2017) (Figs. 7.5a).

Faults that nucleated within a competent mechanical layer may propagate outward until they encounter weaker mechanical layers where they may become arrested (Fig. 7.5a). These same faults may propagate laterally within a mechanical unit with relative ease. Thus, developing very small lateral displacement gradients, and transferring displacement to other faults via relay ramps with very subtle dips are common (Ferrill et al., 2017). Vertical displacement gradients, however, are likely to be more

pronounced, having developed where faults are inhibited from propagating into more ductile layered units (Fig. 7.5a).

In this study, evidence for vertical fault segmentation was observed in the interpreted throw-depth (T-Z) profiles (Fig. 7.5), where the fault segments with local throw minima in the incompetent intervals linked the pre-existing fault segments with local throw maxima in the competent intervals (Fig. 7.5). Incompetent (weak) intervals can prevent or slow propagation of faults from other layers, so that the locus of deformation can be shifted laterally across the incompetent intervals. Such a shift in fault position across an incompetent layer can result in vertical fault segmentation, whereby the fault segments can be hard or soft-linked (Bahroudi et al., 2003; Gabrielsen et al., 2016) (Fig. 7.5). Furthermore, evidence for vertical fault segmentation was observed in the interpreted seismic dataset of Nankai accretionary prism, a character indicating the presence of incompetent (weak) intervals (Figs. 6.11-6.14 and 7.4).

Incompetent intervals can act as detachments that cause decoupling and prevent propagation of faults across specific intervals, resulting in a preferable horizontal propagation of faults to the detriment of their vertical growth (Richardson et al., 2005; Gabrielsen et al., 2016). In fact, IODP Site C0006 (Expedition 316 Scientists, 2009) and Park et al. (2010) recognised the presence of hemipelagic mudstone to sand, mud, and silty-clay sequences interbedded with volcanic ash and tuffs in the Nankai accretionary prism. This hints at a presence of incompetent lithologies dominating the Nankai accretionary prism (Fig. 6.3c). Consequently, nucleation and subsequent propagation of slip from fault segments with local throw maxima in the competent intervals into the incompetent interval can describe the vertically segmented fault arrays

observed in both the throw-depth (T-Z) and seismic profiles (Childs et al. 1995; Mansfield and Cartwright, 1996) (Figs. 7.4 and 7.5).

Discrepancies in throw gradients commonly result from mechanical heterogeneities, fault reactivation and linkage of individual faults (Childs et al., 1996; Baudon and Cartwright, 2008). Therefore, the results of throw-depth (T-Z) interpretation support the view that vertically segmented fault arrays initially nucleate in the more competent, and brittle, lithologies (sandstones and limestones) with local throw maxima and are later linked by faults in the incompetent, and ductile, lithologies (shales) with local throw minima (Ellis and Dunlap, 1988; Childs et al., 1996; Mansfield and Cartwright, 1996) (Fig. 7.5).

There is no obvious structural expression of the evolution of segment dip-linkage on the seismic datasets equivalent to that shown in Fig. 7.5a. This is due to the following reasons: a) the structures are not well resolved by the interpreted seismic data, b) the original segment dip-linkage structures have been deformed during post-linkage slip on the fault, and any original topological irregularities have been largely eliminated, and c) fault segments coalesced during their growth, a character resulting in the straightening of the active fault trace and corresponding changes in fault zone architecture. Local complexities in fault topology resulting from segment dip-linkage structures are unlikely to be well imaged on seismic cross-sectional profiles – the finite trace spacing, and limited frequency content of most seismic data mean that faults are not imaged as single, discrete planes, but rather as diffuse deformation zones (Mansfield and Cartwright, 1996).
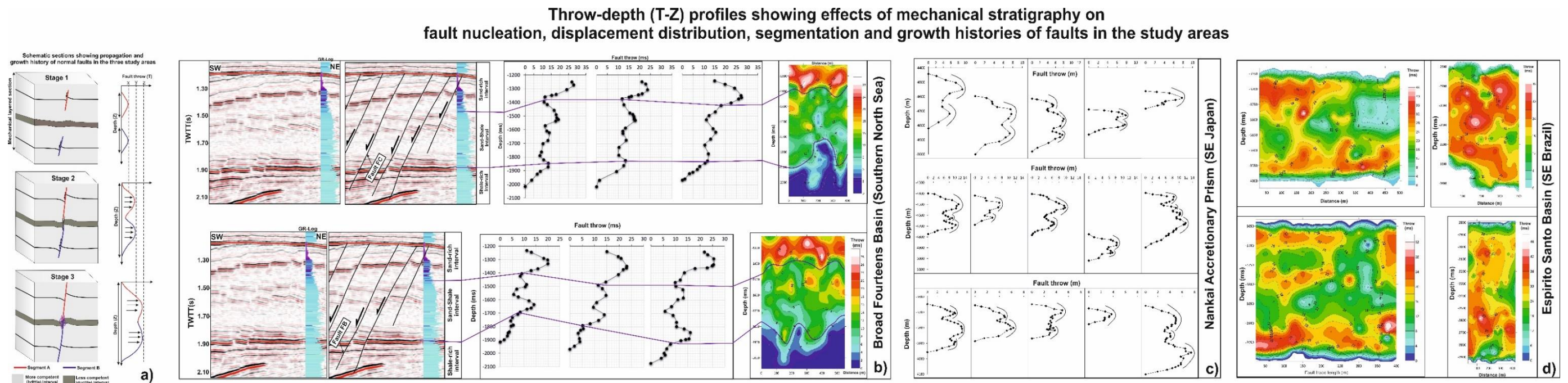
Fig. 7.5. a) **Fig. 7.7.** a) Schematic model depicting the progressive evolution of a normal fault dominated by the segment dip-linkage direction between two initially isolated fault segments. In stage 1, fault segments with local throw maxima are early-stage fault segments and represent regions where faults nucleate first in more competent intervals. Each segment of these early-stage faults accumulates higher displacement and propagates outwards until they encounter other fault strands and link together. Linkage points are located where local throw minima are recorded in less competent intervals (Stage 2). Thereafter, the linked segments rapidly accumulate displacement rather than length. However, further propagation of the two hard-linked fault segments after growth can attenuate the throw variations recorded on throw-depth (T-Z) profiles, and thus obscure differences in the throw distribution with depth (Stage 3). b) Representative throw-depth (T-Z) profiles showing the fault reactivation and growth by segment linkage in the Broad Fourteens Basin. Fault throw is less segmented in competent (sand-rich) intervals with larger throw and more segmented in less competent (shale-rich) intervals with relatively smaller throw. c) Representative vertical throw-depth (T-Z) profiles of the shallow faults in the Nankai accretionary prism. Fault segments with throw maxima nucleate first in more competent (brittle) intervals and are later linked by throw minima in less competent (ductile) intervals. d) Representative of vertical throw-depth (T-Z) plots highlighting throw distribution and segmentation along fault planes in the Espírito Santo Basin.

In addition, segment dip-linkage structures can be expected to have a very low preservation potential during continued fault slip (Mansfield and Cartwright, 1996). By comparison, branch line and relay structures on normal and thrust faults produced during the linkage of overlapping segments in the strike direction have a much higher preservation potential during continued fault slip because the topological irregularity or step on the linked fault surface is parallel to the- slip direction (Scholz 1990) and is therefore more likely to be imaged by seismic data (Walsh and Watterson 1990; Cartwright et al. 1995; Fossen and Rotevatn, 2016).

Offsets, bends and breached relay structures create rough fault plane topologies along the strike of normal and strike-slip faults that have been known to act as barriers to earthquake rupture distribution (Zhang et al. 1991, Cowie and Scholz 1992). In a similar manner, segment dip-linkage sites might also be expected to arrest or impede slip, such that the continued partitioning of slip between relict fault segments after linkage will accentuate the displacement minima at linkage points, producing irregular displacement distributions (Fig. 7.5a). Consequently, whilst seismic data may be unable to resolve the local structures in wholly satisfactory way, the mechanical control of these structures on the local accommodation of slip will leave a strong signature in the displacement field, which can be imaged by detailed mapping of the fault displacement distribution as shown in Fig. 7.5.

7.3.3. Impact of mechanical stratigraphy on fault growth and geometry

Fault segment linkage has been proposed as an important mechanism for fault growth, where more competent (strong) mechanical layer favours nucleation of new faults in distinct mechanical intervals (Peacock and Sanderson, 1991; Peacock and Sanderson,

1992; Cartwright et al., 1995; Childs et al., 1996; Kim et al., 2000; Wilkins and Gross, 2002). In the studied datasets, the interpreted faults present anomalous throw distribution profiles with multiple local throw maxima separated by local throw minima, a character signifying fault growth via segment linkage, i.e., fault growth through coalescence of multiple fault segments (Fig. 7.5).

Their throw-depth (T-Z) profiles do not always show single positive gradients and are mostly characterised by throw profiles that resemble C-type or M-type patterns between their upper-tip points and immediate throw minima (e.g., Cartwright et al., 1995; Lohr et al., 2008; Baudon and Cartwright, 2008). However, further propagation of two hard-linked fault segments after growth can attenuate the throw variations recorded on throw-depth (T-Z) profiles, and thus obscure differences in the throw distribution with depth (Fig. 7.5a; Stage 3). Fault segments are transient features and, as faults evolve, segments may coalesce and new segments may form (Cartwright et al. 1995, Childs et al. 1995). Coalescence of fault segments results in straightening of the active fault trace and a corresponding change in fault zone architecture.

As discussed earlier, where layers have strong mechanical contrasts, a fault is likely to nucleate in a more competent, brittle layer and propagate rapidly within this brittle bed without developing significant displacement gradients or related damage or folding (Fig. 7.6a). However, a different fault nucleating in another competent layer and propagates upward across mechanical stratigraphy into the above-mentioned competent layer will cause folding prior to the fault breaking through the bed (e.g., Fault B; Fig. 7.6b).

Two faults in the same competent layer may, therefore, have radically different fault zone architectures, representing: i) a fault that nucleated in the first competent layer and

produced no associated folding and a relatively narrow (less segmented) damage zone (e.g., Fault A; Fig. 7.6), and ii) a fault that nucleated in a different competent layer and propagated through incompetent units and into the competent layer of interest producing a significant amount (volume and intensity) of fault related damage, including folding and distributed brittle deformation (e.g., Fault B; Fig. 7.6c). In such a setting, fault zone evolution and characteristics are likely to be rather different in a particular layer if this was the nucleation layer for that fault vs. if it was encountered by a fault that nucleated elsewhere in the stratigraphic section and propagated into it, crossing weaker layers along the way (Ferrill and Morris, 2008) (Fig. 7.6).

Recently, Libak et al. (2019) showed that fault zones are more segmented and wider in the claystones, while sandy intervals have fault zones that are narrower and more localized, showing less segmentation. Thus, deformation tends to be more localized (less segmented) with local throw maxima in competent lithologies like sandstones and carbonates, and more distributed (segmented) in incompetent lithologies like claystone- and shales with throw minima. In the Nankai accretionary prism dataset, fault deformations are more segmented and distributed with relatively smaller throw maxima of 14 m, a character indicating the presence of incompetent (weak) intervals blanketing Nankai accretionary prism (Figs. 7.4 and 7.5c). Whereas the faults in the sand-rich and carbonate dominated intervals in the Espírito Santo and Broad Fourteens Basins appear as a continuous and more localized (less segmented) with relatively larger throw maxima between 30 m and 60 m (Figs. 7.2b, 7.3b and 7.5b,c).

Research has shown that faults are often steep in the competent lithologies, while in incompetent lithologies faults have more gentle dips (Peacock 2002; Ferrill et al. 2017). Such differences in fault dip along the fault segment can locally lead to fault refraction-
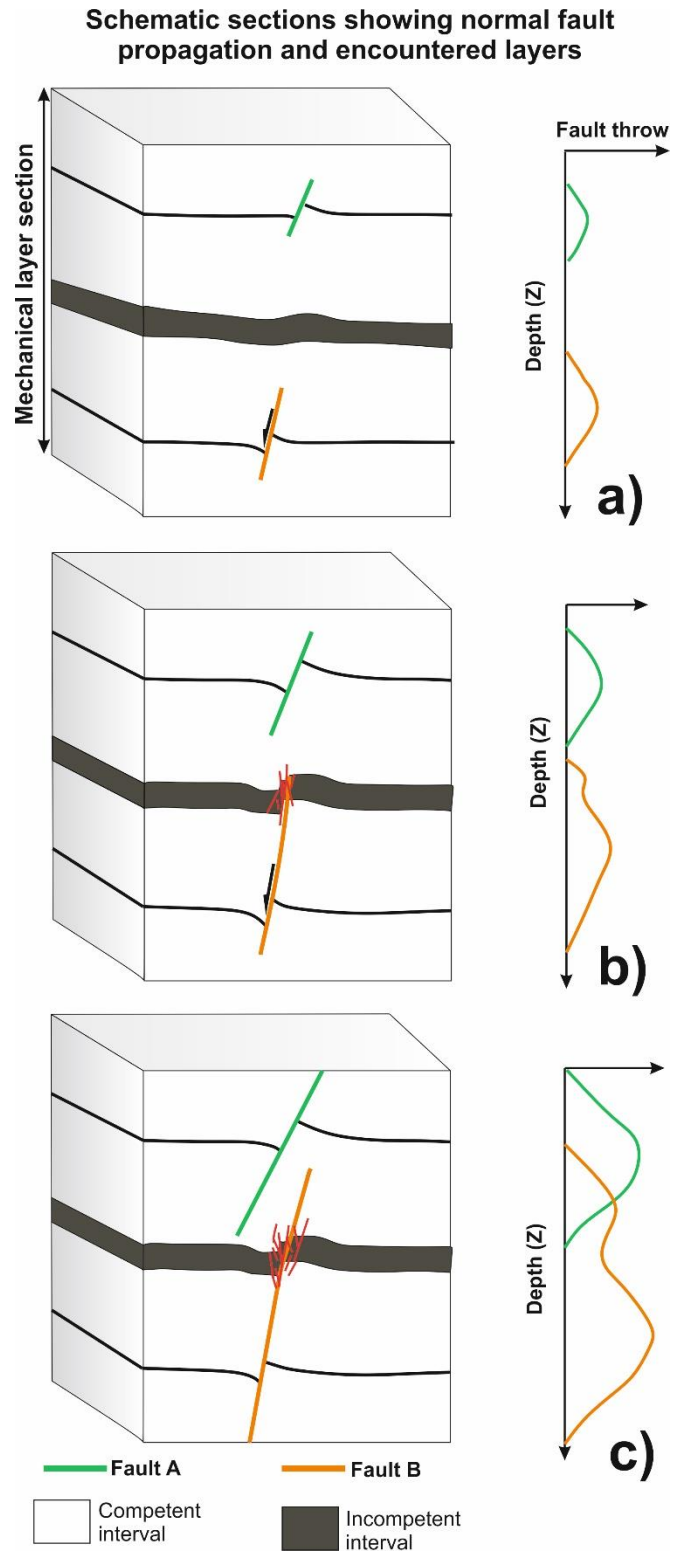
Fig. 7.6. Schematic model depicting the fault nucleation and encountered layers. Normal fault zone evolution and characteristics are likely to be quite different in a particular layer if it was the nucleation layer for that fault versus it was encountered as a fault that nucleated elsewhere in the stratigraphic section and propagated into it, crossing weaker layers along the way.

that causes extensional (dilatational) jogs (Peacock & Sanderson 1991; Ferrill et al. 2017). In the study datasets, no strong evidence is recorded for changes in fault dip geometries, as fault propagates from competent intervals into incompetent intervals, due to intricate nature of the fault geometries and limited resolution of the seismic datasets (i.e. the faults are not resolved by the seismic data). In parallel, the original segment dip-linkage structures may have been deformed during post-linkage slip on the fault, and any original topological irregularities may have been largely eliminated.

Faults are generally localized zones of deformation that may include rotation of layers, local fracturing, cataclasis, dilation, dissolution, and mineral precipitation, and commonly include a fault core (a narrow zone where displacement is concentrated) and a surrounding damage zone that is typically wider, representing distributed deformation (Caine et al., 1996; Faulkner et al., 2011). In practice, determining the fault zone widths can be difficult, with the basis that they vary over several orders of magnitude (Evans, 1990; Shipton et al., 2006), and studies that show relatively uniform increase in fault zone width with displacement are rare and narrowly limited in scope (Shipton and Cowie, 2001). One factor influencing the significant variation in fault zone width is that faults tend to grow by segment linkage (Fig. 7.5), and once linked, the spacing between overlapping fault segments (or width of relay structures; Childs et al., 2009) locally defines the fault zone width (Ferrill et al., 2016).

As previously suggested, fault zones enlarge by the linkage or reactivating of existing faults, causing off-fault damage, i.e. the generation of additional deformation bands and or fractures (Fossen, 2010). Thus, reactivated and growth faults can exhibit relatively larger fault zone architectures when compared with similar structures (Gross et al., 1997; Wilkins and Gross, 2002). The length of faults is generally established during the

phase of faulting that created any pre-existing faults, prior to their reactivation. When the faults are reactivated, a disproportionate increase of maximum displacement shifts the growth path length with relatively larger fault zone architectures. Therefore, it is necessary to understand fault reactivation and growth as an important factor for fault zone evolution and characteristics as it will provide insights into the timing of fault activity which has a direct application to hydrocarbon migration and sealing of faults in petroleum reservoirs, CO_2 reservoirs, and even geothermal prospects (McClay, 1990; Cartwright et al., 2007; Ward et al., 2016). For example, the accurate timing of any reactivation phases with reference to constraints on the filling of hydrocarbon traps would be critical for an evaluation of seal risk (Cartwright et al., 2007). Traps are much more likely to leak during periods of fault reactivation than during periods when the faults are inactive, all other parameters of seal integrity being the same (Hooper, 1991; Gartrell et al., 2002; Cartwright et al., 2007).

7.4. Implications for sub-surface fluid flow

Tectonic faults reactivated or not, typically represent potential pathways for the vertical migration of fluids. But also, barriers to cross-fault flow, due to sealing capacity. The reason for this is the increased structural complexity found at reactivated fault zones, with increased numbers of faults and fractures and a wider range of orientations being recorded in these zones (Peacock and Parfitt, 2002; Fossen et al., 2005). A consequence of fault reactivation through linkage is the development of long and continuous faults at advanced stages. As fault linkage zones form, the long faults that result from this process will compartmentalise reservoirs and produce long and isolated fault blocks that act as individual fluid compartments. The linkage of fault zones leads to more connected fault systems. Fault linkages and intersections are important for the

accumulation and trapping of hydrocarbons. They may act as vertical conduits for fluid migration into traps but may also have negative effect on seal integrity.

In a series of petroleum fields in the Timor Sea, Australia, Gartrell et al. (2004) identified fault intersections as critical hydrocarbon leakage zones. This is also supported by Kristiansen (2011), who found that for fault-controlled structural hydrocarbon traps in the Barents Sea (Norway), traps were generally underfilled or dry where controlled by two or more interacting faults, whereas all discoveries were associated with fault traps controlled by a single fault.

Fault linkage zones may affect fluid flow between structural reservoir compartments on a production time scale. Soft-linked fault zones may offer cross-fault reservoir connectivity through folded but unbreached relay beds (e.g., Rotevatn et al., 2009). However, this effect may be reduced if the fault zone is associated with a linking damage zone of low-permeable deformation bands in porous sandstone host rocks (Rotevatn et al., 2009, Rotevatn and Fossen, 2011). In fault linkage zones, however, increased fracture intensity and orientation variability in the linking damage zone leads to an increased fracture:matrix ratio and connectivity, both of which lead to a higher overall effective permeability (Berkowitz, 1995).

Curewitz and Karson (1997) reported evidence for increased geothermal fluid activity linked to fault linkage zones. They showed that CO_2 springs and seeps were co-located within structurally complex zones in a fault array. Furthermore, fault jogs, which commonly represent the locations of previous fault linkage zones, have been shown to be associated with hydrothermal gold deposits in strike-slip systems (Micklethwaite and Cox, 2004, 2006).

Active fracturing provides a pathway for fluids where distinct fault segments interact, with the loci of fault segment linkage across seal units increasing the permeability of host rocks, thus allowing the migration of fluid out of underlying res ervoirs (Curewitz and Karson, 1997; Knai and Knipe, 1998). Conversely, faults can compartmentalise reservoir units when they form barriers to fluid flow, a character resulting in increasing exploration costs as more wells are needed to retrieve hydrocarbons, or store $CO2$ and other gases (Hardman and Booth, 1991; Caine et al., 1996; Cartwright et al., 2007; Bentham et al., 2013).

7.5. Resolution of seismic data vs. fault analyses

The high quality of the 3-D seismic reflection datasets used in the three study areas allowed for a reliable visualisation and mapping of key stratigraphic horizons, structures, and vertical component of dip separation (throw) distributions. However, each of the seismic datasets has a characteristic resolving power. For instance, the Nankai (SE Japan) 3-D seismic reflection data (see Chapter 6) is of much higher resolution than the other industry seismic datasets in the Espírito Santo and Broad Fourteen Basins (see Chapters 4 and 5). The key aspect in the Nankai dataset is that one can notice (and map) vertical fault segmentation and linkage much better on the seismic profiles because the faults are better imaged (Fig. 7.4d,e). Thus, the relatively high resolution of this latter seismic data allowed the mapping of fault segmentation in great detail and the measuring of their relatively smaller throws to a minimum of 14 m (see Chapter 6; Figs. 6.11-6.14 and 7.6).

In the industry datasets (i.e. Espírito Santo and Broad Fourteen Basins), fault segmentation, linkage and dip changes associated with fault propagating through

mechanically layered sections were imaged as one continuous and localised single fault (Figs. 7.2 and 7.3). There is no obvious structural expression of vertical fault segmentation on the seismic datasets equivalent to that observed in Nankai dataset (Figs. 7.4d, e) and the faults were not fully resolved by the industry seismic datasets. Therefore, detail mapping fault throw-depth (T-Z) needed to be completed reflection-by-reflection to understand how faults were originally segmented, resolution allowing. The sampling interval at which fault displacement is recorded governs the resolution of the final mapped distribution and therefore maintaining a consistently high sampling density is vital for recognising the smallest and most subtle local displacement patterns.

The detection of smaller features on seismic data can be achieved on the modern seismic technology by increasing bin lines and reducing the crossline bin size. Crossline bin size tends to be one of the limiting factors in the resolution of seismic data (Yilmaz, 2001; Vermeer, 2012). During the recording of seismic data, it is necessary to use adequate receiver arrays and antialiasing filters in order to prevent and reduce the loss of high-frequency signal. During the processing of the obtained data, the primary concern is the removing of any unwanted noise that can reduce the high-frequency signal before stacking the data and with the preservation and display of the high-frequency signal.

Deconvolution is the tool used to ensure that the high-frequency signal is displayed on the stacked data. Also, adequate velocity measurements are very important in reflection-data processing because once optimum primary velocity is computed, Normal Moveout (NMO) corrections can be applied to Common Mid-Point (CMP) gathers, which are concurrently stacked, making signal stack in phase and noise out of phase thus increasing the signal-to-noise ratio (Yilmaz, 2001). Where dipping images and diffraction images are found, migration is recommended. The quality of such a

seismic section is considerably improved by modern migration processing (Yilmaz, 2001; Levin, 1971).

7.6. Limitations of this research

The major limitations in this thesis are related to the resolution of the 3D seismic datasets, vertical extent of the datasets and absence of borehole data in the Espírito Santo Basins and Nankai Trough. Chapter 4 uses three-dimensional (3-D) seismic reflection data from the salt-rich Espírito Santo Basin (SE Brazil; Fig. 2.1) to investigate the geometry and reactivation histories of normal faults associated with development rollover anticlines. If well data had been available for the Espírito Santo Basin, it would have been possible to correlate the interpreted seismic units with local stratigraphic data, indicating with greater accuracy the lithology of each sub-unit interpreted. This would have provided a more reliable lithological framework to perform fault reactivation and growth analyses through multi-layered lithology. The availability of well data would also provide internal velocity (Vp) for the interpreted seismic units, allowing the conversion of throw-distribution curves to depth and, consequently, providing a more detailed understanding of the linkage and reactivation histories of faults through layered sequences.

The 3D volume of the Espírito Santo Basin was truncated at a depth of approximately 5000 ms. A greater depth range would have provided a better opportunity to delimit the vertical extent of the Aptian evaporites, Albian rafts and, correlate the pre-salt units with the regional stratigraphy, and map contact (salt weld) between pre-salt units and Albian rafts to help constraining the potential migration of hydrocarbons from welded sub-salt source units into supra-salt reservoirs.

Chapter 5 uses high-quality 3D seismic and borehole data from the Broad Fourteen Basin, Southern North Sea (Fig. 2.4) to investigate the effect of lithology on fault throw distribution and segmentation along fault planes, as well as the geometry and reactivation histories of faults developed due to the Late Cretaceous to Paleogene tectonic inversion. Borehole data were provided and helped to correlate fault throw distribution and segmentation as well as reactivation and growth of faults through layered sequence. The main limitations for this chapter consisted in the resolving power of the 3D seismic volume. The resolution of the seismic data only allowed to image faults as localised (less segmented) and continuous displacement rather than segmented fault arrays with some dip changes as the faults propagated through mechanically layered sections.

Chapter 6 uses three-dimensional (3-D) pre-stack depth migrated seismic data to explore the effect of mechanical stratigraphy on shallow fault geometry and growth history from areas dominated by thrust anticlines in the outer wedge region of the Nankai accretionary prism (SE Japan). The main limitations for this chapter consisted in the absence of well data crossing Thrust Anticlines A and D and the vertical extent of the seismic resolution. The relatively poor seismic signal at depth makes it difficult to identify and map more seismic horizons to precisely constrain the onset of tectonic shortening in the Nankai accretionary prism. Thus, limiting this chapter to focus on calculating shortening for shallow Late Quaternary strata. If well data had been available for the Nankai Trough dataset, it would have been possible to correlate the vertical fault segmentations with lithology. This would have provided a more reliable lithological framework to perform fault growth analyses through layered sequence and more detailed understanding of the linkage and reactivation histories of shallow fault systems interpreted.

7.7. Further work

The conclusions drawn from this research has wide implications for the understanding of fault reactivation and growth in sedimentary basins and its consequences to petroleum systems. Reactivated and growth faults typically represent potential pathways for fluids transport, including hydrocarbons, CO_2 and other volatiles, hydrothermal solutions. Following the methods applied to this thesis, it would be important to investigate, in more detail, the relationships between lithology, mechanical stratigraphy and the geometry of seismic-scale normal faults, as well as the influence of mechanical stratigraphy and lithology on fault throw distributions, fault segmentations, linkages, fault reactivations, fault growth history and the characteristics attributes of fault zone architectures (i.e. fault zone width, thickness and length), considering different geologic settings and integrating new information with the high-quality 3D seismic and borehole datasets. This approach would provide a robust model, improving relationships between faulting and mechanical stratigraphy as well as fault zone architectures.

CHAPTER 8

Conclusions

8. Conclusions

Detailed mapping of stratigraphic horizons, fault geometries and throws of normal faults using high-quality 3D seismic and borehole datasets from the Espírito Santo Basin (SE Brazil), Broad Fourteens Basin, offshore The Netherlands (Southern North Sea) and Nankai Accretionary Prism (SE Japan) provided insights into the geometry and growth histories of normal faults associated with tectonic shortening of overburden rocks. The key conclusions of this study are as follows:

a. In the proximal continental slope of salt-rich Espírito Santo Basin (SE Brazil), differences in the degree of downslope translation of un-welded rafts enhanced the reactivation of rollover faults, a phenomenon that promoted the migration of hydrocarbons from welded sub-salt source units into supra-salt reservoirs. Geometry of the reactivated rollover faults are approximately polygonal because not all the faults connect to create closed cells in plan view and thus they resemble fault systems that are formed in shallower position on the crust, the typical polygonal faults systems. These reactivated polygonal faults are very small features

with displacement ranging between 2 m and 60 m, thus having similar fault throw values when compared with classical polygonal faults. Importantly, the reactivated polygonal geometry interpreted in this study are primarily resulted from tectonic shortening and gravity collapse, and occurred at deeper position compared with classical polygonal faults that commonly resulted from density inversion or compactional loading at shallower position.

b. In the Espírito Santo Basin, tectonically generated pulses of compression and uplift, commonly related to the Andean Orogeny, are not the only mechanisms deforming post-salt overburden units in proximal extensional dominated regions of the southeast Brazilian margin, as the close control of tectonic rafts gravitational instability induced a continuum of overburden deformation and contributed significantly to shaping the supra-salt overburden in the Espírito Santo Basin.

c. The Late Cretaceous to Paleogene tectonic inversion in the Broad Fourteens Basin, Southern North Sea have induced a continuum of deformation and fault reactivation. This reactivation had mostly positive economic impacts, as tectonic movements reactivated older faults and potentially allowed the secondary migration of hydrocarbons into shallower reservoir units. The reactivated faults are vertically segmented and thus increase the chance of compartmentalisation or localised fluid flow through fault linkages, as well as present significant risks when injecting CO_2 into the subsurface such as the Southern North Sea.

d. Offshore Nankai (SE Japan), tectonic shortening and uplift of overburden strata have induced a continuum of internal deformation that is expressed in the form of thrust anticlines that occur, near the seafloor, in association with significant distribution of the shallow fault populations in the uppermost part of the Nankai accretionary prism. These shallow fault populations accommodate a significant part

of the bending and stretching strain occurring during thrust anticlines development, and subsequent local stress distribution and accommodation of strain during seismic events offshore Nankai.

e. In the Nankai accretionary prism dataset, fault deformations are more segmented and distributed with relatively smaller throw maxima of 14 m, a character indicating the presence of incompetent (weak) intervals blanketing Nankai accretionary prism. Whereas, fault deformations in the Espírito Santo and Broad Fourteens Basins appear as a continuous and more localized (less segmented) zones with relatively larger throw maxima between 30 m and 60 m, a character signifying the presence of competent (strong) intervals.

f. The anomalous vertical fault throw distributions documented in the three study areas in this thesis are inconsistent with models of fault growth by uniform slip distribution and radial tip-line propagation. As corollary of these thesis, it is concluded that fault reactivation and growth by segment dip-linkages characterised the mode of evolution and growth of all the faults interpreted in the three study areas in this thesis. Where two separate faults with local throw maxima propagate towards each other and linked in throw-minimum in the throw-depth (T-Z) profiles.

g. Fault segments with local throw maxima in the throw-depth (T-Z) profiles are early-stage fault segments and represent regions where faults localise first in competent intervals. Each segment of these early-stage faults propagates outwards until they encounter other fault strands and link together. Linkage points are located where local throw minima are recorded in less competent intervals. Consequently, the propagation of slip from fault segments (with local throw maxima) in the competent intervals into the incompetent intervals resulted into vertically segmented fault arrays.

References

References

Allen, J. R. (1987) Desiccation of mud in the temperate intertidal zone: studies from the Severn Estuary and eastern England. Philosophical Transactions of the Royal Society of London B. 315, 127-156.

Alsouki, M., Riahi, M. A., Yassaghi, A. 2011. Seismic Imaging of Sub-Circular Salt-Related Structures: Evidence for Passive Diapirism in the Straits of Hormuz, Persian Gulf. Petroleum Geoscience, 17, 101-107.

Alves, T.M., Strasser, M., Moore, G.F., 2014. Erosional features as indicators of thrust fault activity (Nankai Trough, Japan). Mar. Geol. 356, 5–18.

Alves, T. M., Cartwright, J. A., 2010. The effect of mass-transport deposits on the younger slope morphology, offshore Brazil. Marine and Petroleum Geology, 27, 2027-2036.

Alves, T. M., 2010. 3D Seismic examples of differential compaction in mass-transport deposits and their effect on post-failure strata. Marine Geology, 271, 212-224.

Alves, T. M., 2012. Scale-relationships and geometry of normal faults reactivated during gravitational gliding of Albian rafts (Espírito Santo Basin, SE Brazil). Earth and Planetary Science Letters, 331, 80-96.

Alves, T. M. and Elliott, C. 2014. Fluid flow during early compartmentalisation of rafts: A North Sea analogue for divergent continental margins. Tectonophysics, 634**,** 91-96.

Alves, T. M., Fetter, M., Lima, C., Cartwright, J. A., Cosgrove, J., Gangá, A., Queiroz, C. L., Strugale, M. 2017. An incomplete correlation between pre-salt topography, top reservoir erosion, and salt deformation in deep-water Santos Basin (SE Brazil). Marine and Petroleum Geology, 79, 300-320.

Alves, T. M., Cartwright, J., Davies, R. J., 2009. Faulting of salt-withdrawal basins during early halokinesis: effects on the Paleogene Rio Doce Canyon system (Espírito Santo Basin, Brazil). AAPG bulletin, 93**,** 617-652.

Anderson, E. M., 1951. The Dynamics of Faulting, 1951. Oliver and Boyd, Edinburgh.

Anette, B.M.T., Rotevatn, A., Jackson, C.A.L., Fossen, H., Gawthorpe, R.L., 2013. Growth of normal faults in multilayer sequences: a 3D seismic case study from the Egersund Basin, Norwegian North Sea. Journal of Structural Geology, 55, 1–20.

Asmus, H.E., Gomes, J.B., Pereira, A.C.B., 1971. Integração geológica regional da bacia do Espírito Santo. Relatório Interno, PETROBRAS.

Aydin, A., Basu, A., 2005. The Schmidt hammer in rock material characterization. Eng. Geol. 81, 1-14.

Azevêdo, M.C., Alves, T.M., Fonseca, P.E., Moore, G.F., 2018. Strike-slip deformation reflects complex partitioning of strain in the Nankai Accretionary Prism (SE Japan). Tectonophysics 723 (2018), 81–94.

Bacon, M., Simm, R. And Redshaw, T. 2007. 3-D seismic interpretation, Cambridge University Press.

Bahroudi, A., Koyi, H.A., Talbot, C.J., 2003. Effect of ductile and frictional décollements on style of extension. J. Struct. Geol. 25, 1401–1423.

Barnett, J.A., Mortimer, J., Rippon, J.H., Walsh, J.J., Watterson, J., 1987. Displacement geometry in the volume containing a single normal fault. AAPG Bull. 71, 925-937.

Barry, K. M., 1975. Recommended standards for digital tape formats. Geophysics 40, 334-352.

Baudon, C., Cartwright, J., 2008. The kinematics of reactivation of normal faults using high resolution throw mapping. Journal of Structural Geology, 30, 1072-1084.

Barnett, J.A., Mortimer, J., Rippon, J.H., Walsh, J.J., Watterson, J., 1987. Displacement geometry in the volume containing a single normal fault. AAPG Bull. 71, 925-937.

Bentham, M., Green, A., Gammer, D., 2013. The occurrence of faults in the Bunter Sandstone Formation of the UK sector of the Southern North Sea and the potential impact on storage capacity. Energy Procedia 37, 5101–5109.

Berkowitz, B., 1995. Analysis of fracture network connectivity using percolation theory. Math. Geol. 27, 467–483.

Biondi, B., 2006. 3D seismic imaging, Society of Exploration Geophysicists Tulsa.

Bird, P., 2003. An updated digital model of plate boundaries. Geochem. Geophys. Geosyst. 4 (3), 1027.

Boston, B., Moore, G. F., Jurado, M. J., Sone, H., 2016. Deformation of the Nankai Trough inner accretionary prism: The role of inherited structures, Geochem. Geophys. Geosyst., 17, 485– 500, doi:10.1002/2015GC006185.

Brown, A. R., Brown, A. R., Brown, A. R. 2004. Interpretation of three-dimensional seismic data. sixth ed., vol. 42. American Association of Petroleum Geologist. Memoir, p. 541.

Brown, A.R., 2011. Interpretation of three-dimensional seismic data. American Association of Petroleum Geologists and the Society of Exploration Geophysicists.

Bruijn, A. N. 1996. De Wijk gas field (Netherlands): reservoir mapping with amplitude anomalies. Geology of Gas and Oil under the Netherlands. Springer.

Bruhn, C. H., Walker, R. G., 1997. Internal architecture and sedimentary evolution of coarse-Grained, turbidite channel-levee complexes, Early Eocene Regência Canyon, Espirito Santo Basin, Brazil. Sedimentology, 44, 17-46.

Brun, J.-P., Mauduit, T.P.O., 2009. Salt rollers: Structure and kinematics from analogue modelling. Marine and Petroleum Geology 26, 249-258.

Bull, S., Cartwright, J. & Huuse, M., 2009. A review of kinematic indicators from mass-transport complexes using 3D seismic data. Marine and Petroleum Geology, 26, 1132-1151.

Bueno, G.V., 2004. Event diachronism in the South Atlantic rift. Bol. Geociênc. Petrobras 14, 203–229.

Bürgmann, R., Pollard, D. D., Martel, S. J., 1994. Slip distributions on faults: effects of stress gradients, inelastic deformation, heterogeneous host-rock stiffness, and fault interaction. Journal of Structural Geology, 16, 1675-1690.

Busetti, S., Jiao, W., Reches, Z., 2014. Geomechanics of hydraulic fracturing micro seismicity Part I: shear, hybrid, and tensile events. AAPG Bull. 98, 2439-2457.

Byerlee, J., 1978. Friction of rocks. Pure Appl. Geophys. 116, 615-626.

Cameron, T. D. J. 1992. The geology of the southern North Sea, London: HMSO.

Cainelli, C. and Mohriak, W.U., 1999. Some remarks on the evolution of sedimentary basins along the eastern Brazilian continental margin. Episodes, 22 (3), 206-216.

Caine, J.S., Evans, J.P., Forster, C.B., 1996. Fault zone architecture and permeability structure. Geology, 24, 1025–1028.

Cartwright, J. A., Trudgill, B. D., Mansfield, C. S. 1995. Fault growth by segment linkage: An explanation for scatter in maximum displacement and trace length data from the Canyonlands Grabens of SE Utah. Journal of Structural Geology, 17, 1319-1326.

Cartwright, J.A., Mansfield, C.S., 1998. Lateral displacement variation and lateral tip geometry of normal faults in the Canyonlands National Park, Utah. Journal of Structural. Geology. 20, 3–19.

Cartwright, J., Trudgill, B., Mansfield, C., 2000. Fault growth by segment linkage: An explanation for scatter in maximum displacement and trace length data from the Canyonlands grabens of SE Utah: Reply. Journal of Structural Geology 22, 141-143.

Cartwright, J., James, D., and Bolton, Al., 2003. The genesis of polygonal fault system: a review. Geological Society, London, Special Publications, 216, 223-243.

Cartwright, J., Huuse, M., Aplin, A., 2007. Seal bypass systems. American Association of Petroleum Geologists Bulletin 91 (8), 1141–1166.

Chang, H. K., Kowsmann, R. O., Figueiredo, A. M. F., Bender, A., 1992. Tectonics and stratigraphy of the East Brazil Rift system: an overview. Tectonophysics, 213, 97-138.

Chang, C., Song, I., 2016. Present-day stress states underneath the Kumano basin to 2 km below Sea floor based on borehole wall failures at IODP site C0002, Nankai accretionary wedge. Geochem. Geophys. Geosyst. 17 https://doi.org/10.1002/2016GC006562.

Chang, C., Zoback, M.D., Khaksar, A., 2006. Empirical relations between rock strength and physical properties in sedimentary rocks. Journal of Petroleum Science and Engineering, 51, 223–237, https://doi.org/10.1016/j. petrol.2006.01.003

Childs, C., Nicol, A., Walsh, J.J., Watterson, J., 1996. Growth of vertically segmented normal faults. J. Struct. Geol. 18, 1389-1397.

Childs, C., Watterson, J., Walsh, J. 1995. Fault overlap zones within developing normal fault systems. Journal of the Geological Society, 152, 535-549.

Childs, C., Manzocchi, T., Walsh, J.J., Bonson, C.G., Nicol, A., Schöpfer, M.P.J. 2009. A geometric model of fault zone and fault rock thickness variations. Journal of Structural Geology, 31, 117–127.

Childs, C., Nicol, A., Walsh, J., Watterson, J., 2003. The growth and propagation of synsedimentary faults. J. Struct. Geol. 25, 633–648.

Cobbold, P.R., Rossello, E.A., Roperch, P., Arriagada, C., Gómez, L.A., Lima, C., 2007. Distribution, timing, and causes of Andean deformation across South America. In: Ries, A.C., Butler, R.W.H., Graham, R.H. (Eds.), Deformation of the Continental

Crust: The Legacy of Mike Coward: Geological Society, London, Special Publications, 272, pp. 321–343.

Cobbold, R.R., Chiossi, D., Green, P.F., Japsen, Bonow, J.M., 2010. Compressional reactivation of the Atlantic Margin of Brazil: structural styles and consequences for hydrocarbon exploration. AAPG International Conference and Exhibition. American Association of Petroleum Geologists, Rio de Janeiro, Brazil, #30114.

Coward, M., 1995. Structural and tectonic setting of the Permo-Triassic basins of northwest Europe. Geological Society, London, Special Publications, 91, 7-39.

Cowie, P., Gupta, S., Dawers, N. 2000. Implications of fault array evolution for synrift depocenter development: insights from a numerical fault growth model. Basin Research, 12, 241-261.

Cowie, P. A. and Scholz, C. H. 1992. Growth of faults by accumulation of seismic slip. J. geophys. Res. 97(B7), 11,085-11,095.

Cramez, C., Jackson, M.P.A., 2000. Superimposed deformation straddling the continental–Oceanic transition in deep-water Angola. Mar. Pet. Geol. 17, 1095–1109.

Curewitz, D., Karson, J.A., 1997. Structural settings of hydrothermal outflow: fracture permeability maintained by fault propagation and interaction. J. Volcanol. Geotherm. Res. 79, 149–168.

Dahlstrom, C.D. A., 1969. Balanced cross sections. Can. J. Earth Sci. 6, 743-757.

Dahlen, F.A., Suppe, J., Davis, D., 1984. Mechanics of fold-and-thrust belts and accretionary wedges: cohesive Coulomb theory. J. Geophys. Res. Solid Earth 89 (B12), 10087–10101.

Davis, D., Suppe, J., Dahlen, F.A., 1983. Mechanics of fold-and-thrust belts and accretionary wedges. J. Geophys. Res. Solid Earth 88 (B2), 1153–1172.

Davison, I., 2007. Geology and tectonics of the South Atlantic Brazilian salt basins. Geological Society, London, Special Publications, 272, 345-359.

Davison, I., Bosence, D., Alsop, G. I., Al-Aawah, M. H. 1996. Deformation and sedimentation around active Miocene salt diapirs on the Tihama Plain, northwest Yemen. Geological Society, London, Special Publications, 100, 23-39.

Davison, I., 1999. Tectonics and hydrocarbon distribution along the Brazilian South Atlantic margin. Geological Society, London, Special Publications, 153, 133-151.

Davison, I., Alsop, G., Evans, N., Safaricz, M. 2000. Overburden deformation patterns and mechanisms of salt diapir penetration in the Central Graben, North Sea. Marine and Petroleum Geology, 17, 601-618.

Davis, T., Healy, D., Bubeck, A., Walker, R., 2017. Stress concentrations around voids in three dimensions: The roots of failure. Journal of Structural Geology, 102, 193–207, https://doi.org/10.1016/j.jsg.2017.07. 013

Dawers, N.H., Anders, M.H., 1995. Displacement-length scaling and fault linkage. Journal of Structural Geology. 17, 607–614.

Dawers, N. H., Anders, M. H., Scholz, C. H., 1993. Growth of normal faults: Displacement-length scaling. Geology, 21, 1107-1110.

Demercian, S., Szatmari, P., Cobbold, P. 1993. Style and pattern of salt diapirs due to thin-skinned gravitational gliding, Campos and Santos basins, offshore Brazil. Tectonophysics, 228, 393-433.

DeMets, C., Gordon, R. G., Argus, D. F., 2010. Geologically current plate motions, Geophys. J. Int., 181, 1–80.

De Lugt, I. R., Van Wees, J. D. and Wong, T. E. 2003. The tectonic evolution of the southern Dutch North Sea during the Palaeogene: basin inversion in distinct pulses. Tectonophysics, 373, 141-159.

Dooley, T. P., Jackson, M. P., Hudec, M. R. 2009. Inflation and deflation of deeply buried salt stocks during lateral shortening. Journal of Structural Geology, 31, 582-600.

Dorn, G.A., 1998. Modern 3-D seismic interpretation. Lead. Edge 17, 1262–1270.

Donath, F.A., 1970. Some information squeezed out of rock. Am. Sci. 58, 54-72.

Dunham, K.C., 1988. Pennine mineralization in depth. Proc. Yorks. Geol. Soc. 47, 1-12.

Dunn, D.E., LaFountain, L.J., Jackson, R.E., 1973. Porosity dependence and mechanisms of brittle fracture in sandstones. J. Geophys. Res. 78 (14), 2403-2417.

Duin, E., Doornenbal, J., Rijkers, R., Verbeek, J. and Wong, T. E. 2006. Subsurface structure of the Netherlands-results of recent onshore and offshore mapping. Netherlands Journal of Geosciences, 85, 245.

Duval, B., Cramez, C., Jackson, M.P.A., 1992. Raft tectonics in the Kwanza Basin, Angola. Marine and Petroleum Geology 9, 389-404.

Eberli, G.P., Baechle, G.T., Anselmetti, F.S., Incze, M.L., 2003. Factors controlling elastic properties in carbonate sediments and rocks. The Leading Edge, 22, 654–660. https://doi.org/10.1190/1.1599691.

Ellis, M. A., Dunlap, W. J. 1988. Displacement variation along thrust faults: Implications for the development of large faults. Journal of Structural Geology, 10, 183-192

Eisenstadt, G., DePaor, D.G., 1987. Alternative model of thrust-fault propagation. Geology 15, 630-633.

Expedition 315 Scientists, 2009. Expedition 315 Site C0001: Proceedings of the Integrated Ocean Drilling Program. vol. 314/315/316http://dx.doi.org/10.2204/iodp.proc. 314315316.123.2009.

Expedition 316 Scientists, 2009. Expedition 316 Site C0006. In: Kinoshita, M., Tobin, H., Ashi, J., Kimura, G., Lallemant, S., Screaton, E.J., Curewitz, D., Masago, H., Moe, K.T. (Eds.), The Expedition 314/315/316 Scientists, Proc. IODP, 314/315/316, http://dx. doi.org/10.2204/iodp.proc.314315316.134.2009.

Expedition 333 Scientists, 2012. Site C0018. In: Henry, P., Kanamatsu, T., Moe, K. (Eds.), The Expedition 333 Scientists, Proc. IODP, 333. Integrated Ocean Drilling Program Management International, Inc., Tokyo. http://dx.doi.org/10.2204/iodp.proc.333. 103.2012.

Evans, N., Macleod, J., Macmillan, N., Rorison, P., Salvador, P. 2003. The Banff Field, Blocks 22/27a, 29/2a, UK North Sea. Geological Society, London, Memoirs, 20, 497-507.

Evans, J.P., 1990. Thickness-displacement relationships for fault zones. J. Struct. Geol. 12, 1061-1065.

Faulkner, D.R., Jackson, C.A.L., Lunn, R.J., Schlische, R.W., Shipton, Z.K., Wibberley, C.A.J., Withjack, M.O., 2010. A review of recent developments concerning the structure, mechanics and fluid flow properties of fault zones. J. Struct. Geol. 32, 1557–1575.

Faulkner, D.R., Mitchell, T.M., Jensen, E., Cembrano, J., 2011. Scaling of fault damage zones with displacement and the implications for fault growth processes. J. Geophys. Res. Solid Earth 116 (5), 1 May 2011, Article number B05403.

Ferrill, D.A., Morris, A.P., 2003. Dilational normal faults. Journal of Structural Geology. 25, 183-196.

Ferrill, D.A., Morris, A.P., McGinnis, R.N., Smart, K.J., Ward, W.C., 2011. Fault zone deformation and displacement partitioning in mechanically layered carbonates: The Hidden Valley fault, central Texas. AAPG Bull. 95, 1383-1397.

Ferrill, D.A., Morris, A.P., Jones, S.M., Stamatakos, J.A., 1998. Extensional layer parallel shear and normal faulting. J. Struct. Geol. 20, 355-362. Ferrill, D.A., Morris, A.P., McGinnis, R.N., 2009. Crossing conjugate normal faults in field exposures and seismic data. AAPG Bull. 93, 1471-1488.

Ferrill, D.A., Morris, A.P., McGinnis, R.N., 2012. Extensional fault-propagation folding in mechanically layered rocks: the case against the frictional drag mechanism. Tectonophysics 576-577, 78-85.

Ferrill, D.A., Morris, A.P., 2008. Fault zone deformation controlled by carbonate mechanical stratigraphy, Balcones fault system, Texas. AAPG Bull. 92, 359-380.

Ferrill, D.A., McGinnis, R.N., Morris, A.P., Smart, K.J., Sickmann, Z.T., Bentz, M., Lehrmann, D., Evans, M.A., 2014. Control of mechanical stratigraphy on bed restricted

jointing and normal faulting: eagle Ford Formation, south-central Texas, U.S.A. AAPG Bull. 98, 2477-2506.

Ferrill, D.A., Morris, A.P., McGinnis, R.N., Smart, K.J., 2016. Myths about normal faulting. In: Childs, C., Holdsworth, R.E., Jackson, C.A.-L., Manzocchi, T., Walsh, J.J., Yielding, G. (Eds.), The Geometry and Growth of Normal Faults. Geological Society (London) Special Publications 439. http://doi.org/10.1144/ SP439.12.

Ferrill, D.A., McGinnis, R.N., Morris, A.P., McGinnis, R.N., Smart, K.J., Wigginton, S. S., Hill, N.J., 2017. Mechanical stratigraphy and normal faulting. Review article. J. Struct. Geol. 94, 275-302.

Ferrill, D.A., Morris, A.P., Sims, D.W., Stamatakos, J.A., 2000. Crossing conjugate normal faults. AAPG Bull. 84, 1543-1559.

Ferrill, D.A., Morris, A.P., Smart, K.J., 2007. Stratigraphic control on extensional fault propagation folding: Big Brushy Canyon monocline, Sierra del Carmen, Texas. In: Jolley, S., Barr, D., Walsh, J.J., Knipe, R.J. (Eds.), Structurally Complex Reservoirs, pp. 203-217. Geological Society (London) Special Publication 292.

Ferrill, D.A., Groshong Jr., R.H., 1993. Kinematic model for the curvature of the northern Subalpine Chain, France. J. Struct. Geol. 15, 523-541.

Ferrill, D.A., Winterle, J., Wittmeyer, G., Sims, D., Colton, S., Armstrong, A., Morris, A.P., 1999. Stressed rock strains groundwater at Yucca Mountain, Nevada. GSA Today 9 (5), 1-8.

Fiduk, J. C., Brush, E. R., Anderson, L. E., Gibbs, P. B., Rowan, M. G., 2004. Salt deformation, magmatism, and hydrocarbon prospectivity in the Espirito Santo Basin, offshore Brazil. Salt-sediment interactions and hydrocarbon prospectivity: Concepts, applications, and case studies for the 21st century: Proceedings of Gulf Coast Section SEPM Foundation Bob F. Perkins Research Conference, 2004. SEPM, 370-392.

Fort, X., Brun, J., Chauvel, F., 2004. Salt tectonics on the Angolan margin, syn-sedimentary deformation processes. AAPG Bull. 88, 1523–1544.

Ford, M., Williams, E.A., Artoni, A., Verg_es, J., Hardy, S., 1997. Progressive evolution of a fault-related fold pair from growth strata geometries, Sant Llorenç de Morunys, SE Pyrenees. J. Struct. Geol. 19, 413-441.

Fort, X., Brun, J., Chauvel, F., 2004. Salt tectonics on the Angolan margin, syn sedimentary deformation processes. AAPG Bull. 88, 1523–1544.

Forster, W., 1809. A Treatise on a Section of the Strata, Commencing Near Newcastle upon Tyne and Concluding on the West Side of the Mountain of Cross Fell (With remarks on mineral veins in general. Privately published, Newcastle upon Tyne).

Forster, W., 1821. A Treatise on a Section of the Strata, from Newcastle-upon-Tyne to the Mountain of Cross Fell in Cumberland, with Remarks on Mineral Veins in General. Also, Tables of the Strata, in Yorkshire, Derbyshire, &c. To Which Is Added a Treatise on the Discovery, the Opening, and the Working of Lead Mines; with the Dressing and Smelting of Lead Ores, second ed. John Pattinson, Alston, Cumberland.

Fossen, H., Hesthammer, J. 1997. Geometric analysis and scaling relations of deformation bands in porous sandstone. Journal of Structural Geology, 19, 1479- 1493.

Fossen, H., 2010. Structural Geology. Cambridge University Press (463 pp).

Fossen, H., Rotevatn, A. 2016. Fault linkage and relay structures in extensional settings—A review. Earth-Science Review, 154, 14- 28.

Fossen, H., Johansen, T.E.S., Hesthammer, J., Rotevatn, A., 2005. Fault interaction in porous sandstone and implications for reservoir management; examples from Southern Utah. AAPG Bull. 89, 1593–1606.

França, R. L., Del Rey, A. C., Tagliari, C. V., Brandão, J. R., Fontanelli, P. D. R., 2007. Bacia do Espírito Santo. Boletim de Geociencias da PETROBRAS, 15**,** 501-509.

Freeman, B., Yielhng, G., Badeey, M. E., 1990. Fault correlation during seismic interpretation First Break, 8, 87-95.

Gabrielsen, R.H., Sokoutis, D., Willingshofer, E., Faleide, J.I. 2016. Fault linkage across weak layers during extension: an experimental approach with reference to the Hoop Fault Complex of the SW Barents Sea. Petroleum Geoscience, 22, 123–135.

Gadallah, M., Fisher, R., 1999. An introduction to Exploration Geophysics, springer Germany. pp. 274.

Gamboa, D., Alves, T., Cartwright, J., Terrinha, P., 2010. MTD distribution on a 'passive'continental margin: the Espírito Santo Basin (SE Brazil) during the Palaeogene. Marine and Petroleum Geology, 27, 1311-1324.

Gamboa, D., Alves, T., Cartwright, J. 2011. Distribution and characterization of failed (mega) blocks along salt ridges, southeast Brazil: Implications for vertical fluid flow on continental margins. Journal of Geophysical Research: Solid Earth (1978–2012), 116.

Gartrell, A., Lils, M., Underschultz, J., 2002. Controls on the trap integrity of the Skua oil field, Timor Sea. In: Keep, M., Moss, S.J. (Eds.), The Sedimentary Basins of Western Australia 3: Proceedings of the Petroleum Exploration Society of Australia Symposium, pp. 389–407. Perth

Gartrell, A., Zhang, Y., Lisk, M., Dewhurst, D., 2004. Fault intersections as critical hydrocarbon leakage zones: integrated field study and numerical modelling of an example from the Timor Sea, Australia. Mar. Pet. Geol. 21, 1165–1179.

Gaullier, V., Brun, J.P., Gue´rin, G., Lecanu, H., 1993. Raft tectonics: the effects of residual topography below a salt décollement. Tectonophysics 228, 363-381.

Geoffery, A. D., Mary, J.C., Kenneth, M.T., 1995. Visualization in 3-D seismic interpretation. Acro Exploration and Production Technology Plano, Texas. The Leading Edge. pp. 1045-1049.

Gerling, P., Geluk, M., Kockel, F., Lokhorst, A., Lott, G. and Nicholson, R. 1999. 'NW European Gas Atlas'–new implications for the Carboniferous gas plays in the western part of the Southern Permian Basin. Geological Society, London, Petroleum Geology Conference series, 1999. Geological Society of London, 799-808.

Gibbs, P. B., Brush, E. R., Fiduk, J. C., 2003. The evolution of the syn rift and transition phases of the central/southern Brazilian and W. African conjugate margins: the implications for source rock distribution in time and space, and their recognition on

seismic data. 8th International Congress of the Brazilian Geophysical Society, September 14-18, 2003, Brazil.

Glennie, K. and Provan, D. 1990. Lower Permian Rotliegend reservoir of the southern North Sea gas province. Geological Society, London, Special Publications, 50, 399-416.

Glennie, K. 1997. History of exploration in the southern North Sea. Geological Society, London, Special Publications, 123, 5-16.

Granier, T., 1985. Origin, damping, and pattern of development of faults in granite. Tectonics, 4, 721-737.

Gregory-Wodzicki, K.M., 2010. Uplift history of the Central and Northern Andes: a review. Geol. Soc. Am. Bull. 112, 1091–1105.

Groshong Jr., R.H., 2006. 3-D Structural Geology. Springer-Verlag, Heidelberg, 400pp. Gudmundsson, A., 1987. Tectonics of the Thingvellir fissure swarm, SW Iceland. J. Struct. Geol. 9, 61-69.

Gross, M.R., Gutiérrez-Alonso, G., Bai, T., Wacker, M.A., Collinsworth, K.B. 1997. Influence of mechanical stratigraphy and kinematics on fault scaling relations. Journal of Structural Geology, 19, 171–183, https://doi.org/10.1016/S0191-8141 (96)00085-5

Guardado, L.R., Gamboa, L.A.P. and Lucchesi, C.F., 1989. Petroleum geology of the Campos Basin. a model for a producing Atlantic-type basin. In: J.D. Edwards and P.A. Santogrossi (Editors), Divergent/Passive Margin Basins. Am. Assoc. Pet. Geol. Mem., 48: 3-79.

Gubbins, D., 1990. Seismology and Plate Tectonics. Cambridge University Press, Britain. pp. 339.

Hamblin, W.K., 1965. Origin of 'reverse drag' on the down-throw side of normal faults. Geological Society of American Bulleting. 76, 1145-1164.

Harmsen, S.C., 1994. The Little Skull Mountain, Nevada, earthquake of 29 June 1992: Aftershock focal mechanisms and tectonic stress field implications. Seismol. Soc. Am. Bull. 84, 1484-1505.

Hancock, P.L., 1985. Brittle microtectonics: principles and practice. J. Struct. Geol. 7, 437-457.

Hardman, R., Booth, J., 1991. The significance of normal faults in the exploration and production of North Sea hydrocarbons. Geol. Soc. Lond., Spec. Publ. 56, 1–13

Hart, B.S., 1999. Definition of subsurface stratigraphy, structure and rock properties from 3-D seismic data. Earth-Science Rev. 47, 189–218. doi:10.1016/S0012-8252(99)00029-X

Hardy, S., Poblet, J., 2005. A method for relating fault geometry, slip rate and uplift data above fault-propagation folds. Basin Res. 17, 417-424.

Handin, J., Hager Jr., R.V., 1957. Experimental deformation of sedimentary rocks under confining pressure: tests at room temperature on dry samples. AAPG Bull. 41, 1-50.

Harris, R. A. 1998. Stress Triggers, Stress Shadows, and Implications for Seismic Hazard, Introduction to the Special Issue, J. Geophys. Res., 103, 24347-24358.

Hegna, S., Krokan, B., Selbekk, T., 2001. Single 3D acquisition – A high quality and cost-effective alternative: 71st Annual International Meeting, SEG, expanded Abstract, 48-51.

Heim, S., Lutz, R., Nelskamp, S., Verweij, H., Kaufmann, D., Reinhardt, L., 2013. Geological evolution of the North Sea: cross-border basin modeling study on the Schillground High. Energy Procedia 40, 222–231.

Hoek, E., Brown, E.T., 1988. The Hoek-Brown failure criterionda 1988 update. In: 15th Canadian Rock Mechanics Symposium, pp. 31-38.

Holland, M., Urai, J.L., Martel, S., 2006. The internal structure of fault zones in basaltic sequences. Earth Planet. Sci. Lett. 248, 301-315.

Holdsworth, R.E., Butler, C.A., Roberts, A.M., 1997. The recognition of reactivation during continental deformation. Journal of the Geological Society London 154, 73–78.

Hooper, E.C.D., 1991. Fluid migration along growth faults in compacting sediments. Journal of Petroleum Geology 14 (2), 161–180.

Hudec, M.R., Jackson, M.P. a., 2007. Terra infirma: Understanding salt tectonics. Earth-Science Rev. 82, 1–28. doi:10.1016/j.earscirev.2007.01.001

Ide, S., Baltay, A., Beroza, G.C., 2011. Shallow Dynamic Overshoot and Energetic Deep Rupture in the 2011 Mw 9.0 Tohoku-Oki Earthquake. Science, 332(6036), 1426-1429.

Isaksen, G. H., 2004. Central North Sea hydrocarbon systems: Generation, migration, entrapment, and thermal degradation of oil and gas. AAPG bulletin, 88, 1545-1572.

Jackson, C. A. L. and Rotevatn, A. 2013. 3D seismic analysis of the structure and evolution of a salt-influenced normal fault zone: A test of competing fault growth models. Journal of Structural Geology, 54, 215-234.

Jackson, M. P. A., Vendeville, B. C. 1994. Regional extension as a geologic trigger for diapirism. Geological Society of America Bulletin, 106, 57-73.

Jackson, M. P. A., Talbot, C. J., 1991, A glossary of salt tectonics: The University of Texas at Austin, Bureau of Economic Geology Geological Circular No. 91-4, 44 p.

Jackson, M.P.A., Talbot, C.J., 1994. Advances in salt tectonics. Cont. Deform. 159–179.

Jackson, C. A. L., Jackson, M. P. A., Hudec, M. R., Rodriguez, C. 2014. Internal structure, kinematics, and growth of a salt wall: Insights from 3-D seismic data. Geology, 42, 307-310.

Jackson, C. A. L., Larsen, E., 2009. Temporal and spatial development of a gravity-driven normal fault array: Middle–Upper Jurassic, South Viking Graben, northern North Sea. Journal of Structural Geology, 31, 388-402.

Jackson, C., Lewis, M. M. 2012. Origin of an anhydrite sheath encircling a salt diapir and implications for the seismic imaging of steep-sided salt structures, Egersund Basin, Northern North Sea. Journal of the Geological Society, 169, 593-599.

Jolly, B.A., Lonergan, L., Whittaker, A.C., 2016. Growth history of fault-related folds and interaction with seabed channels in the toe-thrust region of the deep-water Niger delta. Marine and Petroleum Geology 70 (2016) 58-76.

Kearey, P., Brooks, M., Hill, I., 2013. An introduction to geophysical exploration. John Wiley & Sons.

Kettermann, M., Urai, J.L., 2015. Changes in structural style of normal faults due to failure mode transition: first results from excavated scale models. J. Struct. Geol. 74, 105-116.

Knai, T.A., Knipe, R.J. 1998. The Impact of Faults on Fluid Flow in the Heidrun Field. In: Jones, G., Fisher, Q.J. & Knipe, R.J. (eds) Faulting, Fault Sealing and Fluid Flow in Hydrocarbon Reservoirs. Geological Society, London, Special Publications, 147, 269–282, https:// doi.org/10.1144/GSL.SP.1998.147.01.18

Koledoye, B.A., Aydin, A., May, E., 2003. A new process-based methodology for analysis of shale smear along normal faults in the Niger Delta. Am. Assoc. Pet. Geol. Bull. 87, 445–463. Korvin, G. 1992. Fractal models in the Earth Sciences. Elsevier Science Ltd, Oxford, Amsterdam, London.

Kimura, G., Moore, G.F., Strasser, M., Screaton, E., Curewitz, D., Streiff, C., Tobin, H., 2011. Spatial and temporal evolution of the megasplay fault in the Nankai Trough. Geochem. Geophys. Geosyst. 12 (3).

Kimura, G., Koge, H., and Tsuji, T, 2018. Punctuated growth of an accretionary prism and the onset of a seismogenic megathrust in the Nankai Trough. Progress in Earth and Planetary Science, 5(1), 78.

Kim, Y.-S., Andrews, J.R., Sanderson, D.J., 2000. Damage zones around strike-slip fault systems and strike–slip fault evolution, Crackington Haven, southwest England. Geoscience Journal 4, 53-72

Kim, Y.-S., Sanderson, D.J., 2005. The relationship between displacement and length of faults: a review. Earth-Sci. Rev. 68, 317–334.

Kinoshita, M. H., Tobin, N., Eguchi, S. N., 2010. Integrated Ocean Drilling Program Expedition 326 Scientific Prospectus, doi:10.2204/iodp.sp.326.2010.

Kopf, A, M., Strasser, N., Monsees, M. B., Underwood, J. G., 2010. Data report: Particle size analysis of sediments recovered during IODP Expeditions 315 and 316, Sites C0001–C0008, Nankai Trough forearc, off Japan, in Proceedings of the IODP,

vol. 314/315/316, edited by M. Kinoshita et al., Integr. Ocean Drill. Prog. Manage. Int., Inc., Washington, D. C., doi: 10.2204/iodp.proc.314315316.207.2011.

Kristiansen, K., 2011. Vertical fault leakage in the western part of the Hammerfest Basin. Unpublished MSc thesis, University of Bergen, (94 pp.)

Krueger, S. W., Grant, N. T., 2006. Evolution of fault-related folds in the contractional toe of the deep-water Niger Delta. AAPG Annual Convention, 2006. 12.

Lanson, B., Beaufort, D., Berger, G., Baradat, J. & Lacharpagne, J.C. 1996. Illitization of diagenetic kaolinite-to-dickite conversion series: References 367 Late-stage diagenesis of the Lower Permian Rotliegend sandstone reservoir, offshore of the Netherlands. Journal of Sedimentary Research, 66.

Levin, F.K., 1971. Apparent velocity from dipping interface reflections. Geophysics 36, 510-516.

Lackey, J, K., Regalla, C. A., and Moore, G, F., 2020. Tectonic influences on trench slope basin development via structural restoration along the outer Nankai accretionary prism, southwest Japan. Geochemistry, Geophysics, Geosystems, 21, 2020 GC009038. https://doi.org/ 10.1029/2020GC009038

Laubach, S.E., Olson, J.E., Gross, M.R., 2009. Mechanical stratigraphy and fracture stratigraphy. AAPG Bull. 93, 1413-1426.

Lee, S.J., Huang, B.S., Ando, M., Chiu, H.C., Wang. J.H., 2011. Evidence of large-scale repeating slip during the 2011 Tohoku-Oki earthquake, *Geophys. Res. Lett.*, 38, L19306.

Lewis, J.C., Byrne, T.B., Kanagawa, K., 2013. Evidence for mechanical decoupling of the upper plate at the Nankai subduction zone: constraints from core-scale faults at NantroSEIZE Sites C0001 and C0002. Geochem. Geophys. Geosyst. 14 (3), 620–633.

Lewis, K.B., Carter, L., Davey, F.J., 1994. The opening of Cook Strait: interglacial tidal scour and aligning basins at a subduction to transform plate edge. Marine Geology 116, 293–312.

Libak, A., Torabi, A., Alae, B., 2019. Normal fault geometric attribute variations with lithology: examples from the Norwegian Barents Sea. Geological Society London Special Publications, 495, DOI: 10.1144/SP495-2018-164.

Lin, W., Byrne, T.B., Kinoshita, M., McNeill, L.C., Chang, C., Lewis, J.C., Yamamoto, Y., Saffer, D.M., Casey Moore, J., Wu, H.-Y., Tsuji, T., Yamada, Y., Conin, M., Saito, S., Ito, T., Tobin, H.J., Kimura, G., Kanagawa, K., Ashi, J., Underwood, M.B., Kanamatsu, T., 2015. Distribution of stress state in the Nankai subduction zone, southwest Japan, and a comparison with Japan Trench. Tectonophysics 692, 120–130.

Liner, C.L., 2004. Elements of 3D Seismology, Elements of 3D Seismology. PennWell.

Lima, C., 1999. Expressions topographiques et structurales de l'état de compression généralisée au sein de la plaque sud-américaine. PhD Thesis, Université de Rennes 1, France.

Lohr, T., Krawczyk, C.M., Oncken, O., Tanner, D.C., 2008. Evolution of a fault surface from 3D attribute analysis and displacement measurements. Journal of Structural Geology 30, 690-700.

Lonergan, L., Cartwright, J.A. & Jolly, R. 1998. 3-D Geometry of Polygonal Fault Systems. Journal of Structural Geology, 20, 529-548.

Mandl, G., 1988. Mechanics of Tectonic Faulting, Models and Basic Concepts. Elsevier, 407 pp.

Mandl, G., 2005. Rock Joints: The Mechanical Genesis. In: Rock Joints: The Mechanical Genesis.

Mandl, G., Jong, L.N.J., Maltha, A., 1977. Shear Zones in Granular Material. In: Rock Mechanics Felsmechanik Mecanique des Roches, vol. 9, pp. 95-144.

Mansfield, C.S., Cartwright, J.A., 1996. High resolution fault displacement mapping from three-dimensional seismic data: evidence for dip linkage during fault growth. Journal of Structural Geology. 18, 249–263.

Mansfield, C., Cartwright, J., 2001. Fault growth by linkage: observations and implications from analogue models. J. Struct. Geol. 23, 745–763.

Mattos, N. H., Alves, T. M., 2018. Corridors of crestal and radial faults linking salt diapirs in the Espírito Santo Basin, SE Brazil. Tectonophysics, 728, 55-74.

Mauduit, T., Guerin, G., Brun, J.P., Lecanu, H., 1997. Raft tectonics: the effects of basal slope angle and sedimentation rate on progressive extension. Journal of Structural Geology 19, 1219-1230.

Maunde. A., Alves. T.M., Moore, G. F., 2021. Shallow fault systems of thrust anticlines responding to changes in accretionary prism lithology (Nankai, SE Japan). Tectonophysics 812 (2021) 228888, https://doi.org/10.1016/j.tecto.2021.228888.

Maunde, A., Alves, T.M., 2020. Impact of tectonic rafts' gravitational instability on fault reactivation and geometry. J. Struct. Geol. 130 (2020) 103916.

McLeod, A.E., Dawers, N.H., Underhill, J.R., 2000. The propagation and linkage of normal faults: insights from the Strathspey-Brent-Statfjord fault array, northern North Sea. Basin Res. 12, 263-284.

McClay, K. R. 1990. Extensional fault systems in sedimentary basins: a review of analogue model studies. Marine and Petroleum Geology, 7, 206–233.

Mégard, F., 1984. The Andean orogenic period and its major structures in central and northern Peru. J. Geol. Soc. Lond. 141, 893–900.

Mégard, F., Noble, D.C., McKee, E.H., Bellon, H., 1984. Multiple pulses of Neogene compressive deformation in the Ayacucho intermontane basin, Andes of central Peru. Geol. Soc. Am. Bull. 95, 1108–1117.

Meisling, K.E., Cobbold, P.R., Mount, V.S., 2001. Segmentation of an obliquely rifted margin, Campos and Santos basins, southeastern Brazil. American Association of Petroleum Geologists Bulletin 85 (11), 1903–1924.

Mello, M., Maxwell, J. 1990. Organic Geochemical and Biological Marker Characterization of Source Rocks and Oils Derived from Lacustrine Environments in the Brazilian Continental Margin: Chapter 5.

Meyer, V., Nicol, A., Childs, C., Walsh, J., Watterson, J., 2002. Progressive localisation of strain during the evolution of a normal fault population. Journal of Structural Geology, 24, 1215-1231.

Micallef, A., Mountjoy, J.J., 2011. A topographic signature of a hydrodynamic origin for submarine gullies. Geology 39, 115–118.

Micklethwaite, S., Cox, S.F., 2004. Fault-segment rupture, aftershock-zone fluid flow, and mineralization. Geology 32, 813.

Micklethwaite, S., Cox, S., 2006. Progressive fault triggering and fluid flow in aftershock domains: examples from mineralized Archaean fault systems. Earth Planet. Sci. Lett. 250, 318–330.

Miyazaki, S., Heki, S., 2001. Crustal velocity field of southwest Japan: Subduction and arc-arc collision, J. Geophys. Res., 106, 4305–4326.

Mondol, N.H., Bjørlykke, K., Jahren, J., Høeg, K., 2007. Experimental mechanical compaction of clay mineral aggregates – Changes in physical properties of mudstones during burial. Marine and Petroleum Geology, 5, 289–311, https://doi.org/10.1016/j.marpetgeo. 2007.03.006

Moore, G. F., Bangs, N. L., Taira, A., Kuramoto, S., Pangborn, E., and Tobin, H. J., 2007. Three-dimensional splay fault geometry and implications for tsunami generation. Science, 318(5853), 1128–1131.

Moore, G. F., Boston, B. B., Sacks, A. F., Saffer, D. M., 2013. Analysis of normal fault populations in the Kumano Forearc Basin, Nankai Trough, Japan: 1. Multiple orientations and generations of faults from 3-D coherency mapping, Geochem. Geophys. Geosyst., 114, 1989–2002.

Moore, G.F., Park, J.O., Bangs, N.L., Gulick, S.P., Tobin, H.J., Nakamura, Y., Sato, S., Tsuji, T.,Yoro, T., Tanaka, H., Uraki, S., Kido, Y., Sanada, Y., Kuramoto, S., Taira, A., 2009. Structural and seismic stratigraphic framework of the NanTroSEIZE Stage 1 transect. In: Kinoshita, M., Tobin, H., Ashi, J., Kimura, G., Lallemant, S., Screaton, E.J., Curewitz, D., Masago, H., Moe, K.T., the Expedition 314/315/316 Scientists (Eds.), Proc. IODP, 314/315/316. (Integrated Ocean Drilling Program Management

International, Inc.), Washington, DC. http://dx.doi.org/10.2204/iodp.proc. 314315316.102.2009.

Moore, G.F., Boston, B.B., Strasser, M., Underwood, M.B., Ratliff, R.A., 2015. Evolution of tectono-sedimentary systems in the Kumano Basin, Nankai trough forearc. Mar. Pet. Geol. 67, 604–616.

Mountjoy, J.J., Barnes, P.M., Pettinga, J.R., 2009. Morphostructure and evolution of submarine canyons across an active margin: Cook Strait sector of the Hikurangi Margin, New Zealand. Marine Geology 260, 45–68.

Mohriak, W. U., Rabelo, J. L., De Matos, R. D., De Barros, M. C., 1995. Deep seismic reflection profiling of sedimentary basins offshore Brazil: Geological objectives and preliminary results in the Sergipe Basin. Journal of Geodynamics, 20, 515-539.

Mohriak, W., Nemčok, M., Enciso, G., 2008. South Atlantic divergent margin evolution: rift-border uplift and salt tectonics in the basins of SE Brazil. Geological Society, London, Special Publications, 294, 365-398.

Mohriak, W. U., Szatmari, P., Anjos, S. 2012. Salt: geology and tectonics of selected Brazilian basins in their global context. Geological Society, London, Special Publications, 363, 131-158.

Mohriak, W. U., Palagi, P. R., Mello, M. R., 1998. Tectonic evolution of south Atlantic salt basins: AAPG Bull., v.82, no.10, p. 1945.

Mohriak, W.U., 2003. Bacias sedimentares da margem continental Brasileira. In: Bizzi, L.A., Schobbenhaus, C., Vidotti, R.M., Goncalves, J.H. (Eds.), Geologia, Tectonica e Recursos Minerais do Brasil. CPRM, Brasilia, pp. 87-165.

Morad, S. 1998. Carbonate Cementation in Sandstones. Blackwell Science, Oxford.

Moreira, J.L., Carminatti, M., 2004. Eocene slope and basin depositional systems in the Santos Basin. Bol. Geociênc. Petrobras 12, 73–87.

Morley, C.K., 2002. Evolution of large normal faults: evidence from seismic reflection data. AAPG Bull. 86, 961–978.

Morley, C.K., 2007. Development of crestal normal faults associated with deep-water fold growth. J. Struct. Geol. 29, 1148-1163.

Morley, C. K. 1999. Patterns of displacement along large normal faults: implications for basin evolution and fault propagation, based on examples from east Africa. AAPG bulletin, 83, 613-634.

Morris, A.P., Ferrill, D.A., McGinnis, R.N., 2009. Mechanical stratigraphy and faulting in Cretaceous carbonates. AAPG Bull. 93, 1459-1470.

Morris, A.P., Smart, K.J., Ferrill, D.A., Reish, N.E., Cowell, P.F., 2012. Fault compartmentalization in clastic reservoirs. AAPG Bull. 96, 1001-1015.

Morris, A.P., Ferrill, D.A., Henderson, D.B., 1996. Slip tendency analysis and fault reactivation. Geology 24, 275-278.

Mukherjee, S., Talbot, C. J., Koyi, H. A. 2010. Viscosity estimates of salt in the Hormuz and Namakdan salt diapirs, Persian Gulf. Geological Magazine, 147, 497-507.

Nalpas, T., Le Douaran, S., Brun, J.P., Unternehr, P. and Richert, J.P. 1995. Inversion of the Broad Fourteens Basin (offshore Netherlands), a small-scale model investigation. Sedimentary Geology, 95, 237-250.

Nelson, T. H., Fairchild, L. 1989. Emplacement and evolution of salt sills in the northern Gulf of Mexico. Houston Geological Society Bulletin, 32, 6-7.

Nicol, A., Walsh, J., Berryman, K., Nodder, S., 2005. Growth of a normal fault by the accumulation of slip over millions of years. Journal of Structural Geology 27 (2), 327–342.

Ojeda, H., 1982. Structural framework, stratigraphy, and evolution of Brazilian marginal basins. AAPG Bulletin, 66, 732-749.

Omosanya, K.O., Alves, T.M., 2014. Mass-transport deposits controlling fault propagation, reactivation and structural decoupling on continental margins (Espírito Santo Basin, SE Brazil). Tectonophysics, 628, 158-171.

Oudmayer, B. C. and De Jager, J. 1993. Fault reactivation and oblique-slip in the Southern North Sea. In: Parker, J. R., ed. Petroleum Geology of Northwest Europe: Proceedings of the 4th Conference, 1993 London. The Geological Society, 1281-1290.

Park, J.O., Fujie, G., Wijerathne, L., Hori, T., Kodaira, S., Fukao, Y., Moore, G.F., Bangs, N.L., Kuramoto, S., Taira, A., 2010. A low-velocity zone with weak reflectivity along the Nankai subduction zone. Geology 38 (3), 283–286.

Pascoe, R., Hooper, R., Storhaug, K., Harper, H., 1999. Evolution of extensional styles at the southern termination of the Nordland Ridge, Mid-Norway: a response to variations in coupling above Triassic salt. In: Fleet, A.J., Boldy, S.A.R. (eds) Petroleum Geology of Northwest Europe: Proceedings of the 5th Conference. Geological Society, London, 83–90.

Peacock, D.C.P., 2002. Propagation, interaction and linkage in normal fault systems. Earth Sci. Rev. 58, 121–142.

Peacock, D.C.P., Sanderson, D.J., 1991. Displacements, segment linkage and relay ramps in Normal fault zones. Journal of Structural Geology. 13, 721–733.

Peacock, D.C.P., Sanderson, D.J., 1992. Effects of layering and anisotropy on fault geometry. J. Geol. Soc. Lond. 149, 793-802.

Peacock, D.C.P., Parfitt, E.A., 2002. Active relay ramps and normal fault propagation on Kilauea Volcano, Hawaii. J. Struct. Geol. 24, 729–742

Peacock, D.C.P., Zhang, X., 1993. Field examples and numerical modeling oversteps and bends along normal faults in cross section. Tectonophysics 234, 147-167.

Peltonen, C., Marcussen, Ø., Bjørlykke, K., Jahren, J., 2009. Clay mineral diagenesis and quartz cementation in mudstones: The effects of smectite to illite reaction on rock properties. Marine and Petroleum Geology, 26, 887–898, https://doi.org/10.1016/j.marpetgeo. 2008.01.021

Penge, J., Munns, J.W., Taylor, B., Windle, T.M.F., 1999. Rift–raft tectonics: examples of gravitational tectonics from the Zechstein basins of northwest Europe. Geological Society, London, Petroleum Geology Conference series 5, 201-213.

Petri, S. 1987. Cretaceous paleogeographic maps of Brazil. Palaeogeography, Palaeoclimatology, Palaeoecology, 59, 117-168.

Piedade, A., Alves, T. M., 2017. Structural styles of Albian rafts in the Espírito Santo Basin (SE Brazil): Evidence for late raft compartmentalisation on a 'passive' continental margin. Marine and Petroleum Geology 79, pp. 201-221.

Pilcher, R.S., Murphy, R.T., Ciosek, J.M., 2014. Jurassic raft tectonics in the north-eastern Gulf of Mexico. Interpretation 2, SM39-SM55.

Plummer, P. S. and Gostin, V. A. 1981. Shrinkage cracks: desiccation or syneresis. Journal of Sedimentary Petrology 51, 1147-1156.

Posamentier, H. W., Kolla, V. 2003. Seismic geomorphology and stratigraphy of depositional elements in deep-water settings. Journal of Sedimentary Research, 73, 367-388.

Poblet, J., Hardy, S., 1995. Reverse modelling of detachment folds; application to the Pico del Aguila anticline in the South-Central Pyrenees (Spain). J. Struct. Geol. 17, 1707-1724.

Pollard, D. D., Aydin, A. 1984. Propagation and linkage of oceanic ridge segments. Journal of Geophysical Research: Solid Earth, 89, 10017-10028.

Price, N. J., Cosgrove, J. W. 1990. Analysis of Geological Structures. Cambridge University Press, Cambridge.

Price, N.J., 1966. Fault and Joint Development in Brittle and Semi-brittle Rock. Pergamon Press, 176 pp.

Purvis, K. 1992. Lower Permian Rotliegend sandstones, southern North Sea: a case study of sandstone diagenesis in evaporite-associated sequences. Sedimentary Geology, 77, 155-171.

Quirk, D. Interpreting the Upper Carboniferous of the Dutch Cleaver Bank High. Geological Society, London, Petroleum Geology Conference series, 1993. Geological Society of London, 697-706.

Ramsay, J. G. 1967. The Folding and Fracturing of Rocks. McGraw-Hill, New York.

Ramsey, J.M., Chester, F.M., 2004. Hybrid fracture and the transition from extension fracture to shear fracture. Nature 428, 63-66.

Richardson, N.J., Underhill, J.R., Lewis, G., 2005. The role of evaporite mobility in modifying subsidence patterns during normal fault growth and linkage, Halten Terrace, Mid-Norway. Basin Research, 17, 203–223.

Richard, P., Krantz, R.W., 1991. Experiments on fault reactivation in strike-slip mode. Tectonophysics 188 (1-2), 117–131.

Roche, V., Homberg, C., Rocher, M., 2012. Architecture and growth of normal fault zones in multilayer systems: a 3D field analysis in the South-Eastern Basin, France. J. Struct. Geol. 37, 19-35.

Roche, V., Homberg, C., Rocher, M., 2013. Fault nucleation, restriction, and aspect ratio in layered sections: quantification of the strength and stiffness roles using numerical modeling. J. Geophys. Res. Solid Earth 118, 1-15.

Rotevatn, A., Buckley, S.J., Howell, J.A., Fossen, H., 2009. Overlapping faults and their effect on fluid flow in different reservoir types: a LIDAR-based outcrop modeling and flow simulation study. AAPG Bull. 93, 407–427.

Rotevatn, A., Fossen, H., 2011. Simulating the effect of subseismic fault tails and process zones in a siliciclastic reservoir analogue: implications for aquifer support and trap definition. Mar. Pet. Geol. 28, 1648–1662.

Rouby, D., Guillocheau, F., Robin, C., Bouroullec, R., Raillard, S., Castelltort, S., Nalpas, T. 2003. Rates of deformation of an extensional growth fault/raft system (offshore Congo, West African margin) from combined accommodation measurements and 3-D restoration. Basin Research, 15, 183-200.

Rowan, M. G., Lawton, T. F., Giles, K. A., Ratliff, R. A. 2003. Near-salt deformation in La Popa basin, Mexico, and the northern Gulf of Mexico: A general model for passive diapirism. AAPG bulletin, 87, 733-756.

Rowan, M. G., Jackson, M. P. A., Trudgill, B. D. 1999. Salt-related fault families and fault welds in the northern Gulf of Mexico. AAPG Bulletin, 83, 1454-1484.

Rowan, M. G. 2014. Passive-margin salt basins: hyperextension, evaporite deposition, and salt tectonics. Basin Research, 26, 154-182.

Savage, H.M., Brodsky, E.E., 2011. Collateral damage: evolution with displacement of fracture distribution and secondary fault strands in fault damage zones. J. Geophys. Res. 116, B03405. http://dx.doi.org/10.1029/2010JB007665.

Schlische, R. W., Young, S. S., Ackermann, R. V., Gupta, A. 1996. Geometry and scaling relations of a population of very small rift-related normal faults. Geology, 24, 683-686.

Schöpfer, M.P.J., Childs, C., Walsh, J.J. 2006. Localization of normal faults in multilayer sequences. Journal of Structural Geology, 28, 816–833, https://doi.org/10.1016/j.jsg.2006.02.003.

Schoenherr, J., Urai, J. L., Kukla, P. A., Littke, R., Schleder, Z., Larroque, J.-M., Newall, M. J., Al-Abry, N., Al-Siyabi, H. A., Rawahi, Z. 2007. Limits to the sealing capacity of rock salt: A case study of the infra-Cambrian Ara Salt from the South Oman salt basin. AAPG bulletin, 91, 1541-1557.

Scholz, C., Dawers, N., Yu, J. Z., Anders, M., Cowie, P., 1993. Fault growth and fault scaling laws: preliminary results. Journal of Geophysical Research: Solid Earth (1978–2012), 98, 21951-21961.

Scholz. C. H. 1990. Mechanics of Faulting and Earthquakes. Cambridge University Press, Cambridge.

Schultz, R. A., Fossen, H. 2002. Displacement–length scaling in three dimensions: the importance of aspect ratio and application to deformation bands. Journal of Structural Geology, 24, 1389-1411.

Schultz-Ela, D. D., Jackson, M. P. A., 1996. Relation of subsalt structures to suprasalt structures during extension: AAPG Bulletin, v. 80, p. 1896–1924.

Segall, P., Pollard, D. D. 1983. Nucleation and growth of strike slip faults in granite. Journal of Geophysical Research: Solid Earth, 88, 555-568.

Seno, T., Stein, S., Gripp, A.E., 1993. A model for the motion of the Philippine Sea plate consistent with NUVEL-1 and geological data. J. Geophys. Res 98, 17941–17948.

Shaw, J.H., Novoa, E., Connors, C.D., 2004. Structural controls on growth stratigraphy in contractional fault-related folds. In: McClay, K.R. (Ed.), Thrust Tectonics and Hydrocarbon Systems: AAPG Memoir, Vol. 82, pp. 400-412.

Shaw, J.H., Connors, C.D., Suppe, J., 2006. Seismic interpretation of contractional fault-related folds: an AAPG seismic atlas. AAPG Stud. Geol. 53, 156.

Sheriff, R. E., Geldart, L. P., 1995. Exploration Seismology, Second Edition, Cambridge University Press., pp. 3-6.

Shipton, Z.K., Cowie, P.A., 2001. Damage zone and slip-surface evolution over mm to km scales in high-porosity Navajo Sandstone, Utah. J. Struct. Geol. 23, 1825-1844.

Shipton, Z.K., Soden, A.M., Kirkpatrick, J.D., Bright, A.M., Lunn, R.J., 2006. How thick is a fault? Fault displacement-thickness scaling revisited. In: Earthquakes: Radiated Energy and the Physics of Faulting. American Geophysical Union, pp. 193-198. Geophysical Monograph Series 170.

Sibson, R. H., 1985. A note on fault reactivation. Journal of Structural Geology, 7, 751-754.

Smart, K.J., Ferrill, D.A., Morris, A.P., Bichon, B.J., Riha, D.S., Huyse, L., 2010. Geomechanical modeling of an extensional fault-propagation fold: Big Brushy Canyon monocline, Sierra del Carmen, Texas. AAPG Bull. 94, 221-240.

Smart, K.J., Ofoegbu, G.I., Morris, A.P., McGinnis, R.N., Ferrill, D.A., 2014. Geomechanical modeling of hydraulic fracturing: why mechanical stratigraphy, stress state, and pre-existing structure matter. AAPG Bull. 98, 2237-2261.

Soliva, R., Schultz, R.A., Benedicto, A., 2005. Three-dimensional displacement-length scaling and maximum dimension of normal faults in layered rocks. Geophysical Research Letters, 32, 1–4, https://doi.org/10. 1029/2005GL023007.

Stewart, S. A. and Coward, M. P. 1995. Synthesis of salt tectonics in the southern North Sea, UK. Marine and Petroleum Geology, 12, 457-475.

Stewart, S., Ruffell, A., Harvey, M. 1997. Relationship between basement-linked and gravity-driven fault systems in the UKCS salt basins. Marine and Petroleum Geology, 14, 581-604.

Stewart, S.A., 2001. Displacement distributions on extensional faults: implications for fault stretch, linkage, and seal. AAPG Bull. 85, 587–600.

Stone, W.N., Siever, R., 1996. Quantifying compaction, pressure solution and quartz cementation in moderately- and deeply-buried quartzose sandstones from the greater Green River Basin, Wyoming. In: Crossey, L.J., Loucks, R., Totten, M.W. and Scholle, P.A. (eds) Siliciclastic Diagenesis and Fluid Flow. Society for Sedimentary Geology Special Publications, 55, 129–150.

Strasser, M., Dugan, B., Kanagawa, K., Moore, G.F., Toczko, S., Maeda, L., The Expedition 338 Scientists, 2014. Site C0018: Proceedings of the Integrated Ocean Drilling Program. vol. 338. pp. 2.

Strasser, M., Henry, P., Kanamatsu, T., Thu, M.K., Moore, G.F., 2012. Scientific drilling of mass-transport deposits in the Nankai accretionary wedge: first results from IODP Expedition 333. In: Yamada, Y., et al. (Eds.), Submarine Mass Movements and Their Consequences. Advances in Natural and Technological Hazard Research, pp. 671–681. https://doi.org/10.1007/978-94-007-2162-3_60.

Strozyk. F., van Gent. H.W., Urai. J., Kukla. P.A., 2012. 3D seismic study of complex intra-salt deformation: An example from the Upper Permian Zechstein 3 stringer, western Dutch Offshore. Geological Society London Special Publications 363(1):489-501, DOI: 10.1144/SP363.23

Taira, A., 2001. Tectonic evolution of the Japanese Island Arc System. Annual Reviews of Earth and Planetary Science, 29(1), 109–134.

Talbot, C.J., Jackson, M.P.A., 1987. Internal Kinematics of Salt Diapirs. Am. Assoc. Pet. Geol. Bull.

Talbot, C. J., Rogers, E. A. 1980. Seasonal movements in a salt glacier in Iran. Science, 208, 395-397.

Tao, Z., Alves, T.M., 2019. Impacts of data sampling on the interpretation of normal fault propagation and segment linkage. Tectonophysics 762, 79-96.

Torabi, A., Zarifi, Z., 2013. Energy release rate of propagating deformation bands and their hosted cracks. International Journal of Rock Mechanics and Mining Sciences, 67, 184–190, https://doi.org/10.1016/j. ijrmms.2013.10.007

Torabi, A., Berg, S. S. 2011. Scaling of fault attributes: A review. Marine and Petroleum Geology, 28, 1444-1460.

Tsuji, T., Ashi, J., Ikeda, Y., 2014. Strike-slip motion of a mega-splay fault system in the Nankai oblique subduction zone. Earth, Planets Space 66 (1), 1–14.

Tvedt, A.B.M., Rotevatn, A., Jackson, C.A.L., Fossen, H., Gawthorpe, R.L. 2013. Growth of normal faults in multilayer sequences: A 3D seismic case study from the Egersund Basin, Norwegian North Sea. Journal of Structural Geology, 55, 1–20.

Toniatti, G., 2003. Brazil furthers its leadership in deep-water E&P world oil, 224 (11), 68-72. Viana, A., Figueiredo, A., Faugres, J.-C., Lima, A., Gonthier, E., Brehme, I., Zaragosi, S. 2003. The São Tom deep-sea turbidite system (southern Brazil Basin): Cenozoic seismic stratigraphy and sedimentary processes. AAPG bulletin, 87, 873-894.

Ursin, E., 1990. Offset-dependent geometric spreading in a layered medium. Geophysics 55, 492-496.

Van Tuyl, J., Alves, T.M., Moore, G.F., 2015. Strain decoupling reveals variable seismogenic risk in SE Japan (Nankai Trough). Geochem. Geophys. Geosyst. 16 (7), 2025–2037.

Van Balen, R., Van Bergen, F., De Leeuw, C., Pagnier, H., Simmelink, H., Van Wees, J. and Verweij, J. 2000. Modelling the hydrocarbon generation and migration in the West Netherlands Basin, the Netherlands. Geologie en Mijnbouw, 79, 29-44.

Van Hulten, F. F. N. 2010. Geological factors effecting compartmentalization of Rotliegend gas fields in the Netherlands. Geological Society, London, Special Publications, 347, 301-315.

Van Adrichem Boogaert, H. and Kouwe, W. 1993. Stratigraphic nomenclature of the Netherlands, revision, and update by RGD and NOGEPA. Mededelingen Rijks Geologische Dienst, 50, 1-40.

Van Wijhe, D. V. 1987. Structural evolution of inverted basins in the Dutch offshore. Tectonophysics, 137, 171-219.

Van Verweij, J. M. and Simmelink, H. J. 2002. Geodynamic and hydrodynamic evolution of the Broad Fourteens Basin (The Netherlands) in relation to its petroleum systems. Marine and Petroleum Geology, 19, 339-359.

Van Wees, J.-D., Stephenson, R., Ziegler, P., Bayer, U., McCann, T., Dadlez, R., Gaupp, R., Narkiewicz, M., Bitzer, F., Scheck, M., 2000. On the origin of the southern Permian Basin, central Europe. Mar. Pet. Geol. 17, 43–59.

Van Wees, J.D., Stephenson, R., Ziegler, P., Bayer, U., Mccann, T., Dadlez, R., Gaupp, R., Narkiewicz, M., Bitzer, F. & Scheck, M. 2000. On the origin of the southern Permian Basin, central Europe. Marine and Petroleum Geology, 17, 43-59.

Van Keken, P., Spiers, C., Van Den Berg, A., Muyzert, E. 1993. The effective viscosity of rocksalt: implementation of steady-state creep laws in numerical models of salt diapirism. Tectonophysics, 225, 457-476.

Vendeville, B.C., 2005. Salt tectonics driven by sediment progradation: Part I—Mechanics and kinematics. AAPG Bulletin 89, 1071-1079.

Vendeville, B. C., Jackson, M. P. A. 1992. The rise of diapirs during thin-skinned extension. Marine and Petroleum Geology, 9, 331-354.

Vermeer, Gijs, J.O., 2012. 3D Seismic Survey Design, Second Edition, Published by Society of Exploration Geophysicists. pp. 143.

Viana, A., Figueiredo, A., Faugeres, J.-C., Lima, A., Gonthier, E., Brehme, I., Zaragosi, S., 2003. The São Tomé deep-sea turbidite system (southern Brazil Basin): Cenozoic Seismic stratigraphy and sedimentary processes. AAPG Bull. 87, 873–894.

Vieira, P. E., Bruhn, C. H. L., Santos, C. F., Del Rey, A. C., Alves, R. G., 2007. Golfinho Field-Discovery, Development, and Future Prospects. Offshore Technology Conference.

Walsh, J.J., Watterson, J., 1989. Displacement gradients on fault surfaces. Journal of Structural Geology. 11, 307–316.

Walsh, J.J., Watterson, J., 1988. Dips of normal faults in British Coal Measures and other sedimentary sequences. J. Geol. Soc. Lond. 145, 859-873.

Walsh, J., Watterson, J., 1987. Distributions of cumulative displacement and seismic slip on a single normal fault surface. Journal of Structural Geology, 9, 1039- 1046.

Walsh, J. J., Watterson, J. 1991. Geometric and kinematic coherence and scale effects in normal fault systems. Geological Society, London, Special Publications, 56, 193-203.

Walsh, J., Bailey, W., Childs, C., Nicol, A., Bonson, C., 2003. Formation of segmented normal faults: a 3-D perspective. Journal of Structural Geology, 25, 1251-1262.

Walsh, J., Nicol, A., Childs, C. 2002. An alternative model for the growth of faults. Journal of Structural Geology, 24, 1669-1675.

Wallace, W., 1861. The Laws Which Regulate the Deposition of Lead Ores in Veins: Illustrated by Examination of the Geologic Structure of the Mining Districts of Alston Moor. Stanford, London.

Wang, K., Hu, Y., 2006. Accretionary prisms in subduction earthquake cycles: The theory of dynamic Coulomb wedge. J. Geophys. Res. Solid Earth 111 (B6).

Ward, N.I., Alves, T.M., Blenkinsop, T.G., 2016. Reservoir leakage along concentric faults in the Southern North Sea: Implications for the deployment of CCS and EOR techniques. Tectonophysics 690, 97-116.

Warren, J.K., 2006. Evaporites: sediments, resources and hydrocarbons. Springer Science & Business Media.

Watson, T.H., 2009. Project AMES at Gulf Research and Development Company: 35th Anniversary of a landmark 3D survey: The Leading Edge, 28, 1338-1341.

Welch, M.J., Davies, R.K., Knipe, R.J., Tueckmantel, C., 2009. A dynamic model for fault nucleation and propagation in a mechanically layered section. Tectonophysics 474, 473-492.

White, S.H., Bretan, P.G., Rutter, E.H., 1986. Fault-zone reactivation: kinematics and mechanisms. Philosophical Transactions of the Royal Society of London A317, 81–97.

Wilkins, S.J., Gross, M.R., 2002. Normal fault growth in layered rocks at Split Mountain, Utah: influence of mechanical stratigraphy on dip linkage, fault restriction and fault scaling. Journal of Structural Geology 24 (9), 1413–1429.

Willemse, E. J., Pollard, D. D., Aydin, A. 1996. Three-dimensional analyses of slip distributions on normal fault arrays with consequences for fault scaling. Journal of Structural Geology, 18, 295-309

Withjack, M.O., Callaway, S., 2000. Active normal faulting beneath a salt layer: An experimental study of deformation patterns in the cover sequence. AAPG Bulletin, 84, 627–651.

Wiprut, D., Zoback, M.D., 2000. Fault reactivation and fluid flow along a previously dormant normal fault in the northern North Sea. Geology 28, 595–598.

Wiprut, D., Zoback, M.D., 2002. Fault reactivation, leakage potential, and hydrocarbon column heights in the northern North Sea. Norwegian Petroleum Society Special Publications Vol. 11, pp. 203–219.

Wong, T. E., Parker, N. & Horst, P. 2001. Tertiary sedimentary development of the Broad Fourteens area, the Netherlands. Geologie en Mijnbouw, 80, 85-94.

Wu, H.Y., Chan, C.H., Kinoshita, M., Saito, S., 2013. Stress field observation and modelling from the NanTroSEIZE scientific drillings in the Nankai Trough system, SW Japan. Tectonophysics 600, 99–107.

Xiao, H., Suppe, J., 1989. Role of compaction in the listric shape of growth normal faults. AAPG Bull. 73, 777-786

Yilmaz, Ö.Z., 2001. Seismic data analysis. Published by Society of Exploration Geophysicists. pp. 549.

Yu, Y., Tang, L., Yang, W., Huang, T., Qiu, N., Li, W. 2014. Salt structures and hydrocarbon accumulations in the Tarim Basin, northwest China. AAPG Bulletin, 98, 135-159.

Zhou, H.-W., 2014. Practical Seismic Data Analysis. Cambridge University Press.

Zhang, L., Luo, X., Vasseur, G., Yu, C., Yang, W., Lei, Y., Song, C., Yu, L., Yan, J., 2011. Evaluation of geological factors in characterizing fault connectivity during hydrocarbon migration: application to the Bohai Bay Basin. Mar. Pet. Geol. 28, 1634–1647.

Zhang, P., Slemmons, D. B. and Mao, F. 1991. Geometric pattern, rupture termination and fault segmentation of the Dixie Valley-Pleasant Valley normal fault system, Nevada, U.S.A. Journal of Structural Geology, 13, 165-176.

Ziegler, P. A. 1990. Geological atlas of western and central Europe, Shell Internationale Petroleum, Maatschappij B.V., The Hague.

Zoback, M.D., 2007. Reservoir Geomechanics. Cambridge University Press, Cambridge, 449 pp.